Texas A&M Institute for Preclinical Studies
TEXAS A&M UNIVERSITY

NUCLEAR ENGINEERING
TEXAS A&M UNIVERSITY

Monday, August 1, 2016

Office of Science
U.S. Department of Energy
19901 Germantown Road
Germantown MD 20874-1290
U.S.A.

Ref.: Final technical report for award: **DE-SC0008433**

Dear Sirs,

Enclosed, please find a final technical report of our project "The Texas A&M Radioisotope Production and Radiochemistry Program" for the award years 2011-2016. It describes the activities of the project carried out and results produced during the validity of the above award. I hope that you find this report in order. Texas A&M University Sponsored Research Services (SRS) has, as I understand, supplied the DOE accounts office with the detailed financial reports regarding the activities of the award.

Sincerely,

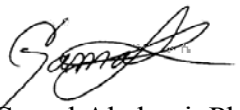

Gamal Akabani, PhD

cc:
Dr. Marc Garland, Program Manager, Office of Science, DOE: marc.garland@hq.deo.gov
Mr. Ryan McDaniel, TAMU Sponsored Research Services: ryanmcdaniel@tamu.edu
Ms. Victoria Curry, Office of Science, DOE: Victoria.curry@hq.doe.gov

800 Raymond Stotzer Parkway, Room 1083A
4478 TAMU
College Station, TX 77843-4478
Phone: 979-458-1699
Mobile: 979-676-0695
Email: akabani@tamu.edu
http://tips.tamu.edu
http://engineering.tamu.edu/nuclear

FINAL TECHNICAL REPORT

August 31, 2016

Report submitted to: Office of Science, Department of Energy.

DOE Award number: DE-SC0008433

Grant Title: The Texas A&M Radioisotope Production and Radiochemistry Program

Personnel:

Dr. Gamal Akabani
Dr. Robert Tribble
Dr. Gabriel Tabacaru

PhD Students

Mr. Michael Martin, Doctoral Candidate
Mr. Ryan Clanton, Doctoral Candidate
Mr. Jordan Douglas, Doctoral Candidate

MS Students

Mr. Tyler Cantrell, MS, Masters of Science
Mr. Zaher Hamoui, MS, Masters of Science
Mr. Michael Hackemack, MS, Masters of Science

Undergraduate Students

Mr. Matt Schaper,
Mr. Eden Marroquin,
Mr. Talal Harahsheh,
Mr. Miltiadis Kennas,
Mr. Yousif Almaazmi
Ms. Elizabeth Tindle
Mr. Richard Vega
Ms. Leanne Kristek

Name of Submitter: Dr. Gamal Akabani, Principal Investigator.
Department of Nuclear Engineering
Department of Veterinary Integrative Biosciences,
Texas A&M University
College Station, TX 77843

Recipient Organization: Texas A&M University
College Station, TX 77843

Grant Period: July 1, 2011 to August 30, 2016
Report frequency: Final

Abstract

The main motivation of the project at Texas A&M University was to carry out the production of critically needed radioisotopes used in medicine for diagnostic and therapy, and to establish an academic program in radionuclide production and separation methods. After a lengthy battle with the Texas A&M University Radiation Safety Office, the Texas Department of State Health Services granted us a license for the production of radionuclides in July 2015 allowing us to work in earnest in our project objectives. Experiments began immediately after licensing and we started the assembly and testing of our target systems. There were four analytical/theoretical projects and two experimental target systems. These were for At-211 production and for Zn-62/Cu-62 production. The theoretical projects were related to the production of Mo-99/Tc-99m using a) a subcritical aqueous target system and b) production of Tc-99m from accelerator generated Mo-99 utilizing a photon-neutron interaction with enriched Mo-100 targets. The two experimental projects were the development of targetry systems and production of At-211 and Zn-62/Cu-62 generator. The targetry system for At-211 has been tested and production of At-211 is chronic depending of availability of beam time at the cyclotron. The installation and testing of the targetry system for the production of Zn-62/Cu-62 has not been finalized. A description of the systems is described. The academic program in radionuclide production and separation methods was initiated in the fall of 2011 and due to the lack of a radiochemistry laboratory it was suspended. We expect to re-start the academic program at the Texas A&M Institute for Preclinical Studies under the Molecular Imaging Program.

Contents:

1. Publications in Peer-Reviewed International Journals and Student Presentation Awards

The present is based on work accomplished with the present award. These are related to radioisotope production and separation methods addressing multiple issues in the isotope community:

Publications:

1. Ryan Clanton*, **Gamal Akabani**. Rapid Synthesis of ^{125}I Integrated Gold Nanoparticles for Use in Combined Neoplasm Imaging and Targeted Radionuclide Therapy. *Applied Radiation and Isotopes*. Under Review (2016).

2. Jien Jie Zhou*, Arnulfo Gonzalez*, Mark W. Lenox, Theresa W. Fossum, R. Keith Frank, Jaime Simon, Stan Stearns, Catherine M. Ruoff, Richard E. Wendt, Gamal Akabani. Dosimetry of ^{90}Y-Hydroxide Treatment of Canine Osteosarcoma Using PET/CT: A Liquid Brachytherapy Approach. *Appl Radiat Isot* **97C,** 193–200 (2014).

3. Thomas M. Martin*, Vihar Bhakta*, Abeer Al-Harbi, Michael Hackemack*, Gabriel Tabacaru, Robert Tribble, Sriram Shankar, and **Gamal Akabani**. Preliminary production of ^{211}At at the Texas A&M University Cyclotron Institute. *Health Phys* **107,** 1–9 (2014).

4. D. Lao*, M. W. Lenox, and **G. Akabani**. The Sparsity-Promoted Solution to Undersampling TOF-PET Imaging: Numerical Simulations. Progress In Electromagnetics Research, Vol. 133, 235–258 (2013).

5. Martin T. M., **Akabani G**. Radiological safety concerns for the accelerator production of diagnostic and therapeutic radionuclides in a university setting. Health Phys. 2012 Nov; 103 (5 Suppl 3).

<u>Dissertations, Maters of Science Thesis, Undergraduate Thesis, and Senior Design Projects</u>

Mr. Michael Thomas Martin. *Production of the Therapeutic Alpha Particle Emitting Radionuclide At-211 at the Texas A&M Cyclotron Institute.* PhD. December 2016*

Mr. Tayler Lee Cantrell. *The Development Of An Optimized Generator Production Method For The Routine Production Of Zinc-62/Copper-62 Generator Systems.* Master of Science. May 2015

Yousif AlMaazmi, Talal Harahsheh, Miltiadis Kennas, Eden Marroquin, Matt Schaper. *Production of Tc-99m from Accelerator Generated Mo-99 Utilizing a Photon-Neutron Interaction With Mo-100 Targets*. NUEN 406 Senior Design Project Plan. April 27, 2015

Ms. Jijie Lou. Radiolysis Of Amino Acids: *A Study Using Raman Spectroscopy, Ultraviolet-Visible Spectrophotometry And Electrospray Ionization Mass Spectrometry.* Master of Science. Dec. 2014

Mr. Richard Vega. *Design Of A Subcritical Aqueous Target System For Medical Isotope Production.* Undergraduate Research Scholars Thesis. May 2014.

Viharkumar Satish Bhakta. *Production of The Alpha-Particle Emitting Radionuclide Astatine-211 at The Texas A&M Cyclotron Institute.* Master of Science. May 2011

Students Presentation Awards

1. Matt Schaper, Eden Marroquin, Talal Harahsheh, Miltiadis Kennas, Yousif Almaazmi. **Production of Tc-99m from Accelerator Generated Mo-99 Utilizing a Photon-Neutron Interaction With Mo-100 Targets.** First place. American Nuclear Society Annual Meeting**.** (Washington, DC. 13 October, 2015).
2. Matt Schaper, Eden Marroquin, Talal Harahsheh, Miltiadis Kennas, Yousif Almaazmi. **Production of Tc-99m from Accelerator Generated Mo-99 Utilizing a Photon-Neutron Interaction With Mo-100 Targets.** First Place. South Texas Chapter of the Health Physics Society. (Waco, TX. 18 April, 2015).
3. Elizabeth Tindle. **Operational Health Physics for the Texas A&M Radionuclide Production Program.** Third Place. South Texas Chapter of the Health Physics Society. (Waco, TX. 18 April, 2015).
4. Tyler Cantrell, **The Development of an Optimized Generator Production Method for the Routine Production of Zinc-62/Copper-62 Generator Systems.** Second Place. South Texas Chapter of the Health Physics Society. (Waco, TX. 18 April, 2015).
5. Ryan Clanton, **Rapid Synthesis of I-125 Integrated Gold Nanoparticles For Use in Combined Neoplasm Imaging and Targeted Radionuclide Therapy.** Third Place. South Texas Chapter of the Health Physics Society. (Waco, TX. 18 April, 2015).
6. Richard Vega, **Design of a Subcritical Aqueous Target System for Medical isotope Production.** First Place. Outstanding Thesis – Science, Technology, Engineering and Mathematics. Undergraduate Research Scholar. (College Station, TX. May 2014.).
7. Mallory Carlson. **Study of the Radiolytic Enhancement of Gold Nanoparticles in Animo Acids.** Third Place. Summer Undergraduate Research Symposium. **(**College Station, TX. August 8th, 2014).
8. Michael Hackemack, **Production of At-211 at the Texas A&M Cyclotron,** Third Place. South Texas Chapter of the Health Physics Society. (Waco, TX. 14 April, 2012).
9. Jordan A. Evans, **Enhancing targeted radionuclide therapy using nanotechnology.** Third Place. South Texas Chapter of the Health Physics Society. (Waco, TX. 14 April, 2012).
10. Dapeng Lao, **TOF-PET imaging within the framework of sparse reconstruction.** Third Place. South Texas Chapter of the Health Physics Society. (Waco, TX. 14 April, 2012).

11. Leanne Kristek, **Target Design and Potential Radionuclide Impurities During the Production of ^{67}Cu via ^{64}Ni(α,p).** Third place. South Texas Chapter of the Health Physics Society. (Waco, TX. 14 April, 2012).

2. Production of At-211

Production of At-211 was carried out using modified methods of previously published work. The system has not been optimized, as there is the need for a dedicated vault for radionuclide production. Beam preparation and optimization at 28.5 MeV was recently carried out allowing for a finer beam spreading over the whole target and including a chiller to dissipate the generated heat at the surface of the target. The distillation system has not yet been optimized. There is the need of further irradiations and distillation apparatus modifications to address current shortcomings. The current yield for At-211 has been between 20 and 37 MBq/μA-h; however, there are significant issues in the distillation apparatus that have not been resolved. The distillation is carried out using a tube furnace. Appendix A provides a summary of the current work.

3. Production of Zn-62/Cu-62

Optimization of the production of the Zn-62/Cu-62 generator was studied using a new separation method. This study was the work of Mr. Cantrell as part of his MS thesis. The objective of this study was to optimize the methods for producing Zn-62/Cu-62 so that they may be better suited for routine production. This involved examination of the bombardment parameters and the procedure utilized to dissolve the irradiated copper target. Additionally, the feasibility in automating the different processes of the production methods through a modular system was examined to aid in streamlining the routine production of the generator systems. The analysis showed that, between proton entry energies of 18 and 30 MeV, a target thickness of 1.0 mm was optimal for producing Zn-62. With a 1.0 mm thick target, the optimal proton entry energy for maximizing the production yield of Zn-62 was 29 MeV. The theoretical Zn-62 yield at 29 MeV directly prior to generator loading was calculated to be between 160 and 180 $GBq \cdot \mu A^{-1} \cdot h^{-1}$. An alternative target processing method based on 30% hydrogen peroxide (H_2O_2) and 2 M hydrochloric acid (HCl) at a temperature of 75 °C successfully dissolved the copper foil within 12 minutes. The color of the solution indicated that the copper (II) ions formed the hexaaquacopper(II) ion in 2 M HCl used for chemical separation. Finally, devices were purchased for automating the generator production process, including heating and transfer of solutions, and electronic manipulation of valves. These devices were controlled using the software LabVIEW, which demonstrated the feasibility of building a system capable of automating the production of this generator system. A detailed overview was provided on how to control these instruments with LabVIEW. Appendix A provides the MS thesis of Mr. Cantrell.

4. Study of Production Methods of Mo-99/Tc-99m

4.1 Production of Mo-99 using a subcritical aqueous target system.

As part of our academic effort, we studied the production of Mo-99 using a subcritical aqueous system. This work was carried out by Mr. Richard Vega as part of his undergraduate thesis. He was awarded Outstanding Thesis – Science, Technology, Engineering and Mathematics. Undergraduate Research Scholar in May 2014. The United States consumes almost half of all medical isotopes produced worldwide, and relies on foreign sources for nearly its entire supply. These isotopes are produced in nuclear reactors, which are very costly to construct. A domestic supply may be realized if research reactors at universities and national laboratories can be enhanced with isotope production capabilities. This re-search is dedicated to the design of an aqueous target system that can be appended to exiting re-search reactors for this purpose. The design aims to combine attributes of solid target irradiation by conventional reactors and in-solution production by aqueous homogeneous reactors in order to realize some of the benefits of each method. The benefits for the former include using existing reactors as the external neutron source hence reducing the investment capital significantly. The benefits for aqueous homogeneous reactors are numerous and include higher efficiency, substantial reduction in waste, lower fuel cost, and reduced isotope separation complexity. Utilizing a flowing fuel design will enable continuous isotope separation and more efficient heat removal, as well as eliminate some of the complications that have plagued solution fueled reactors in the past such as power oscillations and fuel precipitation. The aqueous target system described in this thesis is designed for the Annular Core Research Reactor (ACRR) at Sandia National Laboratories. The system is optimized for Mo-99 production, as this is the medical isotope in highest demand and used in a majority of all medical diagnostic procedures excluding x-ray imaging. The optimized production rate is calculated to be 3044 Ci6-day per week, which accounts for 50.7% of domestic consumption. Appendix C provides a thesis of the present work.

4.2 Production of Tc-99m from Accelerator Generated Mo-99 Utilizing a Photon-Neutron Interaction With Mo-100 Targets.

A alternative method was studied for the production fo Mo-99 using an high-energy electron accelerator using the reaction $^{100}Mo(\gamma,n)^{99}Mo$. A senior design group under Dr. Akabani mentorship studied this alternative method in collaboration with MEVEX, Inc., a company that produces high-energy electron accelerators. The work was submitted internally and was selected to compete at the Annual Winter Meeting of the American Nuclear Society were it was awarded first prize.

The current supply-chain of producing Mo-99 can be unreliable due to unforeseen nuclear reactor outages and upcoming nuclear power plant license expirations. Nuclear reactors also require high initial startup capital and require six days in order for hospitals to receive Mo-99.

Because of these reasons, alternative methods for the production of Mo-99 are currently being researched and are the basis of this design. Mo-99 is important isotope because it decays into Tc-99m, which is used in 80% of nuclear medicine procedures. This design is to propose an alternative method using a photon-neutron interaction with Mo-100 targets in order to acquire Mo-99. The design goal is to address the global demand of Mo-99 in a more efficient and economically feasible method.

This design encompasses the entire production process from the production of Mo-99 to the final product of Tc-99m ready for patient delivery. The design uses 41 MeV electrons produced from a 100 kW accelerator to create photons via bremsstrahlung scattering off a tungsten target. These photons interact with Mo-100 to produce Mo-99. The Mo-99 is then chemically separated from the Mo-100 and the Tc-99m is produced as a final product. This project has been divided into five major subtasks: target design, thermodynamic design, shielding design, chemical separation, and quality management in order to maximize the production of Mo-99 while addressing safety concerns. Computer programs will be used as a tool to model these aspects in order to achieve the objectives of this design.

After the design was subdivided into sections, important optimization variables were assigned for the design. The most important variables to maximize included the production rate of the Mo-99 and the cost Tc-99m. Safety and irradiation risk reduction was also of great interest in order to cohere with ALARA standards and protect the employees of our facility.

The results of this design determined the production rate of the molybdenum-99 after an irradiation time of one day to be 146 Ci per Mo-100 target system. The MEVEX accelerator company is capable of providing an accelerator of the required 35-50 MeV beam energy and 100 kW of power. The separation apparatus was also successful at chemically separating molybdenum for recycling from Tc-99m and producing a deliverable syringe to the patient. The entire process is designed to uphold FDA and cGMP requirements as well as the necessary radiation shielding requirements during the target irradiation and chemical separation process. The final cost for 1 mCi of Tc-99m using this design was calculated to be 20.5¢, which is significantly less expensive than the current consumer cost of 100¢ per mCi. Appendix D provides a senior thesis of the present work.

5. Academic Program

A new course was established at the undergraduate and graduate level to teach radionuclide production and separation methods. The course title was “NUEN 489/689: Radionuclide Production and Separation Methods.” The course has an initial enrollment of 10 students and was well received with an average evaluation of 4.5/5.0. The course will be continued under the auspices of the Texas A&M Institute for Preclinical Studies. We have currently collaboration with more than five companies and academic institutions providing us with incentives and infrastructure in radioisotope production, such as Cardinal Health, IsoTherapeutics, LLC, MD Anderson Cancer Center, and Proportional Technologies, Inc. The syllabus is attached in Appendix E.

6. Overall Impact.

The impact of the present grant was two fold. It has established the ground for radioisotope production at the Texas A&M Cyclotron Institute and separation methods and labeling at the Texas A&M Institute for Preclinical Studies. It allowed many students to graduate knowing the basic methods for radioisotope production and separation methods, which allowed them to obtain work at many educational institutions and corporations. The majority of the students that were mentioned in the present report are currently involved in radioisotope production. Recently a group of students from my laboratory established a private company for radioisotope production, which indicates the commitment they have in this profitable area.

The facilities are still under development as the Radiological Safety Office just provided us with the permit to work in our laboratory at the Cyclotron Institute (July 2015) after a lengthy wait.

Sincerely,

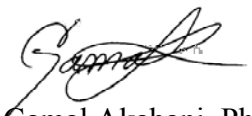

Gamal Akabani, PhD

Appendix A

Work Related to the Production of At-211

PRODUCTION OF THE ALPHA-PARTICLE EMITTING RADIONUCLIDE ASTATINE-211 AT THE TEXAS A&M CYCLOTRON INSTITUTE

A Thesis

by

VIHARKUMAR SATISH BHAKTA

Submitted to the Office of Graduate Studies of
Texas A&M University
in partial fulfillment of the requirements for the degree of

MASTER OF SCIENCE

August 2011

Major Subject: Health Physics

Production of the Alpha-Particle Emitting Radionuclide Astatine-211 at the Texas A&M Cyclotron Institute

PRODUCTION OF THE ALPHA-PARTICLE EMITTING RADIONUCLIDE ASTATINE-211 AT THE TEXAS A&M CYCLOTRON INSTITUTE

A Thesis

by

VIHARKUMAR SATISH BHAKTA

Submitted to the Office of Graduate Studies of
Texas A&M University
in partial fulfillment of the requirements for the degree of

MASTER OF SCIENCE

Approved by:

Co-Chairs of Committee,	Gamal Akabani Hneide
	John Ford
Committee Members,	Robert Tribble
	Craig Marianno
Head of Department,	Raymond Juzaitis

August 2011

Major Subject: Health Physics

ABSTRACT

Production of the Alpha-Particle Emitting Radionuclide Astatine-211 at the Texas A&M Cyclotron Institute.

(August 2011)

Viharkumar Satish Bhakta, B.S., Texas A&M University

Co-Chairs of Advisory Committee: Dr. Gamal Akabani Hneide
Dr. John Ford

The need of a stable production of At-211 is necessary to continue research in alpha-particle targeted radionuclide therapy. Our objectives were to establish the production of Astatine-211 at Texas A&M Cyclotron Institute, optimize the production methods to reduce the generation of contaminants and maximize At-211 production, and assess the radiological safety aspects of At-211 production. The production of the alpha-particle emitting radionuclide At-211 was performed at the Texas A&M Cyclotron Institute using the K500 superconducting cyclotron, following the production reaction Bi-209(α, 2n)At-211 using a thick bismuth target of 500 μm. We carried out two irradiation experiments where the initial energy of the alpha-particle beam, 80 MeV, was degraded using multiple copper and aluminum foils to 27.8 and 25.3 MeV, respectively. The end of beam time was 4 hours for both experiments.

The resulting At-211 yields were 36.0 and 12.4 MBq/μA-h, respectively. Several impurities were produced using the 27.8 MeV, which included At-210 and Po-210. However, when the 25.3 MeV beam was used, the impurities At-210 and Po-210 were

resolved and other contaminants were minimized to less than 0.8% of At-211 yield. The production yields were in accordance with previous published results.

From the success of these initial experiments, additional steps were taken to produce At-211 in excess quantities for distillation purposes. In order to obtain viable quantities of At-211, the gross yield needed to be increased due to losses that are incurred during distillation and radioactive decay. The ability to produce high yields of this isotope required a redesign of the target and use of the K150 cyclotron using a higher beam intensity.

ACKNOWLEDGEMENTS

I would like to thank my committee co-chairs, Dr. Gamal Akabani and Dr. John Ford, and my committee members Dr. Robert Tribble, and Dr. Craig Marianno. Also, I would like to thank Dr. Abeer Alharbi and Dr. Gabriel Tabacaru for their guidance and support throughout the course of this research.

Thanks go to my friends, Akshay Gandhir, Alex Chambers, Mitchelle Carroll, Jessica Hartley, Michael Martin, and Nate Ferdette. I would also like to thank the department faculty and staff for making my time at Texas A&M University a memorable and a great experience.

Finally, thanks to my parents, Satish and Pravina Bhakta, for their encouragement and support through my time at Texas A&M University.

NOMENCLATURE

A	Ampere
Bq	Becquerel
Ci	Curie
EOB	End of Bombardment
FWHM	Full Width Half Max
LET	Linear Energy Transfer
mAb	monoclonal Antibody
NCI	National Cancer Institute
NHL	Non-Hodgkin's Lymphoma
RIT	Radioimmunotherapy
SEER	Surveillance Epidemiology and End Results
SRIM	The Stopping and Range of Ions in Matter
TRT	Targeted Radionuclide Therapy

TABLE OF CONTENTS

Page

LIST OF FIGURES

Page

LIST OF TABLES

Page

1. INTRODUCTION

The Surveillance Epidemiology and End Results (SEER) report published by the National Cancer Institute (NCI) estimated that in 2010 1,529,560 men and women would be diagnosed with cancer in the United States [1]. Of the diagnosed cases, it is estimated that 569, 490 men and women will die from cancer [1]. Currently in the United States, 80% to 90% cancer patients are treated using surgery, chemotherapy and radiation therapy or a combination of these strategies. The remainders of the patients, especially those who have disseminated disease, are treated using palliative methods or experimental biological therapies, such as immunotherapy. However, over the last few decades, there has been a shift in treatment strategies, where physicians and scientists are developing molecular cancer treatments strategies specific to the pathophysiological characteristics of tumors. Among the multiple fields of cancer research, the field of targeted radionuclide therapy (TRT) has received extensive attention.

The initial concept of targeted therapy was first proposed by Dr. Paul Ehrlich in 1898 [2]. Dr. Ehrlich proposed the treatment of disseminated diseases through the use of a concept known as the "Magic Bullet". Dr. Ehrlich coined this term when he described the selective targeting of bacterium without harming the surrounding tissues. This concept of a "Magic Bullet" may be elementary; however, the development of such "Magic Bullet" has been extremely arduous and complex in the area of cancer therapy.

This thesis follows the style of Journal of Nuclear Medicine and Biology.

Due to limitations in knowledge and technology, the concept of targeted therapy remained as a theory until the late 1940s and early 1950s. This theory manifested into a successful experiment by David Pressman, who was able to successfully develop rabbit antibodies that were capable of identifying and targeting tumor malignancies both *in vitro* and *in vivo* experiments [3-7]. Shortly after Pressman's successful attempts, Nungester successfully utilized iodine-131 (I-131) labeled antibodies for the treatment of Wagner osteogenic sarcoma making the first application and use of a radionuclide targeted therapy [8, 9]. These two scientists introduced the concept of targeted radionuclide therapy (TRT). With the successful experiments of Pressman and Nungester, great emphasis was placed on production of radiolabeled antibodies. In 1975, Köhler and Milstein published results of their successful experiments for consistent production methods of monoclonal antibodies (mAbs) [10]. Physicians and scientist could finally conjugate radionuclides with stable mAbs for the treatment of disseminated diseases.

Today, there are two radioimmunotherapy (RIT) drugs approved by the Food and Drug Administration (FDA) for the treatment of cancer, specifically B-cell positive non-Hodgkin's lymphoma (NHL). These are Zevalin (Ibritumomab tiuxetan) and BEXXAR (I-131 labeled tositumomab) approved in 1992 and 1993, respectively [11]. Zevalin and BEXXAR are prescribed to patients with relapsed or refractory low-grade CD20 positive, follicular, or transformed B-cell NHL. The radionuclide utilized in Zevalin is Yttrium-90, a beta emitter whereas iodine-131 is utilized in BEXXAR. Iodine-131 is a mixed beta-gamma emitter. There have been several studies that have compared the

efficacy of these two RIT drugs for the treatment of NHL. A clinical trial at Johns Hopkins University, which involved 38 patients, saw an overall response rate of 50% vs. 44% and complete response rate of 8% vs. 16% for Zevalin and Bexxar respectively [11].

1.1 TRT and Disseminated Diseases

Targeted radionuclide therapy is utilized for the treatment of disseminated diseases due to systemic nature of the diseases involved. TRT strategies are utilized for the treatment of leukemias and lymphomas, metastases from primary cancers, and cancers which have invaded multiple systems within the human body, i.e. lymph nodes. These types of cancer cannot be effectively treated by surgery or radiotherapy due to the invasiveness and inherent risk associated with these treatments. The application of external beam therapy poses unnecessary risks to vital organ systems due to the dose received by normal tissue from treating multiple locations. Therefore, the ability to effectively target the disease and spare normal tissue is compromised. Chemotherapy poses similar risks, as it does not differentiate between normal and tumor tissue. Therefore, the logical strategy is the application of selective, localized radiation using TRT strategies. These strategies can use conjugated mAbs, or other specific targeting agent, with specific radionuclides to effectively treat disseminated diseases.

1.2 Common Radionuclides Used in TRT

In order to create an effective TRT strategy, physical and biological characteristics of the radionuclides must be analyzed. TRT involves the ingestion and injection of particulate radiation with in the human body. Therefore, to minimize residual damage

and dose to normal and healthy organs and tissues, radionuclides which can offer high LET, short range and half-lives are typically considered [12]. There are numerous radionuclides used in targeted radionuclide therapy. These radionuclides have various modes of decay and their radiative emissions can be utilized for the treatment of disseminated diseases [13]. However, radionuclides used for TRT must have certain radiobiological properties. They must be short-lived (short half-life), and decay either via beta (β^-) or alpha-particle (α) emissions [13, 14]. These criteria are required to ensure that the energy of these radiative emissions is deposited locally at the tumor site while minimizing dose to normal tissues. Table 1 provides several common radionuclides currently utilized for TRT.

To maximize delivery of the radioisotope, the physical half-life of the radionuclide must correspond with the biological half-life and overall pharmacokinetics and pharmacodynamics of the mAbs in order to achieve maximum tumor uptake. If the half-life of the radionuclide is longer than that of the mAbs in the tumor volume, then the radionuclide will deposit its energy outside the tumor volume leading to potential normal tissue toxicities, such as hematological toxicity.

Another potential issue is *in vivo* drug stability. After TRT drug delivery, the bond between the mAbs or compound and the radionuclide must remain intact. The radiolabeled compound must be able to withstand changes in radiolysis, blood pH changes, liver catabolism, and *in vivo* blood changes, including immunological reactions. Therefore, a successful TRT strategy must consider both biological and

physical properties of the radiative emission of the radionuclide and the overall pharmacokinetics and pharmacodynamics of the radiolabeled mAb.

Table 1. Physical characteristics of radionuclide utilized for TRT.

Isotope	Half-life (h)	Particle Emitted	Maximum Energy (keV)	LET*	Range in Tissue (mm)
Iodine-131 (I-131)	193	β^-	970	low	2
Rhenium-186 (Re-186)	91	β^-	1,080	low	11
Rhenium-188 (Re-188)	17	β^-	2,120	low	11
Yttrium-90 (Y-90)	64	β^-	2,280	low	1.2
Lutetium-177 (Lu-177)	161	β^-	496	low	1.5
Copper-67 (Cu-67)	62	β^-	577	low	1.8
Bismuth-213 (Bi-213)	0.76	α	8,376	high	0.08
Bismuth-212 (Bi-212)	1	α	8,780	high	0.09
Actinium-225 (Ac-225)	240	α	>6,000	high	0.08
Astatine-211 (At-211)	7.2	α	7,450	high	0.07
Radium-223 (Ra-223)	274.32	α+	>5,000	high	0.08
Thorium-227 (Th-227)	448.32	α+	>6,000	high	0.08

*LET: Linear Energy Transfer. Radiative emissions are divided into low and high linear energy transfer.

1.2.1 Radiobiological Properties of Alpha-Particle Emitting Radionuclides Used in TRT

The enhanced cytotoxicity of alpha-particles makes them extremely attractive for use in TRT [12]. The radiobiological rationale for the use of alpha-particle emitters, such as At-211, is based on the fact that alpha-particles have a very short range in tissue (< 100 μm), making them well matched to cell-specific targeting and highly focal cell killing while sparing normal tissues. Furthermore, because of their high linear energy transfer (LET ~ 100 keV μm^{-1}), they have a greater relative biological effectiveness (RBE), which is about 1,000 times more effective than beta-particles. In contrast to beta-particles, alpha particles are also effective in hypoxic and normoxic tissue conditions, showing a low oxygen enhancement ratio (OER); therefore, they are very effective in eradicating hypoxic radio-resistant tumor cells encountered in most aggressive tumors. This is due to the fact that the biological damage produced by high LET radiations is via direct effects to the cell nucleus. In comparison with low LET radiations, where the majority of the effects are due to indirect effects, and depends on the presence of oxygen to produce free radicals. Finally, the most important radiobiological characteristic of alpha-particles is the absence of dose-rate and cell cycle effects, which makes them extremely compatible with low dose rates encountered in TRT [15]. Figure 1 shows a comparison of the radiobiological characteristics of cell survival fraction between low and high LET radiations.

1.2.2 Preclinical and Clinical Use of Alpha-Particle Emitters

The radionuclide At-211 has been utilized in numerous clinical cancer studies [12, 14, 16-26]. A study at Duke University Medical Center involved the use of At-211

for the treatment of recurrent brain tumors [23, 24]. This study analyzed the production methods of At-211 and labeling of At-211 to mAbs and other biological compounds [12, 23, 25, 26]. The results from open literature showed that the radionuclide At-211 could be produced in therapeutic quantities required for clinical trials (several GBq) and proved the concept of labeling 81C6 anti-tenascin mAb with At-211.

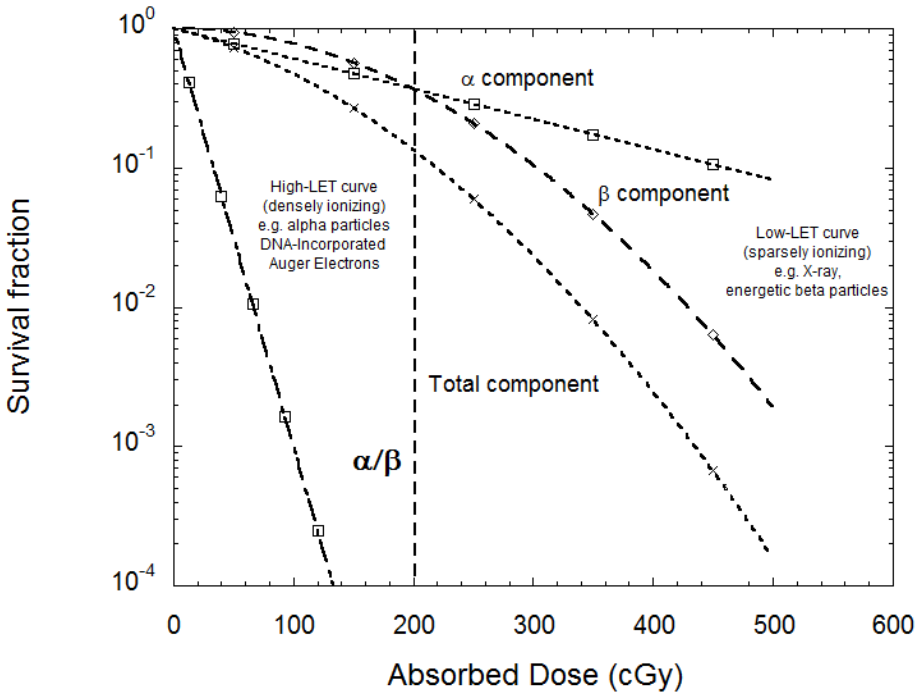

Figure 1. A comparison of the radiobiological characteristics of survival fraction as a function of absorbed dose between low and high LET radiations based on the linear quadratic model.

An *in vitro* study with At-211 observed effects of *in vitro* cytotoxicity of At-211 labeled trastuzumab in several human breast cancer cell lines [16]. This study showed

that the survival fraction of tumor cells when treated with At-211 labeled trastuzumab resulted in a mono-exponential relationship; however, when compared to external beam therapy, the survival fraction showed a linear-quadratic model relationship.

1.3 Purpose

Currently in the United States, there are numerous facilities capable of producing medical radionuclides on a daily basis. However, only three facilities have the capability of producing the radionuclide At-211. These facilities are located at Duke University Medical Center, Durham, NC, the National Institutes of Health, Bethesda, MD, and Washington University, Seattle, WA. In order to further facilitate preclinical and clinical trials that require the use of At-211 for TRT, we studied the feasibility of a viable production method which must be established for proof of concept and to optimize the process. Therefore, the goal of this study was to produce the radionuclide At-211 at the Texas A&M University Cyclotron Institute utilizing the K500 superconducting cyclotron.

2. EXPERIMENTAL METHODS AND MATERIALS

2.1 The Radionuclide Astatine-211

Astatine is a rare element as it is not a naturally occurring element. Therefore, to obtain an isotope of this element, bombardment of other naturally occurring isotopes is required. Particularly for At-211, bombardment of Bi-209 with an alpha-particle yields the production of At-210 and At-211 with threshold energy of 28 and 22 MeV respectively [12, 18, 20-22, 25-34]. In this study, production of At-211 is investigated while searching for methods to minimize production of contaminants.

The radionuclide At-211 is considered a pure alpha-particle emitter due to its decay characteristics (Figure 2). This radionuclide has two specific modes of decay, electron capture and alpha particle emission, with a half-life of 7.241 hours. Table 2 contains the radiative emission for the decay of At-211, where α, ε, and γ denotes alpha-particle, electron capture, and gamma-ray emissions, respectively. The radionuclide At-211 when decaying via alpha-particle, results in the formation of Bi-207. Bi-207 has an extremely long half-life (31.55 years denoted as "a") and it decays via electron capture. The radiative emissions of Bi-207 are provided in Table 3 relative to the decay of At-211. The decay of At-211 via electron-capture results in the formation of Po-211, which is a very short-lived radionuclide (half-life of 0.516 s). The radionuclide Po-211, like At-211, decays via alpha-particle emission and is also considered a pure alpha particle emitter (Table 4). Both Bi-207 and Po-211 decay to a stable isotope of lead (Pb-207). All radiative emissions data were obtained from the LUND/LBNL Nuclear Data [35].

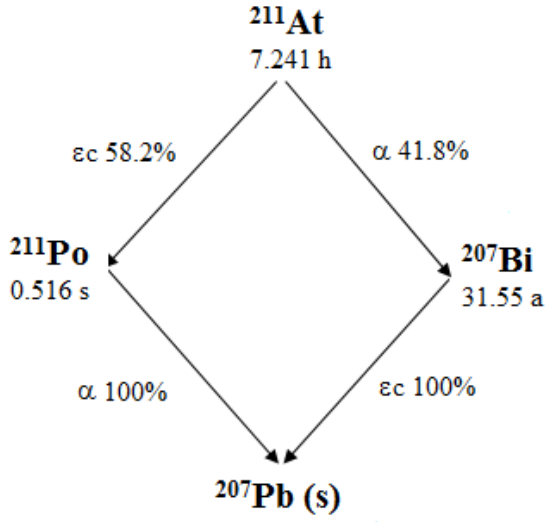

Figure 2. Decay scheme for the radionuclide At-211 [35].

Table 2. Alpha-particle and gamma-ray energies and respective yields for At-211 [35].

Energy (keV)	Rel. Intensity (%)	Decay Mode
5866	41.82	α
99.1	0.274	ε (β^-)
786.1	57.93	ε (β^-)
687	0.261	γ

Table 3. Radiative emissions and yields for Bi-207 [35].

Energy (keV)	Rel. Intensity (%)	Decay Mode
58.25	3.22	ε (β^-)
764.8	38.58	ε (β^-)
569.7	40.87	γ
897.8	0.051	γ
1063.7	31.16	γ
1770.2	2.87	γ

Table 4. Radiative emissions and yields for Po-211 [35].

Energy (keV)	Rel. Intensity (%)	Decay Mode
6570	0.298	α
6893	0.304	α
7450	57.5	α
569.7	0.291	γ
897.8	0.327	γ

2.2 Production of Astatine-211

The production of the radionuclide At-211 has been established via the use of cyclotrons using various targets and reaction channels. The most common reaction channel utilized in the published literature was Bi-209(α,2n)At-211. However, others have tried reactions such as Bi-209(Li-7,5n)Rn-211→At-211, Bi-209(He-3,n)At-211, U_{nat}(p,x)At-211, and Th-234(p,x)Rn-211→At-211 [28]. The most studied method for producing the radionuclide At-211 has remained the Bi-209(α,2n)At-211 reaction due to the availability of alpha-particle beams at the required energy range, the ability to procure Bi-209 targets, and minimal cost involved. This method also allows effective control over the production and minimization of contaminants. Studies using the Bi-209(α,2n)At-211 have been carried out using internal and external target systems [27, 29, 36-38]. Experiments utilizing external and internal targets studied the production of At-211 via direct bombardment of Bi-209 targets or via stacked foils techniques.

The use of internal and external bombardment techniques showed significant variation in production yields of At-211 and contaminants. These discrepancies arise due to the nature of each cyclotron facility, beam profile characteristics, and effective

beam current measurements. Each cyclotron facility has its own inherent characteristics dependent on the equipment utilized, ion source properties, maximum extractable energy, and ability to extract stable beams with high intensity (current) and correct energy. All of these properties can vary from experiment to experiment, thus the variability in results as shown in Table 5.

Table 5. At-211 production yeilds based on previous studies [36].

Source	Eα (MeV)	Target Thickness (μm)	Irradiation Time (h)	Beam Current (μA)	At-211 Yield (MBq/μAh)	Content of At-210
Aaij et al. (1974)	33	500	1 - 2	2 - 4	7.4 - 14.8	0.01 - 0.1%
Rösch el al. (1985)	28	500	5	5	8.56	< 7.10 – 7
Hamwi et al. (1991)	28	30	-	-	27.7	At-210 not detected by γ-spec.
Larsen et al. (1993)	28	250	1-2	10 - 12	8 - 12	At-210 not detected by γ-spec.
Wunderlich et al. (1986)	28	20 (10^{o} offset)	5	5	4	-
Hadley et al. (1991)	28	500 - 800	4	10 - 12	10 - 12	-
Lambrecht and Mirzadeh (1985)	28	100	1.3 - 3.95	6.8 - 9.6	5.3 - 10.4	At-210 not detected by γ-spec.
Larsen et al. (1996)	28	100	0.1396 & 0.1401	7.14 & 1.17	15.2 & 15.6	At-210 activity <0.02% relative to At-211.
	(internal target)	50	1	20 - 40	41 ± 7	

2.2.1 Production at Texas A&M Cyclotron Institute

Production of the radionuclide At-211 was pursued using the K500 superconducting cyclotron at the Texas A&M Cyclotron Institute (Figure 3) [39, 40]. The K500 cyclotron was constructed in 1980s and has gone through several upgrades and improvements since the extraction of the first beam in 1988. This cyclotron is able to produce stable beams ranging from protons, to heavier charged particle beams, such as $(Xenon\text{-}129)^{18+}$. Table 6 lists all possible beams that can be extracted from the K500 cyclotron. For the purposes of this study, He^{+} (alpha-particles) beam was extracted for the bombardment of an external target along the MDM beam line.

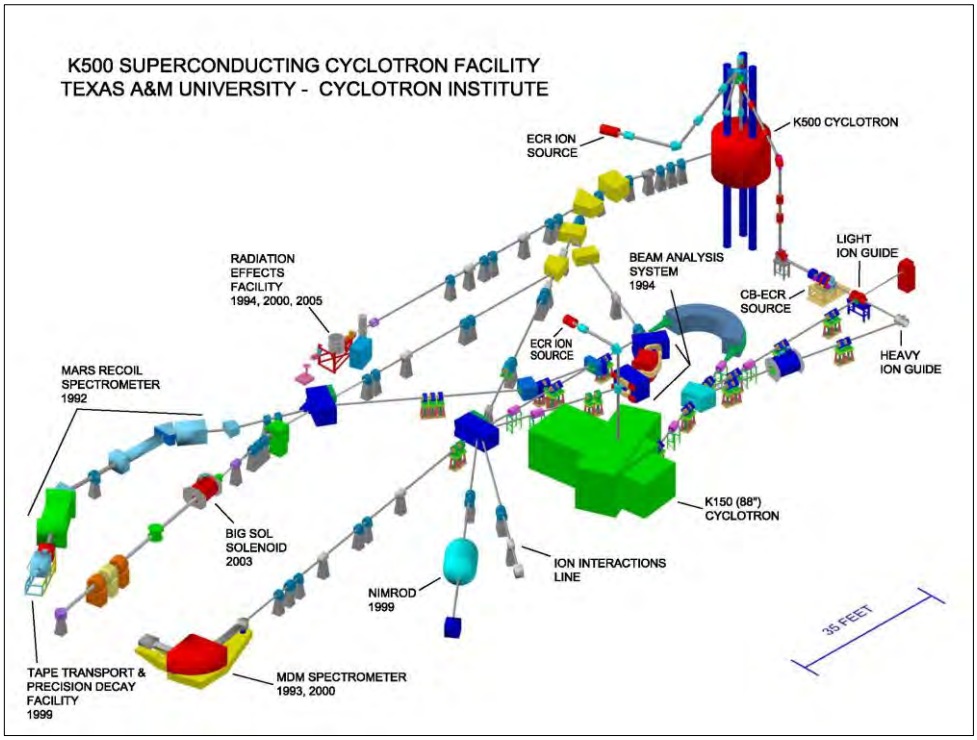

Figure 3. Schematic of K500 superconducting cyclotron facility [40]. The experiments carried out in this research were done at the MDM cave.

Table 6. Beam list for K500 cyclotron as August of 2001 [39, 40].

Ion	E/A (MeV/u)	$I_{extracted}$ (*e*nA)
HD^+	5	70
HD^+	35	15
He-4	15	600
N-14	30.5	120
N-14	40	7
O-16	30	60
Ne-20	14.5	40
Ar-40	2.4	-
Ar-40	20	20
Ar-40	30.5	2
Ar-40	35	1.5
Cu-63	25	3.5
Kr-84	5	1
Kr-84	15	0.3
Xe-129	5	2

HD: Ionized hydrogen

2.3 K500 Cyclotron Beam Analysis

Based on the reaction to be utilized for the production of At-211, the ionized helium beam (He^+) was chosen for bombardment. Energy of the beam was chosen based on preliminary production cross-section analysis obtained from the program TALYS and published literature, including that of the International Atomic Energy Agency (IAEA) [27, 28, 41]. From these preliminary studies, it was determined that the ideal energy for the production of At-211 with a beam of alpha-particles would be 28 MeV. The experiments performed with 28-MeV alpha particles showed that the production of contaminants was minimized while optimizing the production yield of At-211.

2.3.1 Cross-section Analysis

Selection of the alpha-particle beam energy for the first bombardment experiment was primarily based on studies published in the open literature and the IAEA Technical Report Series Number 468. In addition to these studies, the computer code TALYS was utilized to verify the cross-sections for the alpha-neutron reaction [42]. The experimental cross-sections obtained from open literature were obtained through the activation of thin and thick Bi-209 targets [27, 43].

The computer code TALYS simulates nuclear reactions that involve neutrons, photons, protons, deuterons, tritons, helium, and alpha-particles in energy ranges of 1 keV to 200 MeV. This allows the user to theoretically analyze nuclear reactions before experiments are performed. It can also be utilized as a nuclear data tool. Many nuclear reactions have no available data and TALYS can provide data for these reactions via its adjustable parameters. The nuclear reactions considered are those that occur with nuclides with atomic mass of 12 or higher. TALYS utilizes several nuclear interaction models such as the optical model, direction reactions, compound reactions, level densities, pre-equilibrium reactions, multiple emissions, fission, gamma-ray transmission coefficients, and recoil assessment [42]. TALYS produces as output total and partial cross-sections, energy spectrum, angular distributions, double-differential spectra, residual production cross-section, and recoil data.

After reviewing excitation functions and published data for the Bi-209(α,2n)At-211 reaction, the threshold energy was determined to be 22 MeV and optimal bombardment energy range was established between 22 and 28 MeV. However, in this

energy range there are other open reactions, such as Bi-209(α,3n)At-210 and Bi-209(α,t)Po-210 which are considered contaminants (Section 3.1). Direct production cross-section for these three reactions from simulations with TALYS are presented in Figure 4. Table 7 compares cross-section values in the optimal energy range for Bi-209(α,2n)At-211 reaction. After assessing published cross-section data and TALYS output, an alpha-particle with an initial energy of 28 MeV was chosen for the first experiment.

Table 7. Cross-sections for Bi-209(α,2n)At-211 reaction.

	Bi-209(α,2n)At-211 (mb)		
Energy (MeV)	TALYS	Lambercht	Hermanne
22	52.79	68.30	77.75
23	165.92	189.23	191.40
24	310.40	348.80	310.82
25	450.26	478.39	449
26	573.62	587.49	550.59
27	681.80	725.40	665.73
28	773.72	800.89	722.07

Possible contaminants associated with the production of At-211 are At-210 via Bi-209(α,3n)At-210 and Po-210 via Bi-209(α,t)Po-210 reactions. At-210 has similar decay characteristics as At-211 with a half-life of 8.1 hours, but it is not considered a pure alpha-particle emitting radionuclide (Figure 5). At-210 primarily decays via electron capture (99.82 %) thus having a low probability of alpha-particle emission. This decay characteristic is prone to multiple gamma-ray emissions dependent on the

energy of the emitted beta-particle. Table 8 provides energies for the emitted particles and gamma-rays and their relative emission intensity for At-210. The radiative emission of At-210 makes it an unattractive radionuclide for TRT based on the properties discussed previously in Section 1.2.

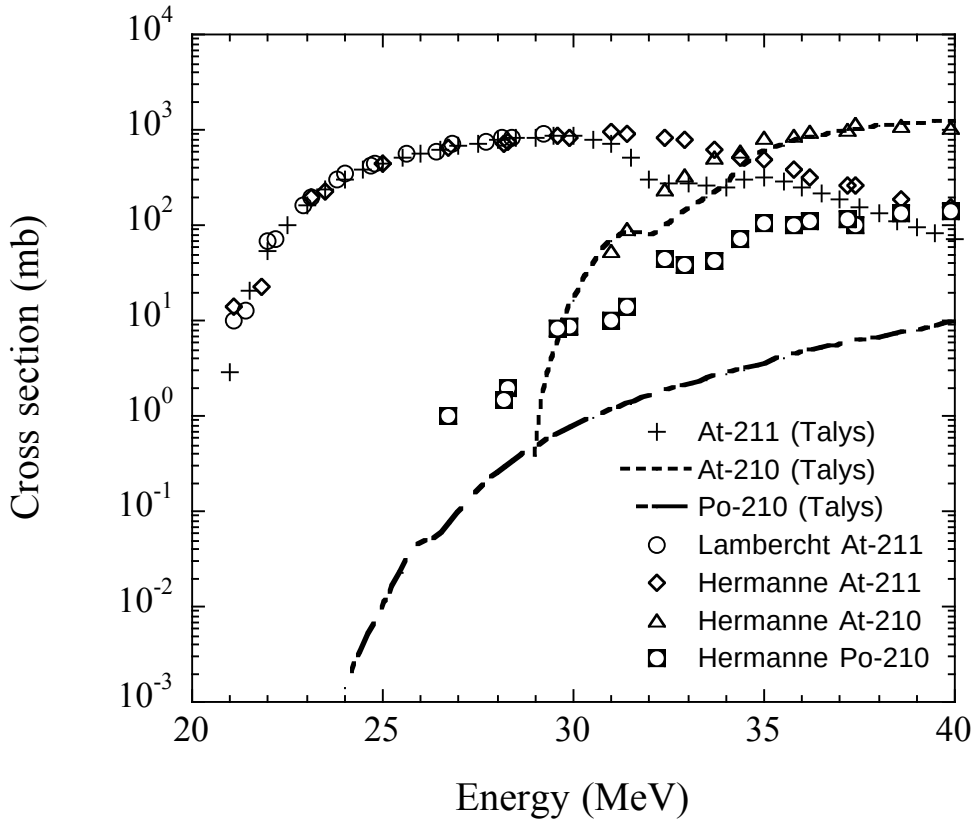

Figure 4. Direct production cross-section for At-211, At-210, and Po-210 [27, 28].

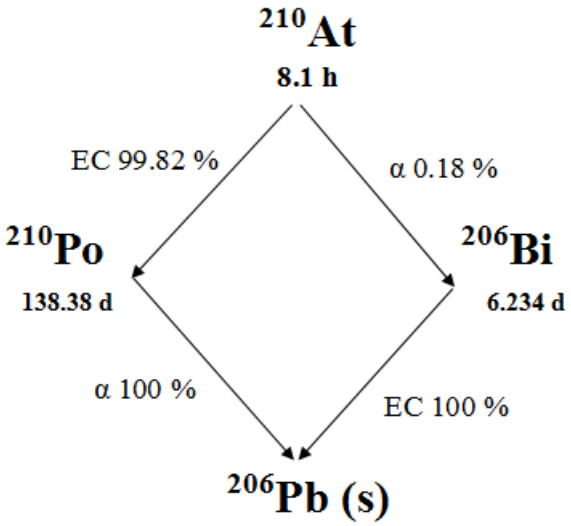

Figure 5. Decay scheme for the radionuclide At-210 [35].

Table 8. Radiative emissions and intensities for At-210 [35].

Decay Mode	Energy (keV)	Intensity (%)
α	5360.9	26.8
	5386	4.6
	5442.4	29.0
	5465	7.8
	5524.1	31.3
ε (β^-)	253.72	5.39
	552.42	2.2
	954.58	19
	1070.95	70
	2507.66	2.9
γ	245.31	79
	1181.39	99.3
	1436.7	29
	1483.39	46.5
	1599.7	13.4

The second potential contaminant is polonium-210 (Po-210). Polonium-210 has a half-life of 138.38 days and the only mode of decay is via alpha-particle emission (5.304 MeV). However, polonium is extremely hazardous to the human body, particularly bone surfaces and liver. If Po-210 is inhaled or ingested, the majority of the activity will be metabolized in the liver and it will be deposited on bone surfaces with biological half-life of 40 and 100 years, respectively. This will result in damage to the liver, bone surfaces and bone marrow posing a serious health risk for the exposed individual. Based on this hazard, great emphasis is placed in minimizing the production of this contaminant.

Along with cross-section data, TALYS also specifies all possible reactions that can occur based on incident particle and target atom. These reactions recoil particles being emitted or other residual radionuclides being produced. For all reactions TALYS computes cross-section, Q-value, and lists all possible particles emitted. This information is extremely useful when performing gamma-ray spectroscopy. Tables 9 – 11 presents the output from TALYS for the Bi-209(α,x) reactions at 28 MeV.

Table 9. Total particle production cross-section for 28 MeV alpha-particles.

Particle Production	Cross-section (mb)
gamma (g)	1.88E+03
neutron (n)	1.56E+03
proton (p)	2.48E-01
deuteron (d)	1.68E-02
triton (t)	2.45E-01
helium-3 (h)	1.91E-08
alpha (a)	2.61E+01

Table 10. Particle production cross-section data for 28 MeV alpha particles.

Reaction	Cross-section (mb)	Emitted Particles					
		n	p	d	t	h	a
(a,g)	6.12E-03	-	-	-	-	-	-
(a,n)	1.17E+01	1	-	-	-	-	-
(a,p)	2.18E-01	-	1	-	-	-	-
(a,d)	1.68E-02	-	-	1	-	-	-
(a,t)	2.45E-01	-	-	-	1	-	-
(a,a')	2.50E+01	-	-	-	-	-	1
(a,2n)	7.72E+02	2	-	-	-	-	-
(a,np)	2.84E-02	1	1	-	-	-	-
(a,nd)	6.31E-07	1	-	1	-	-	-
(a,na)	1.14E+00	1	-	-	-	-	1
(a,pa)	1.88E-03	-	1	-	-	-	1
(a,2a)	1.00E-07	-	-	-	-	-	2
(a,2np)	7.94E-06	2	1	-	-	-	-
(a,2na)	3.63E-02	2	-	-	-	-	1
(a,3a)	1.000E-07	-	-	-	-	-	3

Table 11. Radionuclide production cross-sections for a 28 MeV alpha-particles bombarding bismuth-209 target.

Z	A	Nuclide	Total Cross-section (mb)	Isomeric Cross-section (mb)	Isomeric Ratio
85	213	At-213	6.12E-03	6.12E-03	1
85	212	At-212	1.25E+01	1.25E+01	1
84	212	Po-212	2.18E-01	2.18E-01	1
85	211	At-211	7.74E+02	7.74E+02	1
84	211	Po-211	4.52E-02	4.52E-02	1
84	210	Po-210	2.45E-01	2.45E-01	1
83	209	Bi-209	2.50E+01	2.50E+01	1
83	208	Bi-208	1.14E+00	1.14E+00	1
82	208	Pb-208	1.88E-03	1.88E-03	1
83	207	Bi-207	3.63E-02	3.63E-02	1
81	205	Tl-205	1.00E-07	2.36E-08	0

2.3.2 Beam Degradation Analysis

After performing cross-section analysis to determine the initial energy of the alpha-particle beam, extraction methods for the beam were considered. Based on the external target system being utilized for the experiment, there were two options to obtain the appropriate beam for bombardment. The first option would allow for direct bombardment of the Bi-209 by directly extracting a 28 MeV beam. However, there were concerns that the intensity of the beam would be significantly lower compared to the desired level. Due to these concerns, direct bombardment with K500 was abandoned and analysis for a stacked-foil external target system was performed. Reviews of published experiments with stacked foil system showed that At-211 could be produced at high yields while minimizing production of contaminants [29].

Assessment of published experiments led to the decision to utilize the stacked-foil method. To ensure high beam current could be extracted, the beam was extracted with an initial energy of 80 MeV. This initial energy was attenuated through the use of degrading foils comprised of copper and aluminum foils. The foils and their thickness were chosen such that alpha-particles interacting with the bismuth target would have an average energy of 28 MeV. Beam degradation calculations were performed utilizing the software The Stopping and Range of Ions in Matter (SRIM) and LISE++ [44, 45]. Degradation simulations of the alpha-particle beam were initially performed using the physical calculator of the computer code LISE++, by building a stacked foil system along the MARS-MDM beam line of the K500 cyclotron. These calculations were corroborated using Monte Carlo simulation within the computer code SRIM (Table 12 and Table 13). The foils utilized were based on available thickness of the copper and aluminum foils along with machining capabilities available at the Cyclotron Institute. The SRIM software also provided information with respect to lateral straggling of the beam with the use of the stacked foils (Figure 6). Lateral straggling calculations were simulated using a single point of reference for the incident alpha-particle beam. The diameter of the alpha-particle beam was reduced to 8 mm; therefore, lateral straggling significantly impacts the final energy and intensity of alpha-particles reaching the Bi-209 target. The physical properties of the foils are presented in Table 14.

Table 12. Beam degradation calculation to obtain 28 MeV at Bi-209 target.

Foil	Thickness (μm)	E_{in}[a] (MeV)	E_{out}[a] (MeV)	E_{in}[b] (MeV)	E_{out}[b] (MeV)	σ_{Eout}[b] (MeV)
Cu	100	80.000	74.064	80.000	74.071	0.171
Cu	100	74.064	67.746	74.071	67.744	0.376
Cu	100	67.746	60.957	67.744	60.949	0.326
Cu	100	60.957	53.555	60.949	53.515	0.419
Cu	100	53.555	45.307	53.515	45.245	0.483
Cu	100	45.307	35.773	45.245	35.658	0.630
Al	127	35.773	30.441	35.658	30.213	0.669
Al	50	30.441	28.130	30.213	27.819	0.767
Bi-209	500	28.130	0.000	27.819	0.000	-

*a – LISE++, b - TRIM

Table 13. Beam degradation calculation to obtain 25 MeV at Bi-209 target.

Foil	Thickness (μm)	E_{in}[a] (MeV)	E_{out}[a] (MeV)	E_{in}[b] (MeV)	E_{out}[b] (MeV)	σ_{Eout}[b] (MeV)
Cu	100	80.000	74.064	80.000	74.071	0.171
Cu	100	74.064	67.746	74.071	67.744	0.376
Cu	100	67.746	60.957	67.744	60.949	0.326
Cu	100	60.957	53.555	60.949	53.515	0.419
Cu	100	53.555	45.307	53.515	45.245	0.483
Cu	100	45.307	35.773	45.245	35.658	0.630
Al	127	35.773	30.441	35.658	30.213	0.669
Al	127	30.441	25.665	30.213	25.311	0.966
Bi-209	500	25.665	-	25.311	-	-

*a – LISE++, b - TRIM

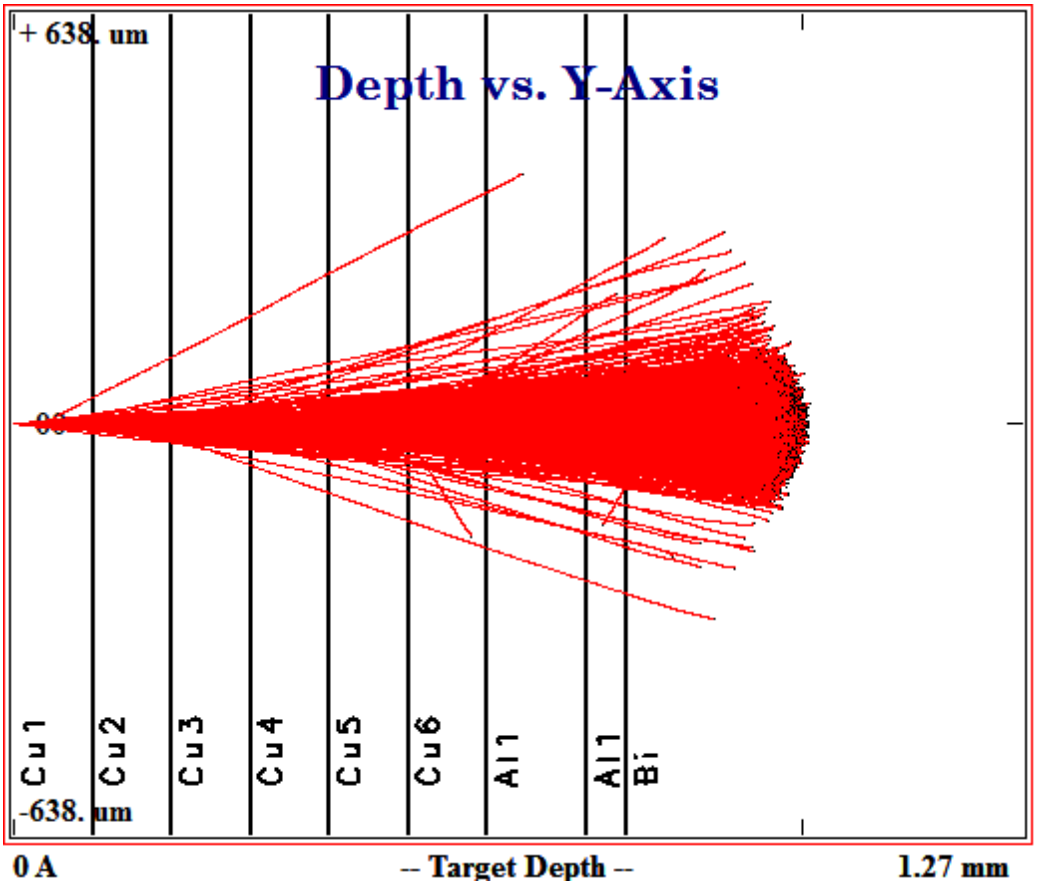

Figure 6. Lateral straggling and range profile for 28 MeV alpha-particles. The characteristics of the foils are given in Table 13. Simulations were performed using a single point of incidence. The diameter of the alpha-particle beam was reduced to 8 mm.

Table 14. Physical properties of stacked foils utilized for At-211 production.

Foil	Density (g/cm3)	Isotope
Copper	8.92	Nat (99.9%)
Aluminum	2.92	Nat
Bismuth	9.81	^{209}Bi (99.999%)

2.4 Target Development

As discussed in Section 2.3.2, a stacked foil external target system was utilized for the production of At-211. We utilized a system that was originally designed by Dr. Abeer Alharbi and Alexandra Aspiridon (personal communication) for other experimental purposes. The foils utilized for the target system had a radius of approximately 1 cm and had varying thickness as required for beam degradation (Table 12 and 13). Figure 7 displays the foil, punch, and ancillary equipment utilized to generate this target system. The initial beam size was reduced to 8 mm in diameter through the use of several collimators as shown in Figure 8. The stacked foils were housed in an aluminum cylinder with insulators on each side. Included in the target cylinder housing was a multimeter to monitor beam current throughout the experiment. Figure 9 displays an enclosed external target system prepared for bombardment. A close-circuit camera system was utilized to monitor the alpha-particle beam before commencement of bombardment.

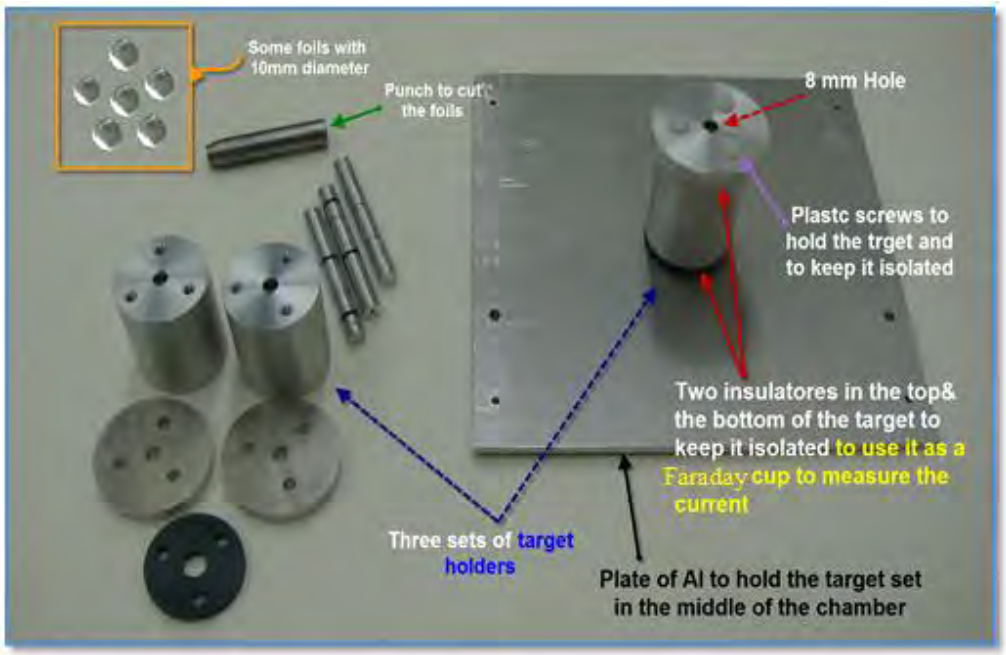

Figure 7. Equipment utilized to build the external target system for At-211 production.

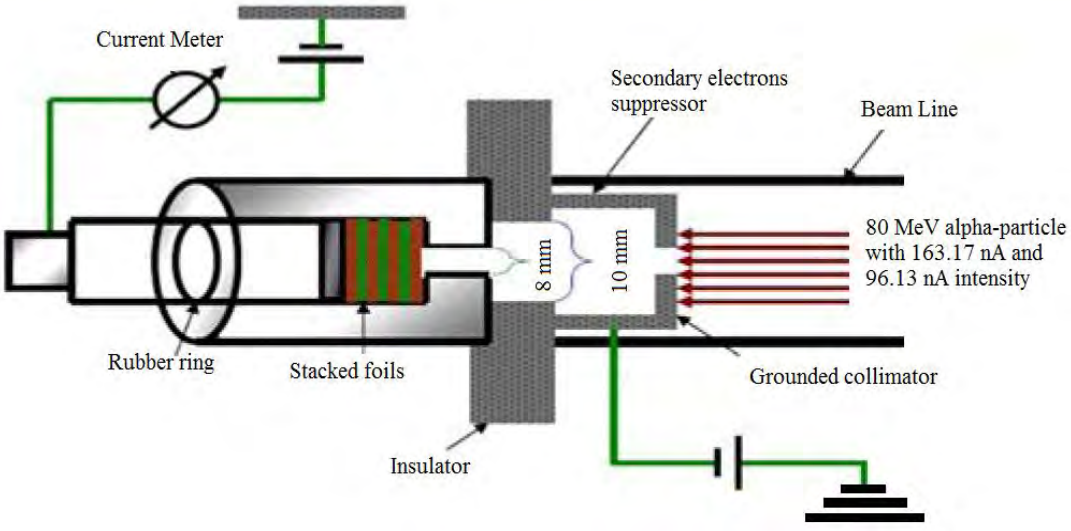

Figure 8. Stacked foil geometry and target holder system for At-211 production.

Figure 9. External target system utilized for the production of At-211. 1) Camera system. 2) Housing of target system. 3) Focusing magnet. 4) Target holder. 5) Faraday cup connections. 6) Vacuum system.

2.5 Detector Calibration

In order to assess the production yields of At-211, a detector counting system was assembled to perform gamma-ray spectroscopy. A Canberra Hyper Pure Germanium (HPGe) detector with an absolute efficiency of 10.9 % was utilized for this purposes. This detector was equipped with a sliding rail system positioned in front of the HPGe detector crystal. The rail system allowed for the movement of an irradiated target and calibration sources to specific distances from the detector. These positions were utilized to characterize the detector efficiency as a function of source distance. Increased distance between the source and the detector can compensate for dead-time effects associated with high activity sources, thus improving quality of obtained spectra.

Calibration of the HPGe detector system was performed with several certified sealed sources consisting of Barium-133 (Ba-133), Cesium-137 (Cs-137), Cobalt-60 (Co-60), and Europium-152 (Eu-152) with an initial activity of 1 μCi [27]. Table 15 lists the decay energies for each radionuclide used for calibration purposes along with their radiological properties. The source spectra were acquired and analyzed using Amptek multi-channel analyzer (MCA) and acquisition software provided by an Amptek. Spectra were acquired at distances of 10, 15, 20, 25, 30, 35, and 50 cm to characterize the efficiency of the detector.

Table 15. Radiological and gamma emissions characteristics of calibration sources utilized for energy calibration and efficiency calculations [35].

Source	Half Life (y)	Energy (keV)	Instensity (%)
Cs-137	30.07	661.657	85.1
Co-60	5.27	1173.27	99.9736
		1332.5	99.9856
Ba-133	10.51	80.9971	34.06
		276.398	7.164
		302.853	18.33
		356.017	62.05
		383.851	8.94
Eu-152	13.537	121.782	28.58
		244.698	7.583
		344.279	26.5
		778.904	12.942
		964.079	14.605
		1085.87	10.207
		1112.07	13.644
		1408.01	21.005

An initial spectrum was acquired for the natural background in order to obtain the characteristics of the detector and to observe any contributions from residual contaminants in the counting room (Figure 10). From the spectrum acquired it was observed that there were no significant residual gamma-ray contributions from the geometry and equipment utilized except for the natural background gamma peak of potassium-40 (K-40) at 1.46 MeV. From preliminary studies of potential production reactions, it was determined that there would not be any conflicts with spectra obtained from irradiated targets (Sections 2.2 and 2.3.1) [28].

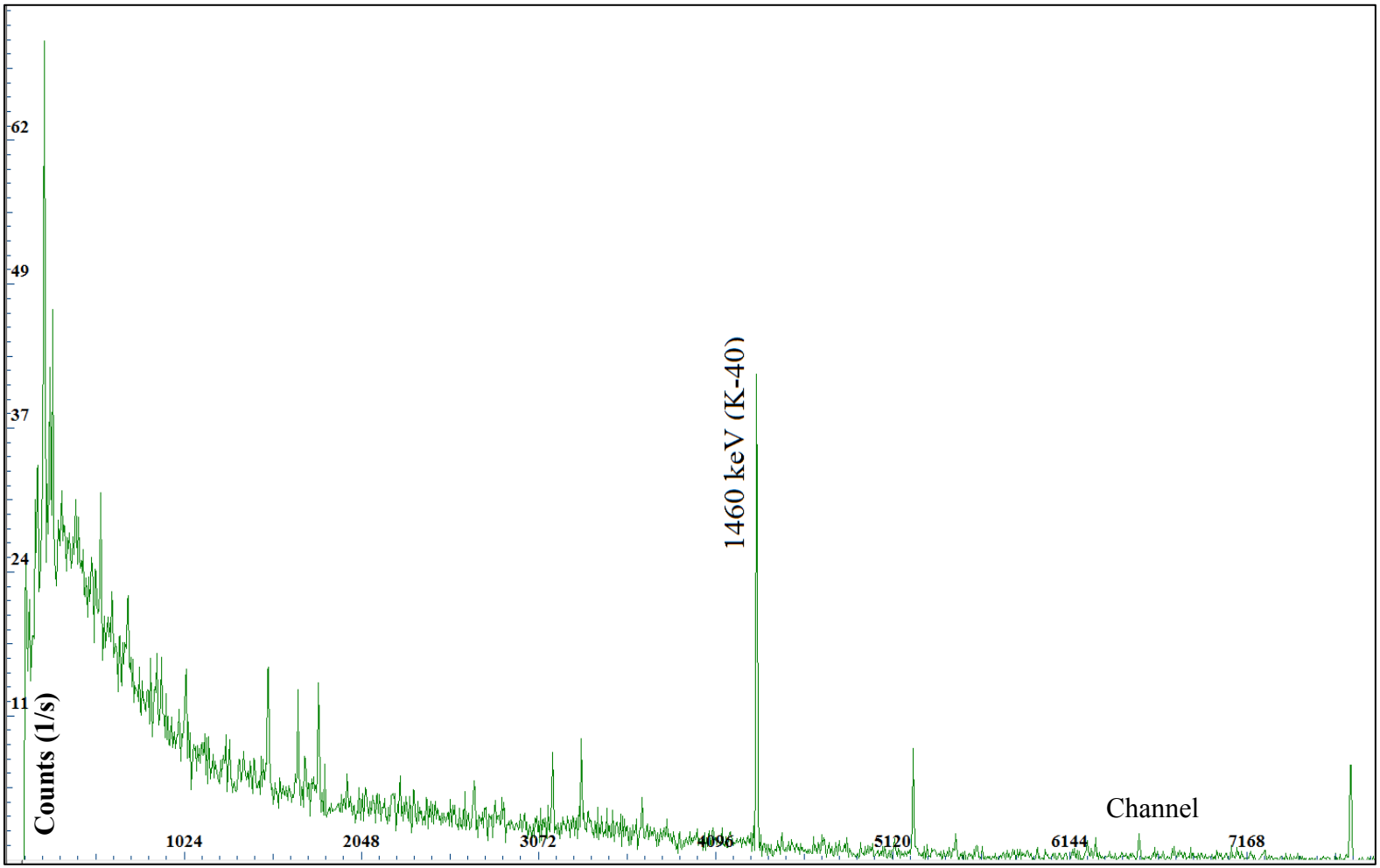

Figure 10. Background spectrum obtained using HPGe detector in the counting room. The only major gamma contribution observed was that of potassium-40 (K-40) at 1.460 MeV.

Initial channel versus energy calibration of the MCA was performed with the Co-60 sources. Co-60 decays via the emission of 1.173 and 1.332 MeV gamma-rays with emission intensity of 99.974 and 99.986 respectively (Figure 11). After loading the spectrum in the ADMCA software, the peaks of Co-60 gamma-rays were associated with appropriate channel numbers. Having two unique energies with corresponding channel, the auto calibration function was able to generate coefficients for the equation utilized to calibrate the entire channel range of the MCA. Once the MCA was calibrated this process was repeated for other distances and radionuclides.

After applying calibration to the acquired spectra, counts measured per gamma-ray emission were obtained by utilizing regions of interests (ROIs). The ROIs are designated at the start and end of the peak for a given gamma-ray emission. By assigning ROIs, the software is able to calculate the area under the associated peak and calculate the counts for the specific energy peak such as net rate (counts/s), net area (total counts), centroid, full-width half max (FWHM), uncertainty, and gross area. Net count rate and uncertainty were utilized to obtain detector efficiency and associated error. The ratio of measured counts and source emission rate is proportional to efficiency as described in Eq. 1.

$$\varepsilon(\mathrm{E}) = \frac{\text{Net Rate(E)}}{\mathrm{A_m I_\gamma(E)}} \pm \frac{\text{Uncertainty(E)}}{\mathrm{A_m I_\gamma(E)}} \qquad (1)$$

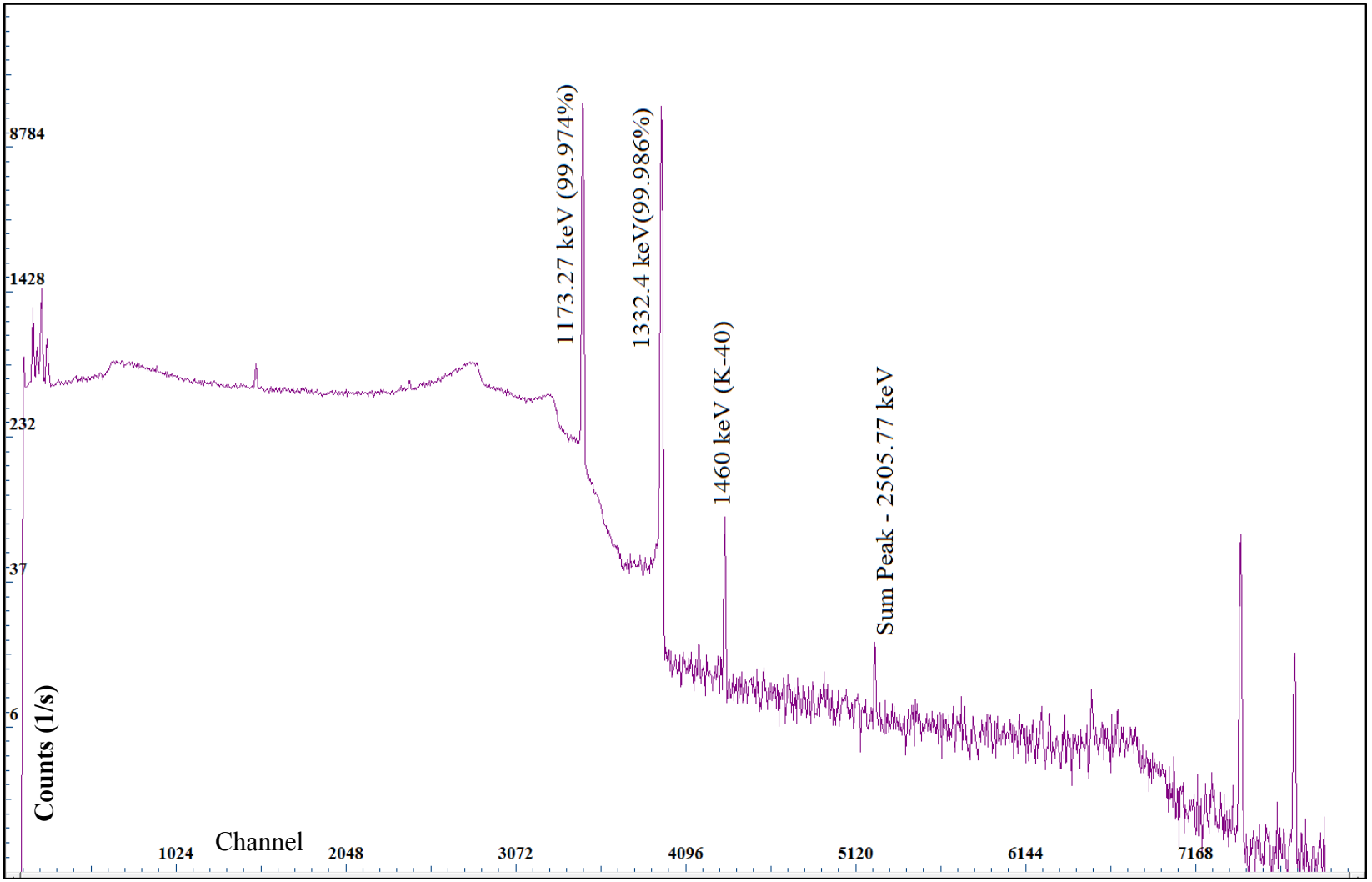

Figure 11. Un-calibrated Co-60 spectrum at 10 cm (Counts v. Channel Number).

In Eq.1, ε denotes efficiency, A_m is the decay corrected activity at time of measurement (source emission rate), and I_γ is the emission intensity of gamma-ray, also known as branching ratio. Efficiency, emission intensity, net count rate and uncertainty are dependent on incident gamma-ray energy. Initial activity for each source was decay corrected, from the calibration date of April and May 1998, by applying Eq. 2,

$$A_m = A_o e^{-\lambda t} \quad (2)$$

where A_o, denotes initial calibrated activity of the source when it was manufactured and certified, A_m is the decay corrected activity, λ is the physical decay constant for the particular radionuclide, and t denotes elapsed time from time of certification of the source activity to the time of measurement. Figure 12 provides a plot of efficiency versus energy as a function of distance for the HPGe detector utilized. Additional data regarding the calibration and efficiency of the HPGe detector is given in Appendix A.

Efficiency for a specific energy range can be calculated obtaining a curve which best fits the acquired data. Since spectra for each source was obtained separately and to minimize error propagation, efficiency curves were obtained based on Eu-152 gamma-ray emissions for all distances by applying the power fit [27]. Fitting a power polynomial function to the efficiency data results in high errors for energies below 150 keV due to the knee effect that occurs in p-type HPGe detectors as the one being utilized in this experiments. This effect is induced due to low energy photon absorption as they pass through the dead layer of the outer contact (crystal housing) of the detector. However, the power trend line provides excellent results for energy ranges above 120

keV. The efficiency curve at 20 cm obtained using Eu-152 is presented in Figure 13 and the Eu-152 spectrum is shown in Figure 14.

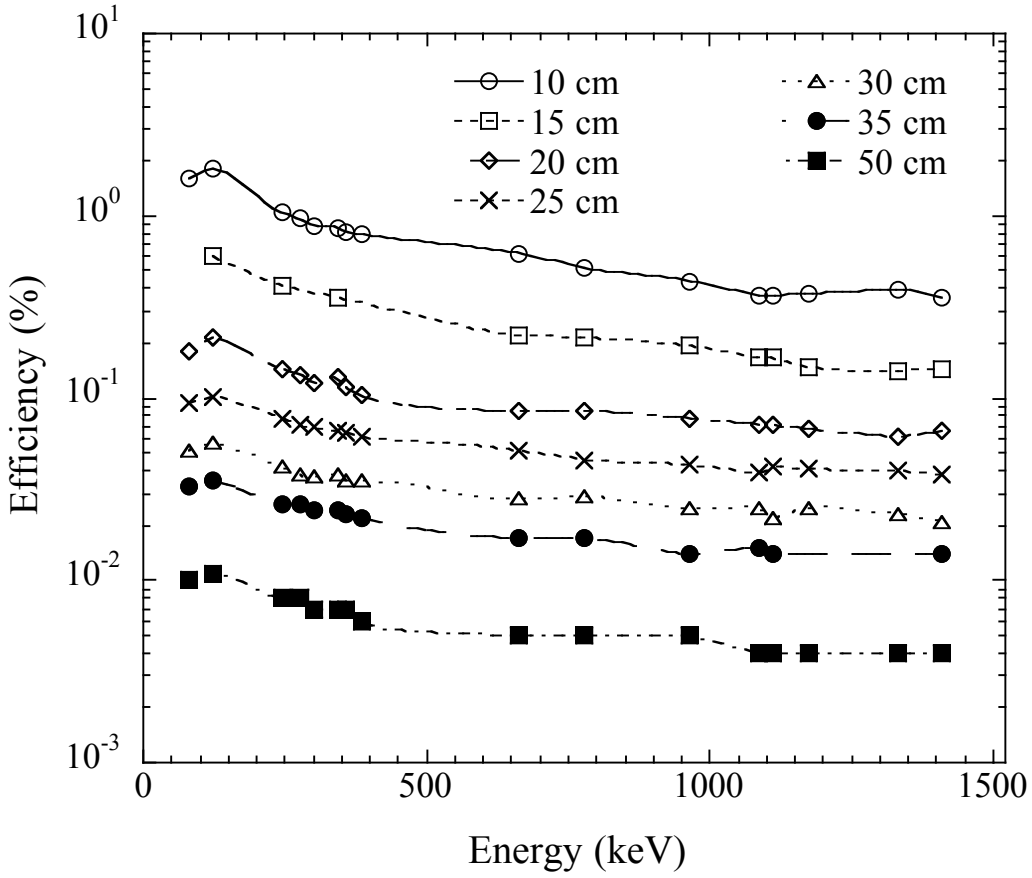

Figure 12. HPGe efficiency curves utilized for gamma-ray spectroscopy at different source distances.

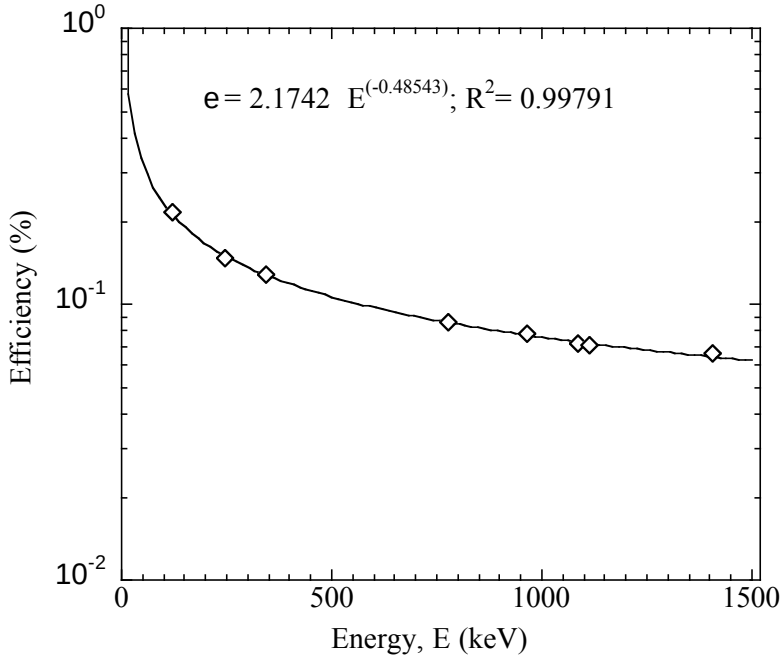

Figure 13. HPGe efficiency curve obtained using Eu-152 at 20 cm.

2.6 Gamma-ray Spectroscopy

Assessment of At-211 yield was performed utilizing activation analysis based on the principles of gamma-ray spectroscopy. Activation analysis is the process of determining activity of a daughter radionuclide based on the measurement of gamma-ray emission during decay. During bombardment of the Bi-209 target with alpha-particles, the Bi-209(α,2n)At-211 reaction accumulate activity of At-211. The rate of production of At-211 depends on the net sum of the production and decay rates as specified in Eq. 3 [46].

$$\frac{dN}{dt} = \phi_o \Sigma_{\alpha,2n} - \lambda N \quad (3)$$

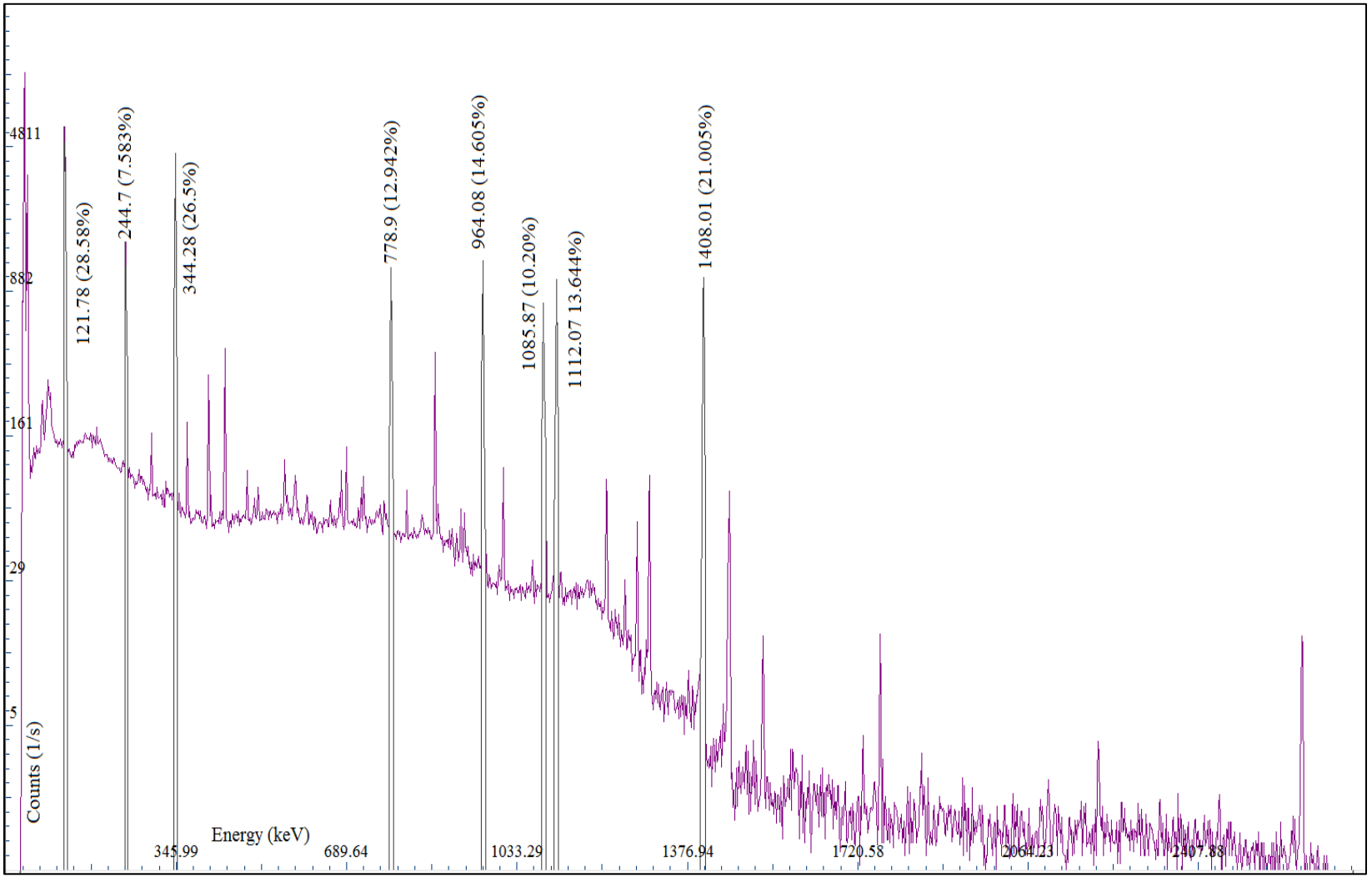

Figure 14. Eu-152 spectrum (20 cm) utilized to obtain detector efficiency.

The rate of decay specified in Eq. 3 is given by the term λN where λ is the physical decay constant and N is the total number of radioactive nuclei present at a given time. The production term is given by $\phi_o\Sigma_{(\alpha,2n)}$, where the alpha-particle flux is represented by ϕ_o and $\Sigma_{(\alpha,2n)}$ defines the activation reaction cross-section, which is averaged over the alpha-particle spectrum between 22 MeV and E_{max}. Solving Eq. 3 for the production term yields a first order ordinary differential equation with constant coefficients, Eq. 4.

$$\frac{dN}{dt} + \lambda N = \phi_o \Sigma_{\alpha,2n} \tag{4}$$

Solution to Eq. 4 can be obtained if the following assumptions are made [46]:

1. Constant alpha-particle flux.
2. Neglect burn-up of daughter atoms (do not get activated).
3. Neglect loss of target atoms.
4. No daughter atoms at t = 0 (N = 0).

Based on these assumptions and initial condition of N = 0 at t = 0, solution for Eq. 4 can be obtained, Eq. 5.

$$\mathrm{N(t)} = \frac{\phi_o \Sigma_{\alpha,2n}}{\lambda}(1 - \mathrm{e}^{-\lambda t}) \tag{5}$$

The exponential term in Eq. 5, accounts for the radioactive decay of the daughter atom during the activation process. By multiplying both sides of Eq. 5 with the decay constant, λ, activity for the daughter radionuclide can be obtained, Eq. 6.

$$\mathrm{A(t)} = \phi_o \Sigma_{\alpha,2n}(1 - \mathrm{e}^{-\lambda t}) \tag{6}$$

If physical decay is neglected, the saturation activity, A_∞, can be obtained at t = ∞ (Figure 15). However, for this study we had constant flux at the target but not through

the target. The target was utilized as a beam stop; therefore, to calculate saturation activity, the attenuation of the flux as a function of depth within the target must be determined. Being able to characterize the attenuation of the flux within the target is extremely difficult and therefore it was not performed. Consequently, the saturation activity was calculated experimentally using the principles of gamma-ray spectroscopy.

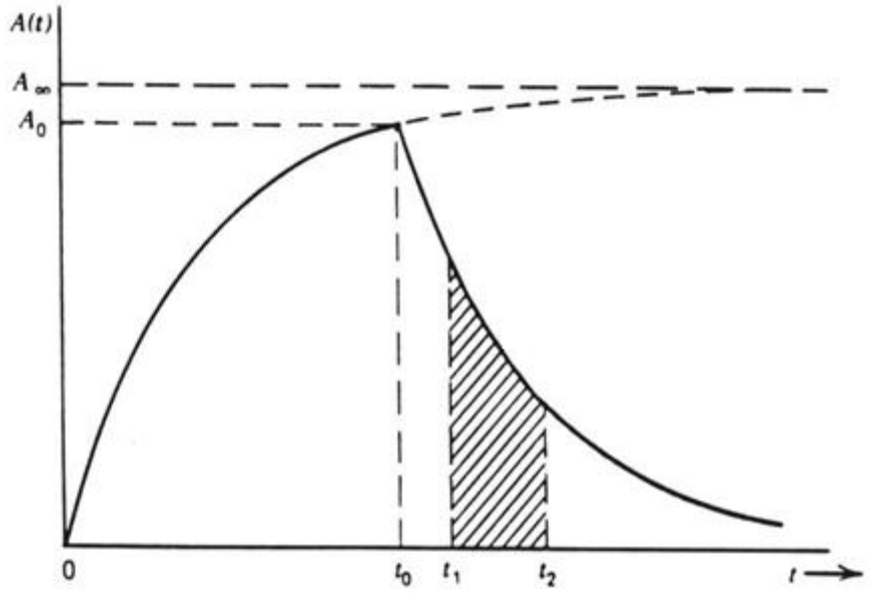

Figure 15. Plot of induced and saturation activity as a function of time [46].

From Figure 15, principles of activation detectors can be applied to measure and calculate activity of the daughter atoms at end of bombardment (EOB). In Figure 5, t_o denotes time of bombardment, t_1 is time when measurement is initiated, and t_2 is end of

measurement. The measured counts acquired between time interval t_1 to $t_2$can be obtained based on Eq. 7 [46].

$$C = \varepsilon \int_{t_1}^{t_2} A_o e^{-\lambda(t-t_o)} dt + B \quad (7)$$

$$C = \varepsilon \left(\frac{A_o}{\lambda}\right) e^{-\lambda t_o} \left(e^{-\lambda t_1} - e^{-\lambda t_2}\right) + B \quad (8)$$

In Eq. 7, C is the observed counts, B is the background counts, and A_o is the activity produced at EOB, and ε is the absolute efficiency of the detector system. From acquired measurements of the radiative emissions (gamma-rays) of the daughter atoms, both activity at EOB, $A(t_o)$, and saturation activity, A_∞, can be calculated by applying Eq. (9) and (10) respectively [46].

$$A_o = \frac{\lambda(C-B)}{\varepsilon_\gamma I_\gamma e^{\lambda t_o}\left(e^{-\lambda t_1} - e^{-\lambda t_2}\right)} \quad (9)$$

$$A_\infty = \frac{\lambda(C-B)}{\varepsilon_\gamma I_\gamma (1-e^{-\lambda t_o}) e^{\lambda t_o}\left(e^{-\lambda t_1} - e^{-\lambda t_2}\right)} \quad (10)$$

ε_γ is the efficiency of the gamma-ray as a function of its energy and I_γ is the relative emission intensity.

2.7 Neutron Production

In preparation for production runs of At-211 required for distillation, neutron shielding assessment was performed. The shielding was developed to minimize neutron activation of equipment in the cyclotron vault. From the Bi-209(α,2n)At-211 reaction, it is known that recoil neutrons will be emitted. Also, there are other reactions that contribute to the production of these neutrons. Therefore, a TALYS simulation was performed for alpha-particle energies between 0 and 28 MeV bombarding a Bi-209 target. This simulation was performed to obtain the neutron emission rate per incident

alpha-particle along with the generated neutron spectrum. The neutron spectrum was then coupled to the Monte Carlo code MCNPX to assess the required shielding and estimate the corresponding neutron dose rates at the surface of the shielding. Table 16 and Figure 16 presents the cross-section data with respect to neutron emission. Figure 17 shows a plot of the neutron yield for the Bi-209(α,xn) reaction. The emitted neutron energy spectrum was estimated by summing over the energy range of the incident alpha-particles (Figure 18). This assumption accounts for attenuation of the beam through the Bi-209 target when considering shielding requirements.

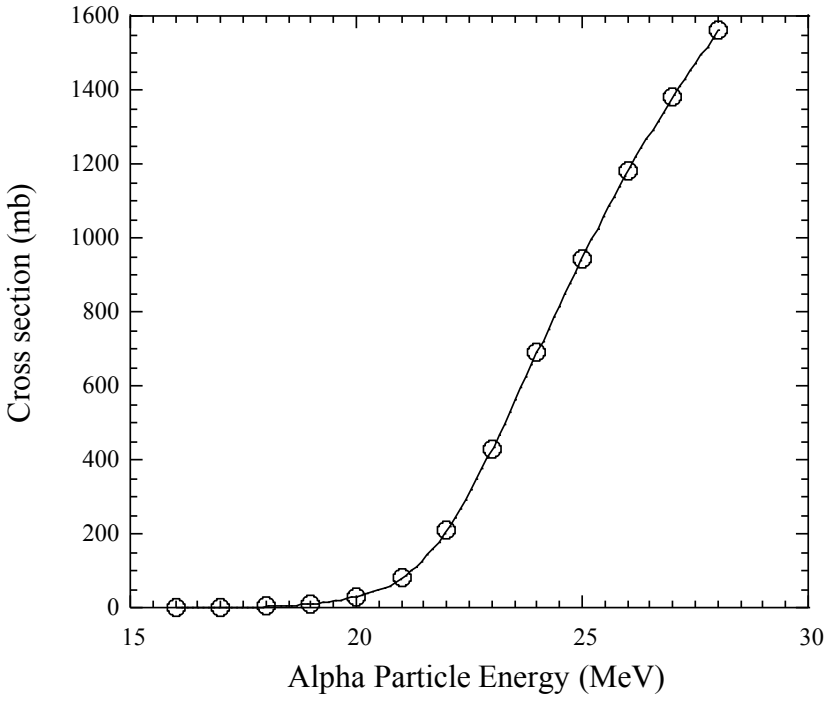

Figure 16. Neutron production cross-section for Bi-209(α,xn) reaction as a function of incident alpha-particle energy estimated using the code TALYS.

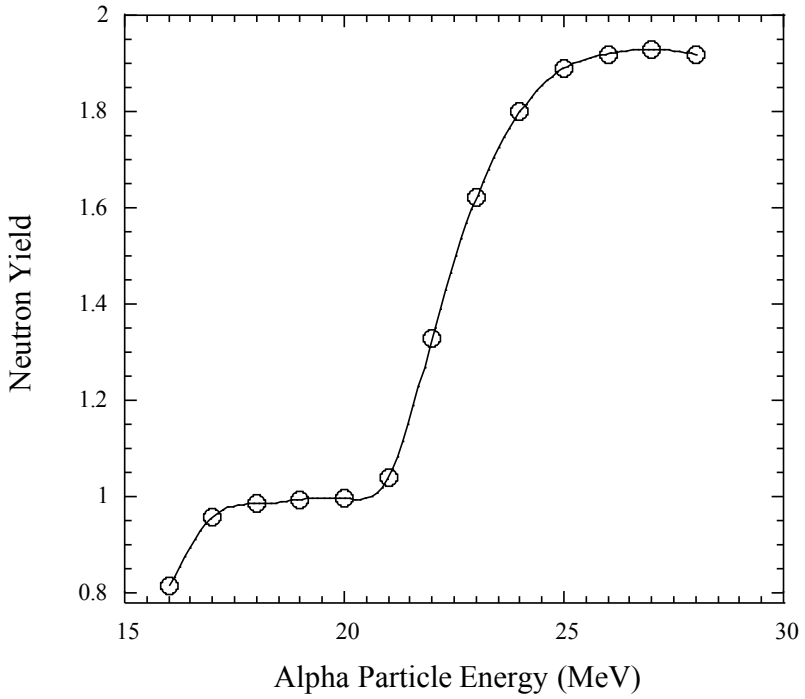

Figure 17. Neutron yield for Bi-209(α,xn) reaction per incident alpha-particle energy.

Table 16. Neutron production data for Bi-209(α,xn) reaction.

$Energy_{\alpha}$ (MeV)	Cross-section (mb)	Yield
16	0.15	0.81
17	0.74	0.96
18	2.89	0.98
19	10.00	0.99
20	30.20	1.00
21	79.13	1.04
22	208.85	1.33
23	428.38	1.62
24	689.73	1.80
25	944.92	1.89
26	1176.47	1.92
27	1383.23	1.93
28	1561.23	1.92

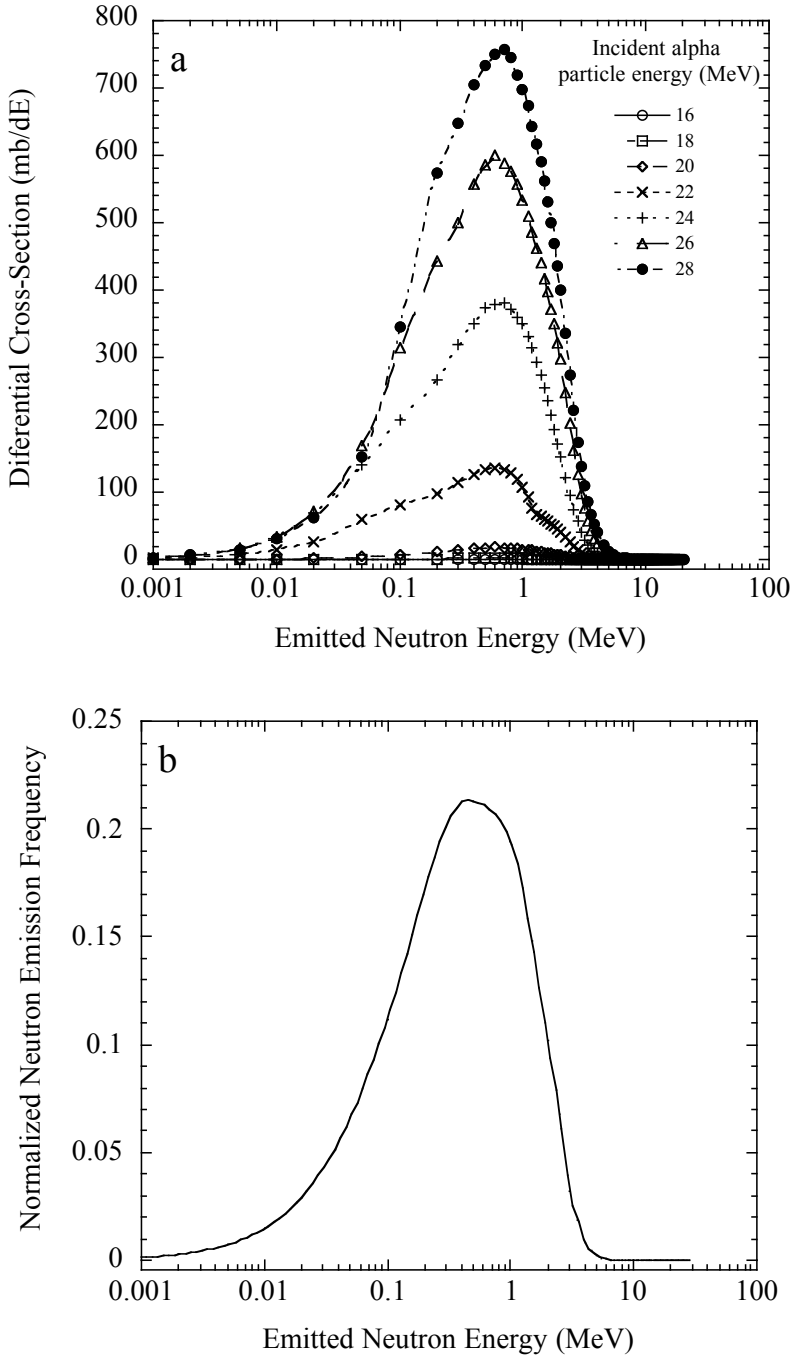

Figure 18. a) Differential cross-section of neutron production as a function of incident alpha-particle energy. b) Normalized neutron energy spectrum for Bi-209(α,xn) reaction from TALYS.

Based on TALYS analysis, the normalized neutron energy spectrum was utilized as the source energy spectrum for the MCNPX simulations. The MCNPX simulation was performed with and without shielding. From Figure 18 the mean energy of the neutron spectrum was calculated to be approximately 1.2 MeV. From the initial MCNPX simulations without shielding, we modeled a 2-inch borated polyethylene (5% boron) shielding to assess the reduction in neutron flux [47, 48]. Figure 19 represents the schematic utilized for the MCNPX simulations. In the simulation several tallies were utilized to obtain flux and dose rate values of neutrons and neutron induced photons. The geometrical placement of the neutron dose tallies in MCNPX was determined through discussions with Dr. Gabriel Tabacaru. Dose rates were obtained through the conversion of neutron and photon flux based on flux-to-dose rate tally modifiers within MCNPX, based on the International Commission on Radiological Protection (ICRP) 21 report [49]. MCNPX input files for the simulations can be found in Appendix B.

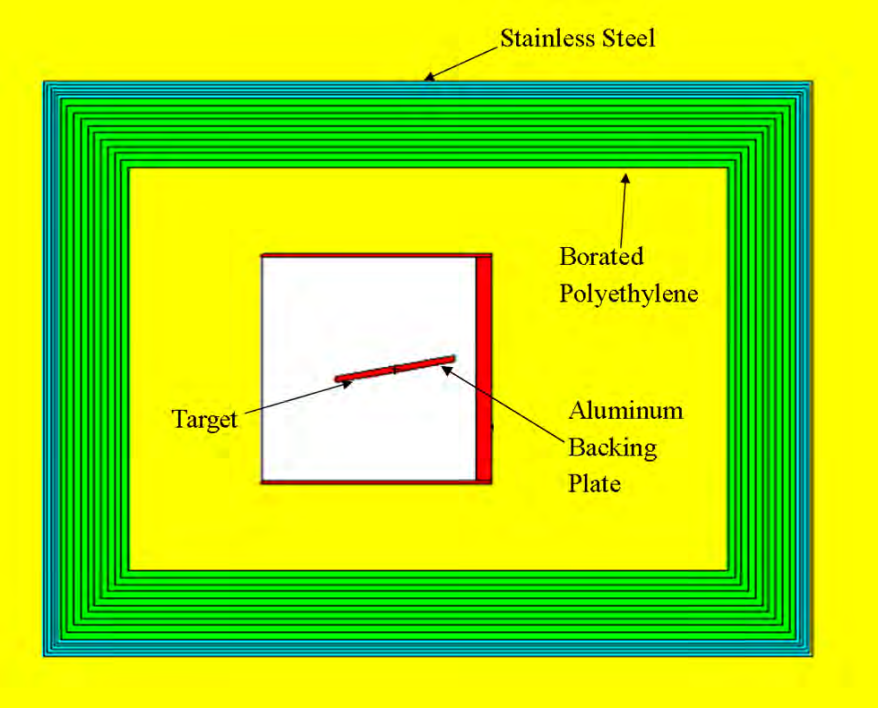

Figure 19. Target geometry utilized for MCNPX shielding simulations.

3. RESULTS AND DISCUSSION

3.1 Results

Production of At-211 was performed with two experiments. Both experiments utilized the target system and principles described in Section 2. The first experiment established the production of At-211 at the Texas A&M Cyclotron Institute. The success of the initial experiment led to the second experiment, where the production of contaminants was analyzed along with production optimization of At-211. Table 17 lists the parameters utilized for both experiments. Based on the given parameters for the experiments and principles of gamma-ray spectroscopy, assessment of At-211 was performed as described in Section 2.6.

Table 17. Experiment parameters for production of At-211 experiments using the K500 cyclotron.

Parameter	Experiment 1	Experiment 2
Bombardment Time (t_o)	4 h	4 h
Cooling time (t_o - t_1)	1.42 h	12.4 h
Measured time (t_1 -t_2)	1 h	1 h
Beam Intensity	163.17 nA	96.13 nA

Since the objective of initial experiment was to establish the feasibility of producing At-211, a nominal alpha particle beam energy of 27.8 MeV was selected. This energy was based on recommendations obtained from the open literature, which is optimal for production of At-211 and residual radionuclides. For the second experiment

the beam energy was estimated at 25.3 MeV as described in Section 2. Gamma-ray spectroscopy was carried out at 35 and 20 cm away from the HPGe detector for Experiment 1 and 2 respectively. After performing energy calibration on the acquired gamma-ray spectra, the peaks of all measured gamma-ray emissions were identified (Figures 20 and 21). These emissions help identify the radionuclide At-211 and other contaminants. Based on principles of gamma-ray spectroscopy discussed in Section 2.6, activity for the various gamma-ray emissions for all produced radionuclide was calculated. Table 18 and 19 represent all identified products paired with their gamma-ray emissions and their respective activities. Based on these principles, the average measured activity for the first experiment for At-211 was 23.48 ± 0.81 MBq with At-210 activity of 0.55 ± 0.07 MBq (<2.5% relative to At-211). Activity yields for the second experiment were less than that for the first experiment; however, production of At-210 and Po-210 was avoided. Activity of At-211 for the second experiment was 4.76 ± 0.13 MBq. Saturation activity of At-211 for both experiments based on Eq. 10 was calculated to be 73.81 MBq and 14.96 MBq.

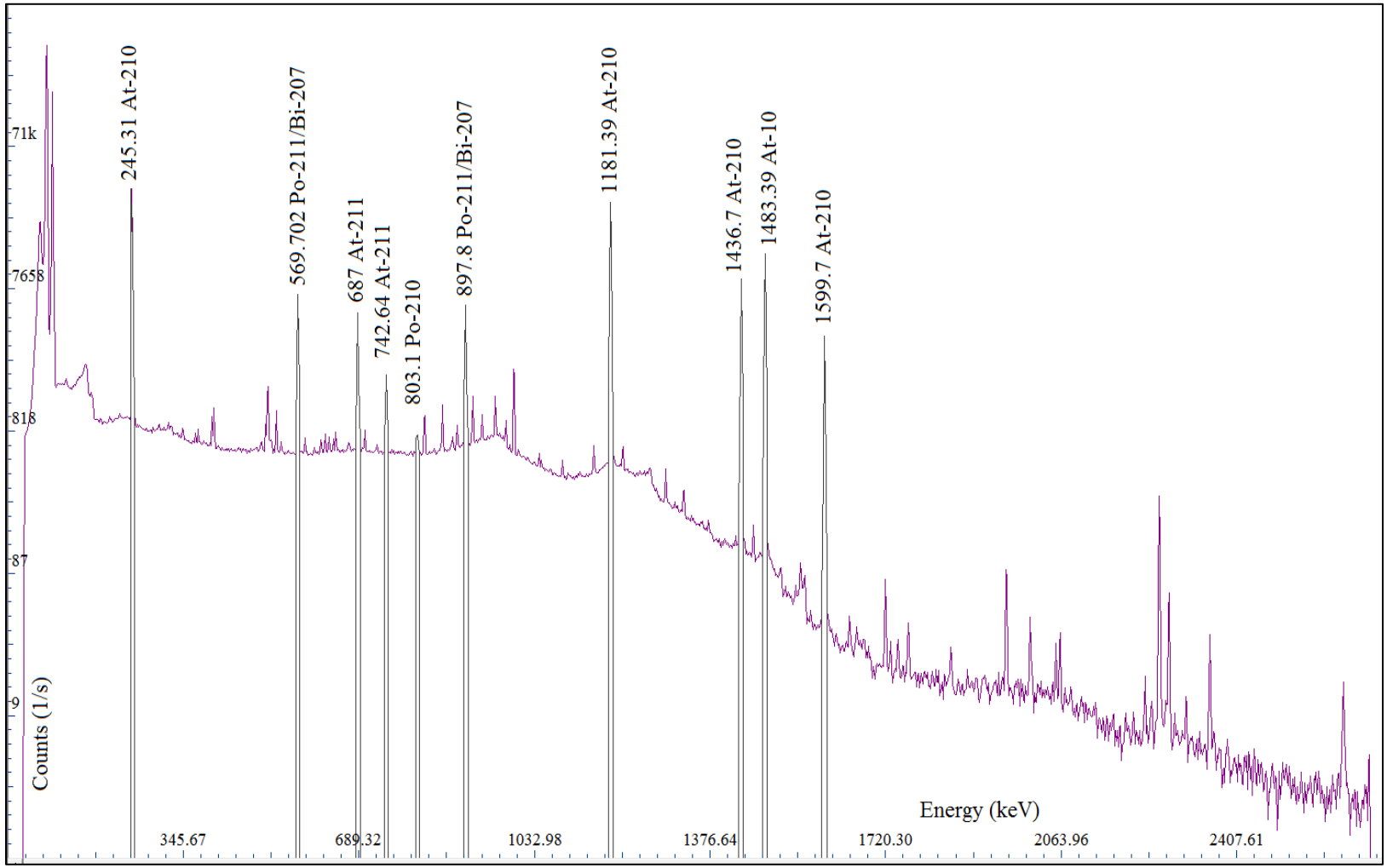

Figure 20. Gamma-ray spectrum based on first experiment measurement at 35 cm.

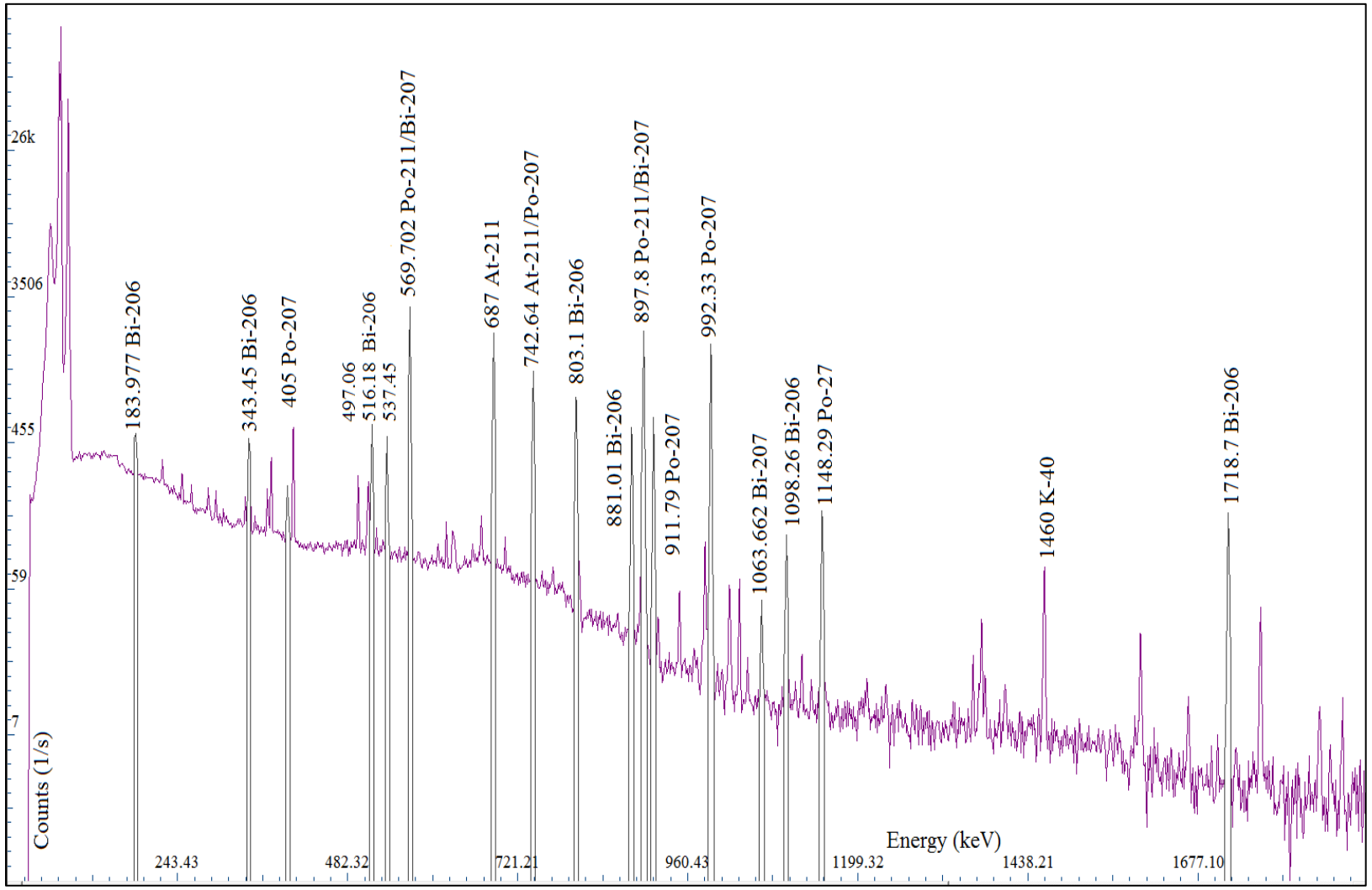

Figure 21. Gamma-ray spectrum based on second experiment measurements at 20 cm.

Table 18. Calculated production yields for the first experiment using an alpha-particle beam (27.8 MeV, 163.17 nA) measured at a distance of 35 cm from the detector.

Radionuclide	E_γ (keV)	I_γ (%)	half life	Peak Net Counts (Area)	Activity (MBq)	Activity (MBq/μAh)
At-211	687	0.261	7.241 h	31016	22.553	34.555
	742.64	0.001		-	-	-
Po-211*	569.702	29.10	0.516 s	39713	24.040	36.833
	897.8	32.65		36888	23.852	36.544
At-210	245.31	79	8.1 h	268566	0.420	0.643
	1181.39	99.3		251782	0.586	0.897
	1436.7	29		67115	0.578	0.885
	1483.39	46.5		108138	0.588	0.901
	1599.7	13.4		30118	0.586	0.897
Po-210**	803.1	0.00121	138.38 d	-	-	-
Bi-207***	569.702	97.74	31.55 y	-	-	-
	897.8	0.121		-		
	1063.662	74.5		-		
	1770.237	6.87		-		

*Po-211gamma-ray intensities are relative to decay of At-211 to Po-211.
** Po-210 activity is dependent on activity of At-210 at EOB.
***Bi-207 activity is a dependent on activity of At-211 at EOB.

Table 19. Calculated production yields for the second experiment using an alpha-particle beam (25.3 MeV, 96.13 nA) measured at a distance of 20 cm from the detector.

Radionuclide	Eγ (keV)	Iγ (%)	half life	Peak Net Counts (Area)	Activity (MBq)	Activity (MBq/μAh)
At-211	687	0.261	7.241	11483	4.610	11.990
	742.64	0.001		-	-	-
Po-211*	569.702	29.10	0.516 s	14759	4.852	12.618
	897.8	32.65		13165	4.813	12.518
Bi-207**	569.702	97.74	31.55 y	-	-	-
	1063.662	74.5		-		
	1770.237	6.87		-		
Bi-206	183.977	15.8	6.234 d	1023	0.001	0.003
	343.51	23.4		1193	0.001	0.003
	398	10.74		780	0.002	0.005
	497.06	15.31		959	0.002	0.005
	516.18	40.7		2646	0.002	0.005
	537.45	30.5		1952	0.002	0.005
	803.1	99		5862	0.002	0.005
	881.01	66.2		3850	0.002	0.006
	1718.7	31.8		2174	0.003	0.009
Po-207	405	9.7	5.8 h	2772	0.031	0.082
	742.64	28.2		-	-	-
	911.79	16.95		4153	0.040	0.104
	992.33	59.3		13193	0.038	0.099
	1148.29	5.72		1194	0.038	0.099

*Po-211gamma-ray intensities are relative to decay of At-211 to Po-211.
**Bi-207 activity is a dependent on activity of At-211 at EOB.

3.2 Discussion

The production yield for At-211 was calculated based on measured counts for the 687 keV gamma-ray emission and that of its daughter Po-211, which is extremely short-lived ($t_{1/2}$ = 0.516s). Due to Po-211 short half-life, the atoms of Po-211 which exists at the time of measurement are those that decay from At-211. Therefore, the half-life of Po-211 can be assumed to be similar to At-211, and its radiative emissions are normalized based on relative decay probability of At-211 via electron capture to Po-211 (58.2%). Activities for long lived radionuclides, such as Po-210 and Bi-207, were calculated based on the total number of parent atoms present at EOB and decay probability of the parent (branching ratio). Also, assessment of Po-210 activity is not possible via gamma-ray spectroscopy because Po-210 is a pure alpha-emitter. Therefore, the activity of Po-210 is assumed to be from the decay of At-210 via electron capture (99.82%).

Based on the gamma-ray spectrum for the first experiment, the radionuclide At-211 was observed. However, the radionuclides At-210 and P-210 were also observed. Based on cross-section evaluations in Section 2, the threshold energy for the production of At-210 is above 29 MeV and it should not have been produced. The production of these contaminants can be attributed to the use of stacked foil target system. When utilizing multiple stacked foils for beam degradation, the full-width half max (FWHM) of the beam has been shown to greatly increase [36]. The increase of the FWHM of the beam broadens the energy range of the alpha-particles reaching the Bi-209 target above the 29 MeV thresholds, thus enabling the production of At-210 and Po-210. The

experiment was deemed successful despite production of these contaminants because the total measured activity at EOB of At-210 was 0.55 ± 0.07 MBq. The content of At-210 produced was less than 2.5% of At-211 yield, which is consistent to observations in published literature [28, 29, 36]. In terms of distillation, in published literature it is observed that Po-210 activity was less than 0.02% of the At-211 activity collected and is not considered as the primary contaminant. Due to similar chemical properties of At-210 and At-211, At-210 is considered the primary contaminant to avoid.

Since the first experiment yielded the contaminants At-210 and Po-210, the second experiment was conducted to show that production of these contaminants could be further minimized or avoided completely. From the gamma-ray spectrum of the second experiment, production of At-210 and Po-210 was completely avoided. However, the production yield of At-211 was reduced by approximately 50%. This reduction in yield of At-211 is not desirable when distillation of At-211 is accounted. Based on published literature distillation can lead to a loss of up to 40 – 75% of the EOB At-211 activity [28, 29]. The reduction in yield of At-211 can be explained by low current extracted for the second experiment 96.13 nA compared to 163.17 nA of the first experiment. The cited reason was on going mechanical issues with the cyclotron.

However, production of contaminants was not completely avoided in the second experiment. In Table 17 it is shown that Bi-206 and Po-207 were both produced with yields of less than 0.04% and 0.8% relative to the At-211 yield, respectively. Based on these relative yields, Po-207 is considered the primary contaminant. The production channel for Po-207 was not identified.

3.3 Neutron Shielding

From MCNPX simulations, the dose rate was calculated based on emitted neutron spectra and induced photons (n, p) (Table 20). The actual dose rate during the experiment is proportional to the intensity of the alpha-particle beam extracted and the integral neutron yield of the beam energy through the target. From the simulations it is shown that neutron transmission is reduced by a maximum factor of 2.2. This value is comparable to those found in published literature [46]. Based on these calculations a shielding cart was developed based on the geometry of the simulation. The walls of the cart were layered with four inches of borated polyethylene and covered with an external plane of stainless-steel of 0.5 inches (Figure 22).

Table 20. MCNPX contact dose rate projections for neutrons and induced photons.

Tally Type	x	y	z	Dose rate without shielding (Sv/h)	Dose rate with shielding (Sv/h)
Neutron	23	0	0	1.42E-10	6.29E-11
Photon				2.74E-14	4.71E-13
Neutron	-23	0	0	1.30E-10	5.97E-11
Photon				2.58E-14	4.50E-13
Neutron	0	10	-33	4.26E-11	1.92E-11
Photon				1.24E-14	2.56E-13
Neutron	0	-10	-33	4.25E-11	2.02E-11
Photon				1.25E-14	2.69E-13
Neutron	10	0	-33	5.73E-11	2.48E-11
Photon				1.24E-14	2.61E-13

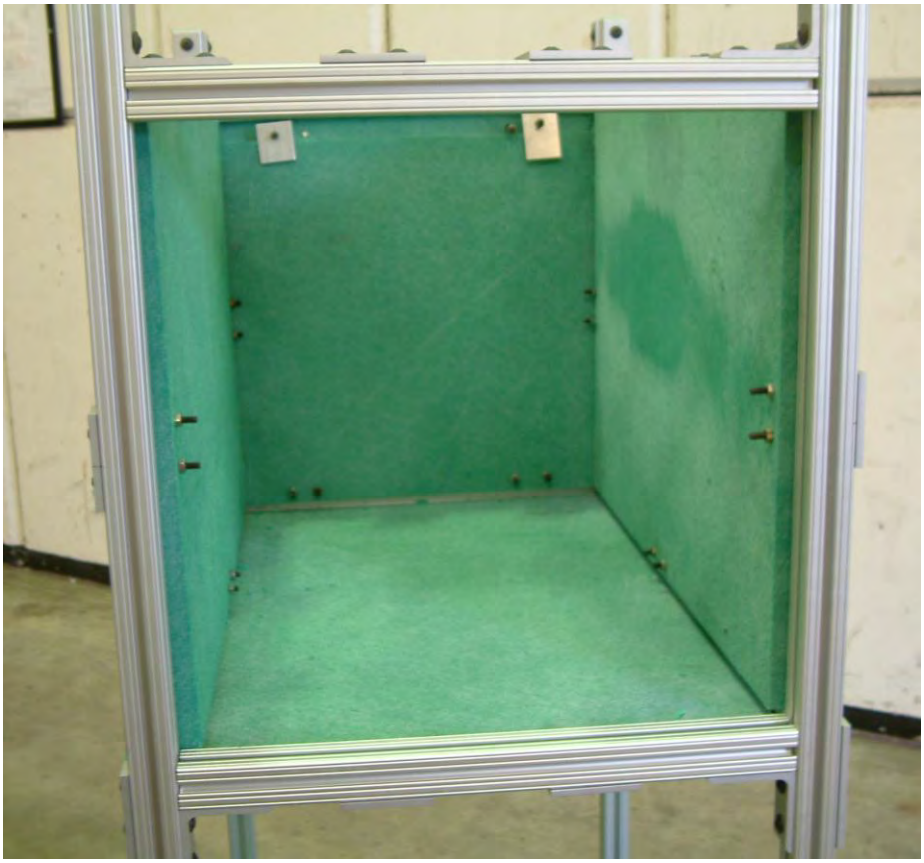

Figure 22. Borated-polyethylene shielding cart designed to reduce neutron transmission during the irradiation of bismuth-209 with alpha-particles.

4. SUMMARY AND RECOMMENDATIONS

4.1 Conclusion

The production of At-211 was established through two experiments at the Texas A&M Cyclotron Institute. In preparation for these experiments, numerous preliminary computational studies were carried out and analyzed the initial production of At-211. These studies include cross-section evaluations, beam degradation analysis, target development, and HPGe detector calibration. Based on these studies, it was proven that At-211 could be produced at the Texas A&M Cyclotron Institute while minimizing and controlling the production of contaminants, mainly At-210.

The following are observations and results obtained from the two experiments:

1. At-211 yields were 35.98 and 12.38 MBq/(μA-h) based on principles of gamma-ray spectroscopy. Saturation activity of At-211 for each experiment was calculated to be 73.84 MBq and 14.96 MBq.
2. Contaminants yields were less than 0.9% relative to At-211 activity except for At-210 which was less than 2.5% of At-211, and with lower beam energy production of At-210 and Po-210 was avoided.

The following are recommendations for future research into this area:

1. Production of At-211 should be assessed through direct bombardment of Bi-209.
2. Use of silicon detectors to characterize the initial beam extracted so FWHM calculations can be performed.

3. Production of At-211 should be characterized with experiments utilizing the K150 cyclotron.
4. Different software for gamma-ray spectroscopy should be utilized. The AMPTEK software had a tendency to crash during analysis as it requires significant amount of computing resources.

4.2 Future Work

The successful production of At-211 will allow the continuation of future research in the area of TRT. Future goals included the production of At-211 for distillation purposes, development of radioactive nanoparticles, and functionalization with monoclonal antibodies and other biological compounds. In order to produce the activity of At-211 required for distillation, a new target was developed. Development of this target was stimulated by the concerns of melting the Bi-209 target foil during bombardment. This concern arose due to the use of K150 cyclotron beam which can deliver higher beam intensity. The energy profile of the extracted K150 beam is extremely discrete with a small FWHM of less than 2%. These properties of the K150 cyclotron make it an ideal production source; however, the high intensity equates to dissipation of higher energies by the Bi-209 target.

The dissipation of alpha-particle beam energy requires an active cooling system for the target to prevent the melting of bismuth (the melting point of bismuth is 271 ^{o}C). An aluminum block target was designed to withstand the heat produced during bombardment. This design was developed by Dr. Larsen at Duke University [29]. The dimensions of the aluminum target were 9 cm by 2 cm by 0.5 cm and a groove of 100

μm was machined on the top layer for the direct deposition of bismuth (Figure 22). This groove was developed to deposit melted bismuth (Sigma-Aldrich, 99.99% purity). This target was also machined at the bottom to generate a u-shape and have two thin fins that are in contact with the target holder and cooling system. This shape was deemed best suited to dissipate the heat. The aluminum target for At-211 distillation experiments is designed to be mounted onto a target holder with a coolant channel. The target holder was developed and designed at the Texas A&M Cyclotron Institute (Figures 23 and 24). The coolant channel will be utilized to cool the aluminum target and prevent the melting of bismuth.

Figure 23. Aluminum target with groove designed to dissipate heat produced during the bombardment of melted bismuth.

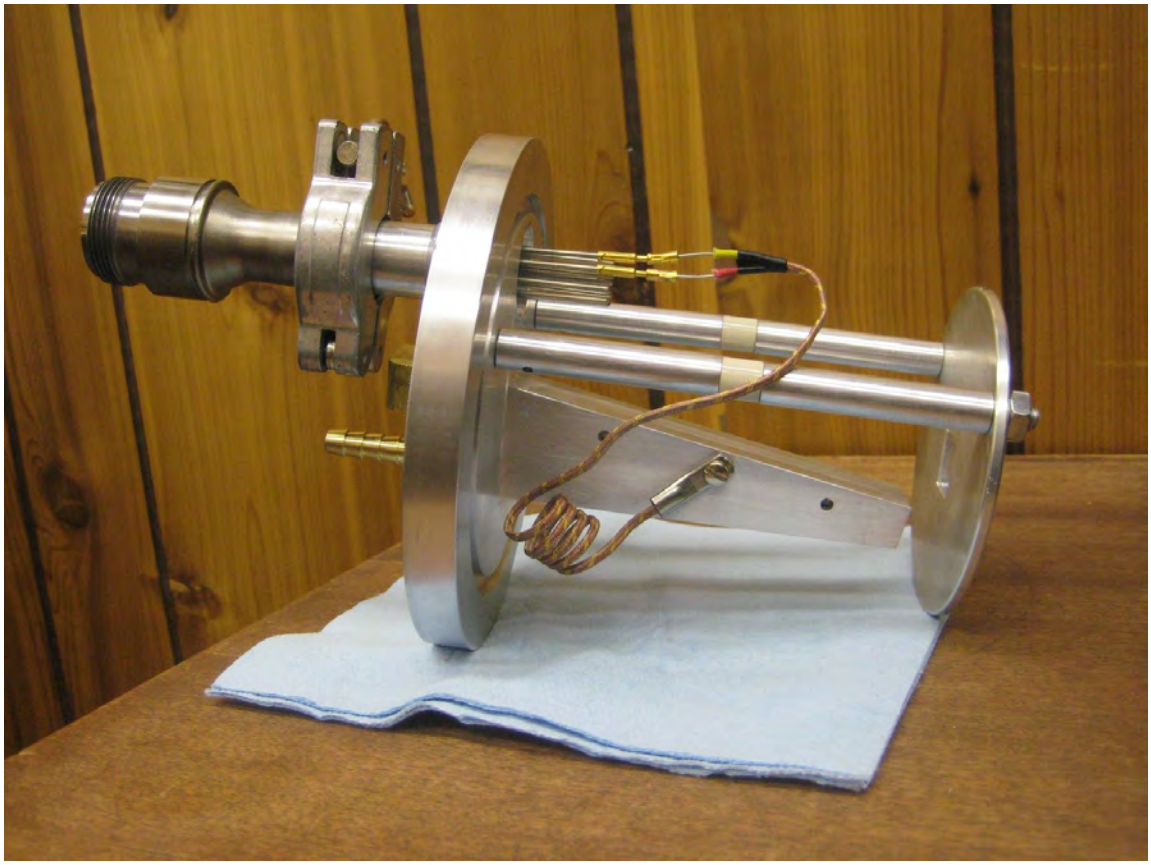

Figure 24. Redesigned target holder for the production of At-211 for distillation experiments.

REFERENCES

[1] Altekruse SF, Kosary CL, Krapcho M, Neyman N, Aminou R, Waldron W, Ruhl J, Howlader N, Tatalovich Z, Cho H, Mariotto A, Eisner MP, Lewis DR, Cronin K, Chen HS, Feuer EJ, Stinchcomb DG, Edwards BK (eds). Bethesda, MD, SEER Cancer Statistics Review, 1975-2008, National Cancer Institute. http://seer.cancer.gov/csr/1975_2008/.

[2] Speer TW. Targeted Radionuclide Therapy, Philadelphia: Lippincott Williams & Wilkins, 2011.

[3] Pressman D. Tissue localizing antibodies. Ann N Y Acad Sci 1955;59:376-80.

[4] Pressman D. Radiolabeled antibodies. Ann N Y Acad Sci 1957;69:644-50.

[5] Pressman D. The development and use of radiolabeled antitumor antibodies. Cancer Res 1980;40:2960-4.

[6] Pressman D, Korngold L. The *in vivo* localization of anti-Wagner-osteogenic-sarcoma antibodies. Cancer 1953;6:619-23.

[7] Pressman D, Watanabe T. Tumor localization of radiolabeled antibodies raised by a mouse plasma cell tumor. Immunochemistry 1975;12:581-4.

[8] Nungester WJ, Fisher H. The inactivation *in vivo* of mouse lymphosarcoma 6C3HED by antibodies produced in a foreign host species. Cancer Res 1954;14:284-8.

[9] Nungester WJ, Garrison D, Fuller D, Hartman RS. Assay of antitumor properties of serum. Med Bull 1955;21:365-70.

[10] Kohler G, Milstein C. Continuous cultures of fused cells secreting antibody of predefined specificity. Nature 1975;256:495-7.

[11] Jacene HA, Filice R, Kasecamp W, Wahl RL. Comparison of ^{90}Y-ibritumomab tiuxetan and ^{131}I-tositumomab in clinical practice. J Nucl Med 2007;48:1767-76.

[12] Zalutsky MR, Reardon DA, Pozzi OR, Vaidyanathan G, Bigner DD. Targeted alpha-particle radiotherapy with ^{211}At-labeled monoclonal antibodies. Nucl Med Biol 2007;34:779-85.

[13] Volkert WA, Hoffman TJ. Therapeutic radiopharmaceuticals. Chem Rev 1999;99:2269-92.

[14] Larsen RH, Vaidyanathan G, Zalutsky MR. Cytotoxicity of alpha-particle-emitting 5-[^{211}At]astato-2'-deoxyuridine in human cancer cells. Int J Radiat Biol 1997;72:79-90.

[15] Sgouros G. Alpha-particles for targeted therapy. ADDR 2008;60:1402-6.

[16] Akabani G, Carlin S, Welsh P, Zalutsky MR. *In vitro* cytotoxicity of ^{211}At-labeled trastuzumab in human breast cancer cell lines: effect of specific activity and HER2 receptor heterogeneity on survival fraction. Nucl Med Biol 2006;33:333-47.

[17] Andersson H, Elgqvist J, Horvath G, Hultborn R, Jacobsson L, Jensen H, et al. Astatine-211-labeled antibodies for treatment of disseminated ovarian cancer: an overview of results in an ovarian tumor model. Clin Cancer Res 2003;9:3914S-21S.

[18] Bloomer WD, McLaughlin WH, Lambrecht RM, Atcher RW, Mirzadeh S, Madara JL, et al. ^{211}At radiocolloid therapy: further observations and comparison with radiocolloids of ^{32}P, ^{165}Dy, and ^{90}Y. Int J Radiat Oncol Biol Phys 1984;10:341-8.

[19] Larsen RH, Hoff P, Vergote IB, Bruland OS, Aas M, De Vos L, et al. Alpha-particle radiotherapy with ^{211}At-labeled monodisperse polymer particles, ^{211}At-labeled IgG proteins, and free ^{211}At in a murine intraperitoneal tumor model. Gynecol Oncol 1995;57:9-15.

[20] Lindegren S, Frost S, Back T, Haglund E, Elgqvist J, Jensen H. Direct procedure for the production of ^{211}At-labeled antibodies with an epsilon-lysyl-3-(trimethylstannyl)benzamide immunoconjugate. J Nucl Med 2008;49:1537-45.

[21] Palm S, Andersson H, Back T, Claesson I, Delle U, Hultborn R, et al. *In vitro* effects of free ^{211}At, ^{211}At-albumin and ^{211}At-monoclonal antibody compared to external photon irradiation on two human cancer cell lines. Anticancer Res 2000;20:1005-12.

[22] Pozzi OR, Zalutsky MR. Radiopharmaceutical chemistry of targeted radiotherapeutics, Part 2: radiolytic effects of ^{211}At alpha-particles influence N-succinimidyl 3-^{211}At-astatobenzoate synthesis. J Nucl Med 2005;46:1393-400.

[23] Zalutsky MR, Pozzi OR. Radioimmunotherapy with alpha-particle emitting radionuclides. Q J Nucl Med Mol Imaging 2004;48:289-96.

[24] Zalutsky MR, Reardon DA, Akabani G, Coleman RE, Friedman AH, Friedman HS, et al. Clinical experience with alpha-particle emitting ^{211}At: treatment of recurrent

brain tumor patients with ^{211}At-labeled chimeric antitenascin monoclonal antibody 81C6. J Nucl Med 2008;49:30-8.

[25] Zalutsky MR, Vaidyanathan G. Astatine-211-labeled radiotherapeutics: an emerging approach to targeted alpha-particle radiotherapy. Curr Pharm Des 2000;6:1433-55.

[26] Zalutsky MR, Zhao XG, Alston KL, Bigner D. High-level production of alpha-particle-emitting ^{211}At and preparation of ^{211}At-labeled antibodies for clinical use. J Nucl Med 2001;42:1508-15.

[27] Hermanne A, Tarkanyi F, Takacs S, Szucs Z, Shubin YN, Dityuk AI. Experimental study of the cross-sections of alpha-particle induced reactions on ^{209}Bi. Appl Radiat Isot 2005;63:1-9.

[28] Lambrecht RM, Mirzadeh S. Cyclotron isotopes and radiopharmaceuticals-XXXV astatine-211. Int. J. Appl. Radiat. Isot. 1984;36:443-50.

[29] Larsen RH, Wieland BW, Zalutsky MR. Evaluation of an internal cyclotron target for the production of ^{211}At via the ^{209}Bi (alpha,2n)^{211}At reaction. Appl Radiat Isot 1996;47:135-43.

[30] Morzenti S, Bonardi ML, Groppi F, Zona C, Persico E, Menapace E, et al. Cyclotron production of ^{211}At/^{211g}Po by ^{209}Bi(a,2n) reaction. Journal of Radioanalytical and Nuclear Chemistry 2008;276:843-7.

[31] Neirinckx RD, Smit JA. Separation of astatine-211 from bismuth metal. Anal Chim Acta 1973;63:201-4.

[32] Pozzi OR, Zalutsky MR. Radiopharmaceutical chemistry of targeted radiotherapeutics, Part 1: effects of solvent on the degradation of radiohalogenation precursors by ^{211}At alpha-particles. J Nucl Med 2005;46:700-6.

[33] Pozzi OR, Zalutsky MR. Radiopharmaceutical chemistry of targeted radiotherapeutics, Part 3: alpha-particle-induced radiolytic effects on the chemical behavior of ^{211}At. J Nucl Med 2007;48:1190-6.

[34] Schultz MK, Hammond M, Cessna JT, Plascjak P, Norman B, Szajek L, et al. Assessing the ^{210}At impurity in the production of ^{211}At for radiotherapy by ^{210}Po analysis via isotope dilution alpha spectrometry. Appl Radiat Isot 2006;64:1365-9.

[35] Chu SYF, Ekstrom LP, Firestone RB. WWW Table of Radioactive Isotopes, Online Database. LBNL Berkeley, CA; 1999. http://nucleardata.nuclear.lu.se/nucleardata/toi/

[36] Henriksen G, Messelt S, Olsen E, Larsen RH. Optimisation of cyclotron production parameters for the ^{209}Bi(alpha, 2n) ^{211}At reaction related to biomedical use of ^{211}At. Appl Radiat Isot 2001;54:839-44.

[37] Lebeda O, Jiran R, Ralis J, Stursa J. A new internal target system for production of ^{211}At on the cyclotron U-120M. Appl Radiat Isot 2005;63:49-53.

[38] Lindegren S, Back T, Jensen HJ. Dry-distillation of astatine-211 from irradiated bismuth targets: a time-saving procedure with high recovery yields. Appl Radiat Isot 2001;55:157-60.

[39] Youngblood DH. The Texas A&M K500 cyclotron facility. Nuclear Instruments, Methods in Physics Research 1991;B56:991 - 5.

[40] Tribble R. A proposed uacility upgrade for the Texas A&M University Cyclotron Institute. Internal Report, College Station, TX 2001.

[41] Agency IAEA. Cyclotron produced radionuclides: physical characteristics, production pethods: Technical Reports Series No. 468. 2009, p. 33 - 40.

[42] Koning A, Hilaire S, Duijvestijn M. TALYS. Software Manual, NRG; 2008. http://www.talys.eu/

[43] Ramler WJ, Wing J, Henderson DJ, Huizenga JR. Exictation Functions of Bismuth, Lead. Physical Review 1959;114:154 - 62.

[44] Ziegler J. SRIM & TRIM. Software, 2011. http://www.srim.org/

[45] Group L. LISE++: a simulation of fragment separators. Software, NSCL/MSU, 2011. http://groups.nscl.msu.edu/lise/lise.html

[46] Knoll GF. Radiation Detection, Measurement, New York: Wiley,2000.

[47] Allen FJ, Futterer AT, Wright WP. Neutron Transmission versus Thickness for Some Common Materials. Internal Report, Aberdeen Proving Ground Bethesda, MA, 1962.

[48] Wuest CR. TART Calculations of Neutron Attenuation, Neutron-induced Photons on 5%, 20% Boraded Polyethylene Slabs. Lawrence Livermore National Laboratory. Livermore, CA; 1992.

[49] Ford MR. Report of the Task Group on Dose Calculations to ICRP Committee 2, March 17-21, 1980; Department of Enegry, Oak Ridge National Laboratory. Oak Ridge, TN 1980.

APPENDIX A

DETECTOR EFFICIENC AND CALIBARTION DATA

Table A.2. HPGe efficiency values as a function of source to detector distance based on Co-60, Ba-133, Cs-237, and Eu-152.

Energy (keV)	Efficiency (%)						
	SDD 10 cm	SDD 15 cm	SDD 20 cm	SDD 25 cm	SDD 30 cm	SDD 35 cm	SDD 50 cm
80.9971	1.591	-	0.182	0.094	0.052	0.033	0.010
121.7817	1.805	0.606	0.215	0.102	0.057	0.035	0.011
244.6975	1.046	0.414	0.146	0.078	0.042	0.026	0.008
276.398	0.961	-	0.135	0.071	0.038	0.026	0.008
302.853	0.878	-	0.121	0.069	0.037	0.024	0.007
344.2785	0.860	0.356	0.129	0.066	0.038	0.024	0.007
356.017	0.823	-	0.114	0.065	0.035	0.023	0.007
383.851	0.796	-	0.104	0.062	0.035	0.022	0.006
661.657	0.623	0.222	0.085	0.052	0.028	0.017	0.005
778.904	0.519	0.215	0.086	0.046	0.029	0.017	0.005
964.079	0.440	0.195	0.078	0.043	0.025	0.014	0.005
1085.869	0.367	0.167	0.072	0.039	0.025	0.015	0.004
1112.074	0.367	0.167	0.071	0.042	0.022	0.014	0.004
1173.273	0.375	0.149	0.068	0.041	0.025	-	0.004
1332.501	0.397	0.142	0.062	0.040	0.023	-	0.004
1408.006	0.359	0.146	0.066	0.038	0.021	0.014	0.004

APPENDIX B

INPUT FILES FOR MCNPX SIMULATION

MCNPX – Dose rates without shielding

Neutron Spectrum for 209-Bi(alpha,n) reaction - GT

```
c ===========================================================================
c CELL CARD
c ===========================================================================
10    1 -2.700   -10               $ Al Target Holder
11    2 -9.800   -11               $ 30 Micron Bi Target
12    1 -2.7     -12 -13 14          $ Target Holder Backing Plate
13    1 -2.7     -15 12 -16 14       $ Al Beam Line Pipe
14    3 -1.22E-7  10 11 -12 13 -16    $ Volume inside Pipe
17    3 -1.22E-3 -17 (-14:15:16)      $ air around the pipe
18    3 -1.22E-3   -18 17            $ air around the pipe
19    3 -1.22E-3   -19 18            $ air around the pipe
20    3 -1.22E-3   -20 19            $ air around the pipe
21    3 -1.22E-3   -21 20            $ air around the pipe
22    3 -1.22E-3   -22 21            $ air around the pipe
23    3 -1.22E-3   -23 22            $ air around the pipe
24    3 -1.22E-3   -24 23            $ air around the pipe
25    3 -1.22E-3   -25 24            $ air around the pipe
26    3 -1.22E-3   -26 25            $ air around the pipe
27    3 -1.22E-3   -27 26            $ air around the pipe
28    3 -1.22E-3    -28 27           $ air around the pipe
29    3 -1.22E-3    -29 28           $ air around the pipe
30    3 -1.22E-3    -30 29           $ air around the pipe
31    3 -1.22E-3    -31 30           $ air around the pipe
32    3 -1.22E-3    -32 31           $ air around the pipe
```

```
47    3 -1.22E-3 -90  32            $ Outside World
90    0         90                $ Void

c ===========================================================================
c SURFACE CARD
c ===========================================================================
10  1  rpp -0.25 0.25 -1 1 -4.5 4.5              $ Al block
11  1  rpp 0.25 0.253 -1 1 -4.5 4.5              $ Bismuth-209
12    cz  8.25                                  $ Al back plate cylinder
13    pz -6                                     $ Backing Plate Plane (Top)
14    pz -7.2                                   $ Backing Plate Plane (Bottom)
15    cz 8.55                                   $ Beam Line Pipe Cylinder
16    pz 10                                     $ Beam Line Pipe plane
17    rpp -15.00 15.00 -15.00 15.00 -24.92 20.00   $ 2" of Borated Polyethylene
18    rpp -15.51 15.51 -15.51 15.51 -25.43 20.51   $ 2" of Borated Polyethylene
19    rpp -16.02 16.02 -16.02 16.02 -25.94 21.02   $ 2" of Borated Polyethylene
20    rpp -16.52 16.52 -16.52 16.52 -26.44 21.52   $ 2" of Borated Polyethylene
21    rpp -17.03 17.03 -17.03 17.03 -26.95 22.03   $ 2" of Borated Polyethylene
22    rpp -17.54 17.54 -17.54 17.54 -27.46 22.54   $ 2" of Borated Polyethylene
23    rpp -18.05 18.05 -18.05 18.05 -27.97 23.05   $ 2" of Borated Polyethylene
24    rpp -18.56 18.56 -18.56 18.56 -28.48 23.56   $ 2" of Borated Polyethylene
25    rpp -19.06 19.06 -19.06 19.06 -28.98 24.06   $ 2" of Borated Polyethylene
26    rpp -19.57 19.57 -19.57 19.57 -29.49 24.57   $ 2" of Borated Polyethylene
27    rpp -20.08 20.08 -20.08 20.08 -30.00 25.08   $ 2" of Borated Polyethylene
28    rpp -20.33 20.33 -20.33 20.33 -30.25 25.33   $ 0.5" of SS Plate
29    rpp -20.59 20.59 -20.33 20.33 -30.51 25.59   $ 0.5" of SS Plate
30    rpp -20.84 20.84 -20.59 20.59 -30.76 25.84   $ 0.5" of SS Plate
31    rpp -21.10 21.10 -20.59 20.59 -31.02 26.10   $ 0.5" of SS Plate
32    rpp -21.35 21.35 -20.59 20.59 -31.27 26.35   $ 0.5" of SS Plate
90    so 300                          $ Tally ROI & Outside Environment
```

```
c ===========================================================================
c DATA CARD
c ===========================================================================
c Target Plate offset by 10 Degrees
*TR1 0 0 0 10 90 80 90 0 90 100 90 10
c
c Polyethylene Block Translocation
TR2 0 0 -30 1 0 0 0 1 0 0 0 1
TR3 -22.62 0 0 1 0 0 0 1 0 0 0 1
TR4 22.62 0 0 1 0 0 0 1 0 0 0 1
c
MODE N H D T P A S #
IMP:N 1 21R 0
IMP:P 1 21R 0
IMP:H 1 21R 0
IMP:D 1 21R 0
IMP:A 1 21R 0
IMP:T 1 21R 0
IMP:S 1 21R 0
IMP:# 1 21R 0
c
PHYS:N 100 0 0 -1 -1 0 2
PHYS:H 100 0 -1 J 0 J 1
PHYS:A 100 3j 0
PHYS:# 140 J J J 0
c
CUT:# J 0.01
CUT:H J 0.01
CUT:A J 0.01
CUT:D J 0.01
CUT:S J 0.01
```

```
CUT:N J 1e-9
c
LCA 2 1 1 23 1 1 0 1 0
c
sdef PAR=1 x=d1 y=d2 z=d3 CCC=11 ERG=d4 VEC=0 0 -1 DIR=d5 EFF=0.0001
SI1  -0.4 0.9
SP1  0 1
SI2 -1 1
SP2  0 1
SI3 -3.5 3.5
SP3  0 1
SI4 H 0 0.001 0.002 0.005 0.01 0.05 0.1 0.5 1 1.5 2 2.5 3 3.5 4 4.5 5 5.5 6 6.5
    7 7.5 8 8.5 9 9.5 10 10.5 11 11.5 12 12.5
SP4 D 0 0.001406153 0.002831182 0.007373327 0.014942203 0.066366757 0.112268423
    0.212833861 0.194489262 0.148338576 0.102227302 0.06804882 0.032269259
    0.018947065 0.008382303 0.004312252 0.002205652 0.001131632 0.000618138
    0.000351801 0.000223496 0.000145165 0.00010153 6.85231E-05 4.80271E-05
    3.03043E-05 1.97037E-05 1.02224E-05 5.99723E-06 1.82244E-06 1.22686E-06
    1.27672E-08
SI5  -1 9i 1
SP5   0 0.10 9r
SB5   0 0.02 8r 0.84
c ----
PTRAC cell=17 max=10000 TYPE=N FILE=asc
c ----
c Rectangular mesh
tmesh
rmesh1:N
cora1 -27 53i 27
corb1 -27 53i 27
corc1 -54 29i -24
```

```
rmesh11:P
cora11 -27 53i 27
corb11 -27 53i 27
corc11 -54 29i -24
endmd
c Detector tallies
F5:N 23 0 0 1
DF5 IU=1 IC=10
FC5 Neutron Dose on the side of the box +x
F15:P 23 0 0 1
DF15 IU=1 IC=10
FC15 Photon Dose on the side of the box +x
c
F25:N -23 0 0 1
DF25 IU=1 IC=10
FC25 Neutron Dose on the side of the box -x
F35:P -23 0 0 1
DF35 IU=1 IC=10
FC35 Photon Dose on the side of the box -x
c
F45:N 0 10 -33 1
DF45 IU=1 IC=10
FC45 Neutron Dose forward direction
F55:P 0 10 -33 1
DF55 IU=1 IC=10
FC55 Gamma Dose forward direction
c
F65:N 0 -10 -33 1
DF65 IU=1 IC=10
FC65 Neutron Dose forward direction for symmetry
F75:P 0 -10 -33 1
```

```
DF75 IU=1 IC=10
FC75 Gamma Dose forward direction for symmetry
c
F85:N 10 0 -33 1
DF85 IU=1 IC=10
FC85 Neutron Dose forward direction for symmetry
F95:P 10 0 -33 1
DF95 IU=1 IC=10
FC95 Gamma Dose forward direction for symmetry
c
c End Tally
m1     13027 -1.00
m2     83209 -1.00
c air internet 15 deg at sea level
m3 7014.66c -0.745962 8016.66c -0.228590 18000.42c -2.5448e-2 GAS=1
c 5% Borated Polyethylene
c Source:  TART LLNL
c Specified elemental Composition
c Total Mass Density :     0.936 g/cm^3
c
m4    1001 -0.11598
      1002 -0.00002
      5010 -0.0098
      5011 -0.0402
      6000 -0.612
      8016 -0.222
mt4 poly.10t
c
c SS Plate for Gammas
m5    26000 -0.9865
       6000 -0.0015
```

```
     25055 -0.0060
     14000 -0.0060
c ------------------------------------------------
NPS 1000000
c PRDMP 1E5 1E5
```

MCNPX – Dose rates with shielding

Neutron Spectrum for 209-Bi(alpha,n) reaction - GT

```
c ===========================================================================================
c CELL CARD
c ===========================================================================================
10    1 -2.700   -10               $ Al Target Holder
11    2 -9.800   -11               $ 30 Micron Bi Target
12    1 -2.7     -12 -13 14          $ Target Holder Backing Plate
13    1 -2.7     -15 12 -16 14       $ Al Beam Line Pipe
14    3 -1.22E-7  10 11 -12 13 -16    $ Volume inside Pipe
17    3 -1.22E-3 -17 (-14:15:16)      $ air around the pipe
18    4 -0.936   -18 17              $ Borated Polyethylene
19    4 -0.936   -19 18              $ Borated Polyethylene
20    4 -0.936   -20 19              $ Borated Polyethylene
21    4 -0.936   -21 20              $ Borated Polyethylene
22    4 -0.936   -22 21              $ Borated Polyethylene
23    4 -0.936   -23 22              $ Borated Polyethylene
24    4 -0.936   -24 23              $ Borated Polyethylene
25    4 -0.936   -25 24              $ Borated Polyethylene
26    4 -0.936   -26 25              $ Borated Polyethylene
27    4 -0.936   -27 26              $ Borated Polyethylene
28    5 -7.86    -28 27              $ SS Plate
29    5 -7.86    -29 28              $ SS Plate
```

```
30    5 -7.86    -30 29              $ SS Plate
31    5 -7.86    -31 30              $ SS Plate
32    5 -7.86    -32 31              $ SS Plate
47    3 -1.22E-3 -90  32               $ Outside World
90    0          90                 $ Void

c ===========================================================================
c SURFACE CARD
c ===========================================================================
10  1  rpp -0.25 0.25 -1 1 -4.5 4.5              $ Al block
11  1  rpp 0.25 0.253 -1 1 -4.5 4.5              $ Bismuth-209
12    cz  8.25                            $ Al back plate cylinder
13    pz -6                               $ Backing Plate Plane (Top)
14    pz -7.2                             $ Backing Plate Plane (Bottom)
15    cz 8.55                             $ Beam Line Pipe Cylinder
16    pz 10                               $ Beam Line Pipe plane
17    rpp -15.00 15.00 -15.00 15.00 -24.92 20.00   $ 2" of Borated Polyethylene
18    rpp -15.51 15.51 -15.51 15.51 -25.43 20.51   $ 2" of Borated Polyethylene
19    rpp -16.02 16.02 -16.02 16.02 -25.94 21.02   $ 2" of Borated Polyethylene
20    rpp -16.52 16.52 -16.52 16.52 -26.44 21.52   $ 2" of Borated Polyethylene
21    rpp -17.03 17.03 -17.03 17.03 -26.95 22.03   $ 2" of Borated Polyethylene
22    rpp -17.54 17.54 -17.54 17.54 -27.46 22.54   $ 2" of Borated Polyethylene
23    rpp -18.05 18.05 -18.05 18.05 -27.97 23.05   $ 2" of Borated Polyethylene
24    rpp -18.56 18.56 -18.56 18.56 -28.48 23.56   $ 2" of Borated Polyethylene
25    rpp -19.06 19.06 -19.06 19.06 -28.98 24.06   $ 2" of Borated Polyethylene
26    rpp -19.57 19.57 -19.57 19.57 -29.49 24.57   $ 2" of Borated Polyethylene
27    rpp -20.08 20.08 -20.08 20.08 -30.00 25.08   $ 2" of Borated Polyethylene
28    rpp -20.33 20.33 -20.33 20.33 -30.25 25.33   $ 0.5" of SS Plate
29    rpp -20.59 20.59 -20.33 20.33 -30.51 25.59   $ 0.5" of SS Plate
30    rpp -20.84 20.84 -20.59 20.59 -30.76 25.84   $ 0.5" of SS Plate
31    rpp -21.10 21.10 -20.59 20.59 -31.02 26.10   $ 0.5" of SS Plate
```

```
32     rpp -21.35 21.35 -20.59 20.59 -31.27 26.35   $ 0.5" of SS Plate
90     so 300                          $ Tally ROI & Outside Environment

c ===========================================================================
c DATA CARD
c ===========================================================================
c Target Plate offset by 10 Degrees
*TR1 0 0 0 10 90 80 90 0 90 100 90 10
c
c Polyethylene Block Translocation
TR2 0 0 -30 1 0 0 0 1 0 0 0 1
TR3 -22.62 0 0 1 0 0 0 1 0 0 0 1
TR4 22.62 0 0 1 0 0 0 1 0 0 0 1
c
MODE N H D T P A S #
IMP:N 1 21R 0
IMP:P 1 21R 0
IMP:H 1 21R 0
IMP:D 1 21R 0
IMP:A 1 21R 0
IMP:T 1 21R 0
IMP:S 1 21R 0
IMP:# 1 21R 0
c
PHYS:N 100 0 0 -1 -1 0 2
PHYS:H 100 0 -1 J 0 J 1
PHYS:A 100 3j 0
PHYS:# 140 J J J 0
c
CUT:# J 0.01
CUT:H J 0.01
```

```
CUT:A J 0.01
CUT:D J 0.01
CUT:S J 0.01
CUT:N J 1e-9
c
LCA 2 1 1 23 1 1 0 1 0
c
sdef PAR=1 x=d1 y=d2 z=d3 CCC=11 ERG=d4 VEC=0 0 -1 DIR=d5 EFF=0.0001
SI1  -0.4 0.9
SP1  0 1
SI2 -1 1
SP2  0 1
SI3 -3.5 3.5
SP3  0 1
SI4 H 0 0.001 0.002 0.005 0.01 0.05 0.1 0.5 1 1.5 2 2.5 3 3.5 4 4.5 5 5.5 6 6.5
    7 7.5 8 8.5 9 9.5 10 10.5 11 11.5 12 12.5
SP4 D 0 0.001406153 0.002831182 0.007373327 0.014942203 0.066366757 0.112268423
    0.212833861 0.194489262 0.148338576 0.102227302 0.06804882 0.032269259
    0.018947065 0.008382303 0.004312252 0.002205652 0.001131632 0.000618138
    0.000351801 0.000223496 0.000145165 0.00010153 6.85231E-05 4.80271E-05
    3.03043E-05 1.97037E-05 1.02224E-05 5.99723E-06 1.82244E-06 1.22686E-06
    1.27672E-08
SI5  -1 9i 1
SP5   0 0.10 9r
SB5   0 0.02 8r 0.84
c ----
PTRAC cell=17 max=10000 TYPE=N FILE=asc
c ----
c Rectangular mesh
tmesh
rmesh1:N
```

```
cora1 -27 53i 27
corb1 -27 53i 27
corc1 -54 29i -24
rmesh11:P
cora11 -27 53i 27
corb11 -27 53i 27
corc11 -54 29i -24
endmd
c ===========================================================================
c Neutron,  Photon Tally 1 m from Origin Ring Detector
c ===========================================================================
F15z:n 0 100 0.0
E15   0 1E-7 1E-3 0.5 1 14i 15
c
F25z:p 0 100 0.0
E25   0.001 0.5 1 14i 15
c ===========================================================================
c Neutron,  Photon Point Detector Tally @ 1 M from source w/ shielding
c ===========================================================================
F35:n 0 0 -100 0.0
de35  log 2.5E-8  1.0E-7  1.0E-6  1.0E-5 1.0E-4 1.0E-3 1.0E-2 1.0E-1 5.0E-1
       1.0     2.0     5.0    10.0   20.0
C MESH OF FLUX TO DOSE CONVERSION FACTOR VALUES ICRP-21 (REM/h per unit flux)
df35  log 3.85E-6 4.17E-6 4.55E-6 4.35E-6 4.17E-6 3.70E-6 3.57E-6 2.08E-5
       7.14E-5 1.18E-4 1.43E-4 1.47E-4 1.473E-4 1.54E-4
c
F45:p 0 0 -100 0.0
de45  log 0.01    0.015   0.02    0.03    0.04    0.05    0.06
       0.08    0.1     0.15    0.2     0.3     0.4     0.5
       0.6     0.8     1.0     1.5     2.0     3.0     4.0
       5.0     6.0     8.0     10.0
```

```
C MESH OF FLUX TO DOSE CONVERSION FACTOR VALUES ICRP-21 (REM/h per unit flux)
df45  log 2.78e-6 1.11e-6 5.88e-7 2.56e-7 1.56e-7 1.20e-7 1.11e-7
        1.20e-7 1.47e-7 2.38e-7 3.45e-7 5.56e-7 7.69e-7 9.09e-7
        1.14e-6 1.47e-6 1.79e-6 2.44e-6 3.03e-6 4.00e-6 4.76e-6
        5.56e-6 6.25e-6 7.69e-6 9.09e-6
c
F55:n 0 0 -100 0.0
E55   0 1E-7 1E-3 0.5 1 14i 15
c
F65:p 0 0 -100 0.0
E65   0.001 0.5 1 14i 10
c
c End Tally
m1     13027 -1.00
m2     83209 -1.00
c air internet 15 deg at sea level
m3 7014.66c -0.745962 8016.66c -0.228590 18000.42c -2.5448e-2 GAS=1
c 5% Borated Polyethylene
c Source:  TART LLNL
c Specified elemental Composition
c Total Mass Density :     0.936 g/cm^3
c
m4    1001 -0.11598
      1002 -0.00002
      5010 -0.0098
      5011 -0.0402
      6000 -0.612
      8016 -0.222
mt4 poly.10t
c
c SS Plate for Gammas
```

```
m5    26000 -0.9865
       6000 -0.0015
      25055 -0.0060
      14000 -0.0060
c ------------------------------------------------
NPS 1000000
c PRDMP 1E5 1E5
```

VITA

Name:	Viharkumar Satish Bhakta
Address:	129 Zachry Engineering Center 3133 TAMU College Station, TX 77843-3133
Email Address:	bhaktavs@gmail.com
Education:	M.S., Health Physics, Texas A&M University, 2011 B.S., Nuclear Engineering, Texas A&M University, 2009

Production And Distillation Of At-211 At The Texas A&M Cyclotron Institute

T. Michael Martin, Department of Nuclear Engineering

Overview of ^{211}At Production

1. Necessity and Background
2. Production Goals
3. Targetry
4. Distillation
5. QA/QC
6. Process Safety and Automation
7. End Use
8. Summary

2

Necessity and Background

- Localized cancers have increased survivability, while mortality due to metastases has remained stable or increased.
- 2005 – 2011 Female Breast Cancer 5 Yr Survival Rates

  Localized: 99% Metastatic: 26%

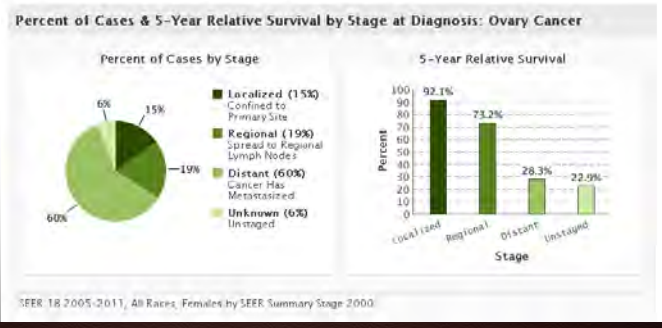

American Cancer Society. Breast Cancer Facts & Figures 2015-2016. Atlanta: American Cancer Society, Inc. 2015

3

Targeted Radionuclide Therapy

- Radionuclides bound to molecules with specific tumor targeting properties
- Method for treating metastases, cancer stem cells
- Improved treatment of surgical margins

Cell Surface Receptors	Organ Specific Uptake	Intravascular Trapping Increased Retention
Immunoconjugates (mAb)	Chemical	Microspheres
Peptides	Chelation	Nanoparticles
		EPR
^{90}Y-anti-CD20	^{153}Sm-EDTMP	^{90}Y-microspheres

4

Targeted Radionuclide Therapy

- ^{131}I Tositumomab and ^{90}Y Ibritumomab (Anti-CD20; NHL)
- ^{90}Y microspheres (intravascular trapping; hepatocellular carcinoma, liver metastases)
- ^{90}Y Octreotide (somatostatin; neuroblastoma, carcinoid paraganglioma, etc.)
- ^{223}Ra Xofigo (preferential absorption, CRPC bony metastases)

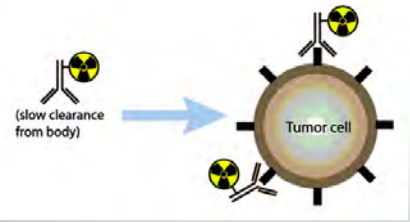

Borrmann A, van Hest JCM. Bioorthogonal chemistry in living organisms. Chem Sci. 2014;5:2123-2134.

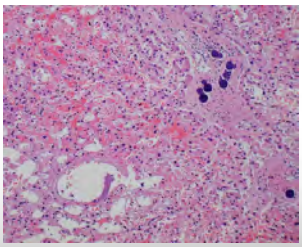

Kennedy A. Radioembolization of hepatic tumors. J Gastrointestinal Onc. 2014;5(3)

Ersahin D, Doddamane I, Cheng D. Targeted Radionuclide Therapy. Cancers. 2011;3(4):3838-3855.

5

Why ^{211}At?

- Alpha-emitter
  - Low range in tissue (50-100 μm)
  - High energy (5.87, 6.57, 6.89, 7.45 MeV)
  - High LET → High RBE
    Negligible dose rate or hypoxic effects
- "Optimal" half life (7.214 h)
  - Short enough for higher specific activity, no long term accumulated dose
  - Long enough for easy handling (target cool down, distillation, labeling, packaging, shipping, etc.)
  - ^{211}Po in secular equilibrium
- Other
  - Well known halogen chemistry - radioiodine analog
  - ^{211}Po x-rays for dose calibration, imaging

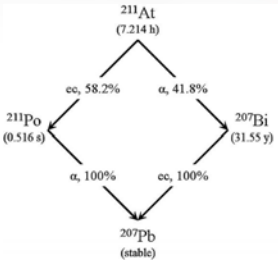

6

Production Goals

Primary Aims

1. Target Development
   (thermal analysis, ease of use, repeatability)
2. Distillation and Process Development
   (repeatability, ISO/cGMP/USP standards, QA/QC)

Secondary Aims

1. Radiological Safety / Health Physics
   (mixed field dose analysis, shielding, ALARA, etc.)
2. Remote Instrumentation and Automated Controls
   (reduced dose, move towards commercial production)
3. End Use
   (immunoconjugation to anti-HER2, incorporation in AuNP, etc.)

7

Production Mechanism

- ^{209}Bi (α, 2n) ^{211}At
- ^{209}Bi (α, 3n) ^{210}At

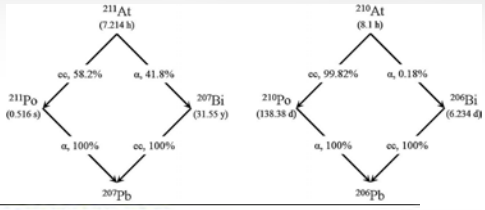

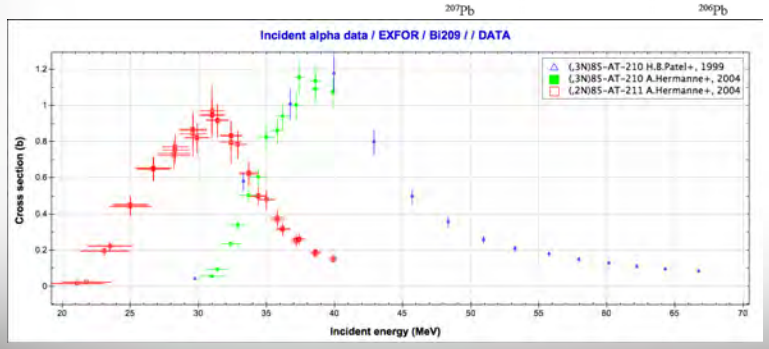

8

Previous Work

- 80 MeV (20 MeV nuc^{-1}) $^{4}He^{2+}$ beam incident on Cu and Al degrader foils
- 150 particle-nA, 4 hr irradiations
- Beam energy on target nominally 25 MeV and 28 MeV
  - Energy degradation and straggling calculated by LISE++ and SRIM
  - Verified by activation analysis of copper degradation foils

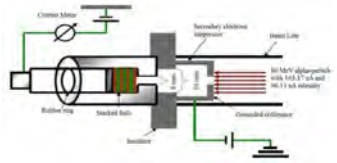

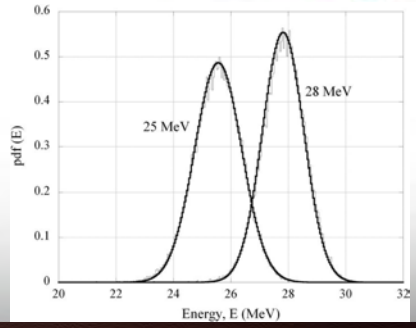

9

Previous Work

- **25.5 ± 0.82 MeV**
  - 96.13 particle-nA
  - 12.4 MBq μA-hr^{-1}
  - No ^{210}At
- **27.8 ± 0.72 MeV**
  - 163.17 particle-nA
  - 36.0 MBq μA-hr^{-1}
  - 2.3% ^{210}At

Source	Incident energy (MeV)	Target thickness (μm)	^{211}At yield (MBq μA^{-1} h^{-1})
Exp.1, this paper	27.8	500	36.0
Exp. 2, this paper	25.5	500	12.4
Wunderlich et al. 1986	28	20	4
Lambrecht and Mirzadeh 1985	28	100	5.3 – 10.4
Aaij et al. 1974	33	500	7.4 – 14.8
Rosch et al. 1985	28	500	8.56
Larsen et al. 1993	28	250	8 – 12
Hadley et al. 1991	28	500 – 800	10 – 12
Larsen et al. 1995	28	100	15.2 – 15.6
Hamwi et al. 1991	28	30	27.7
Groppi et al. 2005	28.8	—	31.9
Lebeda et al. 2005	29.5	3 – 5	38
Larsen et al. 1996[g]	28	50	41[a]
Alfarano et al. 2006	28	250	48

[a]Internal target.

10

Targetry

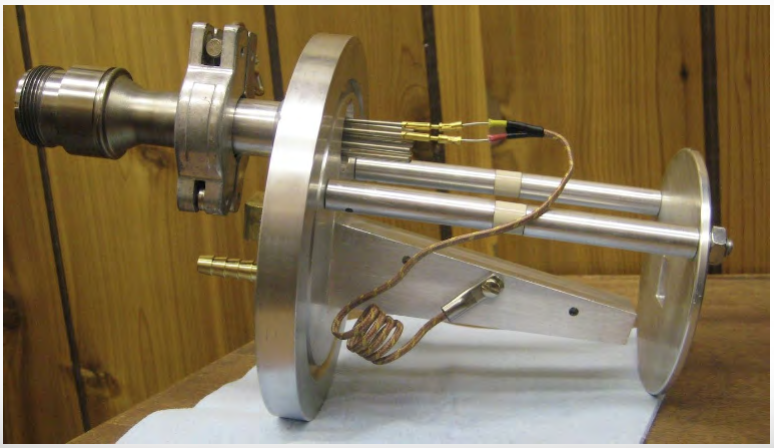

11

Targetry

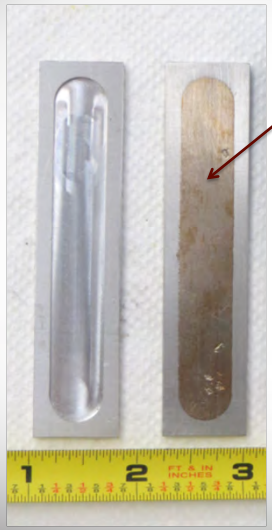

Bismuth Layer

Target Holder

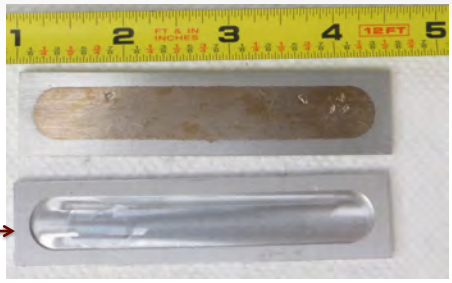

- 30 μm Bi layer (≈ 0.002”)
- 1/8” Al plate (0.125”)

12

Targetry – Heat Transfer

- Previous Experiments
  - $q''_{max} \approx 13$ W cm^{-2}
  - Passive cooling

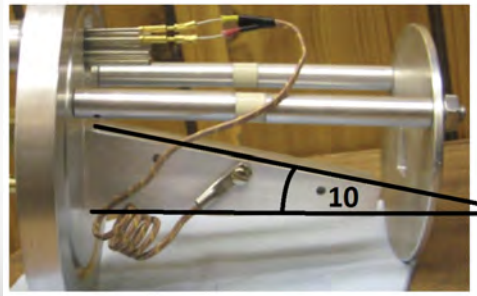

- Planned Experiments
  - $q''_{max} \approx 225$ W cm^{-2}
  - (same beam diameter, K150, 25 MeV)
  - Active cooling
  - $q''_{max} \sin(10°) \approx 40$ W cm^{-2}
  - $t = 30\ \mu m / \sin(10°) = 173\ \mu m$
  - $K_{(Al)} = 237$ W m^{-1} K^{-1}
  - $K_{(Bi)} = 7.86$ W m^{-1} K^{-1}

13

Distillation

- Dry Distillation
  1) Vaporize ^{211}At
  2) Entrain with argon flow
  3) Capture in cold trap
  4) Elute with solvent or carrier

Element	T_{melt} (°C)	T_{boil} (°C)
Aluminum	660	2470
Bismuth	271	1564
Astatine	302	337

- Other Methods
  - PEEK entrapment
  - Bubble in chloroform
  - Wet chemistry (DIPE/ MIBK, solvent extraction)

14

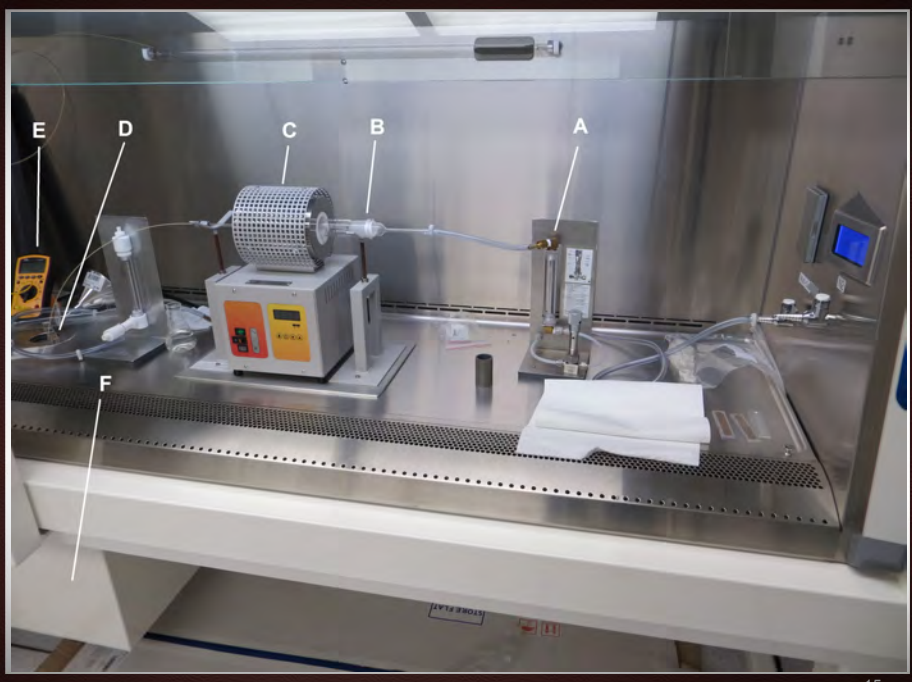

15

Distillation

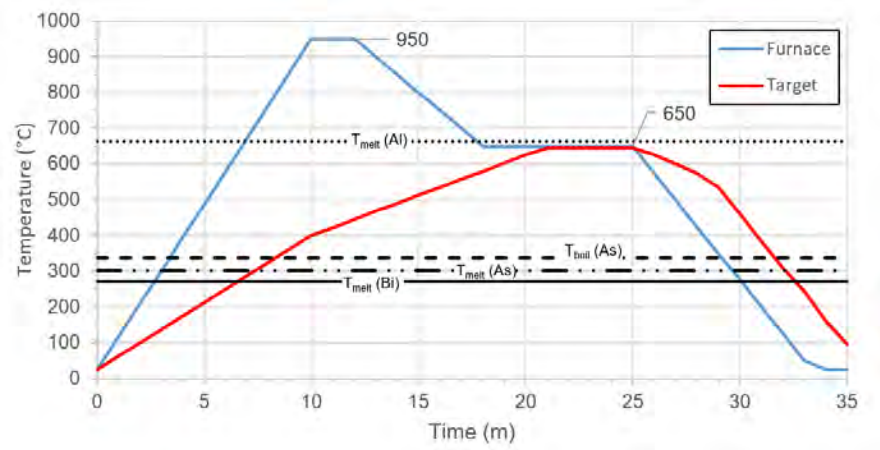

16

Distillation Issues and Improvements

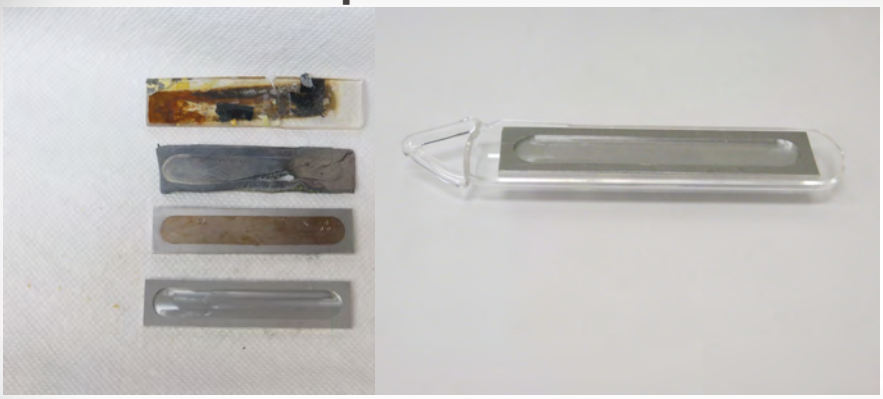

17

Detection and Assay QA/QC

- Gamma Spectrometry
  - HPGe / Genie 2000

Nuclide	γ Energy (keV)	Yield (Bq^{-1} s^{-1})
^{211}At	687.0	2.61×10^{-3}
^{211}Po	569.7	5.35×10^{-3}
^{211}Po	897.8	5.51×10^{-3}
^{210}At	245.3	7.95×10^{-1}
^{210}At	1181.4	9.93×10^{-1}
^{210}At	1436.7	2.90×10^{-1}
^{210}At	1483.4	4.65×10^{-1}
^{210}At	1599.5	1.34×10^{-1}

- Alpha Spectrometry
  - PIPS detector

Nuclide	α Energy (MeV)	Yield (Bq^{-1} s^{-1})
^{211}At	5.870	4.18×10^{-1}
^{211}Po	7.450	9.89×10^{-1}
^{211}Po	6.892	5.46×10^{-3}
^{211}Po	6.568	5.37×10^{-3}

18

Detection and Assay QA/QC

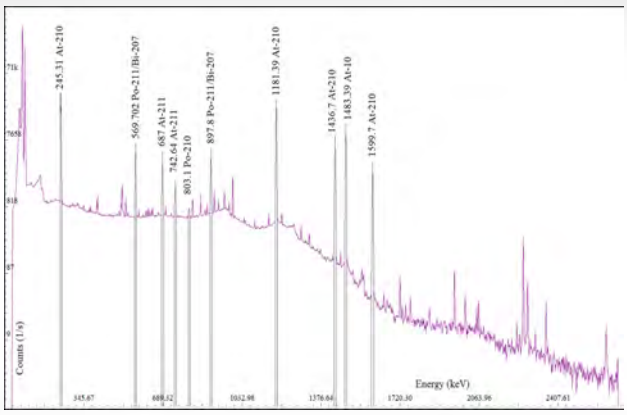

$$Y = \frac{3600 \times A_i}{\int_0^t I(t)dt}$$

$$A_i = \lambda_i N_{i,\gamma} \varepsilon_\gamma^{-1} y_{i,\gamma}^{-1} e^{-\lambda_i t_{EOB}} \left(e^{\lambda_i t_1} - e^{\lambda_i t_2}\right)$$

19

Detection and Assay QA/QC

- Dose Calibrator
  - Biodex AtomLab 500
  - Monte Carlo and empirical corrections from Sun Microsystems

20

Radiological Safety

- Hot Lab
  - iCam α/β particulate monitor
  - G64 γ monitor
- Cyclotron
  - Facility radiation monitors
  - Neutron detector target monitoring

21

Radiological Safety
Neutron Production

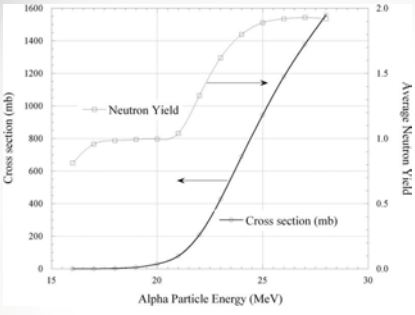

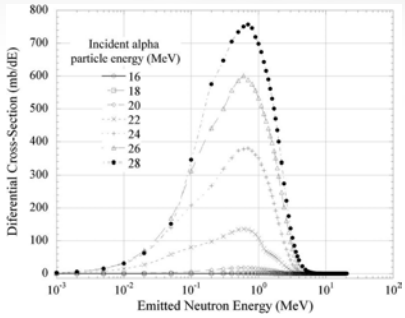

Point location (x,y,z)* (cm)	Neutron dose rate (mSv h^{-1} particle-μA^{-1})		Gamma dose rate (μSv h^{-1} particle-μA^{-1})	
	w/o Shield	w/ Shield	w/o Shield	w/ Shield
0, 0, −33	54.7	25.8	17.9	8.03
23, 0, 0	0.820	0.363	0.158	2.72
−23, 0, 0	0.750	0.345	0.149	2.60
0, 10, −33	0.246	0.111	0.072	1.48
0, −10, −33	0.245	0.117	0.072	1.55
10, 0, −33	0.331	0.143	0.072	1.51

22

Process Automation

- LabView

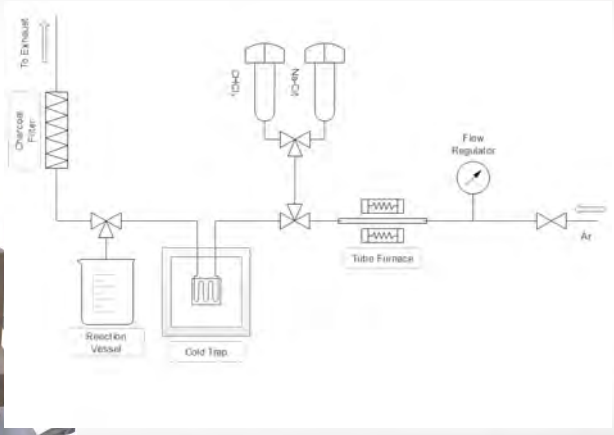

23

Immunoconjugation

- Radiolabelled AuNP
  - AuNP production via Turkevich method
  - Previous studies included ^{125}I
  - 5 kDa PEG corona
  - Multiple mAb conjugation

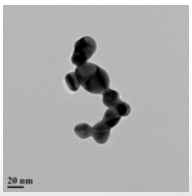

- Anti-CD340 (Anti-HER2)
  - SKBr3 cell lines

24

Flow Cytometry Studies

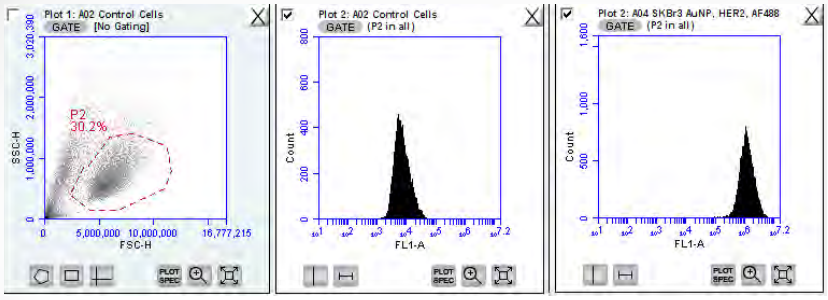

Immunoconjugation of AuNP with HER-2 an EGFR mAbs and PE and Alexa Fluor 488 on SKBr-3 breast cancer cell lines.
Experiments were carried out using ^{125}I as a surrogate therapeutic load of ^{211}At.

25

Further Studies

- In Vitro Studies
  - AuNP, direct conjugation
  - MCF-7, U-87, BT-474
- Preclinical Studies
  - PK/PD
  - Imaging
  - Long term radiotoxicity
- Automation
  - Full control and synthesis in LabView controlled module

26

Thank You

T. Michael Martin, Department of Nuclear Engineering

28

Appendix B

Work Related to the Production of Zn-62/Cu-62

THE DEVELOPMENT OF AN OPTIMIZED GENERATOR PRODUCTION METHOD FOR THE ROUTINE PRODUCTION OF ZINC-62/COPPER-62 GENERATOR SYSTEMS

A Thesis

by

TYLER LEE CANTRELL

Submitted to the Office of Graduate Studies and Professional Studies of
Texas A&M University
in partial fulfillment of the requirements for the degree of

MASTER OF SCIENCE

Chair of Committee,	Gamal Akabani
Committee Members,	Craig Marianno
	Charles M. Folden III
Head of Department,	Yassin Hassan

May 2015

Major Subject: Health Physics

ABSTRACT

The demand for radionuclides used in positron emission tomography (PET) must be met if the role for PET in Nuclear Medicine is to be expanded. The best method for supplying PET radionuclides to satellite PET facilities is through the use of radionuclide generators. The generator of interest in this study was the $^{62}Zn/^{62}Cu$ generator system. The objective of this study was to optimize the methods for producing $^{62}Zn/^{62}Cu$ so that they may be better suited for routine production. This involved examination of the bombardment parameters and the procedure utilized to dissolve the irradiated copper target. Additionally, the feasibility in automating the different processes of the production methods through a modular system was examined to aid in streamlining the routine production of the generator systems.

The analysis showed that, between proton entry energies of 18 and 30 MeV, a target thickness of 1.0 mm was optimal for producing ^{62}Zn. With a 1.0 mm thick target, the optimal proton entry energy for maximizing the production yield of ^{62}Zn was 29 MeV. The theoretical ^{62}Zn yield at 29 MeV directly prior to generator loading was calculated to be between 160 and 180 $GBq \cdot \mu A^{-1} \cdot h^{-1}$. An alternative target processing method based on 30% hydrogen peroxide (H_2O_2) and 2 M hydrochloric acid (HCl) at a temperature of 75 °C successfully dissolved the copper foil within 12 minutes. The color of the solution indicated that the copper (II) ions formed the hexaaquacopper(II) ion in 2 M HCl used for chemical separation. Finally, devices were purchased for automating the generator production process, including heating and transfer of solutions, and electronic

manipulation of valves. These devices were controlled using the software LabVIEW which demonstrated the feasibility of building a system capable of automating the production of this generator system. A detailed overview was provided on how to control these instruments with LabVIEW.

ACKNOWLEDGEMENTS

Many thanks go to my committee chair Dr. Gamal Akabani and my committee members Dr. Craig Marianno and Dr. Charles Folden, for all their help, support, and guidance. I would also like to thank all of my friends who were kind enough to give me assistance throughout the course of this research.

Most of all, I would like to thank my wife, Hannah, for standing beside me, supporting me, encouraging me, and most importantly, putting up with me these past two years.

NOMENCLATURE

Bq	Becquerel
CAD	Coronary Artery Disease
CT	X-ray Computed Tomography
DV1	Dissolution Vessel 1
DV2	Dissolution Vessel 2
EOB	End of Bombardment
JANIS	Java-base Nuclear Data Information System
MRI	Magnetic Resonance Imaging
NIST	National Institute of Standards and Technology
PET	Positron Emission Tomography
SF	Saturation Factor, $(1 - e^{\lambda t})$
SRIM	The Stopping and Range of Ions in Matter

TABLE OF CONTENTS

LIST OF FIGURES

LIST OF TABLES

1. INTRODUCTION

1.1 PET Diagnostic Imaging

Positron Emission Tomography (PET) is one of the fastest growing diagnostic specialties in nuclear medicine (Bailey et al., 2005). PET is a nuclear diagnostic method that can quantitatively measure the physiological activities and chemical reactions occurring within specific regions of tissue or organs (Coleman, 1988; Green et al., 1990; Qaim, 2012; Schiepers and Hoh, 2006). This is accomplished with the use of a molecular probe or pharmaceutical compound labeled with a positron emitting radionuclide (Qaim, 2012). One of the most common examples of a molecular probe in PET imaging is the use of a glucose analogue, 2-^{18}F-fluoro-2-deoxy-D-glucose (FDG), labeled with the PET tracer ^{18}F to non-invasively measure glucose metabolism in tumors (Schiepers and Hoh, 2006). PET is useful not only for providing diagnostic imaging of existing disease but also for detecting disease in its earliest stages. Other imaging modalities such as computed tomography (CT) or magnetic resonance imaging (MRI) only provide anatomic information (Coleman, 1988). Generally, anatomic changes are only evident after the disease has manifested. PET is able to detect chemical changes in the form of functional abnormalities that occur prior to anatomic changes (Coleman, 1988). A few examples of functional abnormalities in diseases detectable by PET are epilepsy, Huntington's disease, and coronary artery disease (CAD) (Coleman, 1988).

Since its first acceptance for clinical use in the 1980's, PET imaging has significantly impacted patient management. The decisions on the surgical treatment for diseases are changing with the diagnostic information provided by PET imaging.

Inappropriate surgeries are avoided, curative resections are more likely, diagnosing and treating lymphoma is possible, diagnosis of patients at risk for CAD is possible, and surgical decisions with other types of disease can be greatly benefited with the use of PET imaging (Bailey et al., 2005). This level of patient care has not been achieved before by Nuclear Medicine (Bailey et al., 2005). PET imaging currently finds clinical applications primarily in Oncology, Cardiology, and Neuropsychiatry with focuses in cancer diagnosis/management, cardiac surgery, and neurology/psychiatry, respectively (Bailey et al., 2005).

PET imaging is currently very powerful with the use of FDG, an effective and powerful radiopharmaceutical, but it also currently needs technical advancements before it starts achieving widespread use in Nuclear Medicine (Bailey et al., 2005). More sensitive PET instrumentation is being developed, significantly increasing patient throughput with shorter scanning times. The development of fusion imaging, the simultaneous use of PET with other imaging modalities, shows a promising new methodology. The spatial resolution of PET images are also improving, allowing for images down to a millimeter in resolution. All of the time and money being placed into these technical advancements and more are being driven by an industry who believes that PET imaging is a worthwhile area of expansion (Bailey et al., 2005). As PET imaging continues to grow, there will be increasing opportunities for studies to be conducted with PET radionuclides. The increase in demands for PET radionuclides will have to be met by cyclotron operators and radiochemists who are the sole source of PET radionuclides.

1.2 Common Radionuclides Used in PET

PET radionuclide can only be produced at a cyclotron facility. There are a large number of positron-emitting radionuclides available for production but very few actually fit the requirements of a PET radionuclide. The underlying principle behind diagnostic nuclear medicine is to deliver as little radiation dose to the patient as possible while maintaining the desired quality of the image (Qaim, 2011). This requires that the radionuclide have a short half-life, emit low energy positrons, and have zero high-energy gamma-ray emissions (Qaim, 2012). The other consideration when picking a PET radionuclide is its usability as a radiopharmaceutical. Creating a radiopharmaceutical labeled with a PET tracer and utilizing the same compound in a PET study does not always work together. At the end of synthesis, the labeled compound often doesn't have the level of activity necessary to conduct a PET study, as a result, a major consideration of a PET radionuclide is the time required to complete the synthesis, purification, and sterilization of the final radiopharmaceutical product (Yamamoto, 1984).

The most common PET radionuclides are ^{18}F ($T_{1/2}$ = 110 min) and certain organic analogues of natural body constituents such as ^{11}C ($T_{1/2}$ = 20.4 min), ^{13}N ($T_{1/2}$ = 10 min), and ^{15}O ($T_{1/2}$ = 2 min) (Green et al., 1990; Qaim, 2012; Robinson Jr et al., 1980; Yamamoto, 1984). The radionuclides ^{11}C, ^{13}N, and ^{15}O have such short half-lives that they must be produced with an in-house cyclotron and processed on site. Even in the cases where in-house cyclotrons are available, their available labeled compounds are limited due to their short half-lives. With a longer half-life, ^{18}F can be used at facilities

located within 2 hours of a cyclotron facility (Yamamoto, 1984). Table 1 lists the most common PET radionuclides and Table 2 lists several radiopharmaceuticals and their applications with these PET radionuclides.

In recent years, efforts have been extended towards the development of novel or non-standard positron emitters. This is due to the growing significance of PET in diagnostic nuclear medicine which has manifested in a growing demand for positron emitters that have different and more specialized applications than the common PET radionuclides in Table 1 (Qaim, 2012). To be viable, the novel positron emitters must be producible in a cyclotron with a high degree of yield and radionuclide purity as well as contain the desired decay characteristics for suitable imaging (Qaim, 2011).

Table 1. Short list of common positron emitters used for PET imaging (Qaim, 2012).

Positron Emitters for PET			
Radionuclide	**Half-life (min)**	**Radiation Emitted**	**Production Process**
^{11}C	20.4	β+	$^{14}N(p,\alpha)$
^{13}N	10	β+	$^{16}O(p,\alpha)$
^{15}O	2	β+	$^{14}N(d,n)$ $^{15}N(p,n)$
^{18}F	110	β+	$^{18}O(p,n)$ $^{20}Ne(d,\alpha)$
^{68}Ga	68.3	β+	$^{69}Ga(p,2n)^{68}Ge$ (generator)
^{82}Rb	1.3	β+	$^{nat}Rb(p,x)^{82}Sr$ (generator)

Table 2. List of positron labelled radiopharmaceuticals for PET (Yamamoto, 1984).

Radiopharmaceuticals	Primary Applications
^{15}O-H_2O, ^{15}O-CO_2, ^{18}F-CH_3F, ^{18}F-antipyrine, ^{11}C-alcohols, ^{15}O-N_2O	Cerebral blood flow
^{11}C-CO, ^{15}O-CO	Cerebral blood volume
^{15}O-O_2	Cerebral oxygen utilization
^{18}F-2-FDG, ^{11}C-2-DG, ^{11}C-glucose	Glucose utilization
^{11}C-labelled; L-leucine, L-valine, L-methionine	Protein syntheses
^{11}C-3-O-methyl-D-glucose	Glucose transport
^{18}F- and ^{11}C-spiroperidol, ^{75}Br-bromo-spiroperidol, ^{18}F-haloperidol, ^{11}C-pimozide	Dopaminergic receptors
^{18}F-L-DOPA	Neurotransmitter
^{11}C- and ^{13}N-BCNU	Pharmacokinetics

1.3 Initial and Operational Cost

There are two major components that comprise the cost of utilizing PET imaging that have been cost-prohibitive towards the wider implementation of PET imaging. The first component is the capital cost to purchase and field a cyclotron facility and its staff. The second is the capital cost for purchasing a high-resolution PET imaging equipment. In 1988, a review was conducted on the clinical status of PET in the United States and it found that the cost of PET scanners ranged from $1.0 to $1.8 million. The cost to obtain a medium energy cyclotron ranged from $1.0 to $2.0 million with an estimated additional annual operating cost of $0.4 to $1.0 million (Coleman, 1988).

Currently, there are two cyclotron vendors, IBA Technology Group in Belgium and Advanced Cyclotron Systems, Inc. in Canada, which have the capability to produce medium to high-energy cyclotrons. Advanced Cyclotron Systems, Inc. reports that its

current TR-24 model Cyclotron, 18-24 MeV, has an estimated cost between $2.0 and $4.0 million, including building the facility, and $50k to $300k in maintenance and operational annual cost. More recently, the price of PET scanners have remained within the $2.2 million range and can fluctuate according to the image quality desired (Keppler and Conti, 2001). Given this, it can be shown that the financial burden associated with building and fielding both of these facilities has remained consistent over the past 30 years.

The routine cost for PET scanning, assuming an average of 12 doses per day, ranges between $900 and $1,500. This involves the use of FDG for whole body, brain, and cardiac perfusion imaging. The routine cost for producing radiopharmaceuticals, again with an average of 12 doses per day, ranges between $700 and $1,452 (Keppler and Conti, 2001). The variation in routine costs are associated with the type of facility configuration being used where the most expensive item is the use of one cyclotron to support a single scanning facility and the least expensive being the use of a satellite scanning facility that purchases radiopharmaceuticals (Keppler and Conti, 2001). This indicates that the most financially viable option for utilizing PET imaging, given the start-up/operational costs of fielding an in-house cyclotron and scanning facility, is the use of a scanning facility that can purchase PET radionuclides from a remote manufacturer.

1.4 PET Radionuclide Generators

One of the most commonly utilized PET radiopharmaceuticals, FDG, is extremely limited in its range of shipment from a cyclotron facility due to its 110 min half-life. Other PET radionuclides are simply impossible to ship due to their very short half-life. The answer to the effective distribution of short-lived PET radionuclides is the use of generator systems (Lebowitz and Richards, 1974). The ability to obtain a PET radionuclide from a parent/daughter generator system would effectively increase the distribution range of a cyclotron facility, making PET imaging available on a much broader scale (Fujibayashi, 1989; Green et al., 1990; Mathias et al., 1990; Zweit et al., 1992).

A generator system is composed of a parent radionuclide, with a relatively long half-life, that decays to the desired daughter PET radionuclide. The separation and extraction of the daughter PET radionuclide from the parent is based upon their chemical differences most easily exploited through the use of a column chromatograph. This ion separation technique provides an extremely high chemical, radiochemical, and radionuclide purity making generator systems an ideal source of PET radionuclides for remote facilities (Lebowitz and Richards, 1974). Their rugged and compact design (Lebowitz and Richards, 1974) also makes it economically feasible for cyclotron facilities to distribute these generators to remote facilities.

However, current standard PET radionuclide generator systems contain undesirable characteristics. The $^{82}Sr/^{82}Rb$ generator system requires spallation of molybdenum with 800 MeV protons (Bilewicz, 2006) in an accelerator to produce

sufficient quantities of ^{82}Sr (Lebowitz and Richards, 1974). The generator system can also be produced by irradiating an ^{85}Rb target with protons that have energies greater than 40 MeV. While the 76 second half-life of ^{82}Rb is very well suited for assessing myocardial perfusion, its uses are limited due to the chemistry of the rubidium cation (Beanlands et al., 1992; Green et al., 1988). The other available system, ^{68}Ge/^{68}Ga, can be commercially produced with 20 MeV protons utilizing the reaction ^{69}Ga(p,2n)^{68}Ge. This generator system has an ideal parent half-life of 271 days but a daughter half-life of 68 minutes. In many situations, the half-life of the daughter is sufficiently long that it limits the uses of ^{68}Ge in clinical settings due to the levels of radiation dose delivered to the patients (Robinson Jr et al., 1980). Given this, there are generator systems available that can yield PET radionuclides, but these novel PET radionuclides are limited in their applications similar to the common PET radionuclides. Attention must be directed towards a novel positron emitter and its generator system that is produced cheaply by the PET manufacturer, and has a wide range of implementation into different clinical studies. Such a generator system that has the potential to meet both of these criteria is the ^{62}Zn/^{62}Cu generator.

1.5 The ^{62}Zn/^{62}Cu Generator

^{62}Zn is produced with the use of a medium energy cyclotron and has a half-life of 9.186 hours. It decays to ^{62}Cu ($T_{1/2}$ = 9.74 min), which has a half-life well suited for the time frame of PET perfusion imaging but remains sufficiently long-lived to allow its incorporation in a diverse set of radiopharmaceuticals (Green et al., 1990; Mathias et al.,

1990). Copper has a very well understood chemistry and is dominated by two oxidation states I and II (Blower et al., 1996). This allows for, in many cases, easy manipulation of copper in aqueous solutions due to its flexible coordination chemistry (Smith and Martell, 1975).

The chemistry and half-life of ^{62}Cu makes it an extremely desirable PET radionuclide for pharmaceuticals (Fujibayashi, 1989). Previous studies have utilized ^{62}Cu labeled radiopharmaceuticals for different applications such as ^{62}Cu-PTSM for cerebral and myocardial PET perfusion imaging (Green, 1987; Green et al., 1988; Haynes et al., 2000; Mathias et al., 1990) and ^{62}Cu-DTS-HAS for regional plasma volume measurements (Fujibayashi, 1990). Studies on other possible ^{62}Cu labeled radiopharmaceuticals have been conducted as well (Yokoyama et al., 1986).

The radionuclide ^{62}Zn has a slight disadvantage with its short half-life, giving the generator system a shelf life of approximately 1 to 3 days (Blower et al., 1996; Haynes et al., 2000; Zweit et al., 1992). However, this is somewhat offset by the ability to produce ^{62}Zn with large production yields ranging between 2.6 (Robinson Jr et al., 1980) and 5.2 (Zweit et al., 1992) GBq. Ultimately, the shelf-life is trivial next to the estimated production cost of less than $500 dollar per unit (Haynes et al., 2000). Additionally, with a ^{62}Cu elution available every 30 to 45 minutes (Blower et al., 1996), the throughput potential for this generator system is very high, allowing for PET imaging to be conducted with a large number of patients regardless of the shelf-life (Keppler and Conti, 2001). The economic and clinically versatile characteristics of the ^{62}Zn/^{62}Cu generator system work in an advantageous manner towards establishing the existence of

satellite PET imaging centers (Mathias et al., 1990) and ultimately broadening the role of PET imaging in Nuclear Medicine.

1.5 Purpose

The $^{62}Zn/^{62}Cu$ generators are ideal for establishing satellite PET imaging facilities. The generator system has an economic and clinically versatile application within PET imaging, and can support PET to achieve a broader role in Nuclear Medicine. In addition to its advantageous applications, the generator system's production is very well characterized and defined. The ^{62}Zn reaction cross sections, cyclotron targetry, target processing, chemical processing, and generator loading procedure and methods are all well known. However, the generator systems true economic potential has yet to be realized through the means of mass production.

This is due in part to the large volumes of corrosive fumes generated during the target-processing phase where the target is dissolved with highly concentrated acids. The corrosive fumes are extremely damaging to manufacturing equipment, including hot cells, which makes it difficult to implement at radiochemistry facilities. The lack of mass production is also due in part to the fact that the generator system has been produced primarily by research institutions and has not been optimized for routine production. Lastly, there is no automated system that is capable of streamlining the routine production of the generator system. A semi-automated system has been reported previously (Fukumura, 2006) but lacks a true modular and fully automatic design that is controlled through a single interface.

Therefore, it is the goal of this study to provide the foundation for the mass-production of the $^{62}Zn/^{62}Cu$ generator system. This will be accomplished by 1) developing a noncorrosive target processing procedure, 2) optimizing the routine production of ^{62}Zn, and 3) developing a proof of concept that illustrates the feasibility in automating the specific processes of transferring liquids, heating solutions, and manipulating electronic valves under current Good Manufacturing Practices (cGMP) conditions (21CFR212).

2. EXPERIMENTAL METHODS AND MATERIALS

2.1 The Radionuclides ^{62}Zn and ^{62}Cu

The radionuclide ^{62}Zn is a man-made radioisotope with a half-life of 9.186 h that decays to ^{62}Cu primarily via β^+ decay. The radionuclide ^{62}Cu has a half-life of 9.74 m and decays primarily via β^+ decay to stable ^{62}Ni. The decay scheme for ^{62}Zn is illustrated by Figure. 1. The radiative emissions for both ^{62}Zn and ^{62}Cu can be found in Tables 3 and 4. The symbols β^+ and ε represent positron decay and electron capture, respectively. All nuclear data were obtained from the National Nuclear Data Center's (NNDC) Nuclear structure and Decay data (NuDat) database.

Table 3. The radioactive decay data for ^{62}Zn represented by the energy, intensity, and decay mode of each radiative emission.

Emission	Intensity (%)	Energy (keV)
β^+	8.2	255*
$\gamma^{\pm}$	16.4	511
γ	14.8	508
γ	15.3	548
γ	26.0	597

* represents the maximum beta particle energy released.

Table 4. The radioactive decay data for ^{62}Cu represented by the energy, intensity, and decay mode of each radiative emission.

Emission	Intensity (%)	Energy (keV)
β^+	97.60	1321*
$\gamma^{\pm}$	196.0	511
γ	0.15	876
γ	0.34	1173

* represents the maximum beta energy released.

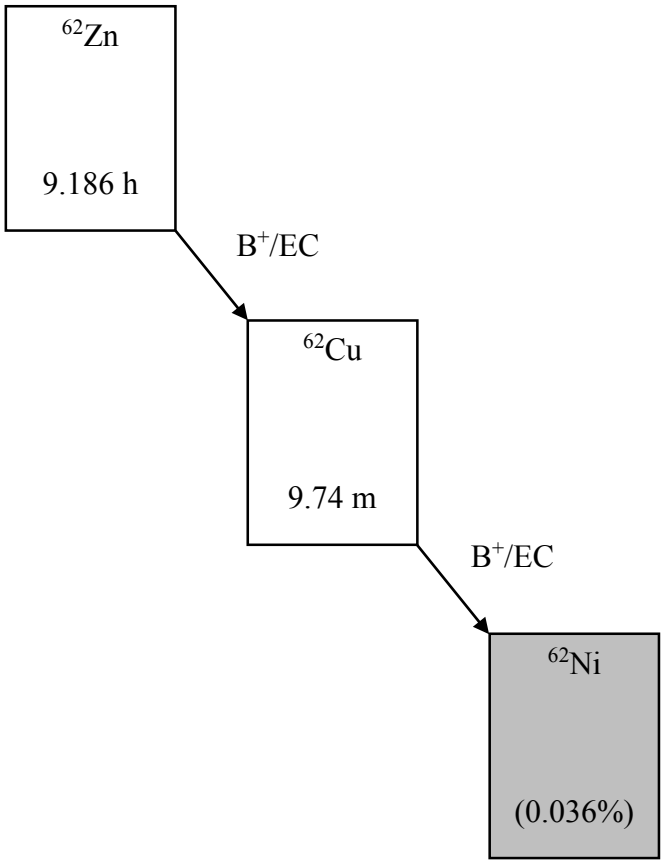

Figure 1. The decay scheme for ^{62}Zn, which decays by positron decay/electron capture to its daughter ^{62}Cu, which in turns decays via the same mechanism to stable ^{62}Ni.

2.2 Target Irradiation

2.2.1 Nuclear Reaction for Production of ^{62}Zn

The radionuclide ^{62}Zn can be produced via the nuclear reaction ^{nat}Cu(p,x)^{62}Zn by bombarding a natural copper target with protons (Grütter, 1982; Gul, 2001). This is the only viable nuclear reaction available for producing ^{62}Zn in a cyclotron. Copper has two naturally occurring isotopes of copper-63 and copper-65 with natural abundances of 69.17% and 30.83%, respectively. The specific nuclear reactions for each of the two isotopes that produce ^{62}Zn are ^{63}Cu(p,2n)^{62}Zn and ^{65}Cu(p,4n)^{62}Zn (Grütter, 1982; Gul, 2001). Due to this, both isotopes in natural copper will contribute towards the

production of ^{62}Zn. The reaction cross section for ^{62}Zn production with the two copper isotopes as a function of proton energy is shown in Figure 2. The reaction ^{63}Cu(p,2n)^{62}Zn has a Q value of -13.265 MeV and a threshold production energy of 13.477 MeV and the cross sections peak at approximately 25 MeV. The reaction ^{65}Cu(p,4n)^{62}Zn has a Q value of -31.092 MeV and threshold production energy of 31.574 MeV and the cross sections peak at 45 MeV. Of these two open channels, the former has a significantly higher cross section for producing ^{62}Zn at lower proton energies. For this reason the nuclear reaction favored for producing ^{62}Zn is ^{63}Cu(p,2n)^{62}Zn, which is the most commonly utilized reaction in previous publications (Blower et al., 1996; Fujibayashi, 1989; Fukumura, 2006; Haynes et al., 2000; Robinson Jr et al., 1980; Zweit et al., 1992). A consequence of this is that ^{65}Cu is not utilized for ^{62}Zn production because the threshold for its nuclear reaction is above the energy used for the ^{63}Cu nuclear reaction.

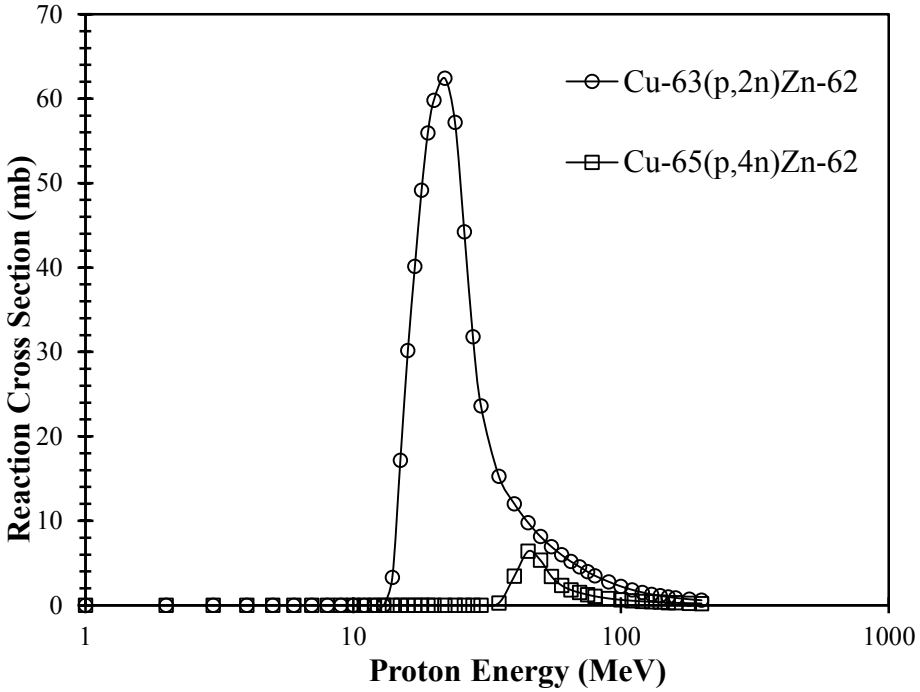

Figure 2. The reaction cross section for ^{62}Zn production via the isotopes copper-63 and copper-65, taken from JANIS (Soppera et al., 2014).

2.2.2 Nuclear Reactions For Production of Contaminants

Both isotopes, ^{63}Cu (69.15% natural abundance) and ^{65}Cu (30.85% natural abundance), contribute to the production of contaminants or unwanted radioactive isotopes during irradiation through a variety of ^{nat}Cu(p,x) nuclear reactions. A summary of each nuclear reaction, resulting contaminants, corresponding half-life, and daughter products is shown in Table 5.

Table 5. The contaminants produced from the nuclear reaction ^{nat}Cu(p,x) during the proton irradiation of a natural copper target (Soppera et al., 2014).

Target Isotope	Nuclear Reaction	Contaminant	Radioactive Half-life	Daughter Product
^{63}Cu	p,n	Zn-63	38.47 min	Cu-63
	p,3n	Zn-61	89.1 s	Cu-61
	p,2n+p	Cu-61	3.33 h	Ni-61
	p,n+p+a	Co-58	70.86 d	Fe-58
	p,γ	Zn-64	Stable	-
	p,p	Cu-63	Stable	-
	p,α	Ni-60	Stable	-
^{65}Cu	p,n	Zn-65	243.6 d	Cu-65
	p,3n	Zn-63	38.47 min	Cu-63
	p,n+p	Cu-64	12.7 h	Ni-64/Zn-64
	p,γ	Zn-66	Stable	-
	p,p	Cu-65	Stable	-
	p,α	Ni-62	Stable	-

2.2.3 Ideal Proton Energy Range

In practice, producing the highest specific activity of ^{62}Zn while minimizing impurities is the main goal when selecting the appropriate proton beam energy. This requires simultaneous consideration of the reaction cross-section for ^{62}Zn and of other contaminants (Table 5) because different quantities of each can be produced at the same proton energies. Figures 3 and 4 show all of the possible ^{63}Cu(p,x) and ^{65}Cu(p,x) nuclear reactions (Table 5), respectively, for proton energies between 1 and 200 MeV

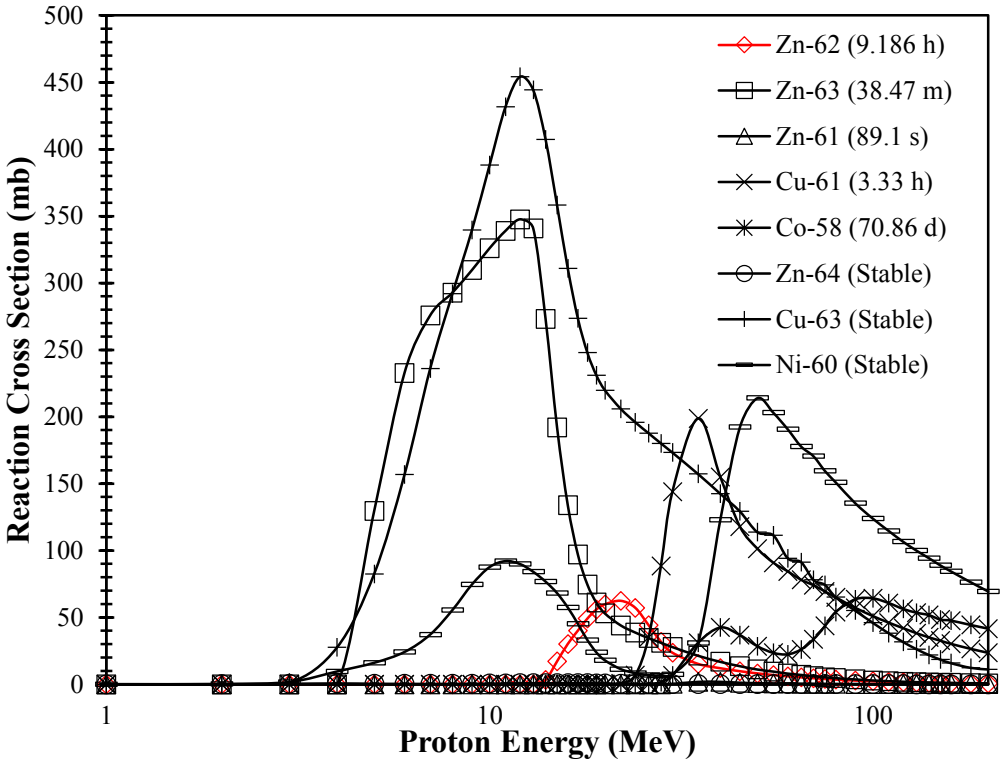

Figure 3. Reaction cross sections taken from JANIS (Soppera et al., 2014) of all possible nuclear reactions for protons bombarding ^{63}Cu with energies between 1 and 200 MeV.

Given the cross section data in Figures 3 and 4, it was determined that the ideal proton energy for maximizing the ^{62}Zn production yield with a high radionuclide purity would be between 18 and 30 MeV. Within this energy range several important contaminants reaction probability cross-sections are minimized. The copper contaminant ^{61}Cu ($T_{1/2}$ = 3.33 h) has a maximum possible reaction cross-section of 199 mb at a proton energy of 35 MeV. With a proton entry energy of 30 MeV, the maximum possible reaction cross-section for ^{61}Cu is 144 mb. This value drops to less than 0.01 mb at a proton entry energy of 18 MeV. Thus, the production of ^{61}Cu is minimized as effectively as possible with proton entry energies between 18 and 30 MeV.

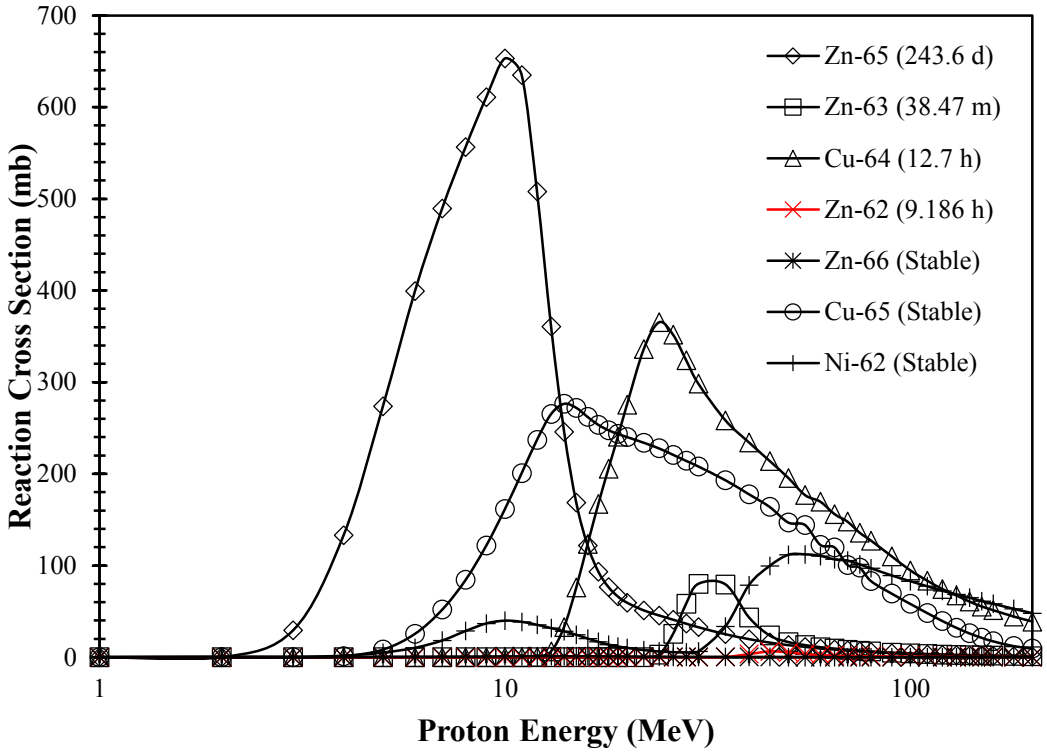

Figure 4. Reaction cross sections taken from JANIS (Soppera et al., 2014) of all possible nuclear reactions for protons bombarding ^{65}Cu with energies between 1 and 200 MeV.

Additionally, the other copper contaminant ^{64}Cu ($T_{1/2}$ = 12.7 h) has a maximum reaction cross-section of 365 mb at a proton energy of 24 MeV. While the production of this contaminant is not effectively minimized between proton entry energies of 18 and 30 MeV, ^{64}Cu only emits one gamma-ray with an emission rate of 0.5% and can be separated during the chemical processing phase. Thus, ^{64}Cu has a negligible impact on the radionuclide purity and presents itself as a negligible external radiological hazard.

The zinc contaminant ^{63}Zn ($T_{1/2}$ = 38.47 m) is produced through reactions with both natural copper isotopes in the target. With ^{63}Cu, the maximum ^{63}Zn reaction cross-section is 348 mb at a proton entry energy of 12 MeV. With the other copper isotope

^{65}Cu, the maximum ^{63}Zn reaction cross-section is 80 mb at proton entry energy of 30 MeV. Thus, between the proton entry energies of 18 and 30 MeV, the ^{63}Zn reaction cross-section is minimized between 74 and 100 mb through both natural copper isotopes. ^{63}Zn does not significantly affect the radionuclide purity of ^{62}Zn due to its short half-life, but can present an external radiological hazard following end of bombardment. Additionally, ^{61}Zn ($T_{1/2}$ = 89.1 s) is another short-lived zinc contaminant that is produced from ^{63}Cu. The production of this contaminant is negligible as it has a maximum reaction cross-section at 1.7 mb at a proton entry energy of 40 MeV with a reaction cross-section of less than 0.3 mb between proton entry energies of 18 and 30 MeV.

The only zinc contaminant that could potentially affect the radionuclide purity of ^{62}Zn is ^{65}Zn ($T_{1/2}$ = 244 d) due to its long half-life. The chemical processing phase separates the contaminants from ^{62}Zn based upon their different chemical properties. The ^{65}Zn contaminant cannot be separated as a result because it shares the same chemistry properties as ^{62}Zn. This contaminant is produced from ^{65}Cu and has a maximum reaction cross-section of 652 mb at a proton entry energy of 10 MeV. Between proton entry energies of 18 and 30 MeV, the reaction cross-section for this contaminant is effectively minimized between 77 and 32 mb, respectively.

The contaminant ^{58}Co ($T_{1/2}$ = 70.86 d) is produced from ^{63}Cu but has a reaction cross-section of less than 0.2 mb between proton entry energies of 18 and 30 MeV. ^{58}Co represents a negligible external radiological hazard and can be separated during chemical processing under the same reasoning listed for the separation of the other contaminants. Other stable isotopes produced are ^{60}Ni, ^{62}Ni, ^{64}Zn, ^{63}Cu, ^{66}Zn, and ^{65}Cu. These stable

isotopes are not an external radiological hazard and can be separated during the chemical processing phase. As a result, they do not impact the production yield or radionuclide purity of the final ^{62}Zn product.

2.2.4 Modeling Isotope Production Rate

The isotope production rate was modeled as a method of determining which proton energy maximized the production of ^{62}Zn. The production rate of an isotope can be defined as the number of nuclei *i* being formed per second minus the number of nuclei *i* decaying per second. This relationship takes the form of a differential equation that relates the gain and loss of nuclei *i* during production through various parameters seen in Equation 1 (Agency, 2009b).

$$A = \frac{N_A}{A_T} I(1 - e^{-\lambda t}) \int_{E_f}^{E_i} \frac{\sigma(E)}{S(E)} dE \quad (1)$$

where

I is the incident particle flux (s^{-1})
N_A is Avogadro's Number (nuclei·mol^{-1})
A_T is the molar mass of the material ($g \cdot mol^{-1}$)
λ is the decay constant of the product (s^{-1})
t is the bombardment time (s)
σ is the reaction cross-section and is a function of energy (cm^2)
S is the mass stopping power and is a function of energy ($MeV \cdot cm^2 \cdot g^{-1}$)
E is the energy of the incident projectile
$\int_{E_f}^{E_i}$ is the integral from initial, E_o, to final energy, E_f, of the projectile
A is the activity of nuclei *i* being produced (Bq)

The production rate of an isotope is directly related to the area under the reaction cross-section curve that spans over a given entry and exit energies (Rowshanfarzad et al., 2006). This is due to the energy loss of the projectile as it traverses through the target, defined by the stopping power. The reaction cross section acts as a function of projectile energy, changing throughout each segment of the target that the projectile traverses. Equation 1 takes this into account by integrating the reaction cross section and stopping power, both as a function of projectile energy, for a given projectile traversing a given target material to acquire the effective area under the reaction probability curve. The thickness of the target material dictates the exit energy, E_0, of the projectile and ultimately the length of the reaction probability curve.

Other important parameters that directly affect the production rate include the total number of incoming particles (beam current) and the saturation factor (SF). The production rate is directly proportional to the beam current. Large beam currents can cause substantial overheating capable of melting the target; therefore, careful thermal and mechanical stress analysis of the target must be carried out to safely produce a radionuclide. Overheating concerns can be addressed through different methods such as altering the irradiation time and beam current or adjusting the incident angle by which the beam strikes the target (Agency, 2009b).

The saturation factor, *SF*, is given by $(1 - e^{-\lambda t})$ and is the measure of the practical production limits of a given radionuclide. This is typically determined by the half-life of the isotope where irradiation times rarely exceed more than 3 half-lives, ~90% saturation, of the isotope. When the saturation activity of a radionuclide is

achieved during irradiation, the number of nuclei of that radionuclide being produced is equal to the number undergoing radioactive decay. It takes approximately 8 half-lives to reach the saturation activity which can result in significant irradiation times when considering longer lived radionuclides. As a result, considerations must be given for the expected yield of the longer lived radionuclides relative to the length of bombardment (Agency, 2009b).

In this study, Equation 1 was used to calculate the theoretical production yields for ^{62}Zn and contaminants (Table 5) for proton entry energies between 18 and 30 MeV. Given that the area under the reaction cross-section curve is dictated by both the entry and exit energy of the proton beam relative to the thickness of the copper target, the theoretical production yields were modeled for varying target thicknesses as well. The target thicknesses investigated were between 0.1 and 1.5 mm, each over the same proton entry energy range between 18 and 30 MeV.

The accuracy of Equation 1 was quantified by using irradiation parameters listed in previous studies to calculate theoretical production yields for ^{62}Zn. The theoretical production yields were compared against measured ^{62}Zn production yields reported in the respective studies. The results of this analysis is reported in the Results section and subsequently used to apply a correction factor to the theoretical yield. Table 6 shows the irradiation parameters used in each study. Reaction cross-section data was taken from a Java-based Nuclear Information Software (JANIS) developed by the Nuclear Energy Agency (Soppera et al., 2014).

Table 6. The values for proton entry energy, target diameter, target thickness, number of discs used, beam current, and irradiation time used in previous papers.

Reference	Projectile Energy	Target Mass	Target Thickness	# of Cu Discs	Beam Current	Irradiation Time
	(MeV)	(g)	(mm)	(#)	(μA)	(h)
Zweit et al., 1992	33.6	4.48	1.6	3	25	1
Robinson et al., 1980	22	3.45	0.4	2	30	1
Fukumura, 2006	29.7	2.06	0.9	1	10	1
Bormons et al., 1992	27	1.70	0.5	1	40	1
Lacy et al., 1998	33	-	1.62	1	37.5	0.75

2.2.5 Estimating Radiation Exposure

The production yield of ^{62}Zn is directly affected by the external radiological hazard presented by the short-lived contaminants produced during irradiation. Each short-lived contaminant contributes in varying degrees of intensity to the gamma-ray radiation field around the target. To be in compliance with 10CFR20.1301, the dose equivalent rate to an unrestricted area from an external radiation source must be less than 20 $\mu Sv \cdot hr^{-1}$ (2 $mRem \cdot hr^{-1}$). This regulatory limit requires a cooling period after EOB where the target must sit to allow for the decay of the short-lived contaminants that compose the largest component of the external radiological hazard around the target (Robinson Jr et al., 1980; Zweit et al., 1992). The larger quantity of short-lived contaminants that are produced, the longer the target must sit to allow for their decay. As a result, the short-lived contaminants directly affect ^{62}Zn's production yield as it can go through as much as one to two half-lives during the cooling period. Estimating the radiation exposure levels around the target provides an estimate of the length of the

necessary cooling period after EOB. Thus, to effectively optimize the production yield of ^{62}Zn, the radiation exposure levels around the target were estimated for proton entry energies between 18 and 30 MeV.

The irradiated target was modeled as a gamma-ray emitting point source contained in a 5 cm thick lead pig (Figure 5). The product and contaminants that were modeled are listed in Table 7. Each of these radionuclides *j* have an activity that emits *N* gamma-rays with a respective emission rate Y_i for each gamma-ray *i*. To calculate the absorbed dose, it was assumed that electronic equilibrium existed in tissue at a distance 1.0 m from the target. Given that gamma-rays are the only penetrating radiation that contribute to the radiation exposure around the target, a quality factor of 1 was assigned. Lastly, attenuation by air was considered negligible but buildup of the dose equivalent rate due to secondary radiations generated by photon interactions with the lead shielding was included into the calculations. Given these assumptions, the dose equivalent rate at a distance of 1.0 m from the irradiated was calculated with Equation 2 (Turner, 2008).

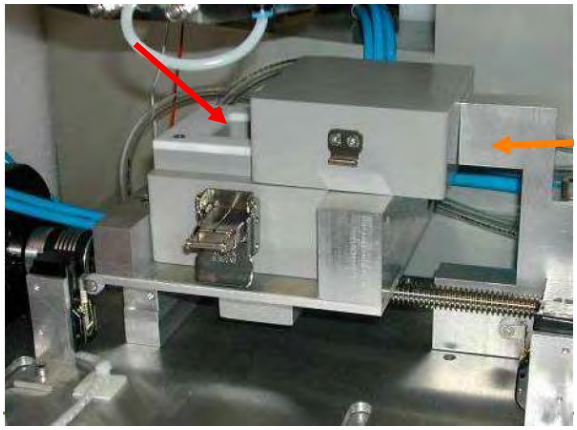

Figure 5. Lead pig used to unload the target disk. The walls of the lead pig are 5.0 cm thick.

$$\dot{H}_T = \sum_{j=1}^{7} \sum_{i=1}^{N} \frac{A_j Y_i E_i k}{4\pi r^2} \left(\frac{\mu_{en}}{\rho}\right)_{i,T} B_i e^{-\mu_i x} e^{-\lambda_j t} Q \quad (2)$$

where

$\dot{H}_T$ is the total dose equivalent rate in air ($\mu Sv \cdot hr^{-1}$)
A_i is the activity of radionuclide j (s^{-1})
E_i is the energy for a given photon i emitted by radionuclide j (MeV)
$\frac{\mu_{en}}{\rho}$ is the mass energy-absorption coefficient of tissue for photon i ($cm^2 \cdot g^{-1}$)
μ_i is the linear attenuation coefficient in lead for photon i (cm^{-1})
x is the thickness of the lead shielded pig (cm)
B_i is the buildup factor given $\mu_i x$, the mean free path in lead for photon i
r is the distance from the irradiated target (cm)
k is a conversion factor of 0.577 to go from $MeV \cdot g^{-1} \cdot s^{-1}$ to $\mu Sv \cdot hr^{-1}$
λ is the decay constant for radionuclide j (hr^{-1})
t is the cooling period after EOB (hr)
Q is the radiation quality factor

Modeling the irradiated target as a point source allowed for the dose equivalent rate to be calculated for each radionuclide and subsequently summed to acquire the total dose equivalent rate. The cooling period after EOB was determined with an iterative method that increased the cooling period in increments of 1 hour until the total dose equivalent rate around the target was below the federal limit. If the total dose equivalent rate was greater than the 20 $\mu Sv \cdot hr^{-1}$, an additional hour was added and the activity for each radionuclide was decay corrected using the new cooling period. This process was repeated for proton entry energies of 18 to 30 MeV.

The energy and yield of each photon emitted by the radionuclides in Table 7 were obtained from the National Nuclear Data Center's (NNDC) Nuclear structure and Decay data (NuDat) database. The activities for each radionuclide were calculated with

the use of Equation 1. The linear attenuation coefficients for lead and mass energy-absorption coefficients for tissue were acquired from the X-Ray and Gamma-Ray Data section of the National Institute of Standards and Technologies (NIST) website. The buildup factors for lead were obtained from the Health Physics and Radiological Health Handbook (Shleien and Terpilak, 1992).

Table 7. The product ^{62}Zn and relevant contaminants present in an irradiated target after bombardment.

Type	**Radionuclides in Irradiated Target**
Product	zinc-62
Contaminants	zinc-63
	zinc-61
	copper-61
	cobalt-58
	zinc-65
	copper-64

2.2.6 Targetry

The target consists of a solid high purity natural copper disc. Copper can be purchased at low cost as a single high purity foil and requires little pre-fabrication prior to irradiation depending on the form. Isotopic enrichment is not required due to the high isotopic abundance of copper-63. Due to this, recycling of the copper target for re-use in future irradiations is not a concern.

Previous experiments commonly cite the use of solid copper discs (Bormans et al., 1992; Fukumura, 2006; Haynes et al., 2000; Robinson Jr et al., 1980; Zweit et al.,

1992). Other types of targets are available, such as the use of electroplating copper onto a backing material (Fujibayashi, 1989). The copper discs can be irradiated as a stack of thin discs (Robinson Jr et al., 1980; Zweit et al., 1992) or as a single thick disc (Bormans et al., 1992; Fukumura, 2006; Haynes et al., 2000). The target has a backing material that typically possesses several desirable qualities such as a high thermal conductivity, low chemical reactivity, low activation cross sections, easy to machine, and high mechanical strength (Agency, 2009b). The backing material should be capable of transferring heat generated in the target to a heat sink while maintaining its integrity. For this reason, the most common material used as a backing material is aluminum (Agency, 2009b). Aluminum is advantageous due to its high thermal conductivity, activation products are short-lived and produced in low abundance, is chemically inert and very malleable (Agency, 2009a).

The most common method of heat dissipation is water cooling against the back of the target. In previous experiments, the water cooling has been listed at 4 L/min against the back of the target (Zweit et al., 1992) or designed such that the back of the target is maintained at 20 °C (Fukumura, 2006). Helium gas cooling directly against the front of the target, maintaining a temperature of -30 ºC, has been utilized previously as well.

Target thickness, target diameter, and number of disks used in previous papers are listed in Table 6. Important aspects of targetry used in this study involve the use of SRIM nuclear code (Ziegler, 2004) to create a simple model that was able to determine the rate of energy deposition for a proton traversing a copper target. Figure 6 shows this

model, which consists of a curve representing the proton range in copper for energies between 1 and 50 MeV. Figure 6 provides the necessary data to calculate the exit energy of a proton with a given entry energy and target thickness. Knowing the entry and exit energy for a given target, the energy deposition every 30 microns was calculated to provide an accurate assessment of the energy loss of the proton as it traversed through the target. This was incorporated into calculations using Equation 1. More detailed information about cyclotron targetry for solid targets, target preparation, and target irradiation practices and procedures can be found in Technical Report Series No. 465 Cyclotron Produced Radionuclides: Principle and Practice published by the IAEA.

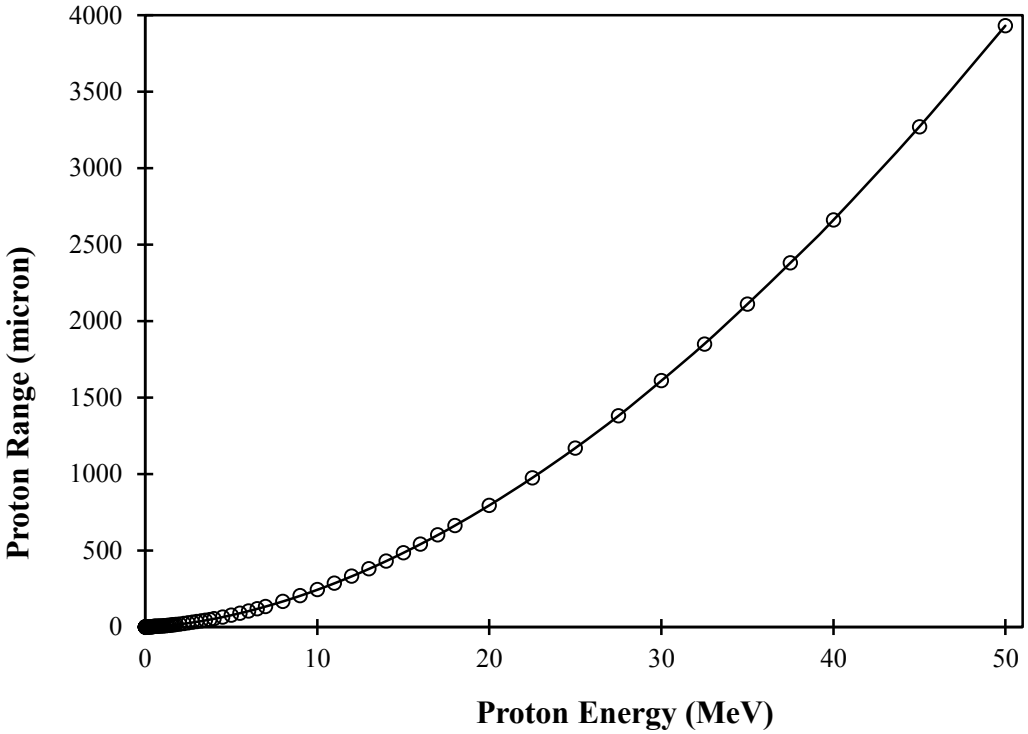

Figure 6**.** The proton range in copper for proton energies between 1 and 50 MeV. Data was taken from SRIM nuclear code (Ziegler, 2004).

2.3 Target Processing

2.3.1 Alternative Target Processing Method

Previous methods for target processing utilize concentrated hot nitric acid (an oxidizer) to quickly dissolve the target down to a copper(II) nitrate ($Cu(NO_3)_2$) solution. This solution was heated to decompose the copper(II) nitrate to copper(II) oxide (CuO), which precipitated out of the solution. When mixed with concentrated hydrochloric acid, copper(II) oxide undergoes a displacement reaction that results in the formation of the coordinate complex, copper(II) chloride ($CuCl_2$). Chemical separation of zinc and copper is based off the difference between their chloride complex formations (Fujibayashi, 1989). This process produces a large volume of corrosive fumes due to the use concentrated hydrochloric and nitric acid.

In this study, an alternative target dissolution method was developed that sought to eliminate the volume of corrosive fumes generated during the target processing phase. This alternative dissolution method involved the use of 30% hydrogen peroxide (H_2O_2) and 2 M hydrochloric acid to dissolve a copper foil representative of an irradiated copper target. The copper foil was placed in a solution of dilute HCl and hydrogen peroxide was added. The hydrogen peroxide will act as an oxidizer that dissolves the copper target, freeing copper(II) ions into the solution. The decomposition of hydrogen peroxide is an exothermic reaction and will release significant amounts of heat into the solution. Thus, the temperature of the solution will be monitored with a glass thermometer. Chloride ions in the solution from the HCl will form coordinate complexes with the copper(II)

ions, forming the desired copper(II) chloride complex. This chemical reaction is depicted in Equation 3.

$$H_2O_{2(aq)} + Cu_{(s)} + 2\,H^+_{(aq)} \rightarrow Cu^{2+}_{(aq)} + 2\,H_2O_{(l)}$$

$$Cu^{2+}_{(aq)} + 4\,Cl^-_{(aq)} \rightarrow [CuCl_4]^{2-}_{(aq)} \quad (3)$$

Following the complete dissolution of a copper foil with the alternative dissolution method, an alternative target processing procedure was developed. This involved the use of copper foils that represented a small copper target with a thickness of 1.0 mm, radius of 6.0 mm, and mass of 1.0 g. The copper was purchased from Sigma Aldrich in the form of a 1.0 mm thick sheet of high purity natural copper. The copper foils cut from this sheet were smaller than the typical copper target of 1.75 to 4.50 g used in previous references (Table 6).

2.4 Chemical Processing

2.4.1 Ion Exchange Chromatography

The accepted technique for separating ^{62}Zn from the solution obtained at the end of the target processing phase is Ion Exchange Chromatography (IEC) (Bormans et al., 1992; Fukumura, 2006; Robinson Jr et al., 1980; Zweit et al., 1992). This technique is preferred due to its extremely high separation efficiency with divalent transition metals. Commonly, the AG-1 (Fukumura, 2006; Zweit et al., 1992) or Dowex-1 (Bormans et al., 1992; Robinson Jr et al., 1980) anion exchange resin in the chloride form is used as the

stationary media within the column. The resin consists of an insoluble matrix that contains bonded functional groups referred to as fixed ions that can be either cationic or anionic (Haddad, 1994). The AG-1 and Dowex-1 resin are both strongly basic with cationic quaternary amino groups, $N^{+}R_4$, as the fixed ion. The chloride form indicates that the counter-ion is a Cl^{-} atom. When passing a solution through the column, ion exchange occurs between the solution in the mobile phase (eluent) and the counter-ion in the stationary phase (resin). The counter-ion can only exchange with another ion in the solution that has a similar charge and a higher affinity for the resin.

The anionic chloride complex that ^{62}Zn and the other contaminants form can exchange with the chloride counter-ions and subsequently be captured on the AG-1 and Dowex-1 resins. The affinity of each type of chloride complex to bind to the resin over the chloride counter-ion is determined by the divalent transition metal at the center of the chloride complex. The large difference in anion exchange behavior between each divalent transition metal is likely due to the large difference in their complexing properties as a function of atomic number (Kraus, 1953). It was observed by Kraus,1953 that the order of complexing strength is directly proportional to the solubility of each metal in hydrochloric acid and how readily they form chloride complexes (Kraus, 1953). For transition metals such as zinc, which dissolve readily in hydrochloric acid, stronger chloride complexes are formed that have a higher affinity to exchange with the chloride counter-ion and bind to the resin than the weaker chloride complexes formed by the contaminants. Figure 7 shows that zinc has an adsorption maximum with a strong anion exchange resin in a 2 M HCl solution while the transition metal contaminants have

significantly less adsorption affinities to the resin at the same concentration. It is this difference in adsorption affinities between zinc and the contaminants that allows the contaminants to be separated by direct elution with 2 M HCl while zinc isotopes remain captured in the resin. Additional detailed information behind the use of ion exchanged chromatography in the chemical processing procedure can be found in Zweit, et al., 1992 and Fukumura, 2006.

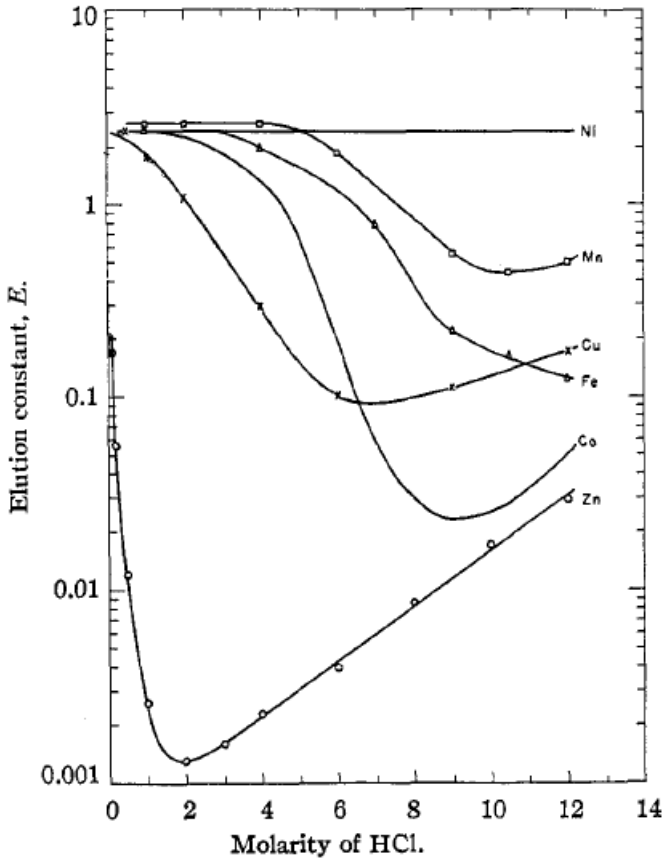

Figure 7. Profile of elution constants taken from Kraus,1953 that depict the adsorption properties of divalent transition metals in a HCl solution with strong anion exchange resin (Kraus, 1953). The elution constant is obtained with E = dA/V, where d is the distance (cm) that an adsorption maximum travels when passing an amount of V (cm^3) eluent through a column with cross-sectional area A (cm^2).

2.5 The $^{62}Zn/^{62}Cu$ Generator Column

The procedure for loading the generator column has been established in previous studies (Haynes et al., 2000; Robinson Jr et al., 1980; Zweit et al., 1992). The generator column itself is composed of a commercially available borosilicate glass column with volumes ranging between 0.75 and 3.85 ml. The generator column is housed inside of a cylindrical lead shield appropriately thick to reduce radiation exposure levels around the generator to below federally regulated limits dictated by 10CFR20.1301. The lead shielding contains input and output ports connected to the top and bottom of the glass column, respectively. These ports allow for loading of ^{62}Zn and elution of ^{62}Cu from the generator column. The generator column is loaded with AG1 anion-exchange resin (Cl^-) and is pre-equilibrated with 0.3 M HCl/40% ethanol for maximum elution yield of ^{62}Cu (Zweit et al., 1992). Different ligand structures, different concentrations, and their effect on ^{62}Cu elution yield and ^{62}Zn leakage have been analyzed by Fujibayashi, 1989 (Fujibayashi, 1989).

2.6 Automating Generator Production

2.6.1 Necessary Hardware

Two single channel OEM model NE-500 syringe pumps were purchased from New Era Pump Systems Inc (Figure 8). The OEM version of the NE-500 model comes with the pump internals attached to a chassis that is mountable. The dimensions of the chassis are 24.13 x 10.16 x 10.5 cm^3. This model type holds a single syringe that is capable of infusion and withdrawal pumping of syringe volumes up to 60 cc full or 140

cc partially filled. Pumping rates with this model can range from as low as 0.73 $\mu l \cdot hr^{-1}$ with a 1 cc syringe to 2120 $ml \cdot hr^{-1}$ with a 60 cc syringe. Detailed information involving syringe types from different manufacturers, their offered syringe volumes, those syringe inner diameters, minimum rate and maximum rate is contained in Table 8. The NE-500 communicates through an RS-232 connection, labeled "To Computer" on the instrument, which connects directly to an RS-232 port on a computer. The NE-500 is also capable of operating in a network with other instruments through a secondary RS-232 connection labeled "To Network". This instrument network can support up to 100 instruments and is not limited solely to the NE-500.

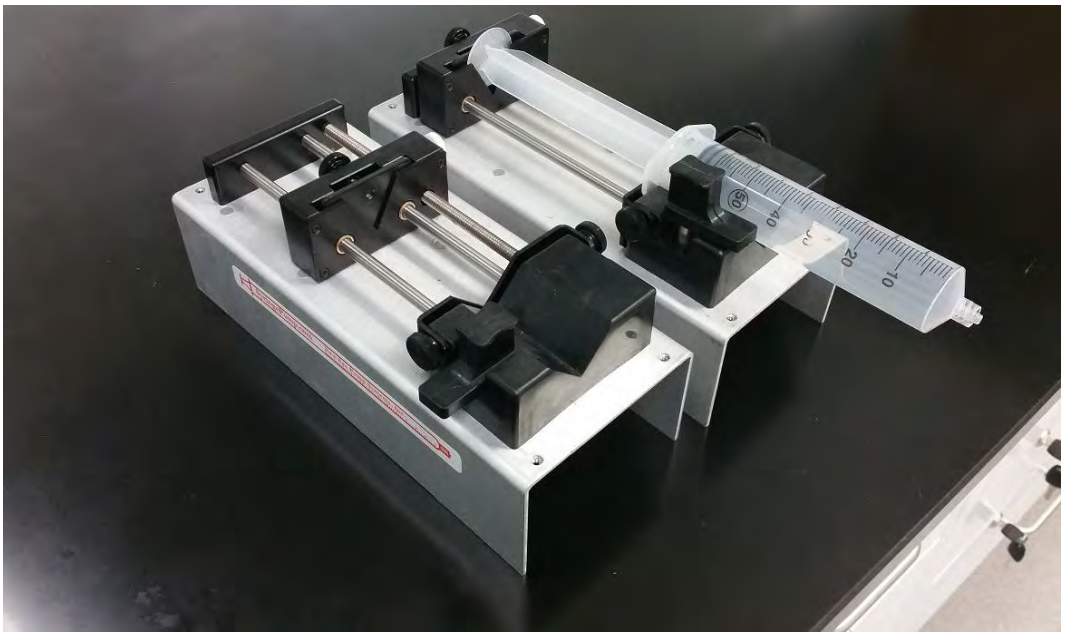

Figure 8. Two single channel OEM model NE-500 syringe pumps.

One syringe heater model HEATER-KIT-1LG was purchased from New Era Pump Systems Inc (Figure 9). The electronics of the HEATER-KIT-1LG are contained

in a case that allows direct manipulation of the instrument through external controls. More importantly, the instrument also contains the same RS-232 connections as the NE-500. The case was not purchased as an OEM version and has dimensions of 11.75 x 6.35 x 3.81 cm^3. The heating element of the instrument is a thermocouple contained in a heating pad with the dimensions 8.8 x 7.5 cm^2. The heating pad is intended to be wrapped around a syringe or item of similar shape. The maximum temperature of the heating pad is 185 °C.

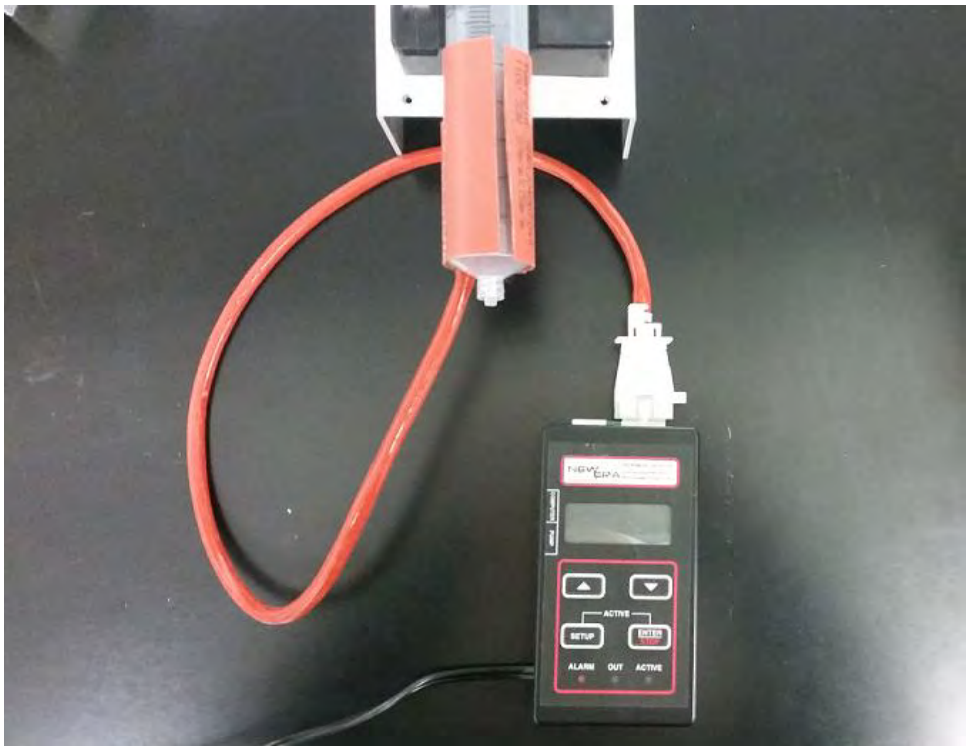

Figure 9. A single syringe heater model HEATER-KIT-1LG.

Table 8. A list of syringe diameter and rate limits for the NE-500 pump using syringes from different manufacturers. This data was taken from the NE-500 syringe pump user manual.

Syringe Manufacturer	Syringe Volume (mL)	Inside Diameter (mm)	Maximum Rate ($mL \cdot hr^{-1}$)	Maximum Rate ($mL \cdot min^{-1}$)	Minimum Rate ($\mu L \cdot hr^{-1}$)
B-D	1	4.70	53.07	0.88	0.73
	3	8.59	177.10	2.95	2.43
	5	11.99	345.50	5.76	4.75
	10	14.43	500.40	8.34	6.88
	20	19.05	872.20	14.53	11.99
	30	21.59	1120.00	18.67	15.40
	60	26.59	1699.00	28.32	23.35
HSW Norm-Ject	1	4.69	52.86	0.88	0.73
	3	9.65	223.80	3.73	3.08
	5	12.45	372.50	6.21	5.12
	10	15.90	607.60	10.12	8.35
	20	20.05	966.20	16.10	13.28
	30	22.90	1260.00	21.00	17.32
	50	29.20	2049.00	34.15	28.16
Monoject	1	5.74	79.18	1.32	1.09
	3	8.94	192.10	3.20	2.64
	6	12.70	387.60	6.46	5.33
	12	15.72	593.90	9.90	8.16
	20	20.12	972.90	16.21	13.37
	35	23.52	1329.00	22.15	18.27
	60	26.64	1705.00	28.42	23.44
	140	38.00	3470.00	57.84	47.69
Terumo	1	4.70	53.09	0.88	0.73
	3	8.95	192.50	3.21	2.65
	5	13.00	406.10	6.77	5.58
	10	15.80	600.00	10.00	8.24
	20	20.15	975.80	16.26	13.41
	30	23.10	1282.00	21.37	17.63
	60	29.70	2120.00	35.33	29.13

One USB Digital I/O Device OEM model USB-6501 was purchased from National Instruments (Figure 10). The OEM version of the USB-6501 is mountable with the dimensions 5.74 x 6.73 cm^2. The instrument has 24 digital I/O lines capable of both sending output logic pulses of 0 V (off) or 5 V (on) and receiving data in the form of logic pulses. The 24 channels are broken up into three different ports of 0, 1, and 2 with 8 channels each. The instrument has a generic 34-pin connection that can be interfaced with any commercially available 34-pin IDC female connector where each pin correspond to different I/O channels and ground connections. The pin assignments for the USB-6501 are shown in Table 9. The USB-6501 communicates with a computer through a USB connection. A detailed summary of all of the hardware purchased, their necessary accessories, and dimensions is contained in Table 10.

Figure 10. A single USB Digital I/O Device OEM model USB-6501 with 34 pins.

Table 9. The pin assignments for Ports 0-2 on the USB-6501 taken from the OEM User Guide.

Signal	Pin	Connector	Pin	Signal
P1.0	1	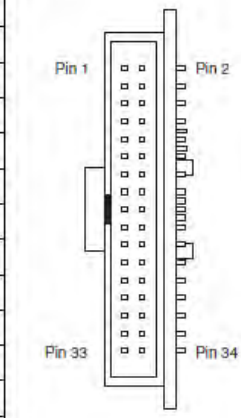	2	GND
P1.1	3		4	P2.0
P1.2	5		6	GND
P1.3	7		8	P2.1
P1.4	9		10	GND
P1.5	11		12	P2.2
P1.6	13		14	GND
P1.7	15		16	P2.3
P0.0	17		18	GND
P0.1	19		20	P2.4
P0.2	21		22	GND
P0.3	23		24	P2.5
P0.4	25		26	GND
P0.5	27		28	P2.6
P0.6	29		30	GND
P0.7	31		32	P2.7
+5V	33		34	+5V

Table 10. A summarized list of the hardware components purchased, their company, relevant accessories, interface, and dimensions.

Hardware	Syringe Pump (NE-500)	Syringe Heater (HEATER-KIT-1LG)	Digital I/O (USB-6501)
Company	New Era Pump Systems Inc	New Era Pump Systems Inc	National Instruments
Accessory	CBL-PUMP	CBL-PUMP	34 pin connector
Interface	RS-232	RS-232	USB
Dimensions	24.13 x 10.16 x 10.5 cm^3 (L x W x H)	54 cm long cord 8.8 x 7.5 cm^2 (pad) (L x W) 11.75 x 6.35 x 3.81 cm^3 (case) (L x W x H)	5.74 x 6.73 cm^2 (L x W)

2.6.2 Necessary Software

The RS-232 connection on the NE-500 is commonly referred to as a serial port and works by sending data one bit at a time. To successfully communicate with the NE-500, a software that was capable of interpreting serial communication was utilized. The software LabVIEW, developed by National Instruments, was particularly well suited for this task. LabVIEW is short for Laboratory Virtual Instrument Engineering Workbench and is a visual programming software put out by National Instruments for use as a system-design platform. LabVIEW consists of two windows: the front panel and block diagram. The front panel is considered the user interface (UI) where controls, inputs, and outputs are connected to code or programming in the block diagram. The front panel represents a completely customizable UI that can be geared toward virtually any application. LabVIEW uses its Virtual Instrument Software Architecture (VISA) as a standard for configuring and programming instrument systems that communicate over serial or USB connections. The VISA interface software comes separately from LabVIEW and must be downloaded and installed manually from National Instruments website.

The NE-500 was controlled with programming developed in LabVIEW. Communications to and from the NE-500 occur through a RS-232 or serial port connection with a computer. LabVIEW must configure the serial port with the same baud rate and data frame as the NE-500 to successfully communicate with the instrument. The data frame information for the NE-500 is listed in Table 11.

Table 11. The RS-232 data frame used by the NE-500 Syringe Pump to communicate through a serial connection.

RS-232 Data Frame	
Baud Rate:	19200
Frame:	10 Bit Data Frame (8N1)
Start Bit:	1
Data Bit:	8
Stop Bit:	1
Parity	None

The NE-500 is controlled by sending commands to the instrument with LabVIEW. When commands are sent, the NE-500 processes it and sends a response back to the serial port. It is important to note that once a command has been sent to the NE-500, it will not accept any further communications until the command has been processed. Commands and responses with the NE-500 consist of characters that are a combination of ASCII codes and numeric data. The numeric data is classified as a floating point number with 4 digits and 1 decimal point. Commands sent to the NE-500 should have a carriage return, 0x0D in ASCII, at the end. Space characters that are placed within the command will be ignored when processed by the pump and can be considered optional when giving inputs.

An instrument network can technically support 100 instruments with addresses from 00 to 99. When the NE-500 is used in a network, each instrument must be assigned an address. The default address for each instrument is 00 and must be set with a direct connection to the port labeled “To Computer” prior to being connected to the network. When placing an instrument into a network, the first instrument must have a connection from the port labeled “To Computer” to the RS-232 port on the computer. Every

instrument after the primary instrument must have a connection from the port labeled "To Network" on the prior instrument to the port labeled "To Computer" on the subsequent instrument. When issuing commands to an instrument in a network, the address number of the desired pump must precede the command.

Table 12 provides simple examples illustrating the syntax of how a command should be sent to the NE-500. Table 13 contains a list of commands taken by the NE-500, their purpose, and the NE-500's query response for each command. Table 12 can be used as a supplement to provide examples of syntax for the various commands in Table 13. More information about the NE-500 syringe pump can be found in the NE-500 OEM Syringe Pump User Manual.

Table 12. A list of examples illustrating the appropriate syntax for a set of common commands and a brief explanation behind what each command does.

Command	Syntax	Explanation
ADR	ADR10x0D	Assign Address 1 to pump
DIA	ADRDIA200x0D	Assign inner diameter of syringe to 20 mm. ID > 10 sets units to mL
VOL	ADRVOL50x0D	Assign 5 mL to be dispensed
RAT	ADRRAT30MM0x0D	Assign a pumping rate of 30 mL/min
DIR	ADRDIRINF0x0D	Assign a pump direction: Infuse
RUN	ADRRUN0x0D	Set pump to run. Infuse 5 mL automatically.

The HEATER-KIT-1LG operates under the same technical and programmable principles as the NE-500. It has an RS-232 port that allows LabVIEW to control it through its VISA interface software. The HEATER-KIT-1LG can operate in the same instrument network as the NE-500 with its own designated address. Additionally, this

instrument uses the same data frame (Table 11) and the same command syntax (Table 12) as the NE-500. However, unlike the NE-500, data changes are not automatically stored in its non-volatile memory unless a save command is given to the syringe heater. Table 14 contains a detailed list of commands taken by the HEATER-KIT-1LG, their purpose, and the HEATER-KIT-1LG's query response for each command. More information about the instrument can be found in the Syringe Heater User Manual.

Table 13. A list of commands, their numeric argument, their purpose, and the instruments response when queried with each command for the NE-500, taken from the NE-500 user manual.

Command	Numeric Argument	Purpose	Instrument Response
DIA	<float>	Syringe Inner Diameter. (0.1 to 10 mm - UL) (10.01 to 50 mm - ML)	<float><units>
RAT	[<float>< units>]	Pumping Rate with units (UM,UH,MM,MH)	<float><units>
VOL	[<float> | <units>]	Volume to be dispensed Manually set volume units (ML,UL)	<float><units>
DIR	[INF | WDR]	Pumping Direction	[INF | WDR]
RUN	-	Starts the pumping program	-
STP	-	Stops the pumping program	-
DIS	-	Query volume dispensed	I<float>W<float><units>
CLD	[INF | WDR]	Clear volume dispensed	-
SAF	<n>	Safe communications mode (n = 0 to 255)	<n>
AL	[<on-off>]	Alarm mode	[<on-off>]
PF	[<on-off>]	Power failure mode	[<on-off>]
BP	[<on-off>]	Key and notification beep mode	[<on-off>]
VER	-	Query firmware version	NE50<n>V<n>.<nn>
ADR	<n>	Network Address	<n>
RESET	-	Clears memory and resets all values	-

Table 14. A list of commands, their numeric argument, their purpose, and the instruments response when queried with each command for the HEATER-KIT-1LG, taken from the Syringe Heater user manual.

Command	Numeric Argument	Purpose	Instrument Response
RUN	-	Enter active mode Maintain heating temp	-
STP	-	Exit Active Mode	-
TMP	-	Query heating pad temp	<n>
SET	<n>	Set heating setpoint	<n>
FTS	<n>	Set fine tune slow down degree setting	<n>
FTH	<n>	Set fine tune temp hold percentage	<n>
SAV	-	Save all new settings in non-volatile memory	-
UNT	[C | F]	Set temp units	[C | F]
PF	[<on-off>]	Alarm mode	[<on-off>]
CAL	[L | H [<n>]]	Heating pad calibration	-
PAD	<n>	Calibration setting 1 - Default 0 - Calibrated	<n>
ADR	<n>	Set network address	<n>
VER	<n>	Query firmware version	NE8<nn>V<n>.<nn>
RESET	-	Clears memory and resets all values	-

As with the serial connection, the same principle applies to a USB connection. The USB-6501, with a USB connection, requires the VISA interface driver to interact with LabVIEW as well. However, because the USB-6501 is a data acquisition (DAQ) device, it also requires additional software drivers from National Instruments to successfully interface with LabVIEW. These software drivers are NI-DAQmx and NI-DAQmx Base and are found on the National Instruments website. NI-DAQmx allows LabVIEW to communicate with the USB-6501 and NI-DAQmx Base provides

specialized functionality for controlling the USB-6501. The NI-DAQmx Base allows for the use of an automated function known as the DAQ Assistant. The DAQ Assistant will take inputs designated by the user and apply them to automatically generated programming that will change the trigger states of the different I/O channels as indicated. In this case, the trigger state represents the on/off state of each channel. It is worth noting that the software drivers from National Instruments are free and automatically update through LabVIEW's driver management software when new driver updates are published. A summary of the necessary hardware components and the software drivers required to use them in LabVIEW is contained in Table 15.

Table 15. Hardware components and their required software.

Hardware Component	**National Instrument Software Drivers**		
	NI-VISA	**NI-DAQmx**	**NI-DAQmx Base**
NE-500	✓	×	×
HEATER-KIT-1LG	✓	×	×
USB-6501	✓	✓	✓

3. RESULTS AND DISCUSSION

3.1 Results

3.1.1 Optimal Irradiation Parameters

Between proton entry energies of 18 and 30 MeV, the only reaction utilized to produce ^{62}Zn is ^{63}Cu(p,2n). However, both ^{63}Cu and ^{65}Cu are utilized in the production of the contaminants listed in Table 5. Theoretical yields at EOB for ^{62}Zn were calculated for target thicknesses of 0.1, 0.5, 1.0, and 1.5 mm. These values, shown in Figure 11, illustrate that the yield of ^{62}Zn increases both as a function of proton entry energy and target thickness up to a maximum.

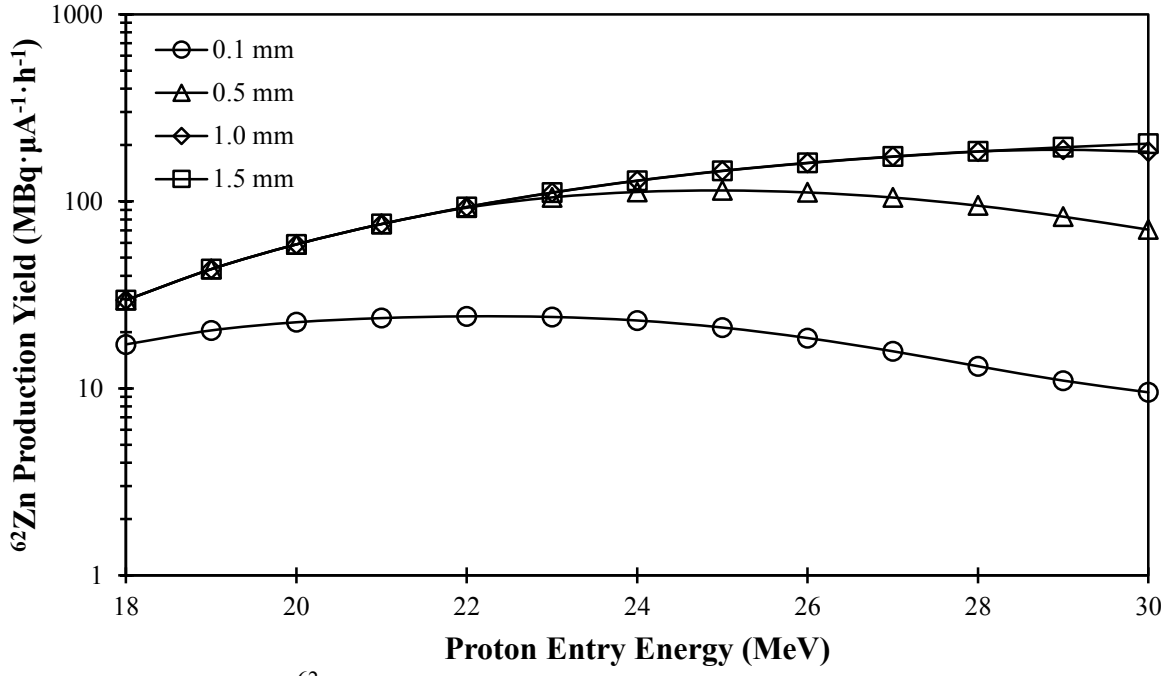

Figure 11. Theoretical ^{62}Zn production yield at EOB with target thicknesses between 0.1 and 1.5 mm for proton entry energies between 18 and 30 MeV.

The ^{62}Zn yield increases with target thickness up to 1.0 mm with diminishing returns on any additional increase in thickness 1.0 mm. Thus, it was observed that the ^{62}Zn yield at EOB for a 1.0 mm thick target was essentially identical to that of a 1.5 mm thick target over the same proton energy range. The results from Figure 11 indicated that the optimal target thickness for the routine production of ^{62}Zn was 1.0 mm.

Utilizing a target thickness of 1.0 mm, the dose equivalent rate in tissue at a distance of 1.0 m was calculated for each radionuclide (Table 7) and summed for the whole target. The cooling period after EOB was calculated based upon the regulatory dose limit set by 10CFR20.1301. The EOB dose equivalent rates for each radionuclide and for the target are shown in Table 16.

Table 16. The EOB dose equivalent rate at 1.0 m for each radionuclide and the total dose equivalent rate for the target.

Proton Entry Energy	**Radionuclide Dose Rates**							**Target Dose Rate**
	Zn-62	**Zn-63**	**Zn-61**	**Cu-61**	**Co-58**	**Zn-65**	**Cu-64**	
(MeV)	**(μSv·hr^{-1})**							**(μSv·hr^{-1})**
18	0.0	94	0	0	0	1	0	95
19	0.1	97	0	0	0	1	0	98
20	0.1	99	0	0	0	1	0	100
21	0.1	101	0	0	0	1	1	103
22	0.1	103	0	0	0	1	1	105
23	0.1	105	0	0	0	1	1	107
24	0.2	102	0	0.1	0	1	1	105
25	0.2	90	0	0.3	0	1	1	92
26	0.2	75	0	1	0	1	1	77
27	0.2	58	0	1	0.0000	0	2	61
28	0.2	41	0	3	0.0001	0	2	46
29	0.2	32	0.1	4	0.0003	0	2	38
30	0.2	27	0.3	6	0.0006	0	2	35

^{63}Zn ($T_{1/2}$ = 38.47 min) dominates between 75 and 99% of the total dose equivalent rate from the target over proton entry energies between 18 and 30 MeV. At proton entry energies of 29 and 30 MeV, ^{61}Cu ($T_{1/2}$ = 3.33 h) dominates 10 and 17% of the total dose equivalent rate, respectively. The other contaminants contribute to 5% or less of the total dose equivalent rate around the target.

The cooling period after EOB is 2 hours from 18 to 27 MeV and 1 hour from 28 to 30 MeV. Using the cooling period for each proton entry energy, the production yield of each radionuclide was decay corrected. The ^{62}Zn production yields for proton entry energies between 18 and 30 MeV, decay corrected with their respective cooling periods, are shown in Table 17.

Table 17. The production yield for each radionuclide, decay corrected with their respective cooling period at each proton entry energy.

Proton Entry Energy	**Cooling Period**	**Radionuclide Production Yields**						
		Zn-62	**Zn-63**	**Zn-61**	**Cu-61**	**Co-58**	**Zn-65**	**Cu-64**
(MeV)	**(hr)**	**(MBq·μA^{-1}·h^{-1})**						
18	2	25	603	0	0	0.000	1.40	85
19	2	37	619	0	0	0.000	1.43	123
20	2	51	634	0	0	0.000	1.46	169
21	2	65	648	0	0	0.000	1.48	222
22	2	80	662	0	0	0.000	1.50	283
23	2	96	674	0	1	0.000	1.53	351
24	2	111	656	0	4	0.000	1.43	423
25	2	125	575	0	11	0.000	1.19	497
26	2	138	478	0	27	0.000	0.88	572
27	2	149	369	0	56	0.000	0.59	646
28	1	171	780	0	125	0.003	0.43	756
29	1	175	596	0	204	0.009	0.34	813
30	1	171	502	0	306	0.020	0.30	850

A maximum ^{62}Zn yield of 175 $MBq \cdot \mu A^{-1} \cdot h^{-1}$ was observed at a proton entry energy of 29 MeV. The $^{65}Zn/^{62}Zn$ ratio is approximately 0.2% at 29 MeV proton entry energies. The calculated $^{65}Zn/^{62}Zn$ ratio is comparable to values of 0.17% (Zweit et al., 1992) and 0.03% (Bormans et al., 1992) found in previous studies. All other contaminants will either decay away over the course of processing or will be separated during chemical processing.

Theoretical production yields were calculated using values of target thickness, beam current, proton entry energy, and irradiation time listed in previous studies (Table 6). The theoretical yields were compared against experimentally measured yields reported in their respective studies. Table 18 shows the theoretical yields, experimental yields for each study.

Table 18. A comparison between measured production yields at EOB from previous studies and calculated theoretical production yields at EOB.

Reference	Measured Yield	Theoretical Yield	Percent Difference
	(MBq/μA)	(MBq/μA)	(%)
Zweit	206	230	-11
Robinson	74	84	-13
Fukumura	184	168	9
Bormons	141	105	29
Haynes	248	171	37
		Average:	10

It was observed from this comparison that the theoretical yields were an average of 10% lower than the experimentally reported yields. This was determined to be the case despite two of theoretical yields having larger values that the reported experimental

yields. There was a lack of quantifiable error reported within the studies investigated. As a result, the best method determined for measuring the accuracy of the calculations was to acquire an average of the percent difference for each study. Given this method, there was a 10% deviation below the experimentally reported yields despite the two outliers.

The 10% deviation is likely attributable to the lack of cGMP applied in producing these generator systems in the previous studies. The practice of cGMP is a federally regulated method of applying quality assurance to generator systems that are produced for the purpose of PET studies. As a result, the irradiation parameters reported in the previous studies may not be entirely accurate, resulting in an experimental production yields that deviate from theoretically predicted values. A Matlab code was written to perform these calculations and can be found in Appendix A. Appendix B holds relevant data used to perform the calculations such as cross-section data, stopping power of protons in copper data, buildup factors, linear attenuation coefficients in lead, mass energy-absorption coefficients in tissue, and gamma-ray energies and yields of the radionuclides.

3.1.2 Alternative Dissolution Method

A foil of high purity natural copper was successfully dissolved in a solution containing 30% hydrogen peroxide (H_2O_2) and 2 M hydrochloric acid (HCl). The dissolution of the copper foil formed a green solution, depicted in Figure 12a, while heated. When the solution was evaporated, it took on a target green color, depicted in Figure 12b. When evaporated to dryness, the copper chloride residue that remained had a

dark brown color, depicted in Figure 12c. This residue was soluble in hydrochloric acid, and could be reconstituted at any concentration of HCl. When reconstituted in 2 M HCl, the solution color returned to a blue hue, depicted in Figure 12d. Additionally, the solution could be shifted back to green when heated or when a stronger concentration of HCl solution was added or shifted back to blue when diluted with additional water.

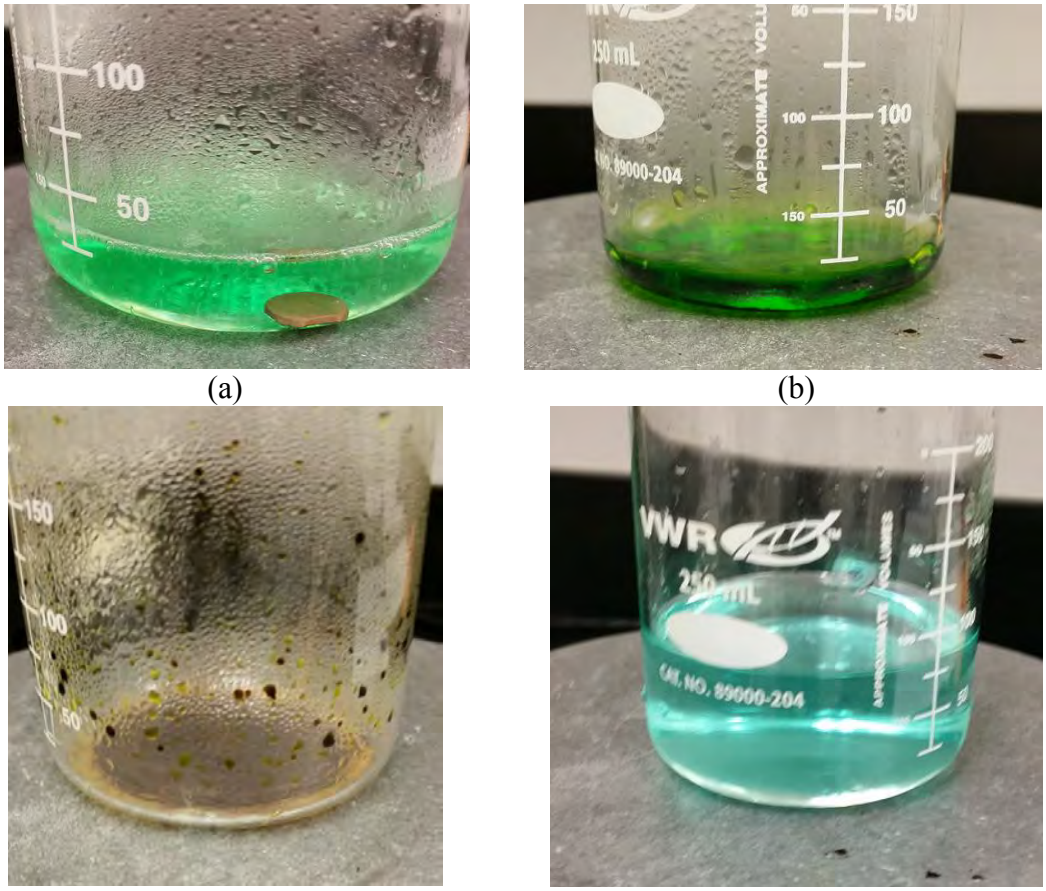

(a) (b)

(c) (d)

Figure 12. The dissolution process broken into 4 stages. The dissolution of the copper foil (a), evaporating the solution to dryness (b), the residue left after evaporation (c), and the reconstituted 2 M HCl solution after reconstitution (d).

With the successful development of an alternative dissolution method, an alternative target processing procedure was developed. This was carried out with subsequent dissolutions involving the use of a 1.0 mm thick copper foil with a radius of 6.0 mm and average mass of 1.0 g. The focus of the alternative target processing procedure was to reduce the total dissolution time while minimizing the total amount of corrosive chemicals used.

The alternative target processing procedure involved the use of two dissolution vessels. A copper disc was placed within dissolution vessel 1 (DV1) along with 10 ml of 2 M hydrochloric acid pre-heated to 60 ºC. To begin the dissolution process, 1 ml of 30% hydrogen peroxide was added to DV1 and a timer was started. Every 30 seconds after the initial 1 ml of H_2O_2 was added, an additional 1 ml of H_2O_2 was added. This continued until 3.5 minutes had passed and a total of 7.0 ml of H_2O_2 had been added to DV1. The target was left to dissolve for 2.0 minutes while the temperature of the solution peaked at 75 °C. This occurred at approximately 5.5 minutes into the dissolution.

The solution was left to sit until the temperature of the solution began to decrease. This occurred at approximately 6.0 minutes into the dissolution. At this point, the solution in DV1 was transferred to dissolution vessel 2 (DV2), leaving the partially dissolved copper foil in DV1. Immediately, an additional 10 ml of ~60 ºC 2 M hydrochloric acid was added to DV1. At 6.5 minutes, 1 ml of 30% hydrogen peroxide was added to the solution in DV1 to renew the dissolution of the copper foil. Every 30 seconds, an additional 1 ml of H_2O_2 was added to the solution in DV1. This continued

until 8.5 minutes had passed into the dissolution and a total of 5.0 ml of H_2O_2 has been added to the solution. The solution was left to sit as the copper foil finished completely dissolving.

Complete dissolution occurred at approximately 12.0 minutes after the start of the dissolution. Once completely dissolved, the remaining solution was transferred to DV2. A total of 20 ml of 2 M hydrochloric acid and 12 ml of 30% hydrochloric acid was used to completely dissolve the copper foil. Going into the next phase, the evaporation of the solution occurs in DV2. A flow diagram that outlines this procedure is shown in Figure 13.

While developing the alternative target processing procedure, several key aspects of using 30% hydrogen peroxide were noted. It was observed that when the hydrogen peroxide was added to the solution too quickly or in too large of a quantity, the temperature of the solution increased to over 100 ºC. This would result in the solution boiling over, effectively losing control of the dissolution and spreading the would-be radioactive materials all over the laboratory equipment. Additionally, the rapid increase in temperature also resulted in the simultaneous thermal decomposition of the hydrogen peroxide in the solution. Given this, it was also observed that the temperature of the solution seemed to directly correlate to the hydrogen peroxide available in the solution to dissolve the copper foil. Thus, it was assumed that controlling the temperature of the solution was closely tied to the quantity of hydrogen peroxide and frequency at which it was added to the solution.

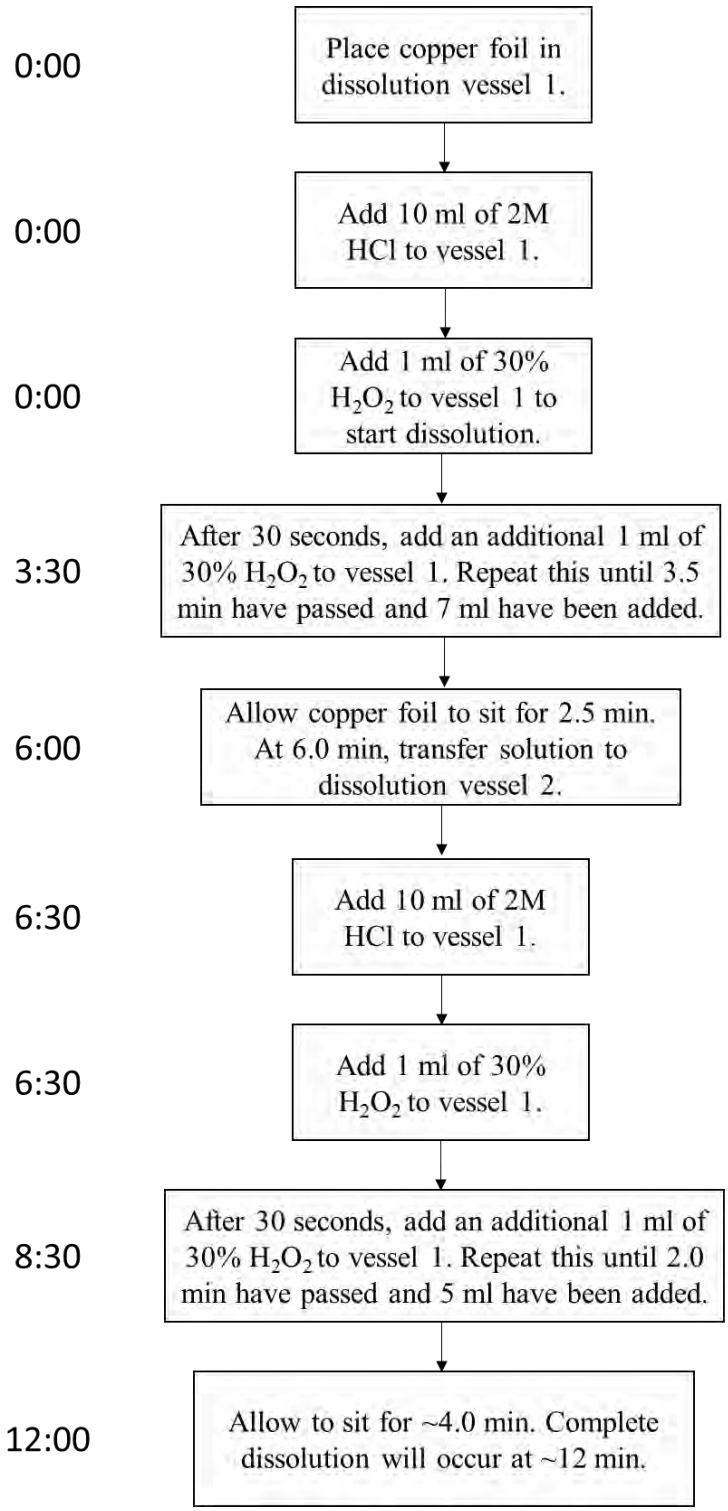

Figure 13. Flow diagram depicting the steps taken in the alternative target processing procedure to achieve a dissolution time of 12 minutes with 30% H_2O_2 and 2 M HCl.

3.1.3 Utilizing LabVIEW

To communicate with a device over a serial connection, a VISA session was opened with the use of the function VISA Open. The computer's serial port was then configured in LabVIEW with the function VISA Serial Port Configuration using the data frame from Table 11. During initialization, the I/O buffer was cleared, flushed, and set to receive and transmit information. Figure 14 shows the code used to open a VISA session and initialize the serial port to communicate with the NE-500 or HEATER-KIT-1LG. The variable VISA resource name is the serial port that the instrument is attached to. This variable is used by each function to identify the port through which the instrument is being used. The function VISA Close was used to end the VISA session once the instrument finished its task. Figure 15 shows the code that was used to close a VISA session.

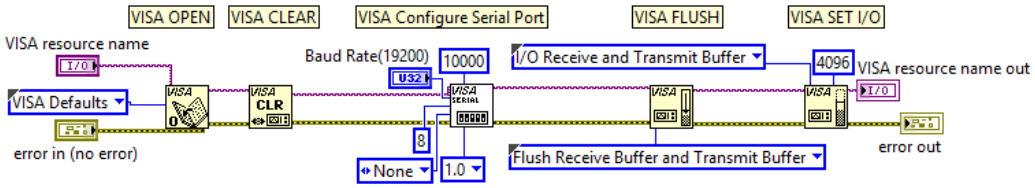

Figure 14. Opening a VISA session and configuring the serial port.

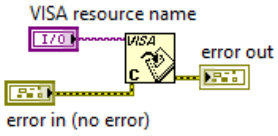

Figure 15. Closing a VISA session once done with the instrument.

The NE-500 program was designed to be able to control up to three pumps each with an address of 0, 1, and 2, respectively. The program could control a singular pump or multiple pumps in a network. When broken down into components, the program utilized the following seven functions to communicate with and control the NE-500: initialize serial port, set inner diameter (ID) of syringe, set pumping rate, set volume to be dispensed, run pump, and close serial port.

The program assumed that a B-D 60 ml syringe with an ID of 26.7 mm was loaded onto the NE-500 (Table 8). The code created for the function set inner diameter function is shown in Figure 16. By setting the ID of the syringe to a value greater than 10 mm, all units when dealing with volume are automatically set to ml. The pumping rate was set to 25 $ml \cdot min^{-1}$, just shy of its maximum pumping rate of 28 $ml \cdot min^{-1}$ (Table 8). The code created for the function set pumping rate is shown in Figure 17. The volume to be dispensed by the NE-500 was designed as an input to be set by the user in the UI during instrument operation. The code created for the function set volume to be dispensed is shown in Figure 18. The activation of the NE-500 was an input to be selected by the user in the UI during instrument operation. The code created for the function run pump is shown in Figure 19.

The program takes each of these parameters and passes the command along to the pump sequentially by using the function VISA write. A wait function was used to pause the program for 50 milliseconds after each VISA write function was executed. This pause allows the instrument sufficient time to process the command. When a command has been successfully processed, the common response from the pump will be

00X, where 00 is the instrument's address and X is some combination of ASCII characters interpreted as an instrument response. The function VISA read (Figure 20) was utilized to acquire the instrument response and display it to the user.

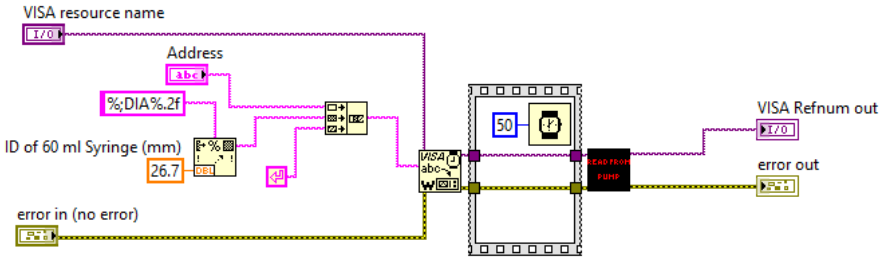

Figure 16. Using the DIA command to set the ID of the syringe.

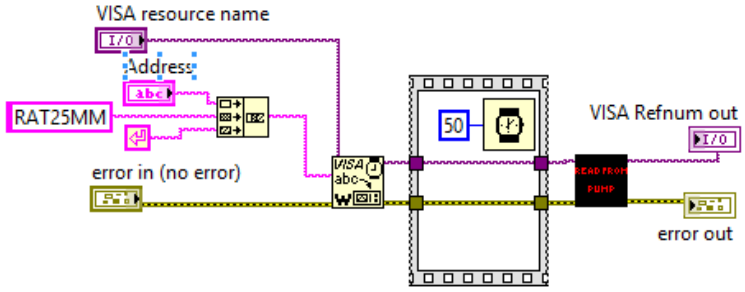

Figure 17. Using the RAT command to set the pumping rate to 25 mm·min^{-1}.

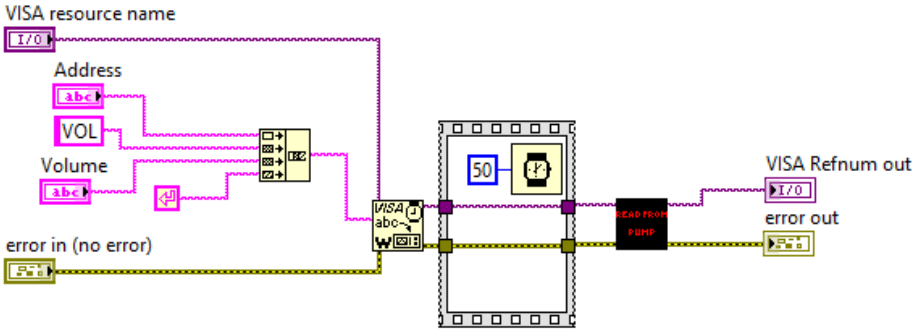

Figure 18. Using the VOL command to set the dispensing volume with an input set by the user.

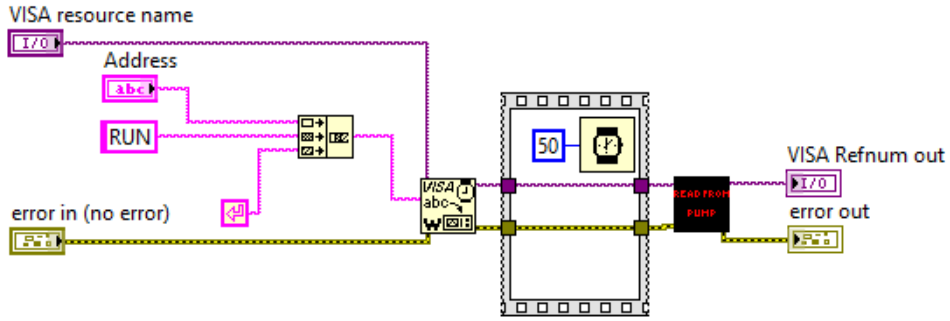

Figure 19. Using the RUN command to start the pump.

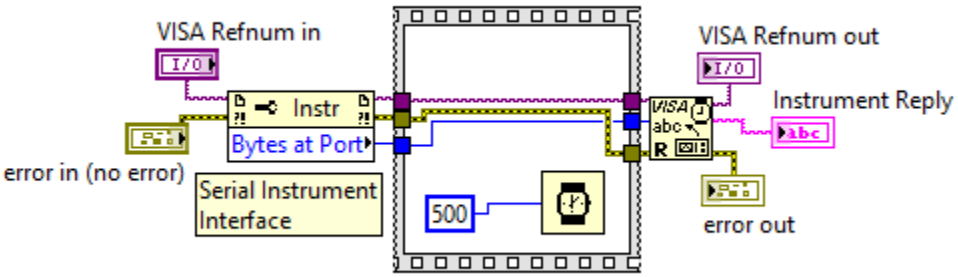

Figure 20. Using the VISA read function to read the instrument response and display it to the user through the variable Instrument Reply.

The HEATER-KIT-1LG program was designed to be able to control up to two heaters each with an address of 3 and 4, respectively. The program could control a singular heater or a heater connected into the same network as the NE-500 pumps. When broken down into components, the program utilized the following seven functions to communicate with and control the HEATER-KIT-1LG: initialize serial port, set heater setpoint, set heater units, start heater, query heater temperature, stop heater, and close serial port. The program sets the heating setpoint to a pre-determined temperature that acts as a constant within the programming. The code created for the function set heater

setpoint is shown in Figure 21. The temperature of the heater was set to 110 °C with this function. The code created for the function set heater units is shown in Figure 22. The activation of the HEATER-KIT-1LG was designed as an input to be set by the user in the UI during instrument operation. The code created for this function is identical to Figure 19. While the instrument was activated, the program began a timer and continuously queried the temperature of the heating pad from the instrument (Figure 20). The code created for the function query heater temperature is shown in Figure 23. The deactivation of the HEATER-KIT-1LG was designed as an input to be set by the user in the UI during instrument operation. The code created for the function stop heater is shown in Figure 24.

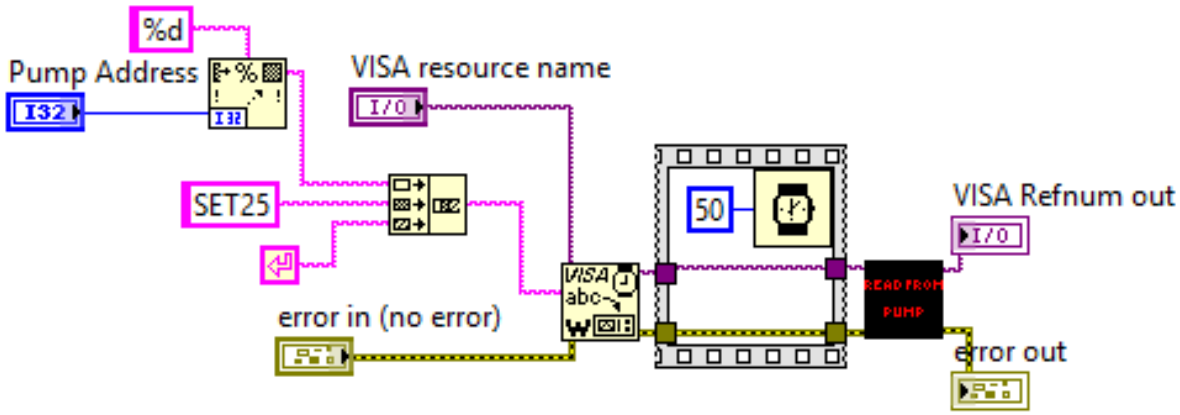

Figure 21. Using the SET command to set the heating setpoint.

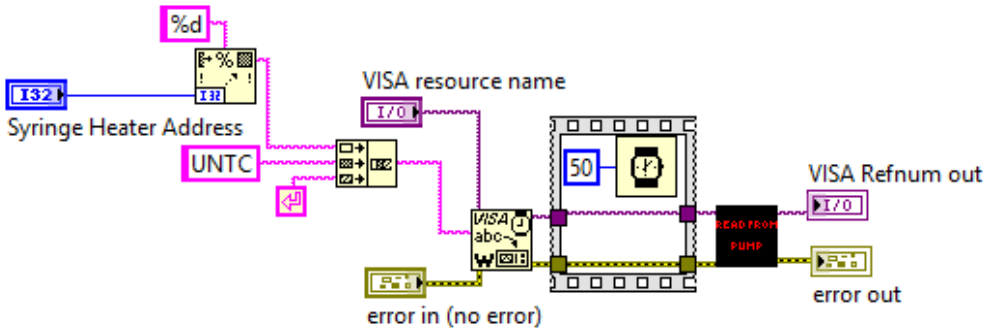

Figure 22. Using the UNT command to set the units to Celsius.

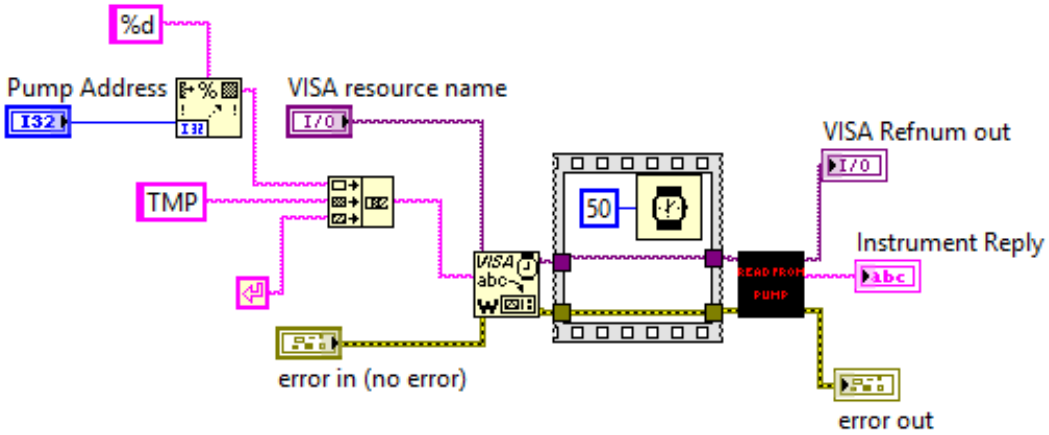

Figure 23. Using the TMP command to query the current temperature of the heating pad.

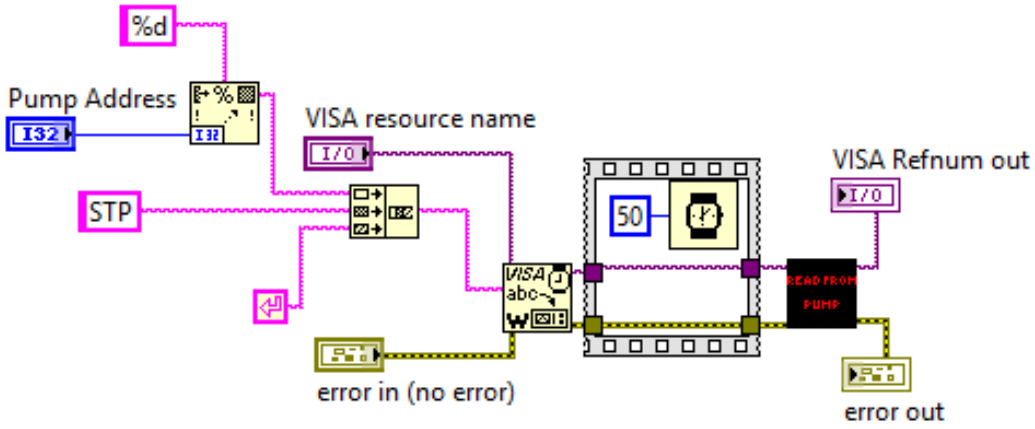

Figure 24. Using the STP command to deactivate the heater.

The USB-6501 program can only control one device at a time. This device did not require an address because it was not part of a network. The UI organizes the 24 channels into 3 different ports, labeled 0-2, with eight channels each, labeled 0-7. The labels for all ports and channels were labeled to conveniently correspond with the pin assignments on the physical device (Table 9). It was designed such that each channel in the UI had its own trigger switch that could be triggered by the user during normal instrument operation. The trigger switch had a true/false value that dictated the on/off state of its channel, respectively. When triggered by the user, an LED indicator next to the channel was designed to provide visual confirmation for the on/off state of the channel.

Each of the three ports were arranged into their own array. These arrays held the true/false values for each of the trigger switches. A looping algorithm was utilized to check each of the true/false values for each of the 8 channels in each port. Two things occurred after this point. First, if true the LED indicator for that trigger switch was turned on and if false, the LED indicator was turned off. Second, the true/value values for each trigger switch were sequentially placed back into an array that was passed to the DAQ Assistant. The DAQ Assistant will take these inputs for each port and automatically generate code that applies the inputs to the USB-6501 and change the physical state of each respective channel.

Figure 25 shows the code for implementing this described method of controlling the USB-6501. To verify that the program successfully controlled the USB-6501, an experiment with LED's was conducted. A simple circuit was constructed with the use of

24 LED's where red, yellow, and green correspond to ports 0, 1, and 2, respectively. Figure 26 shows the results of this experimental setup. Figure 27 shows a simultaneous view of the UI of the program used to control this experimental set. Upon close inspection, it can be observed that the active or green LED channels in the USB-6501 program correctly matched the lit LEDS of experimental setup.

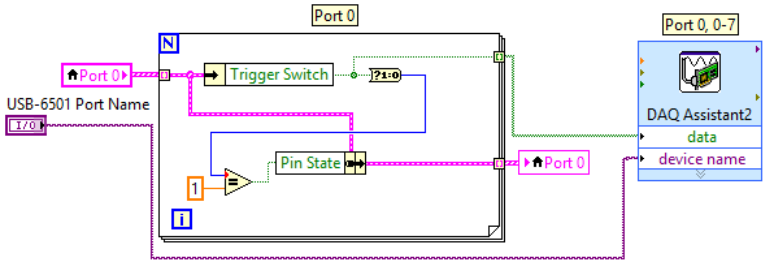

Figure 25. The code used to implement the DAQ Assistant in controlling channels 0-7 on Port 0 of the USB-6501.

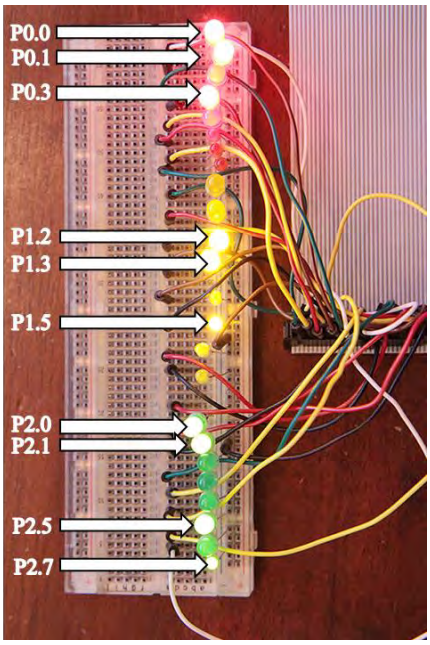

Figure 26. Each LED is attached to a channel on the USB-6501. The ports 0, 1, and 2 are red, yellow, and green, respectively. The lit LEDs correspond to the active channels in Figure 27.

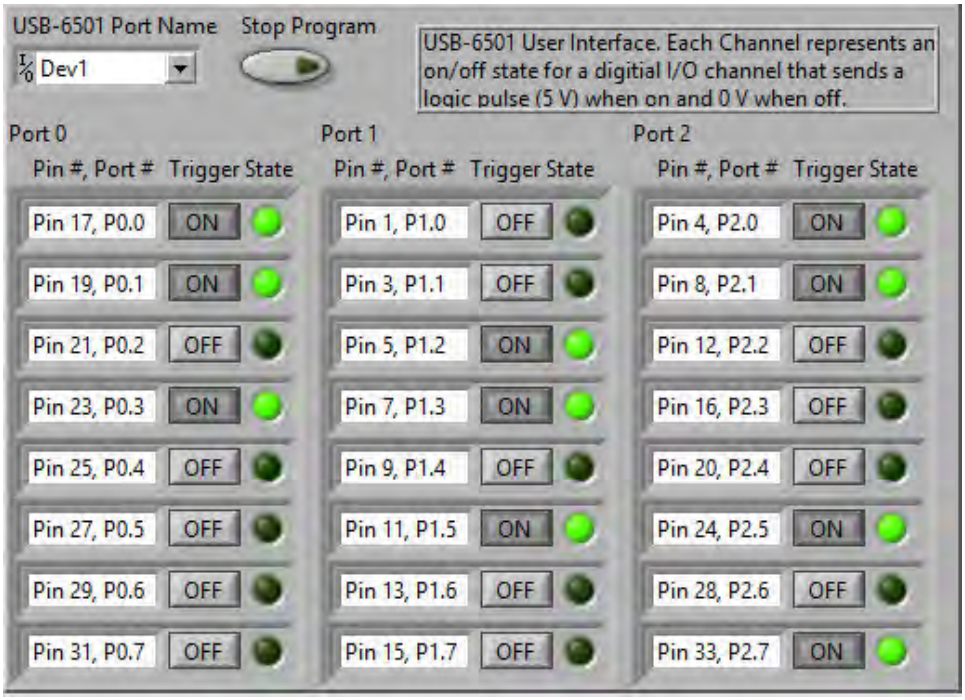

Figure 27. The USB-6501 program that is controlling the 24 LEDs found in Figure 26. Each active channel corresponds to a lit LED.

A fourth program was developed to manually assign an address to any instrument directly connected to the computer. This was done by initializing the serial port, selecting a numerical address, using the ADR command with VISA write to send the address to the instrument, and closing the serial port. The programming is nearly identical to that shown previously for the other programs. This program was necessary to set addresses to instruments prior to being placed in a network.

3.2 Discussion

3.2.1 Optimizing ^{62}Zn Production

The maximum proton entry energy considered relevant towards producing ^{62}Zn while minimizing the yield of other contaminants is 30 MeV. With an proton entry energy of 30 MeV, a copper foil thickness of 1.0 mm will result in a proton exit energy of 17.14 MeV. Between 17.14 and 13.6 MeV, the cross-section for the ^{63}Cu(p,2n) reaction goes from approximately 40 to 3 mb, respectively. To reduce the energy of the proton beam to below the 13.6 MeV threshold for the ^{63}Cu(p,2n) reaction, a copper foil thickness of 1.2 mm is required. Given the small reaction cross-section area available between 1.0 and 1.2 mm, the average difference in ^{62}Zn yield between these two thicknesses is less than 6%. Beyond 1.2 mm, any increase in ^{62}Zn yield is negligible due to the proton beam being reduce to a level below the necessary threshold energy of 13.6 MeV. Given that the increase in ^{62}Zn yield is marginal between 1.0 and 1.2 mm, it was determined that the optimal target thickness was 1.0 mm.

Given that copper is a transition metal, all resulting contaminants are also transition metals. The chemical differences between the product and contaminants allow for easy separation with little difficulty. Given that the contaminants pose little concern towards the radionuclide purity of the final product, their primary concern comes from the necessary decay of the short-lived contaminants to safely handle the irradiated target after EOB. Thus, estimating the radiation exposure from the target at EOB provided the best method for determining how the entry energy affected the production of contaminants and more importantly, how it affected the cooling period.

Table 16 shows the dose equivalent rates calculated for each radionuclide, the total dose equivalent rate from the target for proton entry energies between 18 and 30 MeV. The results show that the short-lived contaminants, ^{63}Zn and ^{61}Cu, contribute entirely to the radiation exposure field around the target. For entry energies between 18 and 27 MeV the cooling period is 2 hours and between 28 and 30 MeV it is 1 hour. The decrease in cooling period at higher energies is due to the reduction in the production of ^{63}Zn. While ^{61}Cu is produced in a greater quantity at the higher energies, it contributes less to the radiation exposure around the target than ^{63}Zn. Additionally, the copper contaminant can easily be separated during chemical processing and does not affect the radionuclide purity of ^{62}Zn.

The respective cooling periods were used to decay correct the EOB production yields for all radionuclides (Table 17). This revealed a peak in the production yield of ^{62}Zn at a proton entry energy of 29 MeV. Given these results, the optimal proton entry energy for maximizing the production yield of ^{62}Zn is 29 MeV. Given these parameters, the maximum production yield calculated for ^{62}Zn was 175 MBq·μA^{-1}·h^{-1} (Table 17). Correcting for the 10% deviation from experimental measurements and accounting for an additional hour of decay due to processing, the maximum potential yield was between 160 and 180 MBq·μA^{-1}·h^{-1}.

This value represents the activity that is expected to be loaded onto a generator column after processing. According to Zweit et al., 1992, it is common for 2.0 GBq to be loaded onto the generator column and hold a sufficient shelf-life of 24-48 hours (Zweit et al., 1992). Given this, a beam current as low as 15 μA·hr would be sufficient to

produce a generator with a ^{62}Zn activity of 2.4 GBq. Thus, it was determined that 160 $MBq \cdot \mu A^{-1} \cdot h^{-1}$ could feasibly provide a generator system with a comparable shelf-life to the standard with a moderate beam current and irradiation time.

3.2.2 Alternative Target Processing Procedure

During the various stages of the dissolution of the copper foil with the 30% hydrogen peroxide and 2 M hydrochloric acid, various color changes of the solution were observed. The color changes were attributable to the copper(II) ions that were displaced into the solution during dissolution. The two colors blue and green were observed in the solution. The blue color is attributable the presence of the hexaaquacopper(II) ion, $[Cu(H_2O)_6]^{2+}$, that is formed when copper(II) ions are in aqueous solution (Rayner-Canham and Overton, 2003). The green color is attributable to the presence of the tetrachlorocuprate(II) ion, $[CuCl_4]^{2-}$, that is formed when copper(II) ions are in an aqueous solution containing a high concentration of chloride ions (Rayner-Canham and Overton, 2003). When diluted, the green solution will shift back to a blue solution. When a stronger concentration of hydrochloric acid was added to the solution, the blue solution shifted back to green.

This illustrated a clear demonstration of Le Châtelier's principle, which describes how the chemical dynamic equilibrium between the formations of different compounds shifts when conditions such as concentration or temperature are changed. In the case of the observed color changes with the aqueous solution containing copper(II) ions, the color shifted towards the formation of one copper complex or the other when these exact

conditions were changed. When water is added to the solution, the concentration of the chloride ions is diluted resulting in an equilibrium shift (Equation 4) to the right and a subsequent increase in the formation of hexaaquacopper(II) ions. When the concentration of chloride ions in the solution was increased, the excess Cl^- shifted the equilibrium (Equation 4) to the left resulting in an increase in the formation of tetrachlorocuprate(II) ions. These equilibrium shifts were responsible for the color changers to blue and green, respectively. This is most clearly illustrated with Equation 4 (Rayner-Canham and Overton, 2003).

$$[CuCl_4]^{2-}_{(aq)} + 6\,H_2O_{(l)} \rightleftharpoons [Cu(H_2O)_6]^{2+}_{(aq)} + \ 4\,Cl^-_{(aq)} \qquad (4)$$

The results from the final solution obtained in Figure. 12d indicate that the hexaaquacopper(II) ion is formed in a 2 M HCl solution due to the blue color. Given that the chemical processing phase utilizes anion exchange chromatography to separate ^{62}Zn from the contaminants using their chloride complexes (Bormans et al., 1992; Robinson Jr et al., 1980) , the hexaaquacopper(II) ion in 2 M HCl is likely the correct copper(II) ion for chemical separation.

The objective in developing this alternative dissolution method was to reduce the volume of corrosive fumes generated during target processing. Given the concentration of hydrogen peroxide, the continued presence of lower concentration HCl, and the temperatures reached during dissolution, it cannot be said confidently that this objective was achieved without performing further experiments that provide evidence to support

such claims. However, it is reasonable to assume that the volume of corrosive fumes generated during target processing with the alternative method are reduced relative to the conventional one. The number of chemical steps involved to dissolve the copper target and form the chloride complexes are reduced from 3 with the conventional method to 1 with the alternative method. The quantity in which the corrosive fumes are reduced or eliminated with the alternative dissolution method will have to be measured in future studies.

The feasibility of implementing the alternative dissolution method into the overall generator production procedure was based upon achieving a dissolution time comparable to that of the conventional procedure. The use of concentrated acids result in the rapid dissolution of a copper target. The term rapid was never quantified in any of the previous studies, but it was interpreted that the dissolution time occurred on a time frame that did not impact the overall processing time of the generator system. Thus, it was assumed that conventional dissolution times were on average 2 minutes. With an average generator processing time of 60 minutes (Zweit et al., 1992), the conventional target processing procedure takes up 4% of the total processing time. Given this, the primary goal was to produce a alternative target processing procedure with the alternative dissolution method that could provide a comparable dissolution time that comprised approximately 4% of the total processing time.

It was determined that the best method for optimizing the use of hydrogen peroxide during the dissolution was to monitor the temperature of the solution. Due to the exothermic nature of the decomposition of hydrogen peroxide, it was assumed that

the temperature of the solution directly correlated to the amount of hydrogen peroxide available for dissolution of the copper foil. Preliminary experiments showed that the addition of hydrogen peroxide in either large quantities at one time or in small quantities too quickly resulted in an exponential increase of solution temperature. This led to the inefficient thermal decomposition of the hydrogen peroxide before it could dissolve the copper foil. It was quickly realized that the addition of hydrogen peroxide had to be controlled in a manner that reduced its thermal decomposition throughout the dissolution.

To completely dissolve a 1.0 g copper foil, 1.6 ml of 30% hydrogen peroxide is required. The use of large quantities of 30% hydrogen peroxide was discarded for a more favorable use of smaller quantities that were both adequate in completely dissolving the copper foil while simultaneously allowing for a better method in controlling the temperature of the solution. By incrementing the addition of hydrogen peroxide over set time intervals, fresh hydrogen peroxide is consistently added to the solution over a time frame that does not drastically impact the temperature of the solution. This method effectively minimized the thermal decomposition of hydrogen peroxide before it could react with the copper foil to dissolve it.

The alternative target processing procedure was detailed in the results and is summarized in Figure 13. A total of 12.0 ml of 30% hydrogen peroxide was used to dissolve the copper foil with the alternative procedure, and was added in increments of 1.0 ml. This is significantly more than the 1.6 ml required to completely dissolve the copper foil. The decision to use this amount was based on the difficulty in quantifying

how much hydrogen peroxide is actually lost through thermal decomposition during dissolution. Thus it was decided that a conservative amount of hydrogen peroxide should be added in each increment while maintaining a sufficiently small volume to remain in control of the solution temperature.

Using this method, the solution temperature peaked at approximately 75 °C after adding 7 ml of hydrogen peroxide over 3.5 minutes to the solution. The solution remained at this temperature for an additional 2.5 minutes after the last ml of hydrogen peroxide had been added. A decrease in temperature indicated that the solution needed to be refreshed with additional hydrogen peroxide. However, the temperature decreased at such a slow rate that any additional hydrogen peroxide added to the solution at that point would quickly raise the temperature above 75 ºC. To achieve a more effective control of the solution's temperature, the solution in DV1 was completely transferred to DV2. This allowed for the fresh addition of hydrochloric acid and hydrogen peroxide to DV1 to continue dissolution of the partially dissolved copper foil. This essentially resets the temperature of the solution and allows for a less restricted addition of hydrogen peroxide in the second half of the procedure.

This resulted in the addition of 5.0 ml of hydrogen peroxide over 2.0 minutes where the solution temperature peaked right under 70 °C. The copper foil was left to completely dissolve after this point. It is worth noting that 16 ml of 2 M HCl is required to completely dissolve a 1.0 g copper foil. A conservative 20 ml of 2 M HCl was utilized with this procedure where 10 ml was added at the start and again after the entire solution is refreshed. To put this in perspective, the conventional method typically utilized 25 ml

of hot 16 M HNO_3 and 25 ml of 12 M HCl completely dissolve the copper target and form the chloride complexes (Robinson Jr et al., 1980; Zweit et al., 1992).

With the alternative target processing procedure outlined in Figure 13, an average dissolution time of 12 minutes was achieved. Assuming a normal dissolution time of 2 minutes, this adds approximately 10 minutes to the 60 minute total processing time, extending it to 70 minutes. As a result, the alternative target processing procedure would consist of 17% of the total 70 minute processing time. Thus, the alternative target processing procedure did not meet the goal of comprising only 4% of the total processing time. However, this dissolution time is still considered very promising.

The current alternative procedure leaves considerable room for further optimization. The use of a glass thermometer provided a sufficient measurement of the solution's temperature for the purpose of reducing the dissolution time to a reasonable time frame. But, it lacked the necessary accuracy and temperature response to properly optimize the use of the hydrogen peroxide. With the use of a more sensitive temperature sensor and the utilization of a more precise method of delivering hydrogen peroxide to the solution, dissolution times could be reduced to less than 10% of the total processing time with the alternative target processing method. However, it is worth noting that regardless of the room for further optimization, a 70-minute processing time still remains viable when producing a generator system whose parent has a half-life of 9.186 hours.

3.2.3 Automating Procedural Processes

Four unique programs were developed in LabVIEW to remotely control the NE-500 (Figure 28), HEATER-KIT-1LG (Figure 29), and USB-6501 (Figure 30) through a computer interface. The fourth program was designed to assign an address to any instrument directly connected to the computer (Figure 31). The three programs were developed as a proof of concept that demonstrated the feasibility in controlling each of the three instruments through a remote-controlled interface. As a result, the development of these programs did not take into account any major error checking that would be required to be in compliance with any good manufacturing practices. Flow diagrams that depict the logic behind each program are shown in Appendix C.

Each of the three programs successfully automate the specific tasks given to each instrument, but only provide a means of semi-automating the overall generator production procedure. The goal was to provide a proof of concept that illustrated the feasibility in automating the overall generator production procedure. When discussing automation in this context, it can be defined as the complete automation of every step of generator production from start to finish without a requirement for any user input during operation. The use of three unique programs, all of which require user-input at critical junctions, to complete separate tasks throughout the procedure understandably fall short of full automation. However, they provided several useful results.

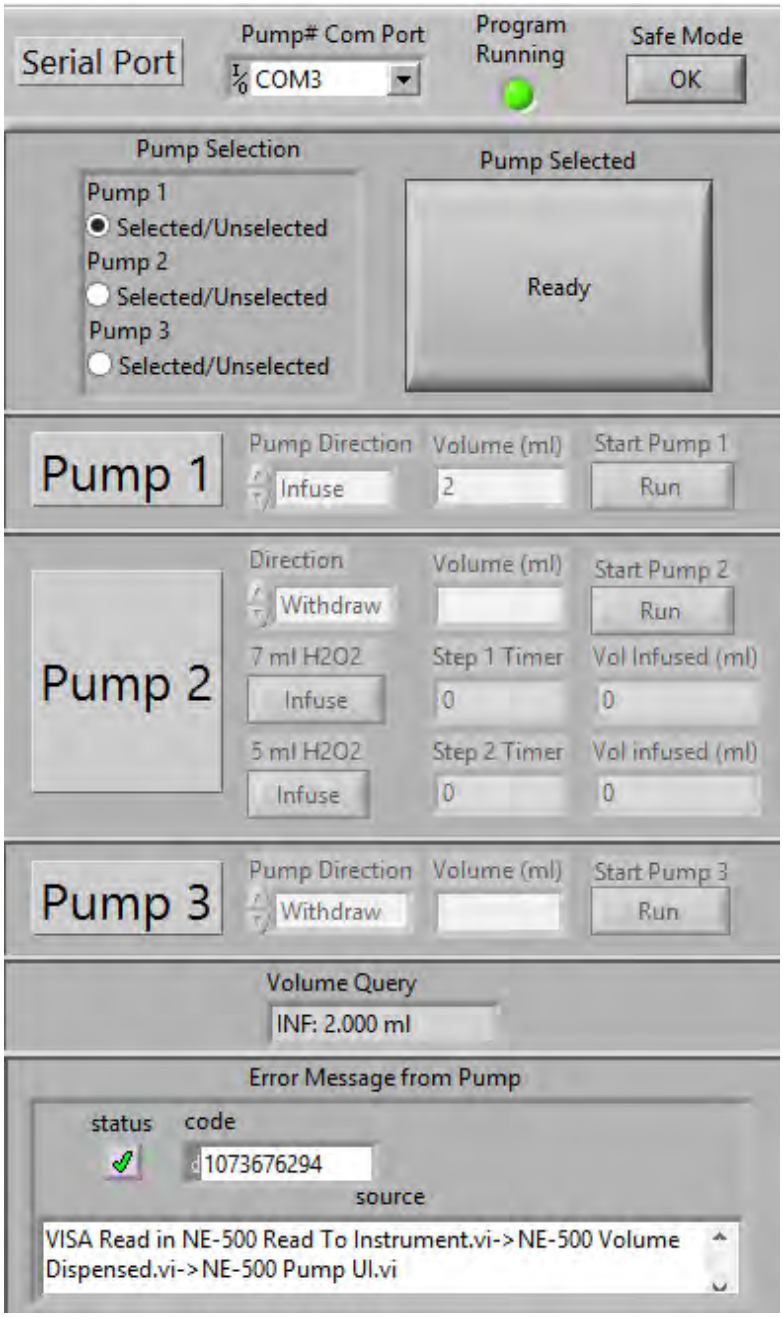

Figure 28. The user interface for the program that controls the NE-500.

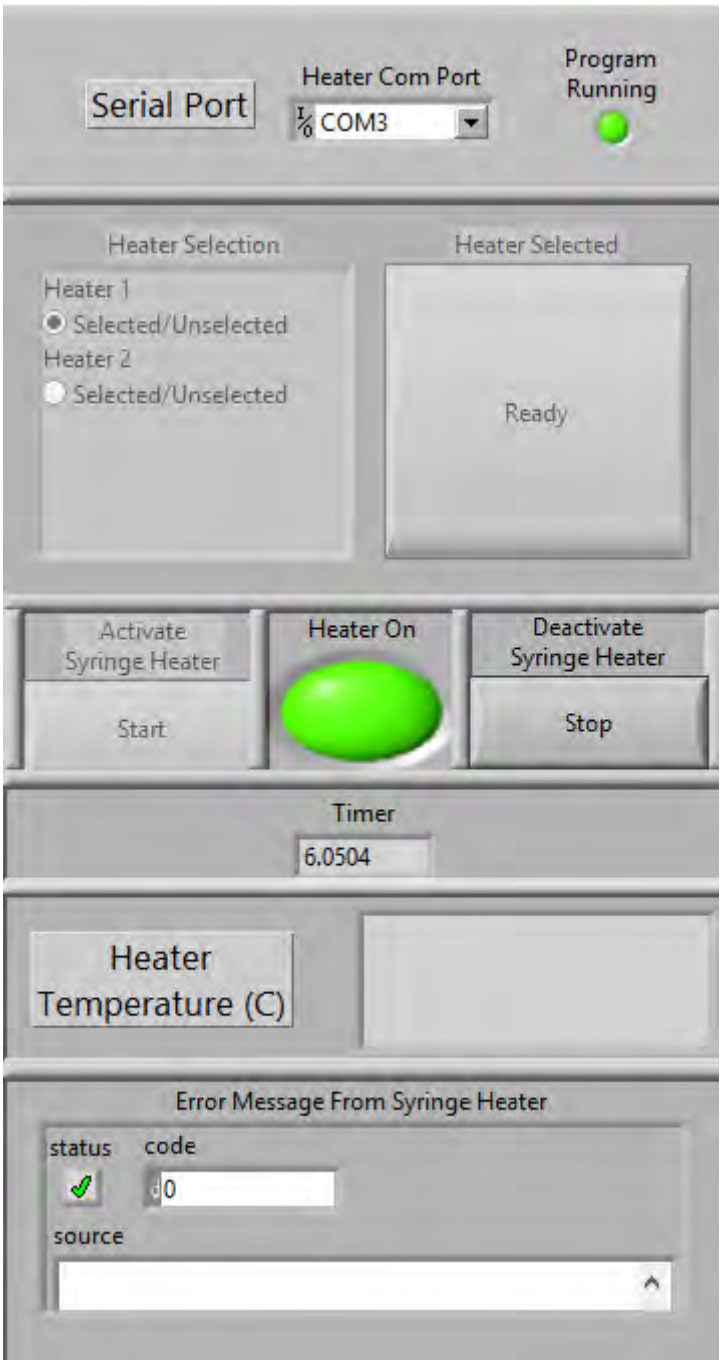

Figure 29. The user interface for the program that controls the HEATER-KIT-1LG.

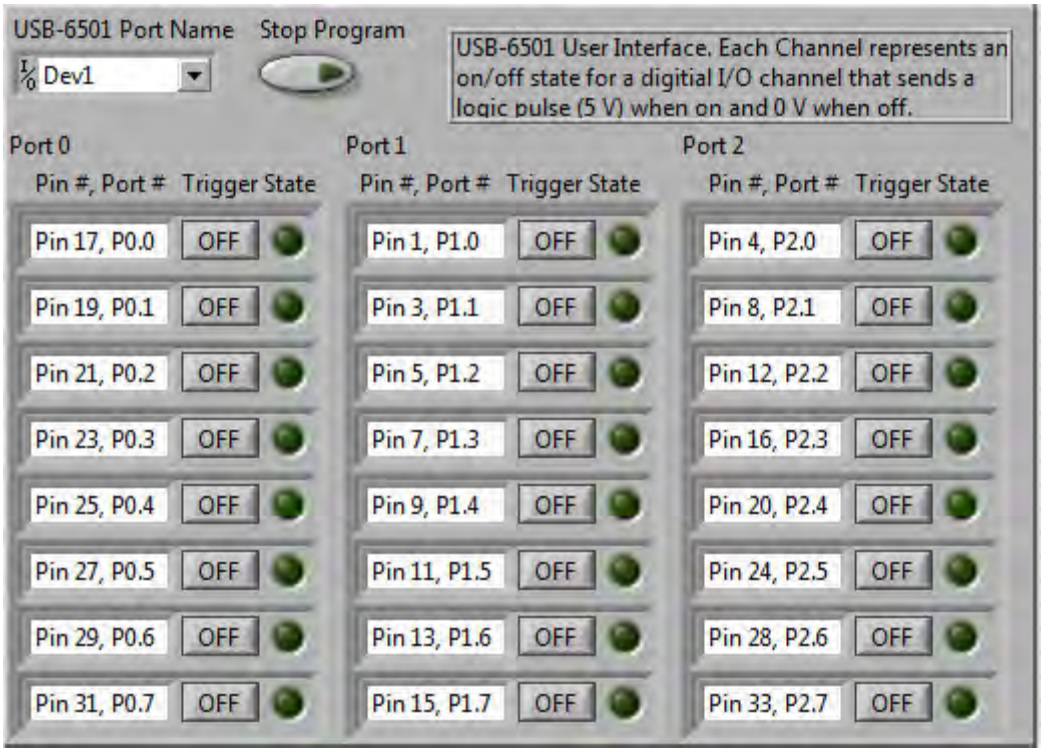

Figure 30. The user interface for the program that controls the USB-6501.

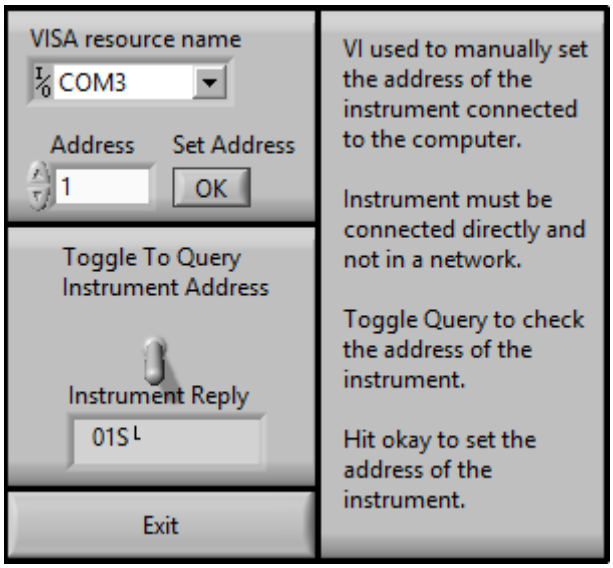

Figure 31. The user interface for the program that assigns addresses to instruments.

Firstly, it was discovered that LabVIEW could be used to successfully control the instruments. Figures 14-25 illustrate very clearly how LabVIEW is utilized to control the instruments and sufficiently provide a foundation to design more complex programs around. Secondly, the use of separate programs was a simple method of illustrating that multiple instruments could be used simultaneously. For example, the HEATER-KIT-1LG program could heat a solution simultaneously while fluids were transferred from one vessel to another with the NE-500 program. Thirdly, a small portion of the procedure outlined in Figure 13 was fully automated in the NE-500 Program. The addition of hydrogen peroxide was broken up into total volumes of 7 ml during the first half of the procedure and 5 ml during the second half. Once the program has acquired an input from the user, it will start a timer, add 1 ml of hydrogen peroxide, and continue to add an additional 1 ml every 30 seconds until 7 ml has been added. The program will then wait for an additional 2.5 minutes before it requests another input from the user to proceed to the next step. The same sequence of steps will occur for adding 5 ml of hydrogen peroxide as well. A timer is visible throughout the automated sequence to provide the user with a visual indication of progression of the procedure. This showcased the feasibility in implementing more complex, automated algorithms utilizing the instrument control functions outlined in Figures 14-25.

These results provide a successful proof of concept for the feasibility in creating a system that can automate the production of the $^{62}Zn/^{62}Cu$ generator systems. Incorporating all these different results into one program is the next logical step towards producing a software that is capable of total automation. This will require characterizing

very well every single step of the overall generator production procedure, isolating all constants, and ensuring variables that fluctuate remain within expected levels. The system itself will ideally adopt a modular design. This design criteria went into the decision behind purchasing each of the three instruments. They are either compact or purchased as an OEM version which include mountable chasses for the feasible implementation into a modular system. The use of modular is intended to imply that the system will be self-contained and capable of operating regardless of its location. This gives the system a measure of flexibility in its implementation.

4. SUMMARY AND RECOMMENDATIONS

4.1 Conclusion

The purpose of this study was to provide a foundation for mass producing $^{62}Zn/^{62}Cu$ generator systems. Firstly, this was approached by developing a method that considered all irradiation parameters. It was identified that the target thickness and proton entry energy impacted the production yield of ^{62}Zn the greatest. The optimal target thickness and proton entry energy for maximizing the production of ^{62}Zn is 1.0 mm, and 29 MeV, respectively. Using estimated radiation exposure values for these parameters, the cooling period for the target was calculated to be 1 hour. A maximum theoretical ^{62}Zn yield of 160 $MBq \cdot \mu A^{-1} \cdot h^{-1}$ after the 1 hour cooling period was calculated. The $^{65}Zn/^{62}Zn$ ratio was calculated to be 0.3% at proton entry energies of 29 MeV. Conveniently, despite the use of a smaller target, theoretically equivalent production yields can be achieved with 29 MeV protons. This is an energy well suited for a medium energy cyclotron.

Secondly, an alternative target processing method was developed that successfully dissolved a copper foil with the use of 30% hydrogen peroxide and 2 M hydrochloric acid. This alternative method ideally reduces or eliminates entirely the total amount of corrosive fumes generated during the target processing phase. Eliminating or simply reducing the volume of corrosive fumes will effectively reduce the damage delivered to the equipment in radiochemistry facilities as a direct result of dissolving the irradiated copper target. The color of the solution was used to determine that the copper(II) ions had correctly formed the hexaaquacopper(II) ion in a 2 M HCl solution

necessary for separation from ^{62}Zn. Additionally, an alternative target processing procedure was developed with this method that yielded a dissolution time of 12 minutes. This dissolution time consisted of approximately 17% of an overall processing time of 70 minutes. Given this, it can be determined that a generator production procedure that implements the alternative target processing method would be better optimized towards routinely producing ^{62}Zn/^{62}Cu generator systems.

Thirdly, software was developed in LabVIEW for controlling specific instruments for the purpose of showing that the generator production procedure could be automated. The instruments NE-500, HEATER-KIT-1LG, and USB-6501 were utilized to automate the transfer of fluids, heating of solutions, and electronic manipulation of valves, respectively. The software was able to successfully demonstrate that the hardware components were successfully controlled with LabVIEW and performed their roles as intended. Specific instructions were created on how to control the three instruments with LabVIEW and can be utilized to develop a more complex program with the intent to fully automate the entire production process. The instruments, NE-500 and USB-6501, purchased as OEM versions both have mountable chassis' that can feasibly be implemented into a modular system. The HEATER-KIT-1LG was not purchased as an OEM version, but maintains dimensions that are small enough to be implemented into a modular system with some innovative engineering.

4.2 Future Work

Future work will involve verifying, optimizing, and implementing the results of this study towards the routine production of $^{62}Zn/^{62}Cu$ generator systems. The first step is verifying that the volume of corrosive fumes generated with the alternative target processing method have been Eliminated. If they have not been eliminated effectively, their quantity should be measured to provide an estimate of the expected damage to be incurred on equipment due to target processing in a radiochemistry facility.

The second step will be in establishing and optimizing the production of ^{62}Zn. It should be determined if a ^{62}Zn production yield of 180 $MBq \cdot \mu A^{-1} \cdot h^{-1}$is not just theoretically possible but physically as well. The production runs should also establish what the ideal beam current and irradiation time should be, as both are subject to manipulation according to the size of the target. Next, the alternative target processing procedure should be optimized to reduce the total dissolution time to below 10 minutes. Currently, this procedure will add an additional 10 minutes to the total processing time. It is worth the effort to optimize this method to achieve better dissolution times.

Lastly, the proof of concept showed that automating the generator production process with the use of a remote controlled modular system was possible. There are three important steps following this study that must be taken. The first is to characterize the generator production procedure very precisely. The second is to take this information and develop a new LabVIEW program that incorporates all of the instruments into one interface. This program should be capable of fully automating the production procedure from start to finish without the need for any user input. The third step is to develop a

physical prototype of the system. This will be crucial for troubleshooting and testing the LabVIEW program as LabVIEW cannot provide any simulated results. Instead, it must be attached to physical instruments or hardware to provide feedback on any software that is being developed.

REFERENCES

Agency, I.A.E., 2009a. Cyclotron produce radionuclides: guidelines for setting up a facility, Technical reports series (International Atomic Energy Agency) ; no. 471. Technical Reports Series, Vienna : International Atomic Energy Agency.

Agency, I.A.E., 2009b. Cyclotron produced radionuclides: princples and practice, Technical reports series (International Atomic Energy Agency) ; no. 465. Tech. Rep, Vienna : International Atomic Energy Agency

Bailey, D.L., Townsend, D.W., Valk, P.E., Maisey, M.N., 2005. Positron emission tomography. Springer.

Beanlands, R., Muzik, O., Mintun, M., Mangner, T., Lee, K., Petry, N., Hutchins, G.D., Schwaiger, M., 1992. The kinetics of copper-62-PTSM in the normal human heart. Society of Nuclear Medicine 33, 684-690.

Bilewicz, A., 2006. Separation of Sr-82 from rubidium target for preparation of Sr-82/Rb-82 generator. Journal of Radioanalytical and Nuclear Chemistry 268, 485-487.

Blower, P., Blower, J., Lewis, J., 1996. Copper radionuclides and radiopharmaceuticals in nuclear medicine. Nuclear Medicine and Biology 23, 957-980.

Bormans, G., Bormans, A., Janssen, P., Adriaens, D., Crombez, A., Witsenboer, J., de Goeij, L., Mortelmans, A., 1992. A 62Zn/62Cu generator for the routine production of 62Cu-PTSM. International Journal of Radiation Applications and Instrumentation. Part A, Applied radiation and isotopes 43, 1437-1441.

Coleman, R.E., 1988. Positron emission tomography: clinical status in the United States in 1987. The Journal of Nuclear Medicine 29, 1136-1143.

Fujibayashi, Y., 1989. A new zinc-62/copper-62 generator as a copper-62 source for PET radiopharmaceuticals. The Journal of Nuclear Medicine 30.

Fujibayashi, Y., 1990. 62 Cu-labeling of human serum albumin-dithiosemicarbazone (HSA-DTS) conjugate for regional plasma volume measurement: Application of new 62 Zn/ 62 Cu generator system. Chemical and Pharmaceutical Bulletin 38, 1946-1948.

Fukumura, T., 2006. An improved 62Zn/62Cu generator based on a cation exchanger and its fully remote-controlled preparation for clinical use. Nuclear medicine and biology 33, 821-827.

Green, M.A., 1987. A potential copper radiopharmaceutical for imaging the heart and brain: Copper-labeled pyruvaldehyde bis(N4-methylthiosemicarbazone). International Journal of Radiation Applications and Instrumentation. Part B. Nuclear Medicine and Biology 14, 59-61.

Green, M.A., Klippenstein, D.L., Tennison, J.R., 1988. Copper (II) bis (thiosemicarbazone) complexes as potential tracers for evaluation of cerebral and myocardial blood flow with PET. J Nucl Med 29, 1549-1557.

Green, M.A., Mathias, C.J., Welch, M.J., McGuire, A.H., Perry, D., Fernandez-Rubio, F., Perlmutter, J.S., Raichle, M.E., Bergmann, S.T., 1990. Copper-62-labeled pyruvaldehyde bis(N sup 4 -methylthiosemicarbazonato)copper(II): Synthesis and evaluation as a positron emission tomography tracer for cerebral and myocardial perfusion. Journal Name: Journal of Nuclear Medicine; (United States); Journal Volume: 31:12, Medium: X; Size: Pages: 1989-1996.

Grütter, A., 1982. Excitation functions for radioactive isotopes produced by proton bombardment of Cu and Al in the energy range of 16 to 70 MeV. Nuclear Physics A 383, 98-108.

Gul, K., 2001. Calculations for the excitation functions of the 63Cu(p,n)63Zn, 63Cu(p, 2n)62Zn and 65Cu(p,n)65Zn reactions. Applied Radiation and Isotopes 54, 147-151.

Haddad, P.R., 1994. Ion chromatography. Handbook on Metals in Clinical and Analytical Chemistry, 135.

Haynes, N.G., Lacy, J.L., Nayak, N., Martin, C.S., Dai, D., Mathias, C.J., Green, M.A., 2000. Performance of a 62Zn/62Cu Generator in Clinical Trials of PET Perfusion Agent 62Cu-PTSM, Journal of Nuclear Medicine, pp. 309-314.

Keppler, J.S., Conti, P.S., 2001. A cost analysis of positron emission tomography. American Journal of Roentgenology 177, 31-40.

Kraus, K.A., 1953. Anion exchange studies. VI. The divalent transition elements manganese to zinc in hydrochloric acid. Journal of the American Chemical Society 75, 1460-1462.

Lebowitz, E., Richards, P., 1974. Radionuclide generator systems, Seminars in nuclear medicine. Elsevier, pp. 257-268.

Mathias, C.J., Welch, M.J., Raichle, M.E., Mintun, M.A., Lich, L.L., McGuire, A.H., Zinn, K.R., John, E.K., Green, M.A., 1990. Evaluation of a potential generator-produced PET tracer for cerebral perfusion imaging: single-pass cerebral extraction measurements and imaging with radiolabeled Cu-PTSM. Society of Nuclear Medicine 31, 351-359.

Qaim, S.M., 2011. Development of novel positron emitters for medical applications: nuclear and radiochemical aspects. Radiochimica Acta 99, 611-625.

Qaim, S.M., 2012. The present and future of medical radionuclide production. Radiochimica Acta 100, 635-651.

Rayner-Canham, G., Overton, T., 2003. Descriptive inorganic chemistry. Macmillan.

Robinson Jr, G.D., Zielinski, F.W., Lee, A.W., 1980. The zinc-62/copper-62 generator: A convenient source of copper-62 for radiopharmaceuticals. The International Journal of Applied Radiation and Isotopes 31, 111-116.

Rowshanfarzad, P., Sabet, M., Reza Jalilian, A., Kamalidehghan, M., 2006. An overview of copper radionuclides and production of 61Cu by proton irradiation of natZn at a medical cyclotron. Applied Radiation and Isotopes 64, 1563-1573.

Schiepers, C., Hoh, C.K., 2006. FDG-PET Imaging in Oncology, Diagnostic Nuclear Medicine. Springer, pp. 185-204.

Shleien, B., Terpilak, M.S., 1992. The health physics and radiological health handbook.

Smith, R.M., Martell, A.E., 1975. Critical stability constants. Springer US.

Soppera, N., Bossant, M., Dupont, E., 2014. JANIS 4: an improved version of the NEA java-based nuclear data information system. Nuclear Data Sheets 120, 294-296.

Turner, J.E., 2008. Atoms, radiation, and radiation protection. John Wiley & Sons.

Yamamoto, Y.L., 1984. Positron emission tomography. Radiation Physics and Chemistry 24, 385-403.

Yokoyama, A., Hosotani, T., Arano, Y., Horiuchi, K., 1986. Development of neutral and bifunctional radiopharmaceuticals using 62Cu-dithiosemicarbazone (DTS) chelate-basic studies on 64Cu chelates. Radioisotopes 35, 249-255.

Ziegler, J.F., 2004. SRIM-2003. Nuclear Instruments and Methods in Physics Research 219, 1027-1036.

Zweit, J., Zweit, R., Goodall, M., Cox, J., Babich, G., Potter, H., Sharma, R., 1992. Development of a high performance zinc-62/copper-62 radionuclide generator for positron emission tomography. European Journal of Nuclear Medicine 19, 418-425.

APPENDIX A

MATLAB FUNCTIONS FOR PRODUCTION YIELD, DOSE RATE, AND COOL DOWN PERIOD CALCULATIONS.

```
function MainFunction()

%*********************************************************%
%*******PARAMETERS TO BE ADJUSTED FOR CALCULATIONS********%
beamCurrent = 25; %uA
n = (6.022E23/63.546); %Describes Target Thickness [atoms/g]
I = (beamCurrent*1E-6)/1.602E-19; %Beam Current for 1 uA [1/s]
time = 1; %Irradiation Time [Hr]
thickness = 1.0; %Target Thickness [mm]
Ei = [18,19,20,21,22,23,24,25,26,27,28,29,30]; %Range of entry energies
[MeV]
leadThickness = 5; %Lead Shielding Thickness [cm]
distance = 100; %Distance measured from point source [cm]
federalLimit = 20; %Federal Regulatory Limit of uSv/Hr
%*********************************************************%
%*********************************************************%

%Stopping power was taken from SRIM
%StpPwr for Copper
enStpPwr = xlsread('CopperStpPwr.xlsx','A1:A92');%[MeV]
StpPwr = xlsread('CopperStpPwr.xlsx','B1:B92');%[MeV-cm^2/g]

%Energy and Cross Section columns for each radionuclide in the excel
spread sheet.
%Cross Sections were taken from JANIS. TENDL 2013
%Ordered by the following: Zn-62, Zn-63, Zn-61, Cu-61, Co-58, Zn-65,
Cu-64
energy_column = {'A2:A46', 'C2:C46', 'E2:E46',
'G2:G46','I2:I46','K2:K46','M2:M46'};
cs_column =
{'B2:B46','D2:D46','F2:F46','H2:H46','J2:J46','L2:L46','N2:N46'};

%Mass Attenuation Factors for Tissue, taken from NIST
enTissue = xlsread('tissueattenuationfactors.xlsx','A1:A44'); %[MeV]
attenuationTissue = xlsread('tissueattenuationfactors.xlsx','B1:B44');
%[cm^2/g]

%Linear Attenuation Factors for Lead, taken from NIST
enLead = xlsread('leadattenuationfactors.xlsx','A1:A49'); %[MeV]
attenuationLead = xlsread('leadattenuationfactors.xlsx','B1:B49');
%[cm^-1]

%Spline function interpolates a value (CrsSec/StpPwr)
```

```
%From an energy value input. Use
ppval(Function_Name,Projectile_Energy).
FStpPwr = spline(enStpPwr, StpPwr);

%Spline function interpolates a value from an energy input. Returns an
%attenuation value for tissue.
FTissue = spline(enTissue,attenuationTissue);
FLead = spline(enLead,attenuationLead);

zinc_sixtytwo_en = xlsread('EnergyAndYield.xlsx','A3:A33');
zinc_sixtytwo_y = xlsread('EnergyAndYield.xlsx','B3:B33');

zinc_sixtythree_en = xlsread('EnergyAndYield.xlsx','C3:C68');
zinc_sixtythree_y = xlsread('EnergyAndYield.xlsx','D3:D68');

zinc_sixtyone_en = xlsread('EnergyAndYield.xlsx','E3:E48');
zinc_sixtyone_y = xlsread('EnergyAndYield.xlsx','F3:F48');

cop_sixtyone_en = xlsread('EnergyAndYield.xlsx','G3:G33');
cop_sixtyone_y = xlsread('EnergyAndYield.xlsx','H3:H33');

cob_fiftyeight_en = xlsread('EnergyAndYield.xlsx','I3:I5');
cob_fiftyeight_y = xlsread('EnergyAndYield.xlsx','J3:J5');

zinc_sixtyfive_en = xlsread('EnergyAndYield.xlsx','K3:K5');
zinc_sixtyfive_y = xlsread('EnergyAndYield.xlsx','L3:L5');

cop_sixtyfour_en = xlsread('EnergyAndYield.xlsx','M3:M3');
cop_sixtyfour_y = xlsread('EnergyAndYield.xlsx','N3:N3');


%Decay constant
%Ordered by the following: Zn-62, Zn-63, Zn-61, Cu-61, Co-58, Zn-65,
Cu-64
decayConstant = [7.54E-2, 1.08, 28, 2.08E-1, 4.07E-4, 1.183E-4, 5.46E-
2]; %[h^-1]


%For loop that calculates the front term of the production rate
equation
%for each radionuclide.
%Ordered by the following: Zn-62, Zn-63, Zn-61, Cu-61, Co-58, Zn-65,
Cu-64
for i=1:7
    frontTerm(i) = n*I*(1-exp(-decayConstant(i)*time));
end

for j=1:length(Ei)
    %Function energyDeposition calculates the rate of energy loss of
projectile
```

```
    %as it travels through the target, with inputs: initial energy and
target
    %thickness, and returns the values to an array enDep.
    enDep = energyDeposition(Ei(j),thickness);

    %Loop that calculates the energy difference between the energy
    %deposited every 30 microns in the target
    for i = 1:length(enDep)-1
        enDiff(i) = enDep(i)-enDep(i+1);
    end

    %Loop that calculates the Zn-62 production yield for each energy
fraction
    %Also calculates the production of the listed impurities.
    %Ordered by the following: Zn-62, Zn-63, Zn-61, Cu-61, Co-58, Zn-
65, Cu-64
    for i=1:7
        sum = 0; %Initialize
        %Load the energy and cross section from spreadsheet
        en =
xlsread('ReactionCrossSections.xlsx',char(energy_column(i)));%[MeV]
        CrsSec =
xlsread('ReactionCrossSections.xlsx',char(cs_column(i)));%[cm^2]
        %Setup a spline function to interpolate a cross-section for
each energy
        %of the proton as it travels through the copper target.
        FCrsSec = spline(en, CrsSec);
            %Second loop that calculates the yield at each section of
energy
            %deposition and then adds the value to each previous value
            %calculated. This is the equivalent of performing the
integral over
            %the entire cross-section curve.
            for k = 1:length(enDep)-1;
                %Calculates the cross section times difference between
the
                %energy being deposited in each section.
                a = ppval(FCrsSec,enDep(k))*enDiff(k); %[MeV-cm^2]
                %Calculates the stopping power for the proton with a
given
                %energy at each section
                b = ppval(FStpPwr,enDep(k)); %[MeV-cm^2/g]
                %c is the production yield calculated.
                c = ((frontTerm(i)*a)/b); %[Bq]
                sum = sum + c;
            end
            %Error checking to ensure that the yield was calculated
correctly.
            if sum > 0
                ProductionYield(j,i) = (sum/1E6)/(beamCurrent*time);
%[MBq/uA-h]
            elseif sum < 0
```

```
                ProductionYield(j,i) = 0;
            end
    end

%     Calculating the dose rate for each radionuclide at a distance r
away
%     from a point source gamma emitter at end of bombardment (EOB).
Each
%     individual dose rate is then summed to acquire a total dose rate
for
%     the entire target at a distance r. This is done for every single
%     initial energy selected in the array previously.
%
**********************************************************************
%     NOTE: The dose rate is converted from Rad to Rem assuming a
quality
%     factor of 1 for gamma-rays.
%
**********************************************************************

    sum = 0;
    %Calculating dose rate for Zinc-62
    for i=1:length(zinc_sixtytwo_en)
        energy = zinc_sixtytwo_en(i);
        yield = zinc_sixtytwo_y(i);
        mu = ppval(FLead,energy);
        mfp = mu*leadThickness;
        B = Buildup(energy,mfp);
        if B<0
            B=1;
        end
        sum = sum +
((ProductionYield(j,1)*beamCurrent*1E6*time*yield*energy)/(4*pi()*dista
nce^2))*ppval(FTissue,energy)*B*exp(-mfp)*0.577; %[uSv/hr]
    end
    doseRate(j,1) = sum

    sum = 0;
    %Calculating dose rate for Zinc-63
    for i=1:length(zinc_sixtythree_en)
        energy = zinc_sixtythree_en(i);
        yield = zinc_sixtythree_y(i);
        mu = ppval(FLead,energy);
        mfp = mu*leadThickness;
        B = Buildup(energy,mfp);
        if B<0
            B=1;
        end
        sum = sum +
((ProductionYield(j,2)*beamCurrent*1E6*time*yield*energy)/(4*pi()*dista
nce^2))*ppval(FTissue,energy)*B*exp(-mfp)*0.577; %[uSv/hr]
    end
```

```
    doseRate(j,2) = sum

    sum = 0;
    %Calculating dose rate for Zinc-61
    for i=1:length(zinc_sixtyone_en)
        energy = zinc_sixtyone_en(i);
        yield = zinc_sixtyone_y(i);
        mu = ppval(FLead,energy);
        mfp = mu*leadThickness;
        B = Buildup(energy,mfp);
        if B<0
            B=1;
        end
        sum = sum +
((ProductionYield(j,3)*beamCurrent*1E6*time*yield*energy)/(4*pi()*dista
nce^2))*ppval(FTissue,energy)*B*exp(-mfp)*0.577; %[uSv/hr]
    end
    doseRate(j,3) = sum

    sum = 0;
    %Calculating dose rate for cu-61
    for i=1:length(cop_sixtyone_en)
        energy = cop_sixtyone_en(i);
        yield = cop_sixtyone_y(i);
        mu = ppval(FLead,energy);
        mfp = mu*leadThickness;
        B = Buildup(energy,mfp);
        if B<0
            B=1;
        end
        sum = sum +
((ProductionYield(j,4)*beamCurrent*1E6*time*yield*energy)/(4*pi()*dista
nce^2))*ppval(FTissue,energy)*B*exp(-mfp)*0.577; %[uSv/hr]
    end
    doseRate(j,4) = sum

    sum = 0;
    %Calculating dose rate for Co-58
    for i=1:length(cob_fiftyeight_en)
        energy = cob_fiftyeight_en(i);
        yield = cob_fiftyeight_y(i);
        mu = ppval(FLead,energy);
        mfp = mu*leadThickness;
        B = Buildup(energy,mfp);
        if B<0
            B=1;
        end
        sum = sum +
((ProductionYield(j,5)*beamCurrent*1E6*time*yield*energy)/(4*pi()*dista
nce^2))*ppval(FTissue,energy)*B*exp(-mfp)*0.577; %[uSv/hr]
    end
    doseRate(j,5) = sum
```

```
    sum = 0;
    %Calculating dose rate for Zn-65
    for i=1:length(zinc_sixtyfive_en)
        energy = zinc_sixtyfive_en(i);
        yield = zinc_sixtyfive_y(i);
        mu = ppval(FLead,energy);
        mfp = mu*leadThickness;
        B = Buildup(energy,mfp);
        if B<0
            B=1;
        end
        sum = sum +
((ProductionYield(j,6)*beamCurrent*1E6*time*yield*energy)/(4*pi()*dista
nce^2))*ppval(FTissue,energy)*B*exp(-mfp)*0.577; %[uSv/hr]
    end
    doseRate(j,6) = sum

    sum = 0;
    %Calculating dose rate for Cu-64
    for i=1:length(cop_sixtyfour_en)
        energy = cop_sixtyfour_en(i);
        yield = cop_sixtyfour_y(i);
        mu = ppval(FLead,energy);
        mfp = mu*leadThickness;
        B = Buildup(energy,mfp);
        if B<0
            B=1;
        end
        sum = sum +
((ProductionYield(j,7)*beamCurrent*1E6*time*yield*energy)/(4*pi()*dista
nce^2))*ppval(FTissue,energy)*B*exp(-mfp)*0.577; %[uSv/hr]
    end
    doseRate(j,7) = sum

    sum = 0;
    for i = 1:7
        sum = sum + doseRate(j,i);
    end
    doseRate(j,8) = sum;

    %Initialize the amount of time that the target is left to sit and
    %decay.
    waitTime = 0; %hours
    %Initializing total dose rate of target to use as a comparison to
see
    %if the dose rate of the target is below federally regulated
limits.
    initialDoseRate = doseRate(j,8);
    %While loop that determines how many hours must past before the
doseRate
    %is less than the federally regulated limit, in mRem/hr. Works by
```

```
    %increasing the wait time in increments of 1 hour.
    while initialDoseRate > federalLimit
        sum = 0;
        waitTime = waitTime + 1;
        for i=1:7
            sum = sum + doseRate(j,i)*exp(-decayConstant(i)*waitTime);
%[mRem/hr]
        end
        initialDoseRate = sum;
    end
    doseRate(j,9) = waitTime; %Hours

    %Calculate the new production yield for each radionuclide after
decay
    %correcting using the previously calculated wait time.
    for i=1:7
        WaitProductionYield(j,i) = ProductionYield(j,i)*exp(-
decayConstant(i)*waitTime);
    end
end

%Saves the Production yield, the dose rate/total dose rate and wait
time,
%and decay corrected production yields after the wait time has passed
to
%three separate text files with their respective names.
dlmwrite('ProductionYields.txt', ProductionYield);
dlmwrite('DoseRates.txt', doseRate);
dlmwrite('CooldownProductionYields.txt',WaitProductionYield);

end

function [enDep] = energyDeposition(Ei,thickness)

%Range values obtained from SRIM nuclear code
%energy for copper [MeV]
energy =
[0.0,0.011,0.012,0.013,0.014,0.015,0.016,0.017,0.018,0.02,0.0225,0.025,
0.0275,0.03,0.0325,0.035,0.0375,0.04,0.045,0.05,0.055,0.06,0.065,0.07,0
.08,0.09,0.1,0.11,0.12,0.13,0.14,0.15,0.16,0.17,0.18,0.2,0.225,0.25,0.2
75,0.3,0.325,0.35,0.375,0.4,0.45,0.5,0.55,0.6,0.65,0.7,0.8,0.9,1,1.1,1.
2,1.3,1.4,1.5,1.6,1.7,1.8,2,2.25,2.5,2.75,3,3.25,3.5,3.75,4,4.5,5,5.5,6
,6.5,7,8,9,10,11,12,13,14,15,16,17,18,20,22.5,25,27.5,30,32.5,35,37.5,4
0,45,50];
%range for copper [microns]
range =
[0.061,0.0668,0.0726,0.0783,0.084,0.0896,0.0952,0.1007,0.1062,0.1171,0.
1306,0.1438,0.1569,0.1699,0.1827,0.1954,0.2081,0.2206,0.2454,0.27,0.294
3,0.3185,0.3424,0.3663,0.4138,0.4612,0.5084,0.5557,0.6031,0.6506,0.6985
,0.7466,0.795,0.8438,0.893,0.9927,1.12,1.25,1.38,1.52,1.66,1.8,1.95,2.1
,2.41,2.74,3.07,3.43,3.79,4.17,4.97,5.82,6.72,7.67,8.66,9.72,10.81,11.9
6,13.15,14.38,15.66,18.35,21.94,25.79,29.88,34.23,38.81,43.63,48.68,53.
```

```
96,65.18,77.29,90.26,104.08,118.73,134.2,167.51,203.96,243.47,285.99,33
1.45,379.79,430.98,484.97,541.72,601.19,663.35,795.54,975.32,1170,1380,
1610,1850,2110,2380,2660,3270,3930];

%Give this value an energy to spit out the range
FRange = spline(energy, range);

%Give this value an range to spit out the energy
FEnergy = spline(range, energy);

%Target Thickness in units of mm to microns [microns]
targetThickness = thickness*1e3;
%Calculate the range of the particle after it exits particle
exitRange = ppval(FRange,Ei)-targetThickness;
if exitRange < 0
    Ef = 0;
else
    %Calculate the energy of particle from its exit range
    Ef = ppval(FEnergy,exitRange);
end

%Initializing values. All of these values are simply used to correct
record
%All values and make sure that they are all recorded within the correct
%array sizes.
plot_range(1,1) = 0; %Track range
%Track energy deposition, initialize first element with entry energy
enDep(1,1) = Ei;
%Start i at 2, because the first element of the array is initialized
i = 2;
%Track the proton energy deposition in copper in increments of 30
microns
increment = 30;
%Initialize the first element of the array to 0, since zero energy
transfer
%has occured at this point.
dE(i,1) = 0;

%While loop that continues until the protons exits the target. This is
pre-
%determined by the target thickness, which calculates an exit or final
%energy. Once Ei is less than Ef, that designates that the proton has
%exited the target and the loop exits.
while Ei > Ef
    range_value = ppval(FRange,Ei); %enter an energy value, interpolate
a range
    dr = range_value - increment; %## micron increment
    E = ppval(FEnergy, dr); %enter a range value, interpolate an energy
    enDep(i,1) = E; %Keep track of all the E values after energy is
deposited
    %Error checking. See if current E is greater the final E
    %If yes, then do this.
```

```
    if E > Ef
        dE(i,1) = Ei - E; %Keep track of energy deposited
        plot_range(i,1) = plot_range(i-1,1) + increment; %Keep track of
the range of the particle
    %If it's less, then back track in smaller increments of 30 to get a
    %closer estimate of the energy deposited right at the barrier.
    elseif E < Ef
        %Range for whatever is between Ef and last energy
        last_range = ppval(FRange, enDep(i-1,1));
        last_range_2= ppval(FRange, Ef); %range for Ef
        %Add the last little range that is less than the increment
        plot_range(i,1) = plot_range(i-1,1) + (last_range-
last_range_2);
        dE(i,1) = enDep(i-1,1) - Ef;
        enDep(i,1) = Ef;
    end
    Ei = E;
    i = i + 1;
end
```

APPENDIX B

RADIONUCLIDE PRODUCTION AND RADIATION EXPOSURE DATA

Table B-1. Photon energy and yield taken from the NNDC NuDat database.

Zn-62		**Cu-61**		**Zn-65**	
Photon Energy	**Photon Yield**	**Photon Energy**	**Photon Yield**	**Photon Energy**	**Photon Yield**
(MeV)	**($\gamma \cdot d^{-1}$)**	**(MeV)**	**($\gamma \cdot d^{-1}$)**	**(MeV)**	**($\gamma \cdot d^{-1}$)**
0.04	0.25480	0.07	0.04233	1.12	0.50600
0.20	0.00011	0.12	0.00010		
0.24	0.02522	0.22	0.00021		
0.25	0.01898	0.28	0.12200		
0.26	0.01352	0.37	0.02147		
0.30	0.00289	0.53	0.00376		
0.35	0.00450	0.55	0.00006		
0.39	0.00017	0.59	0.01168		
0.49	0.00016	0.66	0.10770		
0.51	0.14820	0.82	0.00307		
0.55	0.15340	0.84	0.00214		
0.60	0.26000	0.90	0.00083		
0.63	0.00001	0.91	0.01102		
0.64	0.00255	0.95	0.00010		
0.64	0.00014	1.02	0.00010		
0.66	0.00001	1.03	0.00042		
0.67	0.00004	1.06	0.00048		
0.73	0.00002	1.07	0.00033		
0.79	0.00009	1.10	0.00245		
0.83	0.00003	1.12	0.00032		
0.88	0.00015	1.13	0.00090		
0.92	0.00015	1.19	0.03747		
1.14	0.00035	1.45	0.00045		
1.19	0.00004	1.54	0.00026		
1.22	0.00002	1.61	0.00021		
1.32	0.00001	1.66	0.00053		
1.39	0.00012	1.73	0.00054		
1.43	0.00028	2.00	0.00004		
1.49	0.00001	2.12	0.00010		
1.53	0.00006	2.12	0.00041		

Table B-1. Photon energy and yield taken from the NNDC NuDat database.

Zn-63				Co-58	
Photon Energy (MeV)	**Photon Yield ($\gamma \cdot d^{-1}$)**	**Photon Energy (MeV)**	**Photon Yield ($\gamma \cdot d^{-1}$)**	**Photon Energy (MeV)**	**Photon Yield ($\gamma \cdot d^{-1}$)**
0.24	0.00090	1.55	0.00122	0.81	0.99450
0.37	0.00011	1.57	0.00016	0.86	0.00683
0.44	0.00016	1.67	0.00001	1.67	0.00518
0.45	0.00236	1.70	0.00002		
0.48	0.00006	1.75	0.00004		
0.52	0.00021	1.83	0.00004		
0.58	0.00033	1.86	0.00014		
0.62	0.00014	1.87	0.00020		
0.67	0.08200	2.01	0.00011		
0.68	0.00015	2.03	0.00056		
0.69	0.00004	2.05	0.00004		
0.74	0.00067	2.06	0.00034		
0.75	0.00007	2.08	0.00015		
0.77	0.00007	2.34	0.00075		
0.88	0.00003	2.50	0.00021		
0.90	0.00012	2.51	0.00010		
0.96	0.06478	2.54	0.00066		
1.12	0.00111	2.70	0.00040		
1.13	0.00013	2.72	0.00013		
1.15	0.00019	2.78	0.00016		
1.17	0.00008	2.81	0.00004		
1.21	0.00012	2.86	0.00003		
1.23	0.00002	2.89	0.00002		
1.33	0.00069	3.04	0.00005		
1.34	0.00002	3.10	0.00001		
1.37	0.00034				
1.39	0.00043				
1.39	0.00097				
1.41	0.00746				
1.45	0.00002				
1.48	0.00002				

Table B-1. Photon energy and yield taken from the NNDC NuDat database.

Zn-63				Cu-64	
Photon Energy (MeV)	**Photon Yield ($\gamma \cdot d^{-1}$)**	**Photon Energy (MeV)**	**Photon Yield ($\gamma \cdot d^{-1}$)**	**Photon Energy (MeV)**	**Photon Yield ($\gamma \cdot d^{-1}$)**
0.15	0.00172	2.09	0.00628	1.35	0.00473
0.27	0.00546	2.21	0.00842		
0.42	0.00094	2.36	0.00328		
0.43	0.00148	2.38	0.00109		
0.48	0.16850	2.46	0.00655		
0.59	0.00062	2.47	0.00078		
0.60	0.00086	2.54	0.00076		
0.64	0.00078	2.68	0.00679		
0.69	0.01872	2.79	0.00803		
0.70	0.00429	2.84	0.00248		
0.75	0.00312	2.86	0.00429		
0.92	0.00094	2.93	0.00094		
0.93	0.00086	3.02	0.00187		
0.97	0.02574	3.09	0.00117		
1.13	0.00179	3.52	0.00140		
1.15	0.00156				
1.19	0.01724				
1.31	0.00936				
1.39	0.01217				
1.46	0.00312				
1.48	0.00788				
1.50	0.00140				
1.54	0.00085				
1.57	0.00109				
1.61	0.00296				
1.66	0.07800				
1.73	0.00140				
1.88	0.00480				
1.90	0.00091				
1.93	0.00663				
2.00	0.01178				

Table B-2. Linear attenuation coefficients for lead taken from NIST's X-ray and Gamma-ray data section.

Photon Energy (MeV)	**μ (cm^{-1})**	**Photon Energy (MeV)**	**μ (cm^{-1})**
0.001	59081	0.05	91
0.002	14572	0.06	57
0.002	9079	0.08	27
0.003	19573	0.09	22
0.003	22045	0.10	63
0.003	22283	0.15	23
0.003	21058	0.20	11
0.003	20367	0.30	5
0.004	16965	0.40	3
0.004	16352	0.50	2
0.004	14867	0.60	1
0.004	14186	0.80	1
0.005	8283	1.00	0.8
0.006	5298	1.25	0.7
0.008	2593	1.50	0.6
0.010	1481	2.00	0.5
0.013	760	3.00	0.5
0.015	1266	4.00	0.5
0.015	1222	5.00	0.5
0.016	1606	6.00	0.5
0.016	1524	8.00	0.5
0.020	979	10.00	0.6
0.030	344	15.00	0.6
0.040	163	20.00	0.7

Table B-3. Mass energy-absorption coefficients for tissue taken from NIST's X-ray and Gamma-ray data section.

Photon Energy (MeV)	**$(\mu/\rho)_{en}$ ($cm^2 \cdot g^{-1}$)**	**Photon Energy (MeV)**	**$(\mu/\rho)_{en}$ ($cm^2 \cdot g^{-1}$)**
0.0010	3701	0.06	0.03
0.0010	3376	0.08	0.03
0.0011	3079	0.1	0.03
0.0015	1247	0.2	0.03
0.0020	558	0.2	0.03
0.0021	457	0.3	0.03
0.0023	378	0.4	0.03
0.0025	309	0.5	0.03
0.0026	259	0.6	0.03
0.0028	214	0.8	0.03
0.0030	182	1	0.03
0.0036	106	1.3	0.03
0.0040	80	1.5	0.03
0.0050	41	2	0.03
0.0060	24	3	0.02
0.0080	10	4	0.02
0.0100	5	5	0.02
0.0150	1	6	0.02
0.0200	1	8	0.02
0.0300	0.2	10	0.02
0.0400	0.1	15	0.01
0.0500	0.04	20	0.01

B-4. Proton range in copper for energies between 0.01 and 50 MeV taken from SRIM modeling data.

Proton Energy (MeV)	Proton Range (μm)	Proton Energy (MeV)	Proton Range (μm)	Proton Energy (MeV)	Proton Range (μm)
0.010	0.06	0.17	0.84	3.3	39
0.011	0.07	0.18	0.89	3.5	44
0.013	0.08	0.20	0.99	3.8	49
0.014	0.08	0.23	1.1	4.0	54
0.015	0.09	0.25	1.3	4.5	65
0.016	0.10	0.28	1.4	5.0	77
0.017	0.10	0.30	1.5	5.5	90
0.018	0.11	0.35	1.8	6.0	104
0.020	0.12	0.38	2.0	6.5	119
0.023	0.13	0.40	2.1	7.0	134
0.025	0.14	0.45	2.4	8.0	168
0.028	0.16	0.50	2.7	9.0	204
0.030	0.17	0.55	3.1	10.0	243
0.033	0.18	0.60	3.4	11.0	286
0.035	0.20	0.65	3.8	12.0	331
0.038	0.21	0.70	4.2	13.0	380
0.040	0.22	0.80	5.0	14.0	431
0.045	0.25	0.90	5.8	15.0	485
0.050	0.27	1.00	6.7	16.0	542
0.055	0.29	1.10	7.7	17.0	601
0.060	0.32	1.20	8.7	18.0	663
0.065	0.34	1.30	9.7	20.0	796
0.070	0.37	1.40	11	22.5	975
0.080	0.41	1.50	12	25.0	1170
0.090	0.46	1.60	13	27.5	1380
0.100	0.51	1.70	14	30.0	1610
0.110	0.56	1.80	16	32.5	1850
0.120	0.60	2.00	18	35.0	2110
0.130	0.65	2.25	22	37.5	2380
0.140	0.70	2.50	26	40.0	2660
0.150	0.75	2.75	30	45.0	3270
0.160	0.80	3.00	34	50.0	3930

Table B-5. Reaction cross-sections for the production of relevant radionuclides by bombarding a natural copper target with proton energies between 1 and 200 MeV. This data was taken from JANIS.

Reaction Cross Sections							
Zn-62				Zn-63			
Proton Energy (MeV)	Cross Section (mb)	Proton Energy (MeV)	Cross Section (mb)	Proton Energy (MeV)	Cross Section (mb)	Proton Energy (MeV)	Cross Section (mb)
1	0	28	32	1	0	28	31
2	0	30	24	2	0	30	28
3	0	35	15	3	0	35	21
4	0	40	12	4	0	40	17
5	0	45	9.8	5	129	45	14
6	0	50	8.1	6	233	50	11
7	0	55	6.9	7	276	55	10
8	0	60	6.0	8	293	60	8
9	0	65	5.2	9	310	65	7
10	0	70	4.6	10	326	70	6
11	0	75	4.0	11	339	75	5
12	0	80	3.5	12	348	80	4.6
13	0	90	2.8	13	341	90	3.6
14	3	100	2.2	14	273	100	2.9
15	17	110	1.8	15	192	110	2.3
16	30	120	1.5	16	134	120	1.9
17	40	130	1.3	17	97	130	1.6
18	49	140	1.1	18	75	140	1.4
19	56	150	1.0	19	61	150	1.2
20	60	160	0.9	20	53	160	1.1
22	62	180	0.7	22	44	180	0.9
24	57	200	0.6	24	39	200	0.7

Table B-5. Reaction cross-sections for the production of relevant radionuclides by bombarding a natural copper target with proton energies between 1 and 200 MeV. This data was taken from JANIS.

Reaction Cross Sections							
Zn-61				Cu-61			
Proton Energy (MeV)	**Cross Section (mb)**	**Proton Energy (MeV)**	**Cross Section (mb)**	**Proton Energy (MeV)**	**Cross Section (mb)**	**Proton Energy (MeV)**	**Cross Section (mb)**
1	0	28	0.02	1	0	28	88
2	0	30	0.31	2	0	30	144
3	0	35	1.76	3	0	35	199
4	0	40	1.77	4	0	40	155
5	0	45	1.15	5	0	45	118
6	0	50	0.83	6	0	50	101
7	0	55	0.68	7	0	55	91
8	0	60	0.57	8	0	60	84
9	0	65	0.49	9	0	65	78
10	0	70	0.43	10	0	70	74
11	0	75	0.38	11	0	75	69
12	0	80	0.33	12	0	80	65
13	0	90	0.26	13	0	90	57
14	0	100	0.22	14	0	100	51
15	0	110	0.18	15	0	110	46
16	0	120	0.16	16	0.01	120	42
17	0	130	0.14	17	0.02	130	38
18	0	140	0.12	18	0.04	140	35
19	0	150	0.11	19	0.08	150	33
20	0	160	0.10	20	0.15	160	30
22	0	180	0.08	22	0.61	180	27
24	0	200	0.07	24	6.86	200	24

Table B-5. Reaction cross-sections for the production of relevant radionuclides by bombarding a natural copper target with proton energies between 1 and 200 MeV. This data was taken from JANIS.

Reaction Cross Sections							
Co-58				Zn-65			
Proton Energy (MeV)	**Cross Section (mb)**	**Proton Energy (MeV)**	**Cross Section (mb)**	**Proton Energy (MeV)**	**Cross Section (mb)**	**Proton Energy (MeV)**	**Cross Section (mb)**
1	0	28	2	1	0	28	37
2	0	30	7	2	0	30	33
3	0	35	31	3	29	35	25
4	0	40	42	4	133	40	20
5	0	45	37	5	274	45	16
6	0	50	28	6	399	50	13
7	0	55	24	7	489	55	11
8	0	60	22	8	556	60	9.5
9	0	65	26	9	611	65	8.4
10	0	70	34	10	653	70	7.2
11	0	75	44	11	635	75	6.4
12	0	80	54	12	508	80	5.7
13	0	90	64	13	360	90	4.4
14	0	100	64	14	246	100	3.5
15	0	110	61	15	168	110	2.9
16	0	120	56	16	122	120	2.4
17	0	130	54	17	93	130	2.0
18	0	140	52	18	77	140	1.7
19	0	150	48	19	66	150	1.5
20	0	160	48	20	60	160	1.3
22	0	180	44	22	51	180	1.1
24	0.005	200	42	24	46	200	0.9

Table B-5. Reaction cross-sections for the production of relevant radionuclides by bombarding a natural copper target with proton energies between 1 and 200 MeV. This data was taken from JANIS.

Reaction Cross Sections			
Cu-64			
Proton Energy (MeV)	**Cross Section (mb)**	**Proton Energy (MeV)**	**Cross Section (mb)**
1	0	28	324
2	0	30	298
3	0	35	258
4	0	40	234
5	0	45	214
6	0	50	196
7	0	55	177
8	0	60	170
9	0	65	156
10	0	70	148
11	0.02	75	136
12	0.3	80	127
13	6	90	110
14	33	100	95
15	76	110	84
16	124	120	74
17	167	130	67
18	206	140	61
19	241	150	55
20	275	160	51
22	336	180	44
24	365	200	39

Table B-6. The exposure buildup factors for gamma-rays in lead for energies between 0.1 and 10 MeV with relaxation lengths between 0.5 and 10.

	Energy (MeV)									
MFP	**10**	**8**	**6**	**5**	**4**	**3**	**2**	**1**	**0.5**	**0.1**
0.50	1.28	1.3	1.26	1.25	1.21	1.23	1.21	1.2	1.14	1.51
1.00	1.51	1.51	1.42	1.41	1.36	1.4	1.4	1.38	1.24	2.04
2.00	2.01	1.9	1.73	1.71	1.67	1.73	1.76	1.68	1.39	3.39
3.00	2.63	2.3	2.08	2.05	2.02	2.1	2.14	1.95	1.52	5.6
4.00	3.42	2.91	2.49	2.44	2.4	2.5	2.52	2.09	1.62	9.59
5.00	4.45	3.59	2.96	2.88	2.82	2.93	2.91	2.43	1.71	17
6.00	5.73	4.41	3.51	3.38	3.28	3.4	3.32	2.66	1.8	30.6
7.00	7.37	5.39	4.13	3.93	3.79	3.89	3.74	2.89	1.88	54.9
8.00	9.44	6.58	4.84	4.56	4.35	4.41	4.17	3.1	1.95	94.7
10.00	15.4	9.73	6.61	6.03	5.61	5.56	5.07	3.51	2.1	294

APPENDIX C

LABVIEW PROGRAM LOGIC FLOW DIAGRAMS

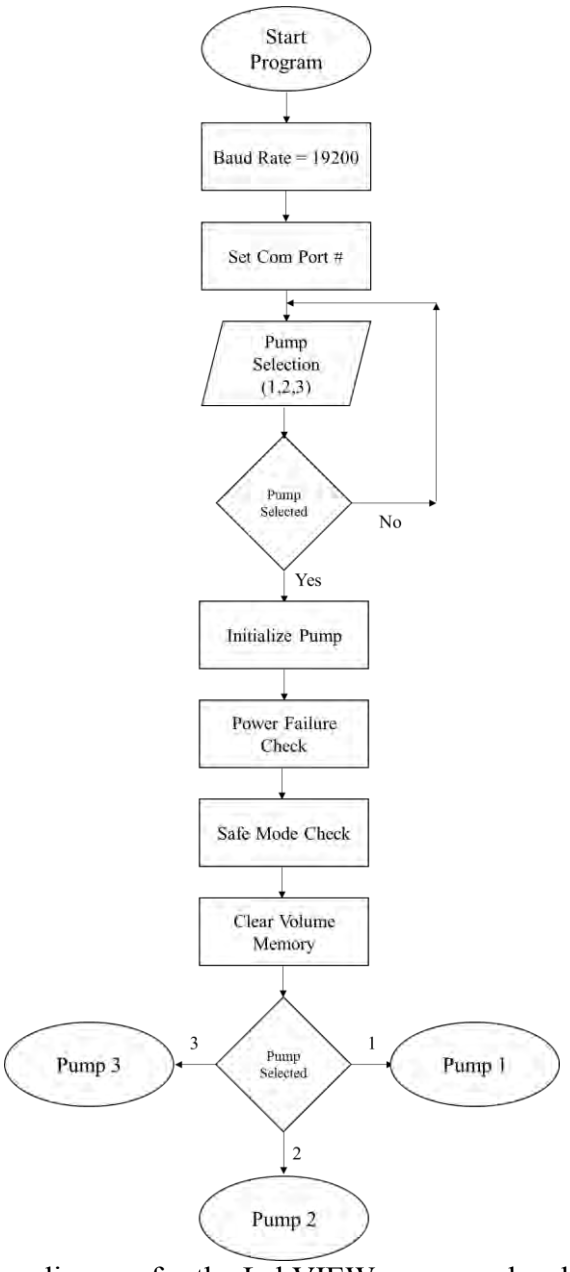

Figure C-1. Logic flow diagram for the LabVIEW program developed for the NE-500

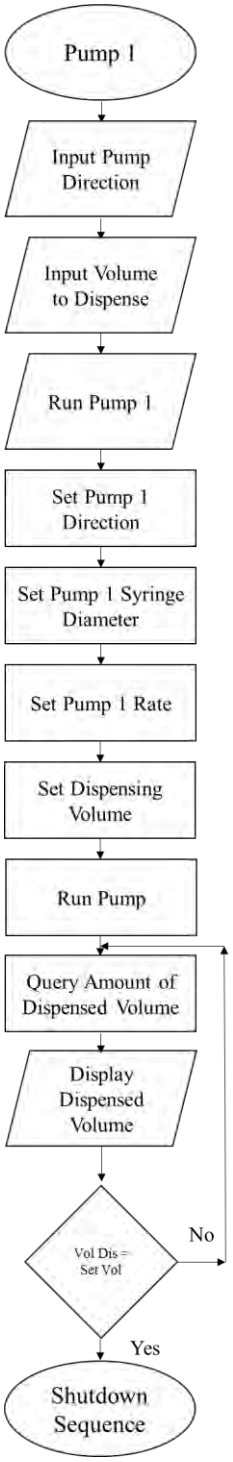

Figure C-2. Logic flow diagram for controlling pump 1 with the LabVIEW program developed for the NE-500

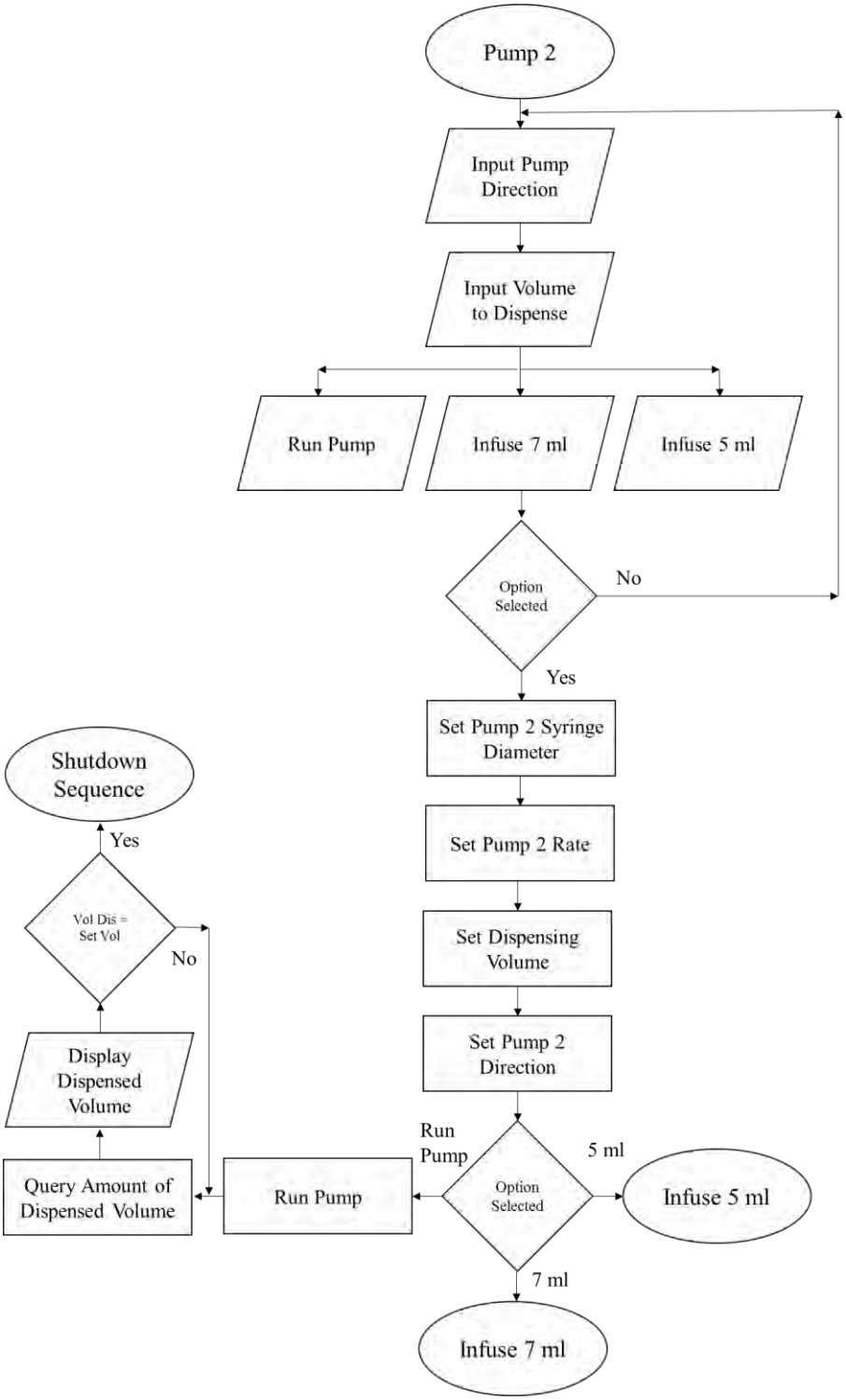

Figure C-3. Logic flow diagram for controlling pump 2 with the LabVIEW program developed for the NE-500

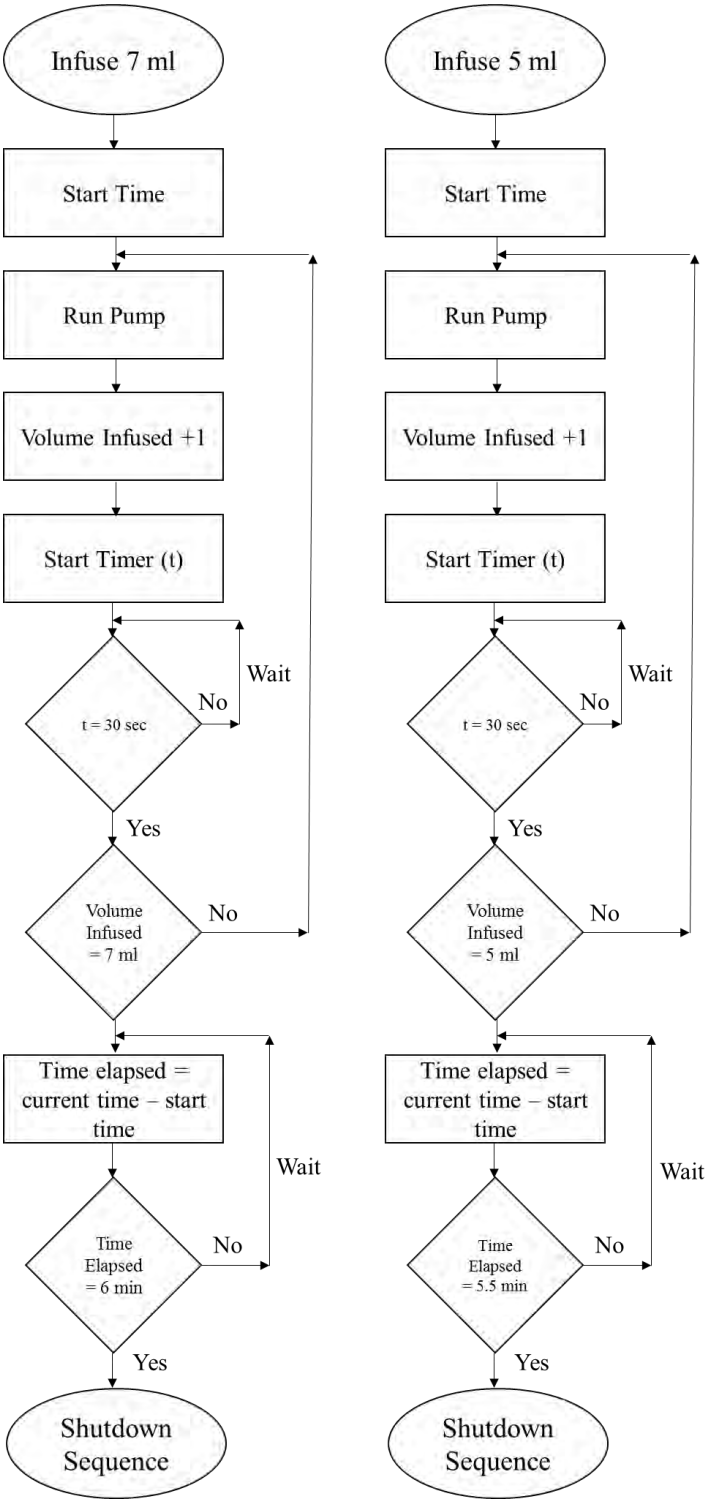

Figure C-4. Logic flow diagram for automating the addition of hydrogen perxoide using pump 2 with the LabVIEW program developed for the NE-500

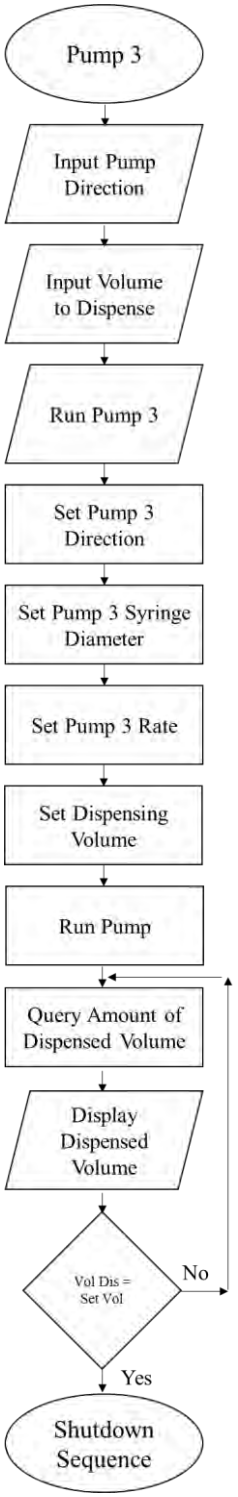

Figure C-5. Logic flow diagram for controlling pump 3 with the LabVIEW program developed for the NE-500

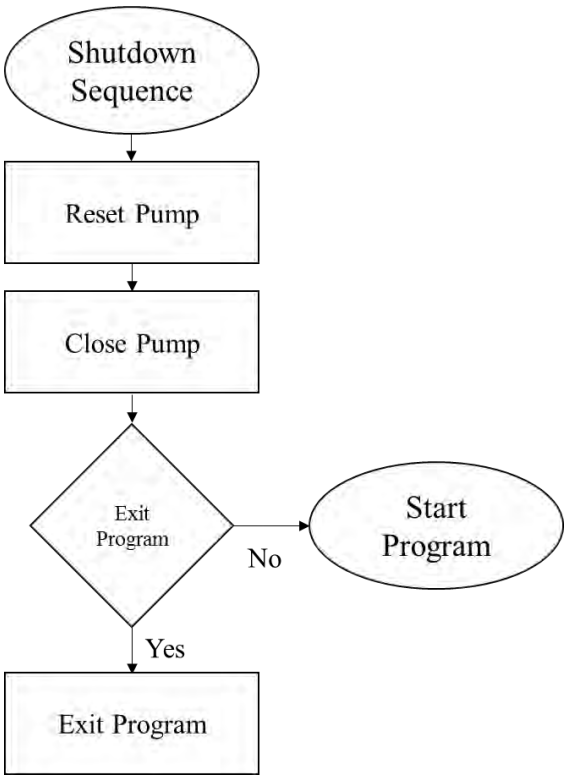

Figure C-6. Logic flow diagram for close down the program developed for the NE-500

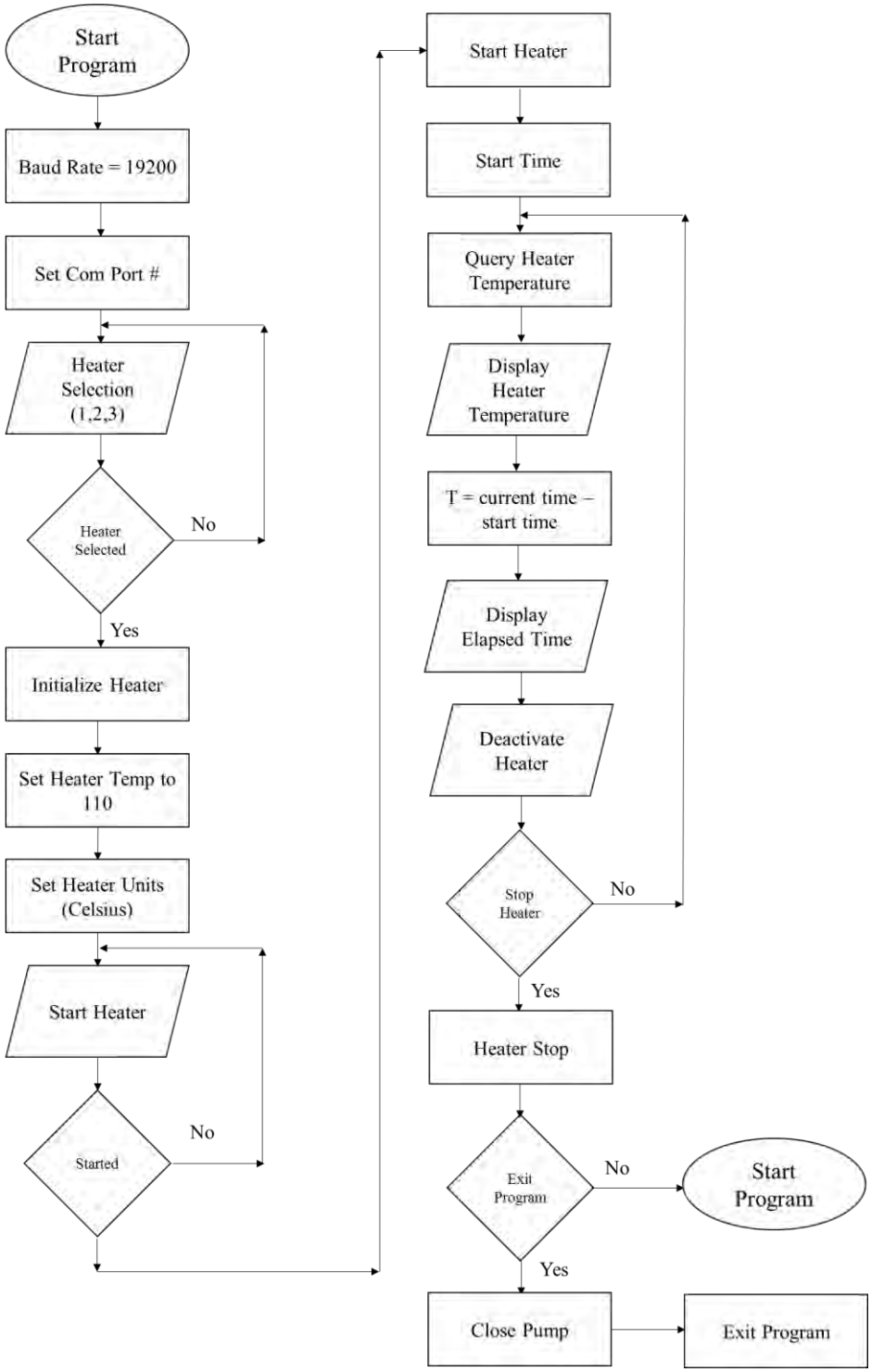

Figure C-7. Logic flow diagram for the LabVIEW program developed for the HEATER-KIT-1LG.

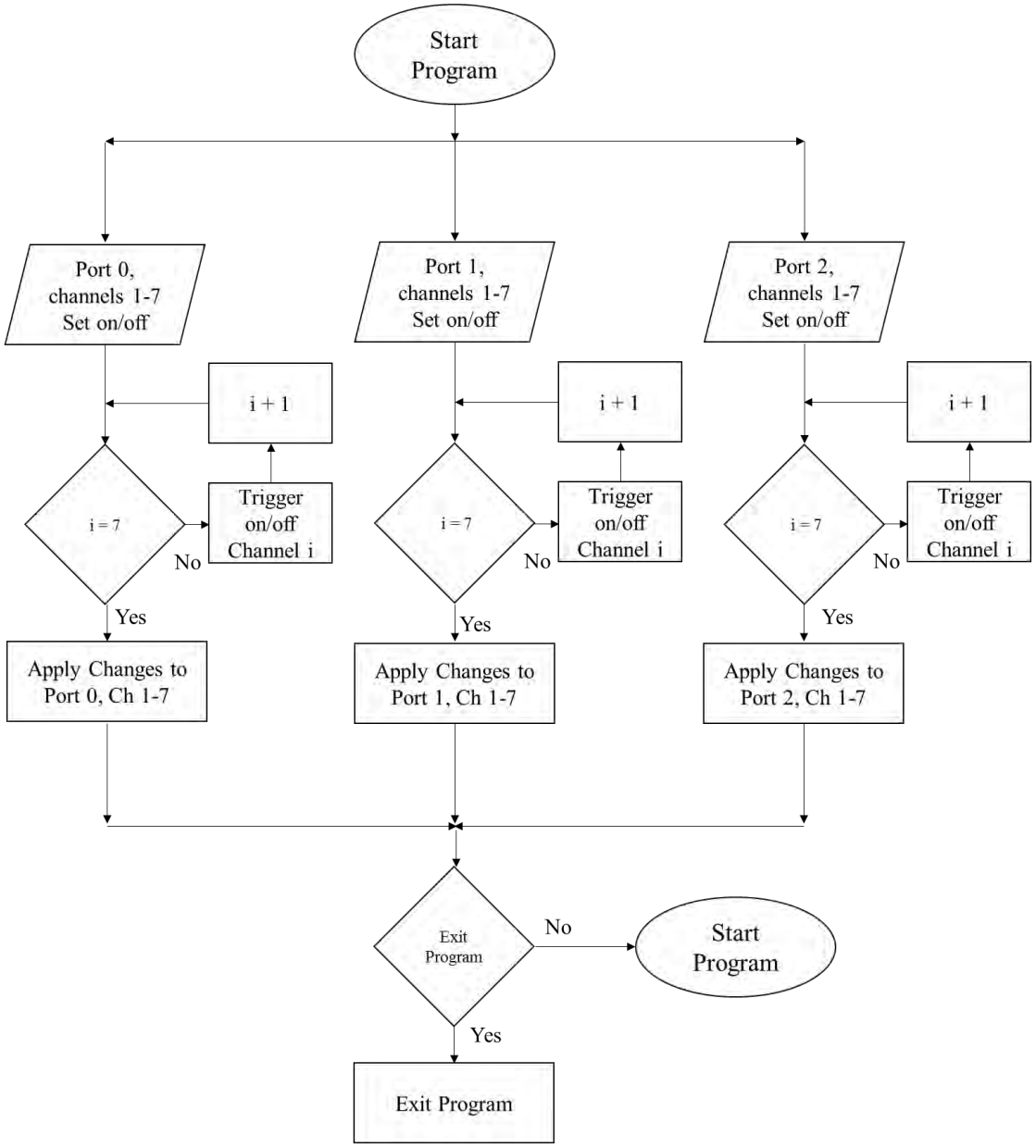

Figure C-8. Logic flow diagram for the LabVIEW program developed for the USB-6501.

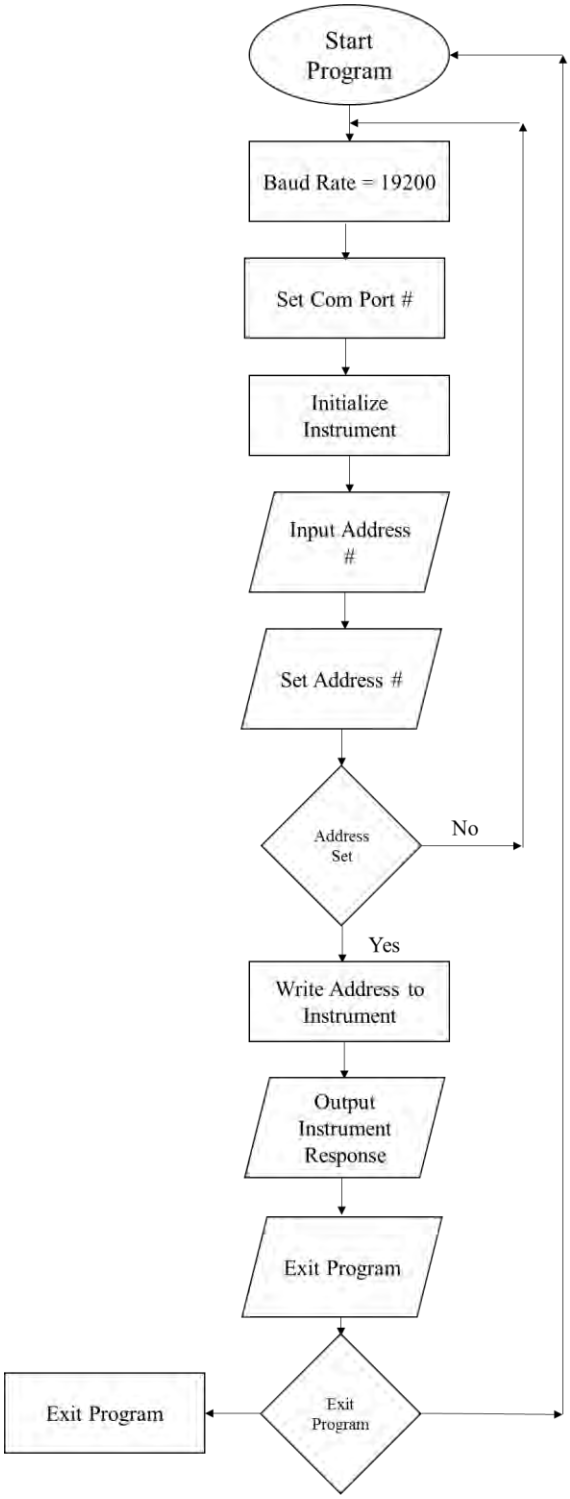

Figure C-9. Logic flow diagram developed for the LabVIEW program that manually sets the address of an instrument.

DESIGN OF A SUBCRITICAL AQUEOUS TARGET SYSTEM FOR MEDICAL ISOTOPE PRODUCTION

An Undergraduate Research Scholars Thesis

by

RICHARD VEGA

Submitted to Honors and Undergraduate Research
Texas A&M University
in partial fulfillment or the requirements for the designation as an

UNDERGRADUATE RESEARCH SCHOLAR

Approved by
Research Advisor: Dr. Gamal Akabani

May 2014

Major: Nuclear Engineering
Physics

TABLE OF CONTENTS

ABSTRACT

Design of a Subcritical Aqueous Target System for Medical Isotope Production. (May 2014)

Richard Vega
Department of Nuclear Engineering
Department of Physics
Texas A&M University

Research Advisor: Dr. Gamal Akabani
Department of Nuclear Engineering

The United States consumes almost half of all medical isotopes produced worldwide, and relies on foreign sources for nearly its entire supply. These isotopes are produced in nuclear reactors which are very costly to construct. A domestic supply may be realized if research reactors at universities and national laboratories can be enhanced with isotope production capabilities. This research is dedicated to the design of an aqueous target system that can be appended to exiting research reactors for this purpose. The design aims to combine attributes of solid target irradiation by conventional reactors and in-solution production by aqueous homogeneous reactors in order to realize some of the benefits of each method. The benefits for the former include using existing reactors as the external neutron source hence reducing the investment capital significantly. The benefits for aqueous homogeneous reactors are numerous and include higher efficiency, substantial reduction in waste, lower fuel cost, and reduced isotope separation complexity. Utilizing a flowing fuel design will enable continuous isotope separation and more efficient heat removal, as well as eliminate some of the complications that have plagued solution fueled reactors in the past

such as power oscillations and fuel precipitation. The aqueous target system described in this thesis is designed for the Annular Core Research Reactor (ACRR) at Sandia National Laboratories. The system is optimized for ^{99}Mo production, as this is the medical isotope in highest demand and used in a majority of all medical diagnostic procedures excluding x-ray imaging. The optimized production rate is calculated to be 3044 $Ci_{6\text{-day}}$ per week which accounts for 50.7% of domestic consumption.

ACKNOWLEDGEMENTS

First and foremost, I would like to thank Dr. Gamal Akabani for his continued guidance over this two year research endeavor that began as a senior design project. His guidance has been pivotal throughout the entire process. I would also like to thank Dr. Marvin Adams for having answers when no one else did. I could just as easily thank the entire Nuclear Engineering department, for none of this would be possible without their excellent teaching and willingness to help at every level of the undergraduate curriculum. In addition, I would like to thank Tammis Sherman and the entire Undergraduate Research program for their efforts to make this process go as smoothly as possible. Last but not least, I would like to thank Landon Brockmeyer for his help with building and running the ABAQUS files.

CHAPTER I

INTRODUCTION

This report is the second stage of the design of an aqueous target system for medical isotope production. The first stage proposed a reactor named the Flowing Fuel Aqueous Homogeneous Reactor (FFAHR) that was different from previous AHR designs in that the fuel flowed through the core allowing for more efficient heat removal and continuous isotope production. The flowing of the fuel was also intended to eliminate some of the technical deficiencies plaguing previous AHR designs such as power oscillations, fuel precipitation, and high temperature corrosion. The low power density of the first design made the ^{99}Mo production insufficient, and hence the need for a new design was realized.

The second stage of this design utilizes many features of the first design. The primary difference between the two systems is that the aqueous target will be subcritical by itself, and externally driven by a research reactor. The reactor chosen as the neutron source is the Annular Core Research Reactor (ACRR) at Sandia National Laboratories, although the current design should be able to be adapted for other research reactors as well. The reason for choosing the ACRR is purely one of familiarity and convenience.

The FFAHR was intended to produce five of the most commonly used radioisotopes in the medical industry. These radioisotopes are ^{99}Mo, ^{133}Xe, ^{89}Sr, ^{90}Y, and ^{131}I. The intent was to produce these isotopes at a rate that would make it a financially viable and competitive option when compared to the research reactors that currently produce the global supply of these isotopes. Of the

five isotopes listed above, ^{99}Mo is by far in the highest demand, and the insufficient production of this isotope by the FFAHR made it unlikely to compete with foreign sources.

It should be remembered that bigger is not always better in this case. Ideally, ^{99}Mo would be produced in small amounts in hundreds of facilities across the world so that an unplanned outage of a large scale production facility would not cause widespread shortages. The difficulty in realizing this is that nuclear reactors are extremely expensive, and small scale production facilities simply do not pay the bills. In addition, the licensing process in the United States makes it nearly impossible to physically realize any new reactor design. This is the reason that the current design is proposed as a target system that could be adapted to existing research reactors.

I.A. Need for Domestic Production of Radioisotopes

This section describes the use of radioisotopes in the medical industry as well as an overview of the current supply and demand of these isotopes. The need for radioisotope production in the United States in particular is emphasized due to its dependence on foreign supplies and its susceptibilities due to this dependence.

I.A.1. *Radioisotopes Used in the Medical Industry*

The medical industry uses radioisotopes for a variety of procedures. These procedures can be split into two categories. The first of these is diagnostic imaging which typically utilizes the long range and monoenergetic properties of gamma decay. [1] The second category is the treatment of various types of cancer through the short range of high energy beta particles to irradiate tumors without delivering a dose to the whole body. The most prominent isotopes used in the medical

industry today, which can be produced with significant yields from a nuclear reactor, are ^{99}Mo, ^{133}Xe, ^{89}Sr, ^{90}Y, and ^{131}I. [2]

Other isotopes used in the medical industry include positron emitting radioisotopes for use in positron emission tomography (PET). These are low Z isotopes that are typically produced by accelerators and have little to no fission yields. These isotopes include ^{11}C, ^{13}N, ^{15}O, and ^{18}F. Accelerators can also be used to produce the high Z isotopes that are typically produced in reactors, but with much less efficiency and very low yields.

I.A.1.1. *^{99}Mo*

The primary use of ^{99}Mo is to produce ^{99m}Tc. ^{99}Mo decays by beta emission with a 65.94 hr half life into ^{99m}Tc. [3] ^{99m}Tc then decays with a half life of 6.01 hr by internal conversion while emitting a 143 keV gamma particle. [4] The primary use of ^{99m}Tc is in medical diagnostic imaging. The ^{99m}Tc can be injected into the body with a pharmaceutical, which transports it to the region of the body that is to be imaged. The low energy gamma ray is then detected giving an image of the region that the ^{99m}Tc has populated. Such images of the lungs and skeleton can be seen in Figure I.1.

^{99m}Tc has a wide range of imaging capabilities that is only limited by the effectiveness of the pharmaceutical that transports it to the site for imaging. In addition to the lungs and skeleton shown in Figure I.1, ^{99m}Tc can be used to image the vascular system, intestines, brain, heart, thyroid, and liver among other organs. ^{99m}Tc is commonly used to detect stress fractures that do not show up clearly in X-ray images.

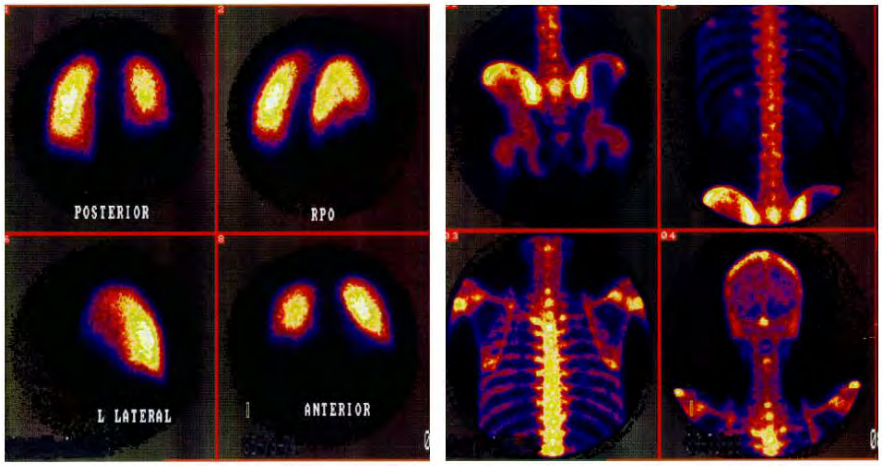

Figure I.1. Images taken with ^{99m}Tc of the lungs (left grid) and of the skeleton (right grid). Figure courtesy of Parma. [4]

Because of the extremely short half life of ^{99m}Tc, it would be inconvenient to try to sell this isotope in pure form. Instead, hospitals typically purchase ^{99}Mo and use a device called a ^{99m}Tc generator that separates the ^{99m}Tc from the ^{99}Mo as it becomes available. Over 80% of diagnostic imaging procedures, excluding X-ray imaging, use ^{99m}Tc. [5]

I.A.1.2. *^{133}Xe*

The primary use of ^{133}Xe is for lung ventilation studies known as lung perfusion. ^{133}Xe decays by beta emission with a 5.243 day half life, while also emitting low energy gamma particles. [3] Since ^{133}Xe exists in a gaseous state at room temperature, the radioactive gas can be inhaled by the patient and scintillation cameras can be used to detect various amounts of radioactivity in different regions of the lungs. This procedure allows the physician to assess how well the lungs are functioning by detecting pulmonary embolisms, determining how much blood is flowing to the

lungs, and determining which areas of the lungs are capable of ventilation. [6] A lung scan using ^{133}Xe can be seen in Figure I.2.

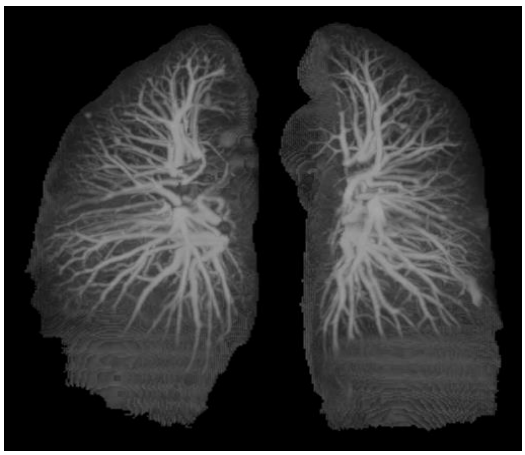

Figure I.2. Lung perfusion scan using ^{133}Xe. Figure courtesy of Johnson. [7]

I.A.1.3. *^{89}Sr*

Various forms of cancer including prostate, breast, and lung cancer are accompanied by painful bone metastases. ^{89}Sr is a beta emitting radionuclide with a half life of 50.53 days. [3] ^{89}Sr is found to localize in areas of active bone formation when consumed by the patient. While ^{89}Sr is not a cure for any type of cancer, it has been found to significantly relieve the pain of bone metastases. The mechanism of this pain relief is unknown. One proposed mechanism is that the beta radiation stops the tumor from releasing pain producing enzymes. [8] Pain relief can occur in as few as 7 days after treatment and last for as long as 6 months.

I.A.1.4. *^{90}Y*

Historically, liver cancer has been one of the most resistant cancers to chemotherapy. ^{90}Y is another beta emitting radioisotope with a half-life of 64 hr. [3] Treatment of liver cancer has recently utilized ^{90}Y in microsphere beads that are injected into the tumor where the short range of the beta radiation kills cancer cells without reaching un-affected portions of the body. [9] Although the dose administered cannot safely be high enough to cure the cancer, the treatment has been shown to increase the lifetime and the quality of life for patients suffering from liver cancer. In addition, ^{90}Y has been used for its beta radiation to sever pain-transmitting nerves in the spinal cord as well as to treat inflamed joints and rheumatoid arthritis. [10] It's only deficiency with respect to other beta emitters is that it is not attracted to a specific region of the body and hence must be injected with a very fine needle to the site of the tumor.

I.A.1.5. *^{131}I*

The use of ^{131}I has been primarily as a treatment of thyroid cancer. ^{131}I is a beta emitting radioisotope with a half life of 8.02 days. [3] The treatment mechanism is similar to that of liver cancer using ^{90}Y, yet much more efficient. The thyroid absorbs iodine in order to produce the hormones that regulate the body's metabolism. In patients with thyroid cancer, it is often the case that cancer cells will also absorb iodine from the blood stream, and if the iodine is radioactive in the form of ^{131}I, the beta radiation emitted will help to kill these cancer cells. [11] This treatment can be as simple as taking a ^{131}I pill because the thyroid can be made to absorb nearly 100% of the iodine in the bloodstream by starving the thyroid of iodine for weeks before treatment.

I.A.2. *Global Supply and Demand*

The need for domestic production of the isotopes mentioned above cannot be overstated. The United States may be even more dependent upon foreign sources for these isotopes than it is on oil. Nearly the entire global supply of these isotopes is produced by only five reactors world-wide. [5] In addition, none of these reactors are in the United States and all five of them are over 40 years old and can be expected to be decommissioned within the next decade. All five of these reactors are also subsidized by their respective governments. Two more reactors have recently entered the market in Australia and Poland, but their contribution to the global supply cannot yet be determined. These reactors are listed in Table I.1 below.

Table I.1. List of current radioisotope producing reactors which produce nearly the entire global supply of high Z isotopes used in the medical industry. Table courtesy of the IAEA. [5]

Existing research reactors used by large-scale producers						
Country	Name	Thermal power, MW	Thermal neutron flux, n/s/cm^2	Target type	Maximum annual operation, days[3]	Typical share of production %
Canada	NRU	135	4.0e14	HEU	315	40
Netherlands	HFR	45	2.7e14	HEU	290	30
Belgium	BR-2	100	1.0e15	HEU	115	10-15
South Africa	Safari-1	20	2.4e14	HEU	315	10-15
France	OSIRIS	70	1.7e14	HEU	220	5-8
Australia	*OPAL*	*20*	*3.0e14*	*LEU*	*340*	*yet to enter market*
Poland	*MARIA*	*30*	*3.5e14*	*HEU (for Covidien)*	*200*	*not known*

Relying on foreign sources for these isotopes means longer travel times between the production facility and the hospitals that uses them. With a half life of 66 hr for ^{99}Mo, this reduces the amount of product received for a given purchase price. More importantly however, relying on foreign sources which each provide such a large fraction of the global supply makes the United States highly susceptible to unplanned or extended outages. A clear example of such an outage occurred recently at the NRU facility in Canada from May 2009 to July 2010. [5] During this time, the other four reactors struggled to meet the demands of the market. At any given time during this period in the United States, 20-70% of all diagnostic imaging procedures were either cancelled or postponed. [5] From these experiences, it seems that the best course of action would be to build a series of reactors with limited isotope production that would supply isotopes to smaller geographical regions. In this case, the market would not be as significantly affected during unplanned outages of a single reactor.

Currently, the United States uses the same amount of ^{99}Mo as the rest of the world combined. The domestic consumption is estimated at 6,000 $Ci_{6\text{-day}}$ per week (a $Ci_{6\text{-day}}$ is the activity in Ci, 6 days after it leaves the producer's facilities). This consumption is expected to grow at a rate of 5-10% per year. [4] The estimated revenue generated by the five reactors listed above from the United States alone is $150 million per year from just ^{99}Mo. [4]

I.B. Current Production Method

Designing a reactor for radioisotope production necessitates an understanding of the current methods of production so that various figures of merit can be developed for comparison. This section will focus on the advantages and disadvantages of the current production methods so that the incentive for a new design can be clearly understood.

I.B.1. *Solid Target Irradiation*

Nearly the entire global supply of radioisotopes for use in the medical industry is produced by solid target irradiation. With this production method, a solid target made of a neutron absorbing material is placed in a neutron beam or near the core of a nuclear reactor. The material is chosen based on the isotopes to be produced. For medical isotope production, the targets are made of highly enriched uranium (HEU) which is over 90% ^{235}U. [2] The ^{235}U atoms fission upon absorbing a neutron and the resulting distribution of isotopes are neutron rich and radioactive. Included in this distribution are the five isotopes mentioned in section I.A.1.

Particle accelerators have been used to produce neutron beams by spallation in which protons are accelerated into a material which absorbs the protons and subsequently emits neutrons. Particle accelerators and cyclotrons are typically used to produce short-lived, low Z isotopes, such as ^{11}C, ^{13}N, ^{15}O, and ^{18}F, which are not typically produced from the fission of uranium, but can be used for positron emission tomography. Unfortunately, they do not efficiently produce ^{99}Mo or other high Z isotopes at quantities suitable to match the medical industry's demand. In addition, the specific activity of the product is simply too low to compete with the product attained by irradiation in a nuclear reactor. One nuclear reactor using HEU can produce the same amount of ^{99}Mo as 160 accelerators. [12]

For this reason, it is no surprise that nuclear reactors are used to produce nearly the entire global supply of high Z isotopes for the medical industry. As previously mentioned, this supply is produced almost entirely by only five nuclear reactors. There are smaller reactors capable of producing these isotopes, but they do so infrequently and in small amounts, or are used primarily as research reactors. HEU is used in the large scale production of medical isotopes because the higher

concentration of ^{235}U allows for a larger production rate. Although the use of HEU creates a large supply of ^{99}Mo, it is criticized for the larger risks associated with nuclear security and proliferation concerns. This has caused regulatory bodies such as the IAEA to call for medical isotope producing reactors that use low enriched uranium (LEU) targets. [13]

I.B.2. *Inefficiencies*

For medical isotope production by a nuclear reactor, solid target irradiation is a rather inefficient process. This is due in part to the high power density ratios between the fuel of the reactor and the HEU target. It is not unusual to have these ratios be as high as 100:1. [2] With such a large ratio, effectively 99% of the neutrons that could be used if the target were inside the core are wasted. It is expected that one might ask why the targets are not placed inside the core. This is because the core is typically designed to be in steady state operation for months or even years at a time to maximize the burnup of its fuel. The targets on the other hand are typically only irradiated for time scales on the order of days before the activity of the desired isotope has reached its saturation value. By placing the target in the vicinity of the core, the target can be irradiated without contributing to the chain reaction and subsequently be removed while the reactor is still in operation.

After the target is irradiated, it is dissolved in solution which allows for isotope separation by a series of sorbents and chemical treatment. Once the separation stage is complete, the remaining fuel in solution is stored as high level waste (HLW). It is not economically attractive to attempt to form this solution into a new solid target because this process would be more expensive than the already costly process of fabricating fresh solid targets. [2]

The isotopes of interest for the medical industry typically have half-lives on the order of days or weeks. The half life of the most profitable medical isotope, ^{99}Mo, is only slightly below 66 hours. For this reason, it is desirable to separate the isotopes as quickly as possible so that the product does not decay entirely before it can be sold. Any unnecessary step in this separation process is costly. As will be seen in section I.C, the dissolution of the fuel in solution is unnecessary if the target exists in this form throughout its irradiation.

I.B.3. *Benefits*

There are benefits to the solid target irradiation method using either a nuclear reactor or an accelerator. The reactors that typically perform solid target irradiation are either pool type reactors, which make it easy to place samples near the core, or they have beam ports that allow for irradiation in a dry environment. An example of such a reactor is the TRIGA nuclear reactor at the Nuclear Science Center at Texas A&M University. In fact, the "I" in TRIGA stands for isotope production.

The use of such reactors allows for great flexibility. For instance, many of these reactors have multiple beam ports that can be used for neutron scattering experiments, neutron tomography, or other forms of research. In addition, these reactors utilize typical heterogeneous lattice cores similar to those found in the power industry. For this reason, reactors such as the TRIGA reactor are commonly used for training senior nuclear engineering students or beginning nuclear reactor operators.

A similar argument holds in favor of solid target irradiation by an accelerator or cyclotron. Accelerators can be used in a number of research areas when they are not being used to irradiate solid HEU targets or other neutron absorbing materials. Accelerators are often used in materials

science to deliver large doses of radiation damage in short time intervals to determine the change in the properties of new and innovative materials in a radiation field. In addition, accelerators can easily be turned on or off, have little security or proliferation risks, and may be scaled to match the local demand if used for isotope production.

I.B.4. *Attempts and Motivation for Using LEU*

The technology of utilizing LEU targets for use in reactors is still under development. There are small scale-producers in both Argentina and Australia that use LEU for isotope production. [13] These facilities have shown that using a lower enrichment increases the purity of the radioisotopes and their yield per unit power. It also allows for the recovery of isotopes other than ^{99}Mo such as ^{131}I. Although the use of LEU seems to be more beneficial because it decreases proliferation risks, increases the variety of isotopes produced, and has a higher purity of ^{99}Mo; it is not economically favorable. This method decreases the amount of ^{99}Mo that companies can supply, significantly decreasing the profit margins. Unless there is government funding for the use of these targets, there will be little incentive for facilities convert to LEU.

I.C. Overview of Solution Fueled Reactors

Recent research into new and innovative methods of radioisotope production has revived interest in the aqueous homogeneous reactor (AHR), which was considered as one of the very first nuclear reactor designs. The FFAHR is a variation of this type of reactor. It is therefore necessary to review AHR's and their benefits for isotope production. It is also necessary to understand the shortcomings of these reactors in order to understand why changes need to be made in their design. This section focuses on these topics and presents various examples of AHR's throughout history and currently in operation.

I.C.1. *History and Technical Deficiencies*

The thought to design a nuclear reactor whose fuel is mixed with its moderator is not exactly unfamiliar. Such designs were considered as early as 1940 for use in the Manhattan Project, and interest has waxed and waned ever since. The motivation for such a design is clear when you consider the cost of solid fuel fabrication that is necessary for typical heterogeneous reactors. This inconvenience is doubled if the end goal is to extract fission products from the fuel; in which case the spent fuel would need to be dissolved in solution to chemically separate the isotopes of interest. This was indeed the case in the early 1940's when the purpose of a nuclear reactor was to produce plutonium. For this reason, it can be understood why chemical engineers of the time were so vocal in support of a reactor whose fuel existed in a liquid form that could be chemically treated for isotope separation, and then reinserted into the reactor.

AHR's utilize various forms of uranium compounds that are soluble in water. In its simplest form, an AHR is simply a container of this solution of the right size and shape to achieve criticality. The earliest examples of AHR's utilized a mixture of uranium oxide (U_3O_8) and heavy water. [14] The cost associated with the predicted amount of heavy water required was the eventual downfall of such early designs. Fortunately, the absorption cross section for deuterium at the time was highly over estimated and the amount of heavy water required was much less than predicted. Further reductions in moderator requirements would be made when enriched uranium became available, making it possible to eliminate the need for heavy water altogether.

Even with the technical advancements made into the mid 1940's, the prominent issue plaguing AHR's was the corrosive properties of the various fuel solutions. This continues to be a challenge today. In the 1940's and 1950's, Los Alamos National Laboratory (LANL) conducted re-

search into the use of AHR's for power production with five experimental reactors known as LOPO, HYPO, SUPO, LAPRE-1, and LAPRE-2. LOPO was a low power reactor which utilized uranyl sulfate fuel, while HYPO and SUPO had higher power outputs and utilized uranyl nitrate fuel. LAPRE-1 and LAPRE-2 utilized uranium oxide mixed in high concentration phosphoric acid. While each of these reactors was able to run for extended periods of time, each one also exhibited ample corrosion rates at high temperatures. [14] Similar reactors were built at Oak Ridge National Laboratory (ORNL) with the same results.

The most recent, and by far the most successful AHR experiment, is the ARGUS reactor at the Kurchatov Institute in Russia. This reactor has been in operation at 20 kW since 1981 and has demonstrated the ability to produce ^{99}Mo and ^{89}Sr for use in the medical industry with extraordinary efficiency. ARGUS has been able to avoid excessive corrosion due to extensive cooling systems and by operating at a lower power density of 0.9 kW/L. This leads to a lower operating temperature than the initial U.S. experiments. ARGUS utilizes a uranyl sulfate solution with a concentration of 73 g U / L and an enrichment of 90% ^{235}U. [15]

Another complication that arose in the design of AHR's was the potential for power oscillations due to several contributing factors. The first of these factors was the bubble formation caused by radiolysis. Even with the temperature of the fuel solution well below its boiling point, radiolysis of water in a radiation field can cause the water molecules to dissociate into hydrogen and oxygen gas, which give the appearance of fuel solution boiling. The constant changing of both the local density and the shape of the critical mass due to bubble evolution at the surface of the fuel can cause oscillations in the reactivity and hence the power. [2] Fortunately, these oscillations are damped and can be worked around, however a truly steady state can never be reached with an AHR in which the fuel is stagnant.

The second contributing factor to the power oscillations was the precipitation of the fuel out of solution. If the hydrogen and oxygen gas is not recombined and reinserted into the system, or if additional water is not added to make up for the lost hydrogen and oxygen gas, the pH of the system may stray from its ideal value of slightly above unity. If the pH rises above 3 or drops below 1, the fuel will precipitate out of solution causing local rises in fissile atom density. [2] The control of the pH is thus an important factor in avoiding power oscillations. It was for these reasons that AHR's were not chosen as the initial design for power producing nuclear reactors.

I.C.2. *Benefits for Isotope Production*

While AHR's may not be suitable for power production due to their limited power density, ARGUS has shown their potential for use in radioisotope production. When compared to the current solid target irradiation production method described in section I.B, the benefits of AHR's for radioisotope production are numerous.

The most striking benefit of AHR's for radioisotope production is their efficiency due to high neutron economy. As mentioned previously, it is not unusual for solid target irradiation systems to have power density ratios between the fuel and the target as high as 100:1. [2] Even with the limited power density of AHR's, the fuel and the target are one and the same, so that the power density can theoretically be comparable to that in the target of solid target irradiation systems while only producing a hundredth of the total power.

Another benefit of AHR's is the reduction in radioactive waste. In solid target irradiation systems, the irradiated target is dissolved in an acid solution to separate the isotopes of interest. What remains is stored as waste due to its high radioactivity. The fuel of an AHR is already in the form of an acid solution, so that once the isotopes are retrieved from the fuel, it can be rein-

serted into the reactor and used repeatedly until the reactor is decommissioned. This significantly reduces the amount of waste produced for a given amount of isotope production.

The targets used in solid target irradiation are also very costly to fabricate. This is in part due to the high enrichment which is normally above 90% ^{235}U. [2] The solid target fabrication step is obviously eliminated by using a liquid fuel in which the uranium dioxide is simply mixed with an acid solution and diluted to the desired concentration.

Another advantage of liquid fueled reactors is their limitless burnup. Heterogeneous reactors are limited in burnup due to radiation damage of fuel elements or loss of reactivity. [14] AHR's could conceivably run for 40 years on the same fuel loading and burn actinides since the only radiation damage to the fuel is radiolysis, which is reversible. In addition, there is no need to shut down an AHR for isotope separation if a separation loop is included into the design so that isotopes are separated continuously as the reactor is running. If it were not for the corrosion issue that necessitates the replacement of reactor components on a regular basis, an AHR could run uninterrupted until the excess reactivity of the initial fuel loading is used up.

The separation of gaseous fission products such as ^{133}Xe is also much more efficient in an AHR where an off-gas extraction line can be designed to remove these isotopes from the reactor while it is running. [2] These isotopes may be released from solid irradiated targets prior to dissolution in acid for isotope recovery.

AHR's are also attractive from a safety perspective due to their large negative temperature coefficients of reactivity. This is due to the reduction in the density at elevated temperatures which reduces the fissile atom density and hence the criticality. The temperature coefficients of reactivity are typically more negative than those of a heterogeneous reactor. In early studies at

LANL, the criticality was able to be controlled simply by adjusting the fuel concentration and relying on this temperature dependent density change without the use of any control rods. [14] Finally, and perhaps most importantly, AHR's are expected to cost almost an order of magnitude less than their research reactor brethren which currently carry out the solid target irradiation. [2]

It is not surprising that with all of these benefits over the current radioisotope production method, interest in AHR design has peaked recently. Babcock & Wilcox has recently proposed a design for an AHR which it calls the Medical Isotope Production System (MIPS). [16] The MIPS is a 200 kW unit that uses LEU that is less than 20% ^{235}U, whereas most of the previously designed AHR's have used HEU. A diagram of MIPS is shown in Figure I.3.

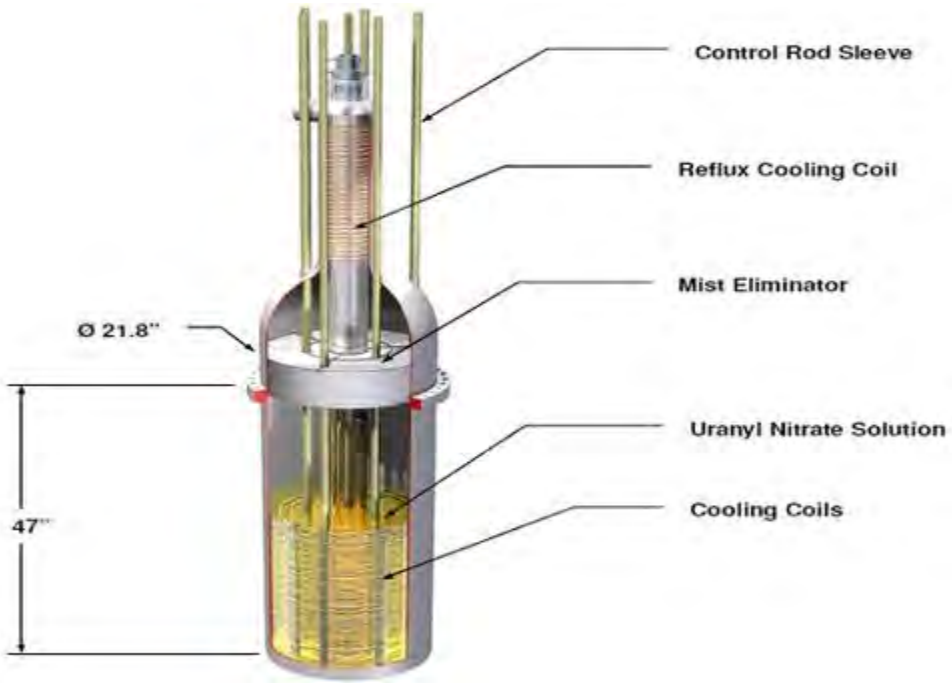

Figure I.3. Diagram of the MIPS design by Babcock & Wilcox. Figure Courtesy of Babcock and Wilcox. [16]

I.C.3. *Necessary Improvements*

Although the benefits of using an AHR for radioisotope production are abundant, the complications associated with AHR's cannot be denied. Especially with the stringent regulations for reactor licensing in the United States, extensive work must be done to improve upon the current AHR designs.

The corrosion issue in particular must be addressed. This can be accomplished by using materials that have strong resistance to corrosion such as zirconium and titanium alloys. Zircaloy-4 in particular has been shown to have a corrosion rate of less than 0.1 mm per year when in contact with uranyl sulfate at 250 °C. [14] Recent designs have limited the corrosion by limiting the operating temperature that the reactor materials are exposed to.

The potential power oscillations must also be confronted. This may be achieved by mixing the fuel to even out local density fluctuations or by reducing the surface area of the fuel that is not in contact with a solid surface to reduce the effect of surface perturbations by bubble evolution. In addition, systems must be in place to carefully control the pH of the solution either by adding fuel or water, or re-combining the gases that result from radiolysis. This is especially important for systems that utilize uranyl nitrate fuel since the nitrate is susceptible to radiolysis in the same way that water is. [2]

The MIPS design by Babcock and Wilcox is intended to use LEU. This is a very attractive feature for future AHR designs, both from a cost perspective as well as a nuclear non-proliferation perspective. This is bound to be a necessity for any AHR seeking licensing in the United States. In fact, the National Nuclear Security Administration recently awarded NorthStar Medical Radi-

oisotopes, LLC, with two cooperative agreements of $2.8 million in federal support to establish a domestic production of ^{99}Mo using LEU. [17]

I.D. Description of Proposed Design

This section focuses on the current design as well as the previous FFAHR design. The FFAHR was intended to improve upon traditional AHR deficiencies primarily by the flowing of the fuel through the active core. The isotope production is directly dependent upon the power density, which is limited by the rate at which heat can be removed from the aqueous fuel. From the design of the FFAHR, it became apparent that a reactor using an aqueous solution as both its fuel and target would be far too limited by these constraints. It is for this reason that a hybrid system was proposed to utilize some of the benefits of both a liquid target system and the heterogeneous lattice configuration of conventional nuclear reactors.

I.D.1. *The FFAHR*

The design of the FFAHR is not very different from the traditional AHR. The primary difference is that in the FFAHR, the fuel solution flows through various regions of the reactor system which is shown in Figure I.4. During a shutdown period, all of the fuel solution resides in the mixing vessel which is kept subcritical by permanently placed absorber rods. During operation, the fuel is pumped upward from the mixing vessel through the active core region where fission reactions take place and isotopes are produced. While in the active core, the temperature of the fuel will rise and after the solution leaves the core, it must be cooled back down to room temperature. To accomplish this, the fuel leaving the active core passes through a heat exchanger. After passing through the heat exchanger, half of the fuel is fed back to the mixing vessel and the other half is transported to the isotope separation system where the various desired isotopes can be separated

from solution. The chemically treated fuel is then returned to the mixing vessel where it is once again pumped upward through the active core. The cycle repeats itself indefinitely until the reactor is shutdown, in which case, all fuel is once again safely stored in the mixing vessel.

1. Mixing vessel
2. Core
3. Fuel heat exchanger
4. Boric acid heat exchanger
5. Pipeline to separation system
6. Pipeline for fuel reinsertion
7. Freeze plug drainage line

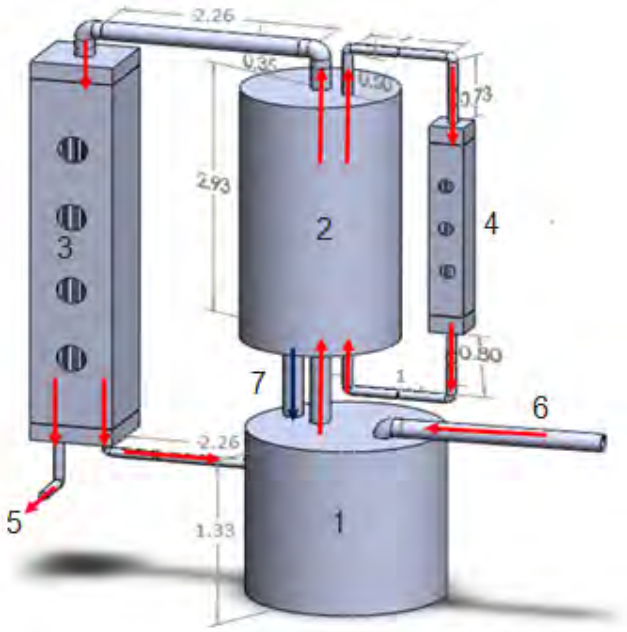

Figure I.4. Conceptual drawing of the FFAHR.

Despite the fact that the fuel is cooled back down to room temperature after leaving the active core, measures must be taken to keep the fuel below its boiling point within the core if the fuel is to reside in this region for an extended period of time. In addition, a control mechanism must be in place to raise and lower the power level. This is accomplished by flowing boric acid through pipes that run through the active core. The boric acid serves as both a heat removal system and a control system. The boric acid flows quickly through the interior pipes removing heat from the

fuel solution and is cooled back down outside of the core in the boric acid heat exchanger. The boric acid also serves as a control mechanism through the large neutron absorption cross section of ^{10}B. In this way, the concentration of the boric acid can be changed to control the criticality of the active core and allow for power level changes. In addition to the boric acid, boron carbide control rods in the core can be raised and lowered for large changes in the reactivity.

The primary benefit of the flowing fuel lies in the fact that the active core no longer has a perturb-able surface as in stagnant AHR designs. There is no exposed fuel surface anywhere within the active core or the pipelines during steady state operation; the only surface is located within the mixing vessel where the fuel is kept subcritical. In this way the power can be maintained at a steady, predictable level without having to adjust control rods to account for changes in the shape of the critical volume, as would have to be done in a stagnant fuel AHR subject to surface perturbations.

The fuel solution of the FFAHR is aqueous uranyl sulfate ($UO_2SO_4 + H_2O$). Uranyl sulfate is highly soluble in water, but its solubility is extremely sensitive to the pH of the solution. The pH should be kept close to unity, and should not exceed a value of three or else the precipitation of uranium and several fission products will become severe. [2]

Changes in the pH level of the solution are due mostly to radiolysis; the water molecules dissociate into hydrogen and oxygen gases. Fortunately, the recombination of these gases to form water is a well-understood existing technology. The hydrogen and oxygen can be separated from the fission product gases in the gaseous isotope separation system which collects the gaseous fission products from the top of the mixing vessel. The gases are then sent through a recombination process in which they will be re-combined to form water, which is then inserted back into the mix-

ing vessel. By keeping the water concentration nearly constant, the pH will remain within a safe range around the target value of unity.

In addition to keeping the pH balanced, precipitation of the uranyl salt out of solution can be discouraged by constantly agitating the fuel solution. This is accomplished in part by the continuous movement of the fuel throughout the reactor system, and implemented further within the mixing vessel.

Solution fuels are notorious for being highly corrosive to standard structural materials. Although corrosion damage is unavoidable, it can be limited to an extent by operating the system at low temperatures where corrosion rates are slower. In stagnant fuel AHRs heat removal is often accomplished by running coolant lines through the fuel solution. Overall, this is an effective way to keep the fuel temperatures below a set limit, but it allows for the formation of hot spots within the core away from the coolant pipe lines. This can lead to changes in fuel density and therefore uneven and inefficient fuel burn up.

The flowing fuel design achieves a uniform cooling of the fuel which will limit the corrosion rates while also reducing excessive hot spot formation within the fuel. The fuel enters the active core at room temperature and exits at a maximum temperature of 75˚C. At these low temperatures the corrosion rates are at a minimum, thus maximizing the lifetime of the structural materials. By keeping each cycle of the fuel through the active core thermodynamically identical there will be no need to worry about fluctuations in the fuel properties due to changes in the temperature profile over the lifetime of the reactor.

An added benefit of the flowing fuel design is the ease of isotope separation. Using solution fuels generally simplifies the isotope separation process compared to using solid target fuel be-

cause the dissolving of the solid target is avoided all together. The isotope yields per kW are also higher because the fuel is the target in a solution reactor, whereas in a solid fuel reactor the fuel and the target are separate components and the majority of the neutron population is used to fission the fuel and not the targets.

The flowing fuel design not only carries the benefits associated with liquid fueled reactors, but also allows for online isotope separation. Typical stagnant AHR's operate for a fixed amount of time, are shut down, drained, and the fuel is sent to the separation facilities all at once. Once the isotopes have been separated, the fuel is added back to the reactor and it is restarted. In the flowing fuel design, a portion of the fuel solution goes directly to the separation facilities after exiting the heat exchanger, while the rest goes back into the mixing vessel. Once the desired isotopes have been extracted the fuel is sent back into the reactor system. Continuously extracting the fuel solution to separate out the desired medical isotopes maximizes the yields by limiting the decay time between activation and isotope separation.

The unfortunate conclusion of the FFAHR design was that the ^{99}Mo production rate was determined to be a fraction of a percent of the current U.S. consumption. As previously mentioned, this production rate was limited by heat removal from the fuel. The heat removal could be made more efficient by increasing the flow rate of either the fuel solution or active coolant through the core; however, increasing the flow rate of the fuel leads to undesired safety issues. Increasing the fuel flow rate decreases the fraction of delayed neutrons that are emitted within the core making the reactivity more difficult to control. The flow rate of the FFAHR was chosen so that over 99.9% of delayed neutrons were emitted within the core, justifying a quasi-static assumption for the criticality calculation. The fraction of delayed neutrons emitted within the core drops off sharply with increasing core flow rate as shown in Figure I.5.

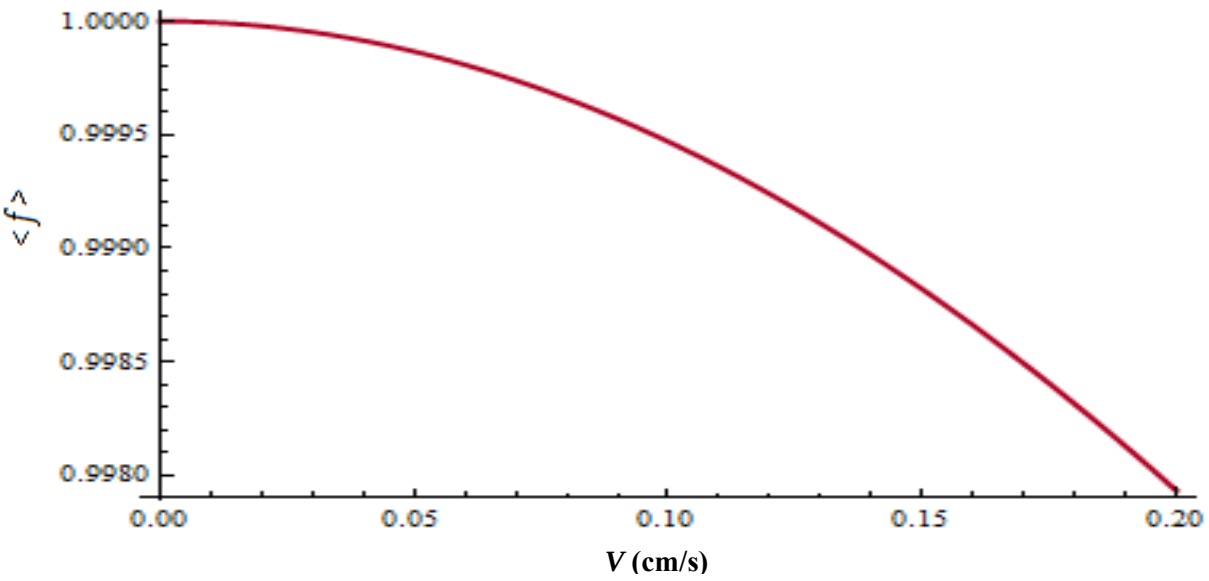

Figure I.5. Fraction of delayed neutrons emitted in the FFAHR core as a function of velocity.

If the solution reactor were designed to be subcritical and coupled to a neutron source with a control system already in place, the importance of these escaping delayed neutrons would be highly diminished. This would allow for a higher, variable fuel flow rate and hence more efficient heat removal and a more flexible isotope separation scheme. This is the motivation behind the design presented in this report which will be referred to as the Aqueous Target System (ATS).

I.D.2. *The ATS*

The ATS design is intended to act as a hybrid of the current solid target irradiation method and the FFAHR. As a first approach, imagine that the solid targets in the current production method were replaced by aqueous solution targets to utilize the waste reduction benefit of traditional AHR's. This benefit may be overwhelmed by the difficulty of target cladding corrosion at high

temperatures that has traditionally plagued all aqueous fuel reactors. In addition, the solution in these targets would eventually boil leading to pressurization and fuel precipitation issues as previously mentioned. Now imagine that the targets exist as pipes that run through the active core so that the liquid target can now flow through the core as in the FFAHR. The primary difference from the FFAHR is that the solution is no longer required to achieve criticality by itself. While this reduces the benefit of high neutron economy that is inherent in AHR designs, it allows for a variable fuel flow rate and more heat removal without sacrificing safety in operation, since the delayed neutrons emitted in the solution are no longer essential to reactivity control.

The reactor chosen as the neutron source for the preliminary ATS design is the Annular Core Research Reactor (ACRR) at Sandia National Laboratories. This reactor is chosen because of its central irradiation cavity in which a flowing aqueous target can be easily placed. Although the current design is focused on using the ACRR as the external neutron source, there is absolutely no reason why the ATS could not be coupled to a more conventional and accessible research reactor such as the TRIGA reactor at the Nuclear Science Center at Texas A&M University. The symmetry of the ACRR core simply allows for a more uniform flux distribution in the cavity where the ATS will be placed. Details such as material compositions and geometry specifications will be presented in Chapter II, but the one sentence description of the ATS is a series of pipes that run upward through the central irradiation cavity of the ACRR carrying a uranyl sulfate fuel, while the rest of the cavity is filled with a coolant flowing in the opposite direction for heat removal. To extend this idea to other research reactors, it may be feasible to simply replace selected fuel rods with pipes that can carry the solution target. For details about the ACRR, one should consult Sandia Report 2006-3067 titled *MCNP/MCNPX Model of the Annular Core Research Reactor* by DePriest *et al*. [18]

CHAPTER II

METHODS

This chapter describes the methods and codes used in the preliminary design of the ATS. The design of a nuclear reactor or target system is an extraordinarily complicated process that involves analyses in multiple disciplines including nuclear engineering, mechanical engineering, chemical engineering, and of course, economics. It would be foolish to claim that any analysis performed by a single individual over the course of a two semester research project could adequately include every aspect of a full design analysis. It is with this in mind that the chapter begins by defining the scope of the ATS design presented in this report.

II.A. Scope

While the FFAHR design was unsuccessful in its attempt to supply a reasonable fraction of the domestic consumption of ^{99}Mo, the scope of that research was quite broad. Nearly every major aspect of a nuclear reactor design process was considered in that analysis. [19] The scope of the FFAHR design included:

- Neutronics
- Thermal hydraulics
- Radiation shielding
- Isotope separation
- Environmental analysis
- Nuclear non-proliferation analysis
- Economic analysis

The FFAHR design was the result of a four person, two-semester long research project. The preliminary evaluation of the ATS will involve a slightly more limited scope, focusing instead on the major physics concerns in reactor design: neutronics and thermal hydraulics.

II.B. Neutronics

The modern nuclear engineer is blessed to have access to a plethora of computer codes that can calculate key parameters in the design of a nuclear reactor or target system. A good starting point to any research in reactor design is choosing the appropriate codes to use based on their capabilities and the researcher's experience level. For the neutronics analysis of the ATS, most of the calculations will be performed with Serpent 2 (Beta).

Serpent 2 is a Monte Carlo neutron transport code that simulates individual neutron histories in a three dimensional model to calculate parameters such as criticality, neutron fluxes, reaction rates, and burnup. As the number of histories increases, the statistical error in the calculation of these parameters decreases significantly. This allows the use of parallel computing to simulate a large number of histories in a relatively short amount of time to reduce the statistical error to an acceptable level. Details including code comparisons and benchmark studies for Serpent 2 can be found at the developer's website. [20]

Prior to using a code as robust as Serpent 2, a model of the target system must be constructed involving all material compositions and geometries. As the construction of this model may be extremely complicated, it is not desirable to try to get everything right on the first shot. This was a mistake made in the design of the FFAHR. The problem with that approach was that an exorbitant amount of time went into creating the model, which left no time to adjust it when the results were not close to what was desired. Thus, the first step must be to approximate the most im-

portant results with a preliminary model, to determine if they are in the desired range, and then to refine the model to perfection. The most important result for the ATS design is the production rate of ^{99}Mo.

The effective strategy to accomplish this estimation will be to add the solution target to the ACRR irradiation cavity and calculate the ^{99}Mo production rate for various target geometries and compositions. Once a configuration is found that both produces a substantial amount of ^{99}Mo and is thermodynamically viable, necessary changes to the design of the reactor can be made. These changes might include the addition of control rods or the removal of fuel rods to counteract the addition of a significant amount of fissile material in the irradiation cavity. Other changes such as the composition of the solid fuel may be necessary from a licensing and economic standpoint. However, these changes have a minimal effect on the ^{99}Mo production rate when compared to the target geometry and composition.

As the model is adjusted after a target geometry and composition are found, many calculations must be performed to insure the feasibility of such as design. These calculations include the reactivity of the reactor/target system, the flux profile in the target, the production rates of other important nuclides, and the lifetime of the fuel loading of the ACRR when run at constant power for isotope production.

The reactivity of the reactor/target system is a standard output of the Serpent 2 simulation. It must be considered because the control mechanisms of the ACRR should not be changed significantly by adding the target system. This may require the addition of control rods in the irradiation cavity and reactor lattice to allow the reactor to achieve criticality at its current control rod heights. What this means is that the addition of burnable poisons in the irradiation cavity and in

the reactor lattice should bring the reactivity of the combined system close to the reactivity of the reactor with a vacant irradiation cavity without adjusting the ACRR control rod heights significantly.

The flux profile in the target solution can be obtained by adding detectors to the Serpent 2 model. The primary purpose of the flux profile is to determine the heat generation rate for use in the thermal hydraulics analysis. Heat generation is directly proportional to the neutron scalar flux and is used to determine the temperature of the target solution exiting the irradiation cavity. As mentioned in Chapter 1, this temperature must be kept below 100˚C to avoid excessive corrosion.

The production rates of nuclides aside from ^{99}Mo are important for a variety of reasons. The first of these is that other nuclides such as ^{133}Xe, ^{89}Sr, ^{90}Y, and ^{131}I are profitable as well and there exist known separation processes for these nuclides. The second reason is that some alpha emitting nuclides are undesirable to have in-solution at high quantities. This is because their presence reduces the purity of the deliverable ^{99}Mo as well as the separation efficiency. [2] Other nuclides such as ^{135}Xe and ^{149}Sm have high neutron cross sections and act as neutron poisons. Their equilibrium concentrations in the target solution will slightly reduce the production rate, and hence must be considered.

The final neutronics consideration is the lifetime of the ACRR fuel. The ACRR is currently operated in pulse mode and is rarely run at constant power. In this mode, the fuel lifetime is so long that it is rarely considered. If the reactor is operated at constant power continuously however, the fuel will eventually be consumed and the reactor/target reactivity will drop below the level to allow continued operation. This requires replacement of the solid fuel elements on a regular ba-

sis. The rate of replacement is anticipated to be on the order of one year, but a better estimation can be obtained via a burnup calculation using Serpent 2.

II.C. Thermal Hydraulics

The primary goal of the thermal hydraulics analysis will be to determine the flow rate and inlet temperature of the coolant required to keep the target solution outlet temperature below 100 ˚C. To perform these calculations, the code ABAQUS will be used. ABAQUS is a finite element solver used to solve the fluid flow and heat transfer equations for a three dimensional meshed geometry. The model built using ABAQUS will be identical to that built in Serpent. The most important inputs for the ABAQUS model will be the space dependent heat generation rate that will be superimposed over the mesh geometry and the target inlet velocity.

One benefit to using active cooling in the irradiation cavity to cool the target is that the ACRR can function in its normal passive cooling mode. This will effectively separate the thermal hydraulics analysis of the reactor and the target. This allows for a simple calculation of the power level in the target because the Serpent 2 model can be normalized so that the power level in the solid fuel of the ACRR can remain below the steady state power rating of 4 MW for the ACRR.

Additional thermal hydraulics considerations would be the design of the exterior coolant and target heat exchangers. As the target flows through the core, the temperature will rise to the outlet temperature and an external heat exchanger will be required to bring the temperature back down to the inlet temperature prior to re-entry. The same considerations must be treated for the coolant so that each cycle through the core is thermodynamically identical.

CHAPTER III

RESULTS

This chapter will discuss the Serpent 2 and ABAQUS models in depth as well as the results of various calculations performed using these models as they are refined. Prior to presenting the model of the ATS, it may be helpful to review the ACRR as it currently exists. The layout of the ACRR can be seen in Figure III.1.

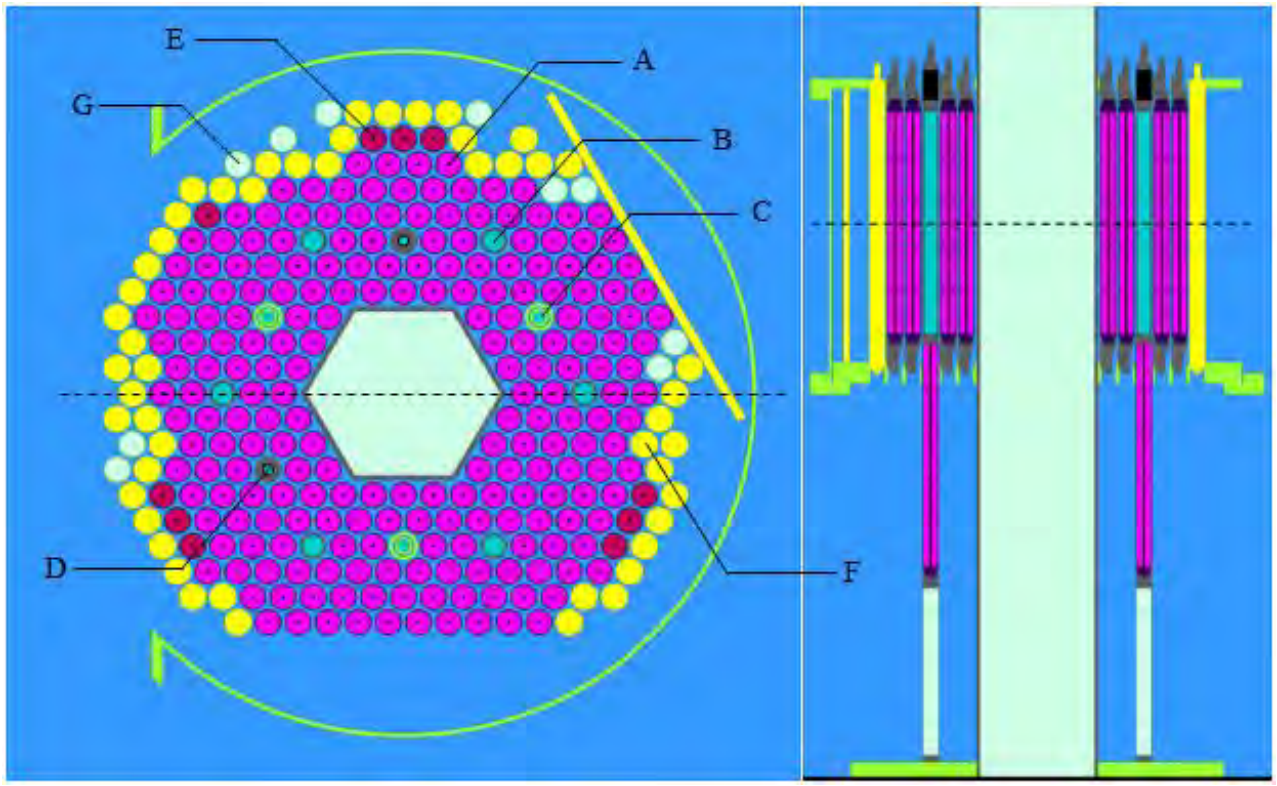

(a) (b)

Figure III.1. (a) Top view of the ACRR core lattice. (b) Side view of the ACRR core lattice. Each view is to be interpreted as a slice through the core along the dotted line of the opposite view.

The reactor core as seen in Figure III.1 is submerged in a pool of water where the fuel elements are cooled by natural convection. The labeled components in Figure III.1 are discussed briefly below; however, the more interested reader is invited to read SAND Report 2006-3067 for a more detailed description. [18]

A: *Standard fuel elements.* These elements are composed of uranium dioxide/beryllium oxide pellets that are stacked in niobium cups as seen in Figure III.1 (b). This fuel material is 21.5 wt. % UO_2 and 35% enriched in ^{235}U. The density is 3.3447 g/cm^3.

B: *Fuel followed control rod.* This type of control rod is common in research reactors. As the control rod is removed, the reactivity of the reactor increases not only due to the removal of the neutron absorbing material, but also due to the addition of fuel. There are six of these in the ACRR lattice and they are inserted or removed together to approach criticality. The absorber material in the upper half of the control rod is boron carbide.

C: *Fuel followed safety rod.* These rods are nearly identical to the fuel followed control rod with the exception that they have a smaller diameter and are housed in a control rod guide tube to facilitate quick movement. These rods are fully removed during operation and are fully inserted in the event of a transient rod being stuck in the removed position during a pulse.

D: *Void followed transient rod.* These rods consist of an upper absorber region followed by a lower void region. They are ejected quickly to cause the reactor to pulse. These rods are also housed in guide tubes to facilitate quick movement.

E: *90% fuel elements.* These fuel elements are identical to the standard fuel elements with the exception that their density is 90% of the density of the standard fuel elements.

F: *Nickel reflector elements.* These rods are designed to have the same exterior dimensions as the fuel rods. They are entirely composed of nickel which acts as a neutron reflector to harden the neutron energy spectrum. Also seen in the upper right hand side of Figure III.1 (a) is a nickel plate that is used to cover the neutron radiography window when not in use.

G: *Experiment tubes/water elements.* These positions in the lattice can contain either air filled or water filled nickel elements, or even experiment tubes used to irradiate samples. They are modelled as air filled nickel elements in Figure III.1.

A primary goal of the ATS design is to add the target to the central hexagonal irradiation cavity without changing the operation of the reactor significantly. This involves two significant calculations. The first of these is that the power in any individual pin with the target in the cavity cannot exceed the power of the highest power pin in the vacant cavity case. This must be the case so that the reactor external to the irradiation cavity can continue to be cooled by natural convection of the pool water. Of course, the power in any individual pin is directly related to the total power produced by all of the standard fuel elements. The power profile in the lattice is expected to change significantly with the addition of the solution target to the cavity. The total power level must then be adjusted, to keep the maximum pin power below its value in the vacant case. The power profile calculated using the Serpent 2 model of the unaltered ACRR is shown in Figure III.2. This power profile assumes a total power in the standard fuel elements of 3 MW. Although the maximum steady state power of the ACRR is cited as 4 MW [21], such operation is rare, and a power of 3 MW was chosen for safety concerns as well as to extend the lifetime of the solid fuel elements of the lattice. Assuming a power level lower than the maximum power level will also allow for an additional degree of freedom in case this parameter needs to be raised in further analysis.

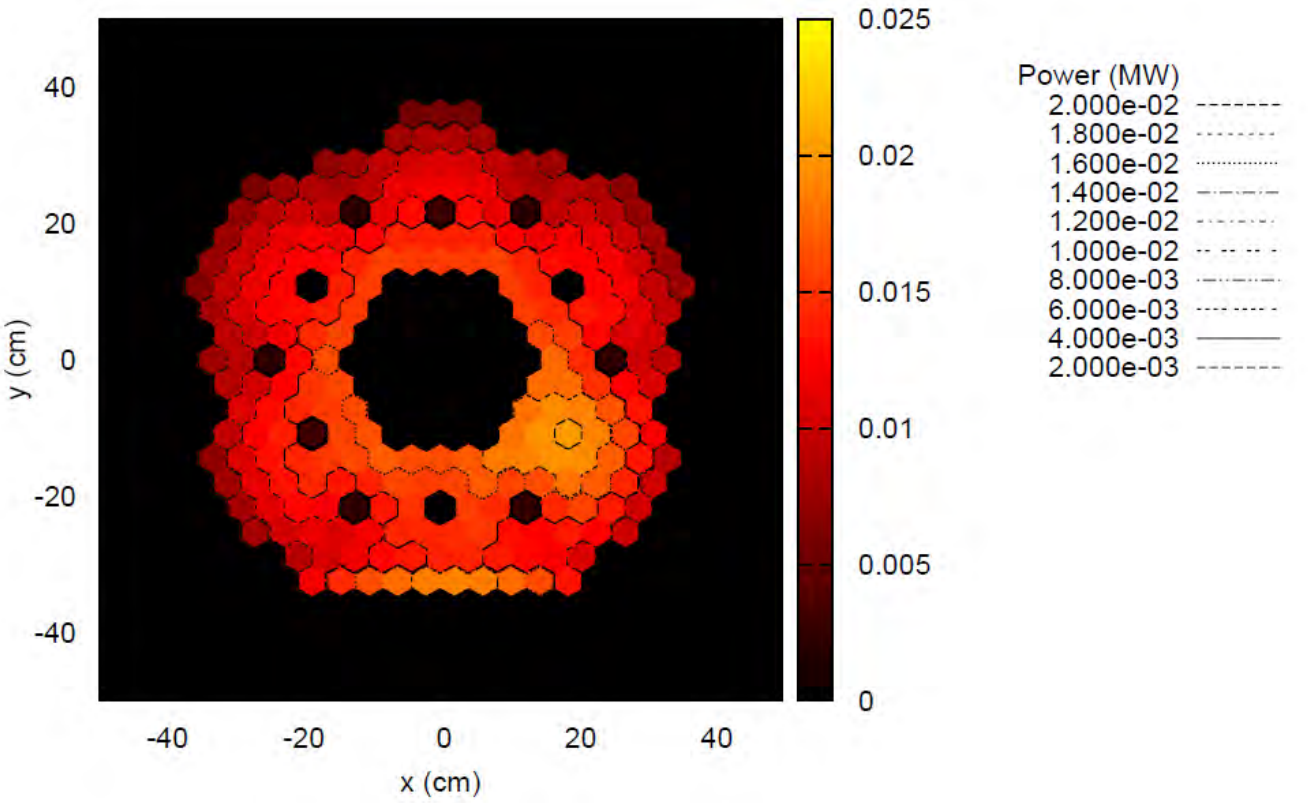

Figure III.2. Power profile of the unaltered ACRR at a steady state power level of 3 MW in the standard fuel elements.

The second calculation that must be performed is an integral rod worth analysis. This involves moving the control rod bank throughout its full range and calculating the criticality of the reactor at each step. The control rods are shown fully inserted in Figure III.1. When the control rods are fully removed, their fuel portion is at the same height as the standard fuel elements. The integral rod worth curve calculated using Serpent 2 for the unaltered ACRR is shown in Figure III.3. The criticality for the ACRR at cold shutdown is calculated to be 0.926, which corresponds to a reactivity of more than ten dollars below critical. The reason for this is that the ACRR is a research reactor designed to allow positive reactivity insertions to the irradiation cavity. For the ATS, it

will be sufficient to have a cold shutdown criticality of roughly 2 dollars below critical with the solution target in the cavity, which is double the requirement set by the NRC in NUREG-1537. [22]

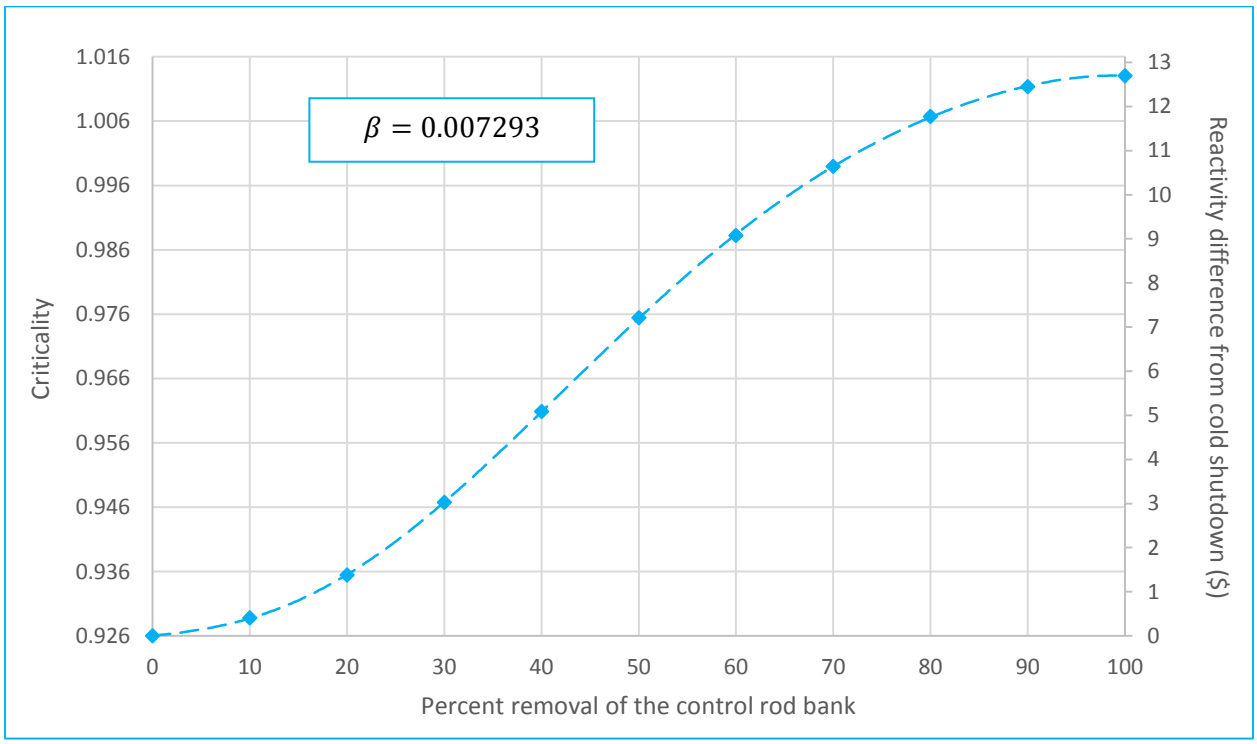

Figure III.3. Integral rod worth curve for the control rod bank of the unaltered ACRR.

It is encouraging that the calculations performed using Serpent 2 match those performed by DePriest *et al* using MCNP very closely. [18] For the ATS, the reactivity worth of the control rod bank is expected to be greater than the already large $12.7 for the unaltered ACRR. This is because the transient rods are of no use for a non-pulsing reactor and will instead be replaced with fuel followed control rods.

III.A. Addition of the Solution Target

In order to get a rough estimate of the production rate for various target geometries and compositions, the first step is to add the solution target to the cavity in various configurations. Once the various configurations are modelled, the total production rate of ^{99}Mo can be determined from the total fission rate in the solution target. This fission rate can be easily calculated through the use of detectors in Serpent 2. The lattice of solution pipes is chosen such that it is self-similar to the lattice of solid fuel rods in the ACRR. This can be seen in Figure III.4.

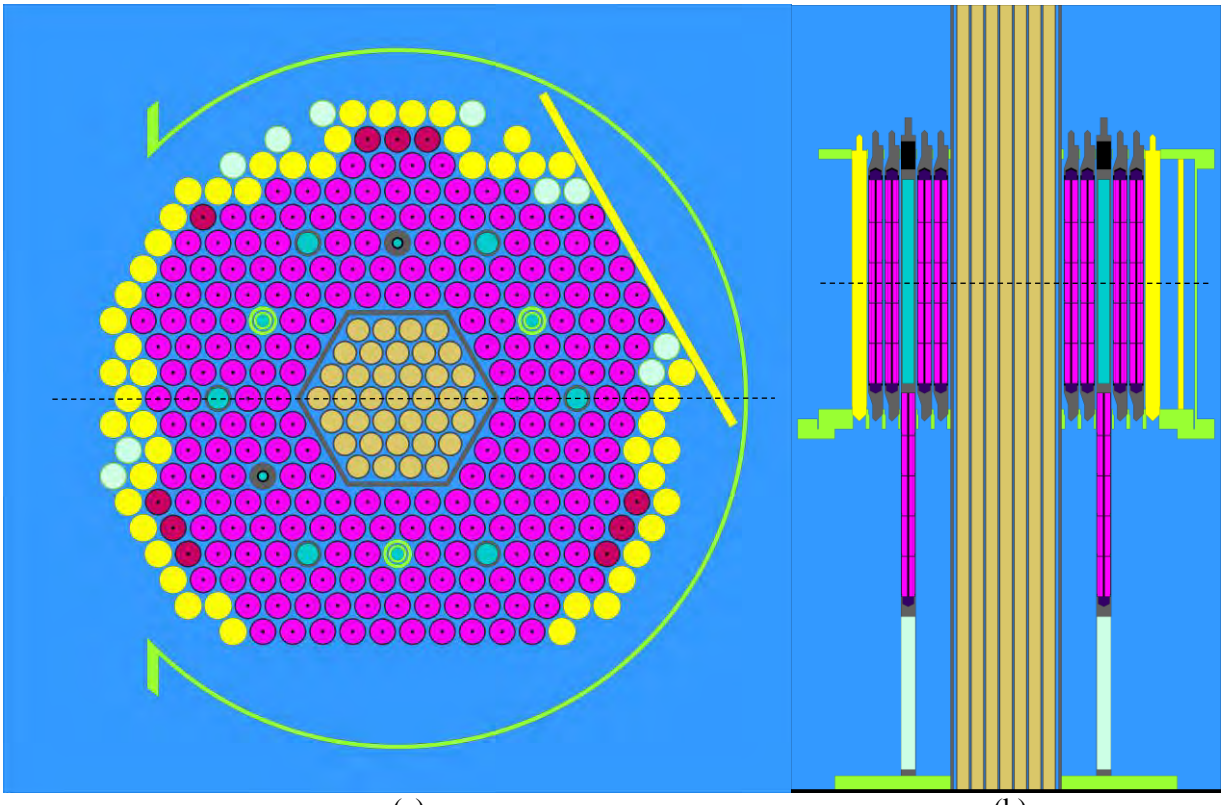

(a) (b)

Figure III.4. (a) Top view of the ACRR and ATS core lattice. (b) Side view of the ACRR and ATS core lattice. Each view is to be interpreted as a slice through the core along the dotted line of the opposite view. The pipe inner radius shown here is 1.5 cm.

There are two properties that can be easily changed at this point that will directly affect the ^{99}Mo production rate; these are the solution pipe radius and the concentration of the solution in g U/L. The enrichment is fixed at 20% ^{235}U in order to classify the target as LEU. The solution concentration has an added constraint in that it affects the separation efficiency of ^{99}Mo for most pass through sorbent extractors. Values of 100 g U/L to 200 g U/L can be found in the literature to produce the highest efficiencies of separation depending upon the sorbent and the nature of the compound. [14] [23]

For the ATS, the solution chosen is uranyl sulfate. There is significant debate among experts over whether the sulfate or nitrate is best for the purpose of ^{99}Mo production. Uranyl sulfate was chosen over uranyl nitrate because of its favorable properties in a radiation field. While it is true that nearly any compound will dissociate if irradiated with a large enough intensity of highly energetic neutrons, the sulfate is much more stable against dissociation. The nitrate on the other hand will undergo radiolysis at a rate comparable to water. [2] This radiolysis produces nitrogen and nitrogen oxide gases that are difficult to separate from other gases in order to reinsert them back into the solution. This makes it more difficult to control the pH of the solution in order to avoid uranium precipitation, which could potentially lead to power oscillations.

A range of radii and concentrations are considered for the initial analysis. The inner radius of the solution pipe is varied from 1.2 cm to 1.5 cm in steps of 1 mm. A smaller radius allows for more coolant in addition to less heat production. This may turn out to be beneficial if it is found that the solution outlet temperature cannot be kept below 100 ˚C in all cases. In each case, the thickness of the pipe wall is 2 mm. The concentration is then varied from 150 g U/L to 180 g U/L in steps of 10 g U/L. The ^{99}Mo production rate and the criticality with all rods completely inserted for each of the 16 combinations of the above radii and concentrations are given in Table III.1.

Table III.1. Pre-separation ^{99}Mo production rates and criticalities for each of the 16 combinations of radius and concentration initially considered for the original ACRR core.

Pipe inner radius (cm)	Concentration (g U/L)	^{99}Mo production rate ($Ci_{6\text{-day}}$ per week)	^{99}Mo production rate relative standard deviation (%)	Criticality	Criticality standard deviation
1.2	150	8205	0.00038	0.95668	0.000089
1.2	160	8747	0.00038	0.96116	0.000088
1.2	170	9290	0.00038	0.96557	0.000088
1.2	180	9802	0.00037	0.96986	0.000087
1.3	150	9999	0.00037	0.97110	0.000086
1.3	160	10650	0.00037	0.97630	0.000086
1.3	170	11261	0.00037	0.98171	0.000085
1.3	180	11848	0.00036	0.98652	0.000085
1.4	150	11930	0.00036	0.98656	0.000084
1.4	160	12662	0.00036	0.99282	0.000084
1.4	170	13367	0.00035	0.99843	0.000084
1.4	180	14044	0.00036	1.00423	0.000083
1.5	150	13944	0.00035	1.00268	0.000083
1.5	160	14757	0.00035	1.00920	0.000082
1.5	170	15509	0.00035	1.01565	0.000081
1.5	180	16207	0.00034	1.02139	0.000081

While each of the production rates above are significantly higher than the 6000 $Ci_{6\text{-day}}$ per week domestic consumption rate, it must be remembered that these production rates do not consider the efficiency of the separation process. After the solution passes through the irradiation cavity, it must pass through the external heat exchanger and the separation loop, and the efficiency of this separation loop is dependent upon many factors. These factors include the contact surface area of the solution and the sorbent, the uptake of the sorbent at the given concentration and temperature, and the time that the solution is in contact with the sorbent. The contact surface area can be

increased by diverging the flow of solution into many small pipes with the sorbent painted on their inner walls. The temperature can be controlled by the placement of the separation loop with respect to the external heat exchangers. The contact time is controlled by the flow rate of the solution as well as the length of the sorbent pipes. As ^{99}Mo is radioactive, there will also be a loss in efficiency due to decay as the time spent in the heat exchangers and separation loop increases.

Design of the separation loop is not within the scope of this report; however, its importance cannot be diminished. Design of this process deserves its own detailed research project in the discipline of chemical engineering. For the purposes of this report, a total separation efficiency will be assumed, and it will also be assumed that external heat exchangers exist that can bring the temperature of the solution back down to room temperature before re-entry into the irradiation cavity. Luckily, there is a wealth of research that has been performed on various separation processes and heat exchanger design is a very well understood field of study. One such process reported by Dale *et al* claims that the separation efficiency using Titania sorbents can be greater than 90% at concentrations from 150 g U/L to 300 g U/L. [24] Another such study shows that the uptake of Thermoxid sorbents can be even higher than that of Titania sorbents at certain concentrations. [25] These studies were likely performed using batch irradiation, and although the processes should be identical to the current case, an extremely conservative total separation efficiency of 50% will be assumed to take into account any added inefficiencies that may come with continuous separation.

Even with the conservative separation efficiency assumed, the lowest production rate reported in Table III.1 constitutes almost 70% of the domestic consumption. These preliminary results are encouraging, although they are expected to decrease slightly as core modifications are made and thermodynamic constraints are applied.

III.B. ACRR Core Modifications

As mentioned in Chapter II, several modifications must be made to the ACRR core to facilitate economic steady state production. The first and most prominent is the replacement of the fuel elements. The standard ACRR fuel elements were specially made to facilitate pulsing operation. Continuous operation at 3 MW would likely deplete this fuel, which was extremely expensive to make and is the only fuel of its kind, within a year. Replacing this fuel with a cheaper alternative that classifies as LEU is expected to decrease the criticality of the reactor significantly. If this decrease is such that it makes it impossible to reach two dollars of negative reactivity with the control rods fully inserted, several options exist to increase it. These include replacing the nickel reflector elements, which are just as unnecessary as the specialized UO_2-BeO fuel for the purpose of ^{99}Mo production, with more fuel elements. If this still does not meet the minimum criticality, fuel compositions can be adjusted.

The fuel type chosen for the modified ACRR core is standard TRIGA fuel which has the same physical dimensions as the standard ACRR fuel. In fact, the ACRR fuel was designed this way because its predecessor, the Annular Core Pulse Reactor (ACPR), used standard TRIGA fuel and the ACRR was designed to use the existing grid plates and irradiation cavity. A comparison of the fuel elements can be seen in Figure III.5. In addition to the ease with which this fuel can be accommodated in the ACRR is the fact that most research reactors at universities across the country use TRIGA fuel, making the ATS design more feasible to be implemented in existing research reactors. Another factor in this decision is the availability of TRIGA fuel. Using a fuel type that may be more beneficial from a neutronics standpoint, but that is not currently in production, would lead to an increase in fuel costs as this fuel type would need to be manufactured specifically for the purpose intended.

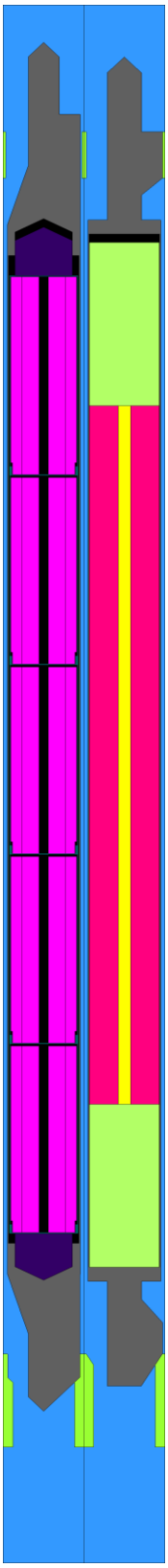

As seen in Figure III.5, although both the ACRR and TRIGA fuel will fit into the ACRR lattice, there are some significant differences between the internals of the fuel elements. Both fuels utilize reflectors on the top and bottom. The graphite TRIGA reflectors are much larger than the BeO ACRR reflectors, leading to a significantly shorter active fuel length. There is also a significant difference in the ^{235}U enrichment; the TRIGA fuel is enriched to 20% while the ACRR fuel is enriched to 35%, which classifies as HEU. In addition, the weight percent of uranium is higher in the ACRR fuel than in the TRIGA fuel; the ACRR fuel is 18.95 wt. % uranium, while the TRIGA fuel is only 11.53 wt. % uranium. On the bright side, TRIGA fuel is available in a variety of weight percents. For instance, the TRIGA fuel at the Nuclear Science Center at Texas A&M University is 30 wt. %. The value of 11.53 wt. % was chosen because this was the composition of the TRIGA fuel that was used in the ACPR.

Other modifications that should be made to the ACRR core before continuing are the replacement of the transient rods and the establishment of symmetry. As mentioned previously, the ATS will have no need for transient rods, and the safety rods may as well be upgraded to fuel rods. Fuel followed control rods that use TRIGA fuel in their follower region are common in research reactors at universities. While the ACRR displays a great deal of symmetry, it is not perfect symmetry. The reasons for the broken symmetries, such as the flat edge to allow coupling to the external FREC II core, are not present in the ATS design. Some

Figure III.5. Comparison of ACRR and TRIGA fuel geometries.

liberty is then taken to establish full symmetry as seen in Figure III.6. In Figure III.6, the fuel rods and safety rods have been replaced with TRIGA rods and the control rods and transient rods have been replaced with TRIGA control rods. In addition all nickel reflector elements and experiment tubes have been removed. Finally, fuel elements were shuffled around until perfect symmetry across angles of 120˚ was established. The results of the ^{99}Mo production rate and criticality calculations are shown in Table III.2.

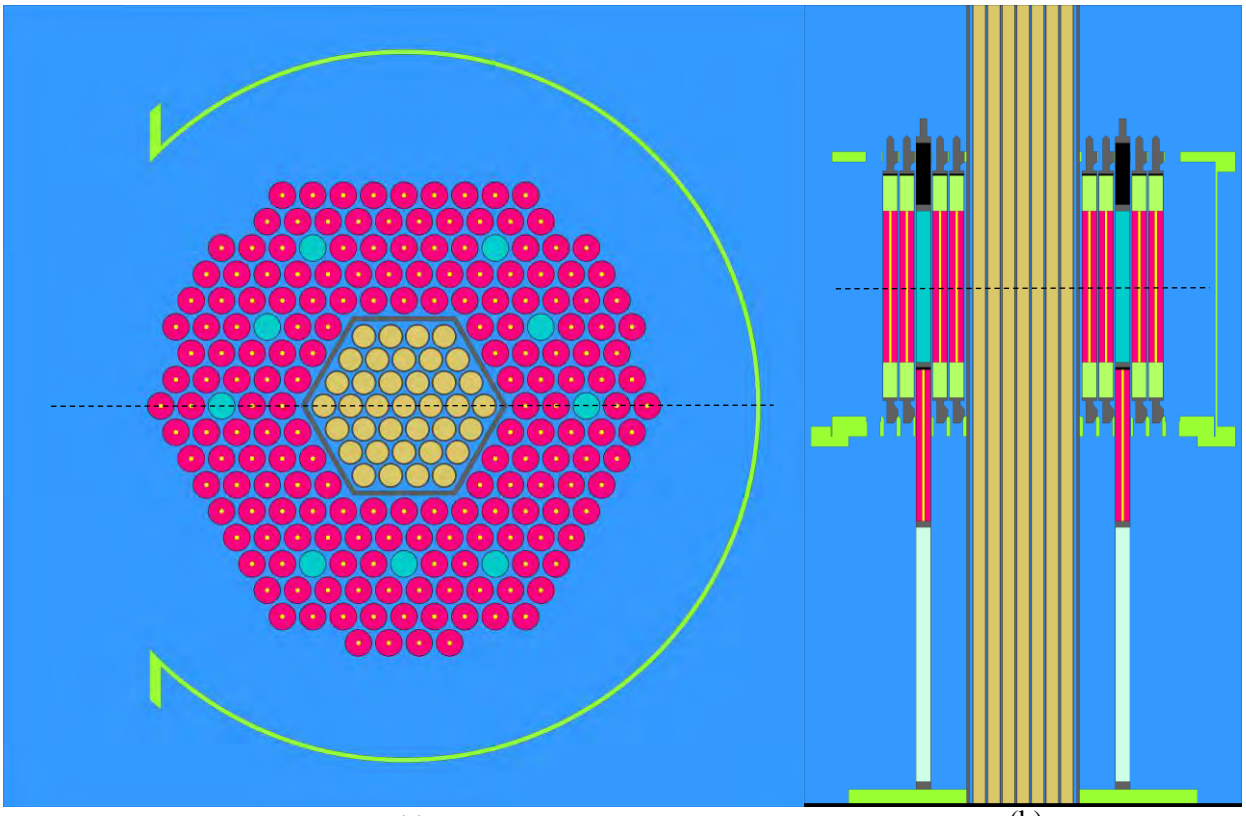

(a) (b)

Figure III.6. (a) Top view of the modified ACRR and ATS core lattice. (b) Side view of the modified ACRR and ATS core lattice. Each view is to be interpreted as a slice through the core along the dotted line of the opposite view. The pipe inner radius shown here is 1.5 cm.

Table III.2. Pre-separation ^{99}Mo production rates and criticalities for each of the 16 combinations of radius and concentration initially considered for the modified ACRR core.

Pipe inner radius (cm)	Concentration (g U/L)	Mo-99 production rate ($Ci_{6\text{-day}}$ per week)	Mo-99 production rate relative standard deviation (%)	Criticality	Criticality standard deviation
1.2	150	5612	0.00042	0.96812	0.000075
1.2	160	6088	0.00042	0.97144	0.000074
1.2	170	6566	0.00042	0.97481	0.000074
1.2	180	7045	0.00041	0.97834	0.000074
1.3	150	6864	0.00041	0.97761	0.000074
1.3	160	7452	0.00041	0.98160	0.000073
1.3	170	8037	0.0004	0.98575	0.000072
1.3	180	8627	0.0004	0.99009	0.000071
1.4	150	8245	0.0004	0.98802	0.000072
1.4	160	8950	0.00039	0.99281	0.000072
1.4	170	9659	0.00039	0.99755	0.000071
1.4	180	10365	0.00039	1.00237	0.000071
1.5	150	9747	0.00039	0.99904	0.000071
1.5	160	10572	0.00038	1.00454	0.000071
1.5	170	11381	0.00038	1.01005	0.000070
1.5	180	12180	0.00038	1.01540	0.000070

III.C. Active Target Cooling

For each case considered in the neutronics analysis, it must be confirmed that the solution can be kept below its boiling point at reasonable flow rates. In order to confirm this, a model of the irradiation cavity is constructed in ABAQUS as shown in Figure III.7. The maximum target velocity is set at 25 cm/s and the inlet temperature of the solution at the bottom of the ACRR core is set at 25 ˚C. The inlet temperature of the coolant at the top of the ACRR core is set at 20 ˚C. All that is left to perform the calculation is the volumetric heat generation rate as a function of position within the solution.

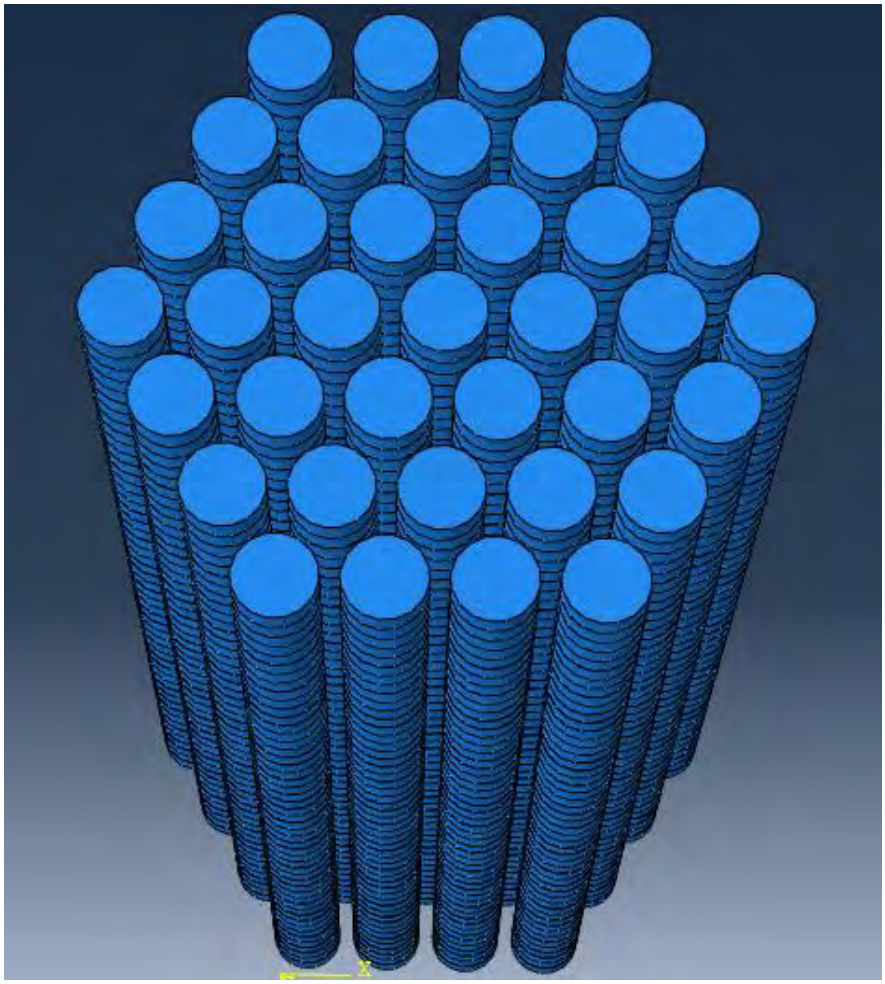

Figure III.7. ABAQUS model of the irradiation cavity showing the solution pipes discretized in the vertical direction.

The volumetric heat generation rate is obtained throught the use of mesh detectors in Serpent 2 which calculates the power in each discrete section of each pipe in the cavity. This power level is then divided by the volume of each discrete section to give a volumetric heat generation rate that ABAQUS uses to calculate the oulet temperature and temperature profile of the target as well as the coolant. Such a temperature profile can be seen in Figure III.8.

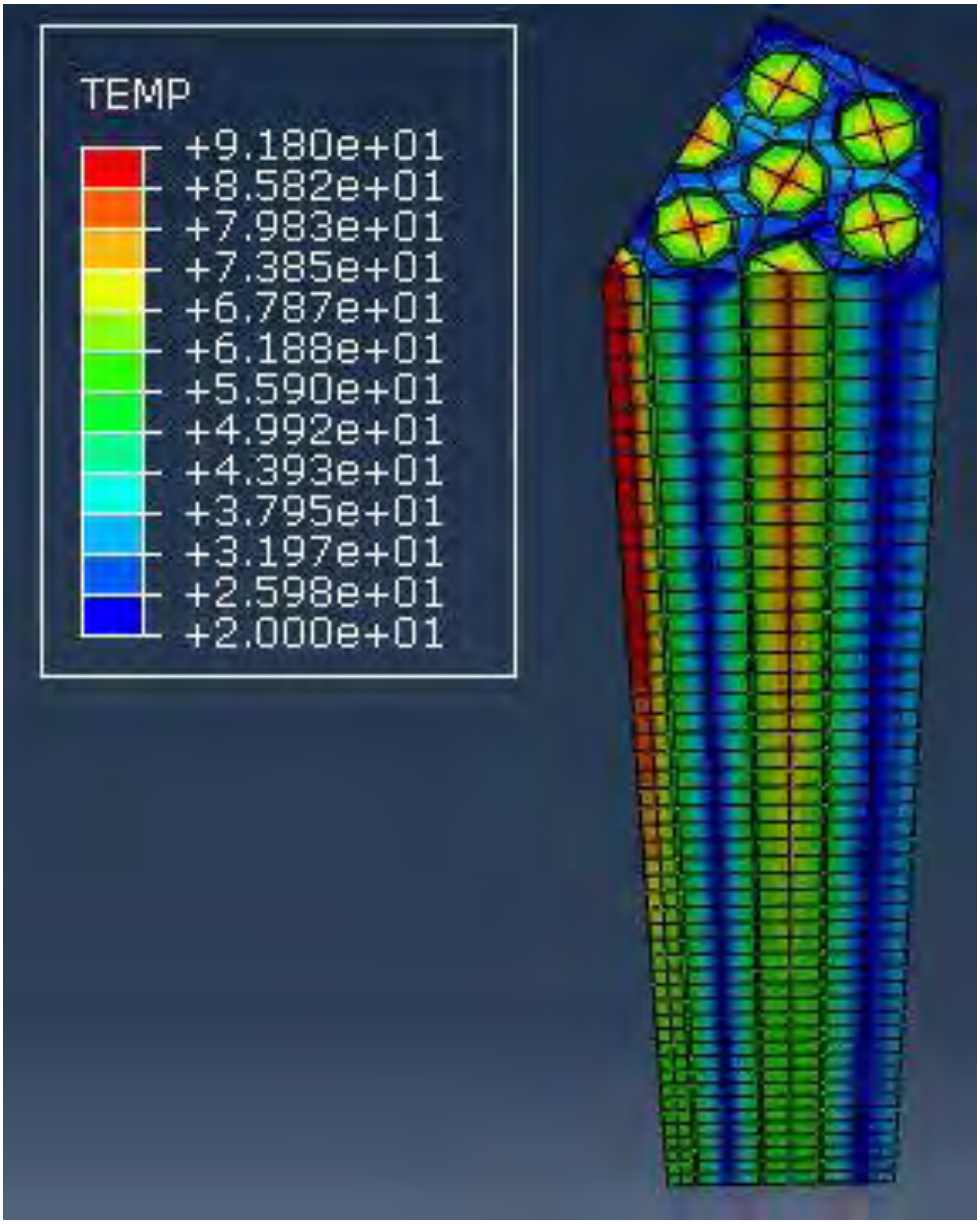

Figure III.8. Temperature profile of a sixth of the irradiation cavity for the 1.4 cm inner radius and 180 g U/L concentration case.

The case shown in Figure III.8 can be considered a worst case scenario in that it is the first case to exceed a criticality of unity with all of the control rods fully inserted, and therefore produces

the more ^{99}Mo, and therefore more heat than any of the neutronically viable cases. Even in this worst case scenario, it is shown that with a target velocity of 25 cm/s, the outlet temperature of the target can remain below the 100 ˚C limit imposed at the start of the design. Table III.3 gives the outlet temperatures of all cases except for those with inner radius of 1.5 cm, as these were already shown not to be neutronically viable. The maximum power per solid fuel element also remained below the 0.025 MW limit imposed in order to maintain passive convective cooling by the pool water in all cases considered.

Table III.3. Outlet temperatures of the target solution for neutronically viable cases.

Pipe inner radius (cm)	Concentration (g U/L)	Peak Temperature (˚C)
1.2	150	82.25
1.2	160	84.36
1.2	170	86.45
1.2	180	88.54
1.3	150	83.72
1.3	160	85.81
1.3	170	88.03
1.3	180	90.30
1.4	150	84.90
1.4	160	87.15
1.4	170	89.49
1.4	180	91.80

CHAPTER IV

CONCLUSION

Of the sixteen combinations of pipe radii and solution concentrations considered, the lowest ^{99}Mo production rate, assuming a 50% separation efficiency, is 2806 $Ci_{6\text{-day}}$ per week, which constitutes 46.8% of the domestic consumption rate. The highest production rate is 6090 $Ci_{6\text{-day}}$ per week, which is over 100% of the domestic consumption rate. It is not desirable however, to have a single reactor producing the entire U.S. supply because an unplanned outage could cause severe shortages nationwide. Instead, the best plan would be to have several reactors in operation, each producing a fraction of the domestic supply, so that if one needs to be shut down for any reason, the impact to the market will be less severe. Unfortunately, limiting the fraction of the domestic supply produced by a single reactor will also dissuade companies from investing in this technology because decreasing the production rate will decrease the profits without significantly decreasing the capital and operating costs. For this reason, an inner pipe radius of 1.2 cm and a concentration of 160 g U/L is suggested, which could produce 50.7% of the domestic consumption rate, is re-commended. Fortunately, there are at least 10 research reactors nationwide at universities alone, that are capable of employing a system similar to the one presented here, including the TRIGA reactor at the Nuclear Science Center of Texas A&M University.

While the research presented in this report is incomplete in that it does not consider fundamental design issues such as isotope extraction and economic analyses, it is certainly a good starting point for proving that such a system is indeed possible. As the current isotope producing reactors are decommissioned, proposals such as this one will be necessary in order to realize a domestic supply. Further research on this design would include a calculation of the TRIGA fuel lifetime as

well as a calculation of the concentrations of other isotopes of interest in the solution target as a function of time after startup. At a certain point, the solution target may need to be re-processed to remove some isotopes that may damage the purity of the ^{99}Mo product.

REFERENCES

[1] R. M. Mayo, Introduction to Nuclear Concepts for Engineers, La Grange Park, IL: American Nuclear Society, 1998.

[2] International Atomic Energy Agency, "Homogeneous Aqueous Solution Nuclear Reactors for the Production of Mo-99 and Other Short Lived Radioisotopes," IAEA, Vienna, 2008.

[3] Knolls Atomic Power Laboratory, Nuclides and Isotopes: Chart of the Nuclides, Bechtel Marine Propulsion Corporation: New York, NY, 2010.

[4] E. Parma, "The Supply of the Medical Radioisotope Tc-99m/Mo-99: Recent Shortages Call for Action in Developing a Domestic Production Capability," Sandia National Laboratories, Albuquerque, NM, 2009.

[5] International Atomic Energy Agency, "Production and Supply of Molybdenum-99," IAEA, Vienna, 2010.

[6] Nordion, "Our Products and Services," 2013. [Online]. Available: http://www.nordion.com/our_products/medical_isotopes_xenon133.asp. [Accessed 20 October 2013].

[7] T. R. Johnson, "Case: Assessment of Normal Lung Perfusion with Flash Scanning," 2010. [Online]. Available: http://www.dsct.com/index.php/case-assessment-of-normal-lung-perfusion-with-flash-scanning/. [Accessed 13 August 2013].

[8] AETNA, "Radiopharmaceuticals Metastron (Strontium-89) and Samarium-153 (Quadramet) for Metastatic Bone Pain," 2012. [Online]. Available: http://www.aetna.com/cpb/medical/data/300_399/0361.html. [Accessed 28 September 2013].

[9] D. Brauser, "Yttrium-90 Microspheres May Increase Survival for Patients with Liver Cancer," *MedScape Today,* 2010.

[10] D. Stewart, "Yttrium," 2012. [Online]. Available: http://www.chemicool.com/elements/yttrium.html. [Accessed 13 September 2013].

[11] C. K. &. S. Mandel, "Radioactive Iodine (I-131) Therapy for Thyroid Cancer," 2011. [Online]. Available: http://www.oncolink.org/types/article1.cfm?c=268&id=9630#.UUy5FxyyCSp. [Accessed

16 September 2013].

[12] Nuclear Energy Agency, “The Supply of Medical Radioisotopes: Review of Potential Molybdenum-99/Technetium-99m Production Technologies,” OECD, Paris, 2010.

[13] International Atomic Energy Agency, “Non-HEU Production Technologies for Molybdenum-99 and Technetium-99m,” IAEA, Vienna, 2013.

[14] J. A. Lane, Fluid Fuel Reactors, Boston: Addison-Wesley Publishing Company, 1958.

[15] V. A. Pavshook, “Effective Method of Mo-99 and Sr-89 Production Using Liquid Fuel Reactor,” IAEA, Moscow, 2007.

[16] E. Reynolds, “Medical Isotope Production System,” B&W Technical Group, Barberton, OH, 2007.

[17] National Nuclear Security Administration, “NNSA Awards Agreement to Establish Non-HEU-Based Production of Molybdenum-99 in US,” Washington D.C., 2012.

[18] P. J. C. E. J. P. K. R. DePriest, “MCNP/MCNPX Model of the Annular Core Research Reactor,” Sandia National Laboratories, Albuquerque, NM, 2006.

[19] K. H. A. A. N. G. R. Vega, "Final Design Report: Flowing Fuel Aqueous Homogeneous Reactor for Medical Isotope Production," Nuclear Engineering Department, Texas A&M University, College Station, TX, 2013.

[20] J. Leppanen, "Serpent: a Continuous-energy Monte Carlo Reactor Physics Burnup Calculation Code," VTT Technical Research Centre of Finland, 4 August 2013. [Online]. Available: http://montecarlo.vtt.fi/index.htm. [Accessed 23 January 2014].

[21] R. L. C. M. K. B. M. R. G. J. J. Dahl, "Documented Safety Analysis (DSA) for the Annular Core Research Facility (ACRRF)," Sandia National Laboratories, Albuquerque, NM, 2013.

[22] Office of Nuclear Reactor Regulation, "Guidelines for Preparing and Reviewing Applications for the Licensing of Non-Power Reactors," United States Nuclear Regulatory Commission, Washington, DC, 1996.

[23] A. J. Youker, "Separation, Purification, and Clean-Up Developments for MIPS and SHINE," Argonne National Laboratory, Lemont, IL, 2011.

[24] D. D. M. G. K. J. C. K. I. M. S. R. G. S. G.E. Dale, "99Mo Separation from High-Concentration Irradiated Uranium Nitrate and Uranium Sulfate Solutions," *Industrial &*

Engineering Chemistry Research, vol. 51, no. 40, pp. 13319-13322, 2012.

[25] S. A. K. Q. G. V. A.J. Bakel, "Thermoxid Sorbents for the Separation and Purification of 99Mo," in *26th International Meeting on Reduced Enrichment for Research and Test Reactors*, Vienna, Austria, 2004.

Appendix C

Work related to the Production of Mo-99/Tc-99m

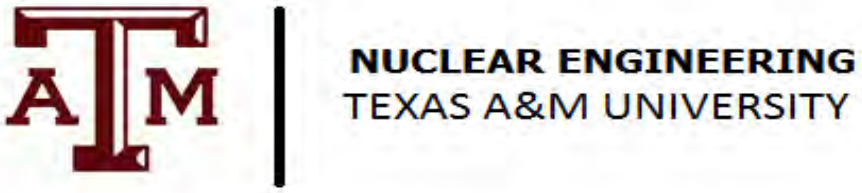

Production of Tc-99m from Accelerator Generated Mo-99 Utilizing a Photon-Neutron Interaction With Mo-100 Targets

Team 1

AlMaazmi, Yousif

Harahsheh, Talal

Kennas, Miltiadis

Marroquin, Eden

Schaper, Matt

April 27, 2015

NUEN 410 Senior Design Final Report
Nuclear Engineering Department
Texas A&M University
College Station, TX 77843-3133

APPROVAL PAGE

Production of Tc-99m from Accelerator Generated Mo-99 Utilizing a Photon-Neutron Interaction With Mo-100 Targets

Senior Design Team 1

AlMaazmi, Yousif

_____ _____

Harahsheh, Talal

_____ _____

Kennas, Miltiadis

_____ _____

Marroquin, Eden

_____ _____

Schaper, Matt

_____ _____

Signature Date

Primary Technical Advisor

Gamal Akabani, Ph.D.

_____ _____

Signature Date

NUEN 410 Senior Design Final Report
Nuclear Engineering Department
Texas A&M University
College Station, TX 77843-3133

Submitted to the Texas A&M University, Department of Nuclear Engineering in partial fulfillment of the requirements for a BACHELOR OF SCIENCE IN NUCLEAR ENGINEERING

Table of Contents

EXECUTIVE SUMMARY

The current supply-chain of producing molybdenum-99 can be unreliable due to unforeseen nuclear reactor outages and upcoming nuclear power plant license expirations. Nuclear reactors also require high initial startup capital and require six days in order for hospitals to receive molybdenum-99. Because of these reasons, alternative methods for the production of molybdenum-99 are currently being researched and are the basis of this design. Molybdenum-99 is important isotope because it decays into technetium-99m, which is used in 80% of nuclear medicine procedures. This design is to propose an alternative method using a photon-neutron interaction with molybdenum-100 targets in order to acquire molybdenum-99. The design goal is to address the global demand of molybdenum-99 in a more efficient and economically feasible method.

This design encompasses the entire production process from the production of molybdenum-99 to the final product of technetium-99m ready for patient delivery. The design uses 41 MeV electrons produced from a 100 kW accelerator to create photons via bremsstrahlung scattering off a tungsten target. These photons interact with molybdenum-100 to produce molybdenum-99. The molybdenum-99 is then chemically separated from the molybdenum-100 and the technetium-99m is produced as a final product. This project has been divided into five major subtasks: target design, thermodynamic design, shielding design, chemical separation, and quality management in order to maximize the production of molybdenum-99 while addressing safety concerns. Computer programs will be used as a tool to model these aspects in order to achieve the objectives of this design.

After the design was subdivided into sections, important optimization variables were assigned for the design. The most important variables to

maximize included the production rate of the molybdenum-99 and the cost technetium-99m. Safety and irradiation risk reduction was also of great interest in order to cohere with ALARA standards and protect the employees of our facility.

The results of this design determined the production rate of the molybdenum-99 after an irradiation time of one day to be 146 Ci per molybdenum-100 target system. The Mevex accelerator company is capable of providing an accelerator of the required 35-50 MeV beam energy and 100 kW of power. The separation apparatus was also successful at chemically separating molybdenum for recycling from technetium-99m and producing a deliverable syringe to the patient. The entire process is designed to uphold FDA and cGMP requirements as well as the necessary radiation shielding requirements during the target irradiation and chemical separation process. The final cost for 1 mCi of technetium-99m using this design was calculated to be 20.5¢, which is significantly less expensive than the current consumer cost of 100¢ per mCi.

ACKNOWLEDGEMENTS

We would like to give special thanks to Dr. Gamal Akabani, our technical advisor; David Brown, Representative of Mevex Corporation; Dr. Paul Schaffer, Researcher at TRIUMF Laboratories; and Dr. Karen Vierow, our academic advisor; for their unwavering and uninterrupted support and guidance. We would also like to thank Dr. Benjamin Wilhite for providing access to his COMSOL research servers, and Jeffery Polasek, for his help setting up COMSOL.

SECTION I
INTRODUCTION – ALL

Background

The production of molybdenum-99 has become an important area of research in the field of nuclear medicine in recent years because of interruptions in the supply-chain, aging reactors, growing concerns over the proliferation of uranium, the large demand for the isotope, and the possibility of alternative methods of production. The purpose of this design project was to address these concerns by offering an alternative method that utilizes a photon-neutron interaction with molybdenum-100 targets and uses a linear accelerator, as opposed to a reactor. This design was subdivided into five major parts in order to redesign the entire process of production: Target design, target cooling, radiation shielding, chemical separation, and quality control. By separating these components, collaboration was necessary between all team members in order to optimize the final design that is written in this document. This section will contain an introduction to molybdenum-99, the current state of the industry, past failures and instabilities, future concerns, the path to sustainability, alternative methods of production, possible alternatives, our proposed design, advantages and disadvantages to this design, and conclude with our design goal and summary.

What is molybdenum-99 and technetium-99m and why is it important?

Technetium-99m is a radionuclide used in over 80% of radiographic imaging procedures [1]. It is crucial as a tracer for oncology and cardiovascular scans in Single-Photon Emission Computed Tomography. Technetium-99m has a half-life of 6.06 hours and photon decays to the essentially stable technetium-99. Because of its short half-life, the element is found nowhere in nature. Its only radioactive parent is molybdenum-99, which has a half-life of 66 hours. Molybdenum-99 has an 87.5% chance to beta decay into technetium-99m and a 12.5% chance to beta decay into technetium-99. The decay scheme of molybdenum-99 into technetium-99m and technetium-99 is shown in Figure 1.1.

Because of the short half-life of technetium-99m, the radionuclide cannot be shipped by itself over long distances. Molybdenum-99's half-life makes it suitable for both shipping and for cyclic extraction of decayed technetium-99m as covered in Section V.

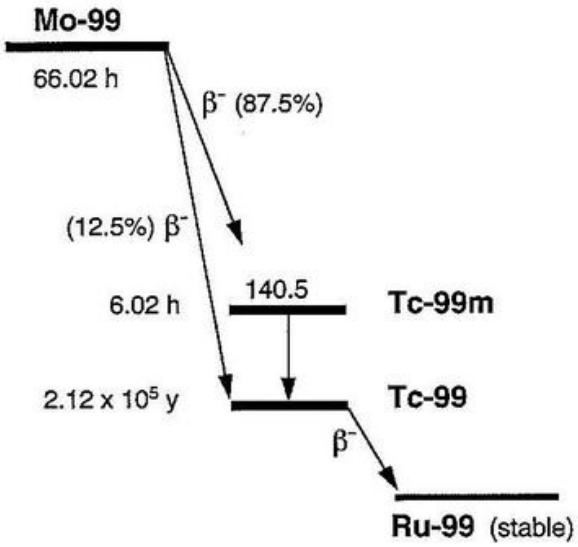

Figure 1.1. Radioactive decay diagram of molybdenum-99.

The method proposed in this project requires enriched molybdenum-100 to act as targets in a photon-neutron interaction. The photons are supplied as Bremsstrahlung from a tungsten preliminary target impacted by 41 MeV (mean value). Molybdenum-100 is a naturally occurring, stable isotope that can be enriched to over 97% purity. Information on molybdenum isotopes is tabulated in Table 1.1.

Table 1.1.

Natural abundances and enrichment of molybdenum-99. [2].

Mo Isotope	Natural Mo (%)	Enriched ^{98}Mo (%)	Enriched ^{100}Mo (%) CIS (Russia)[3]	ORNL (USA)
92	14.84	0.02	0.0011	0.55
94	9.25	0.02	0.0008	0.19
95	15.92	0.04	0.0016	0.29
6	16.98	0.06	0.0020	0.35
97	9.55	0.32	0.0026	0.26
98	24.13	99.45	2.54	0.97
100	9.63	0.09	97.46	97.39

Current Supply Chain

The current process for producing molybdenum-99 begins with the manufacturing of uranium targets and are typically HEU [2]. These uranium targets are than sent to a reactor for irradiation by neutrons in hopes of producing molybdenum-99 as a fission fragment. This process occurs at ~6% fission yield using this method and must therefore be separated at a molybdenum-99 processing facility. After the targets have been processed, they are compacted into a compact generator and sent off to hospitals. Figure 1.2 illustrates this process for delivering molybdenum-99 to the hospitals.

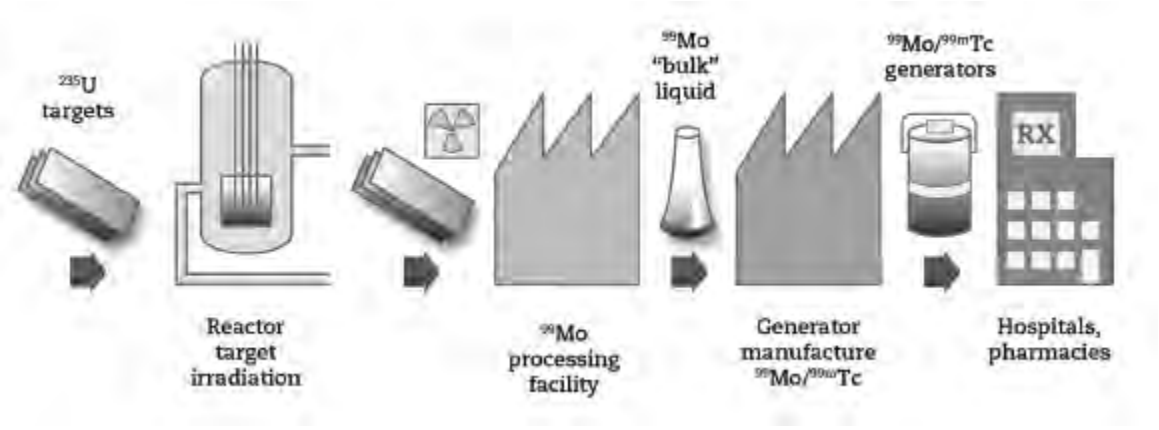

Figure 1.2. Molybdenum-99 supply chain [2].

Historically, the supply chain of molybdenum-99 currently primarily consists of five research reactors. These reactors include the Nation Research Universal (NRU), the Petten High Flux Reactor (HFR), the Belgium BR2 Reactor (BR2), the OSIRIS reactor, and the SAFARI-1 reactor. Figure 1.3 shows the contribution of each reactor to the global molybdenum-99 supply chain.

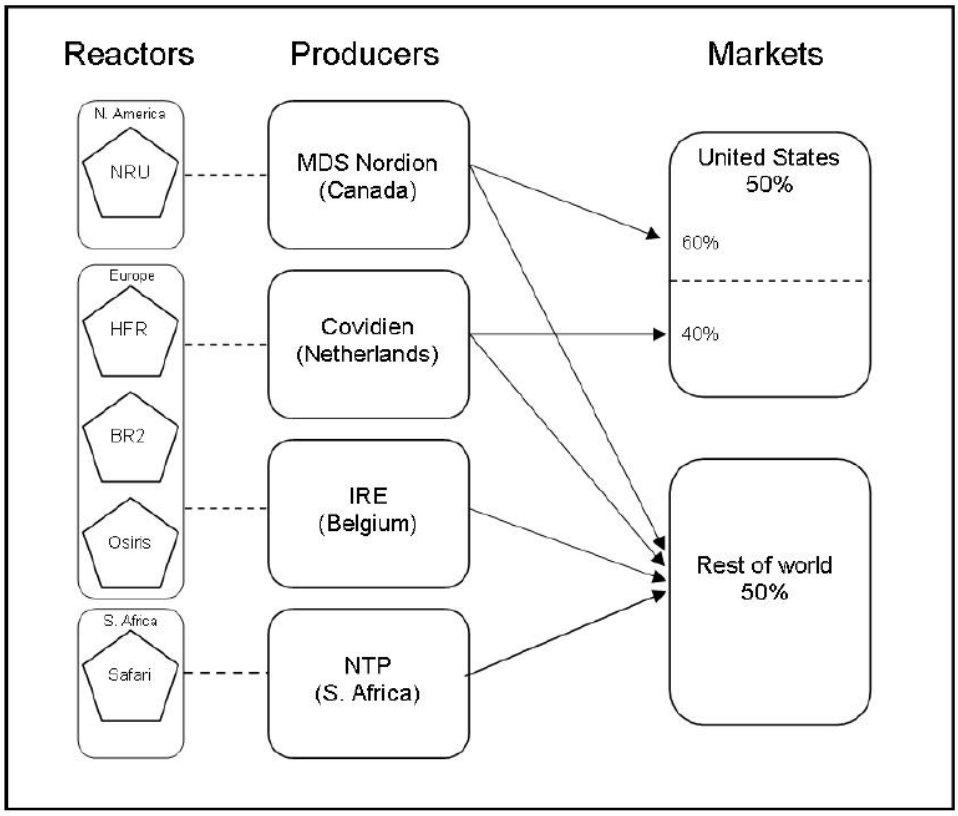

Figure 1.3. Large-scale global production of molybdenum-99 [3]. Since over 95% of the global supply chain of molybdenum-99 is produced in only five reactors [2], a break in the supply chain from an unexpected shutdown or decommissioning in any one of these reactors can lead to a large-scale shortage of the medical isotope.

Past Instabilities

In the year 2009, the NRU reactor which supplied 31% of the world's molybdenum-99 supply was shut down due a heavy water leak detected at the base of the reactor vessel [2]. This unscheduled shutdown had dramatic consequences on price and availability of molybdenum-99 and made it unaffordable or even unattainable to some patients. In 2010, the HFR, the NRU, and the OSIRIS reactors were all down for extended periods and were not producing molybdenum-99 leading to a period of insufficient capacity [2]. In order to ensure reliability of the molybdenum-99 supply chain, different methods of producing molybdenum-99 are currently being researched.

Future Concerns

The future sustainability of the molybdenum-99 supply chain remains uncertain. The current supply chain relies on five reactors that were each licensed 45-55 years ago and are approaching their decommission [2]. For example, the NRU reactor's license was set to expire on October 31, 2016 but was recently extended to March 31, 2018 in order to maintain the supply chain of molybdenum-99 [4]. Aging reactors and instabilities are not the only concern however, it is also important to note the growing demand of molybdenum-99 as shown in Figure 1.4.

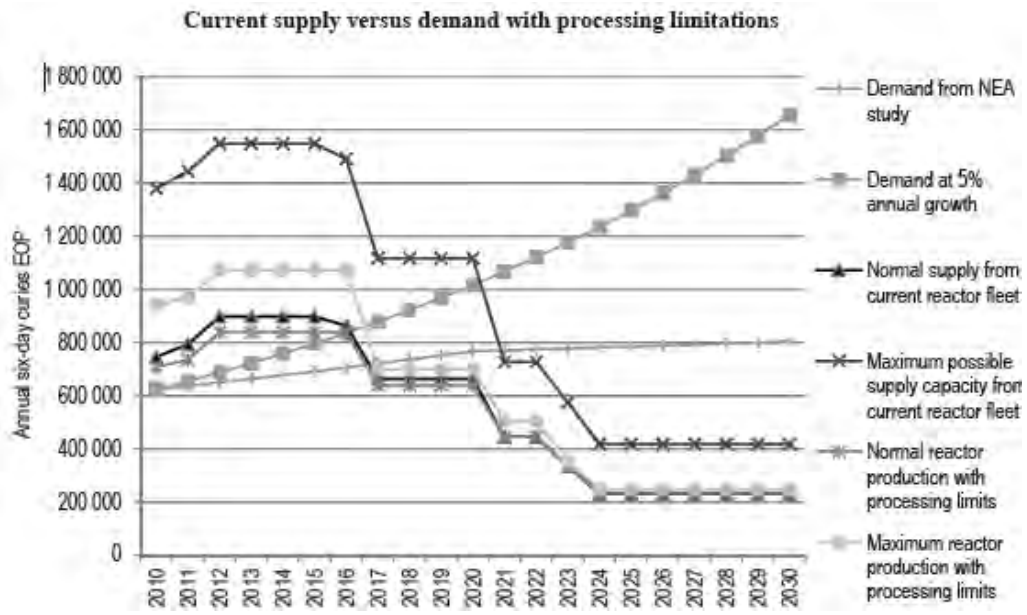

Figure 1.4. Current supply v. demand curve at a conservative estimate of 5% annual growth [2].

As shown in Figure 1.4, assuming an annual growth of 5% for the demand of molybdenum-99, the demand is expected to outgrow the maximum possible supply capacity from the current reactor fleet by 2020. The maximum reactor production with processing limits is outgrown as soon as summer 2016. The growing demand along with the decline in reactor production rate has led to a growing concern about the production of molybdenum-99.

Alternative Methods

The production of molybdenum-99 can be split into two methods. The first method is a reactor based method (see Figure 1.5), and the second method is an accelerator based method (see Figure 1.6). Reactor based methods were found to be unattractive because of the high initial cost, and many regulatory requirements as dictated by the NRC. Even though, reactor based methods produce higher yields of molybdenum-99, it was found that the processing time negates the advantages of a reactor based method. Thus, the best method lies in an accelerator based method.

There are three types of accelerators that can be used to produce molybdenum-99. The first type utilizes a proton beam that can either directly bombard molybdenum-100 targets, or it can bombard a heavy nucleus target such as lead to produce a neutron beam that can then either directly produce molybdenum-99 by targeting molybdenum-98 or uranium-235. The issue with this method is that technectium-99m has a short half-life, therefore it requires the accelerator to be located close to the customer. Furthermore, bombarding a heavy nucleus target to produce a beam has a low yield when targeting molybdenum-98, and it raises proliferation risk when it's used in uranium-235 targeting. Therefore using a proton beam to produce molybdenum-99 is impractical.

The second type utilizes an electron beam that bombards a heavy nuclear target like tungsten to produce gamma rays that can then either produce molybdenum via uranium-238 or molybdenum-100. Using uranium-238 to produce molybdenum-99 requires using a high powered accelerator which has limited availability. While using molybdenum-100 require using expensive targets that can increase the initial cost of production.

The last accelerator type uses a deuteron beam to bombard a carbon target to generate neutrons that then collide with molybdenum-100 to produce molybdenum-99. This method requires using a high energy deuterium reactor that is currently being built in France. Thus, this option is unattractive because there is no accelerator that can produce deuterium with the energy required for molybdenum-99 production.

Reviewing our accelerator options it is clear that the only practical option is using photons and a molybdenum-100 target.

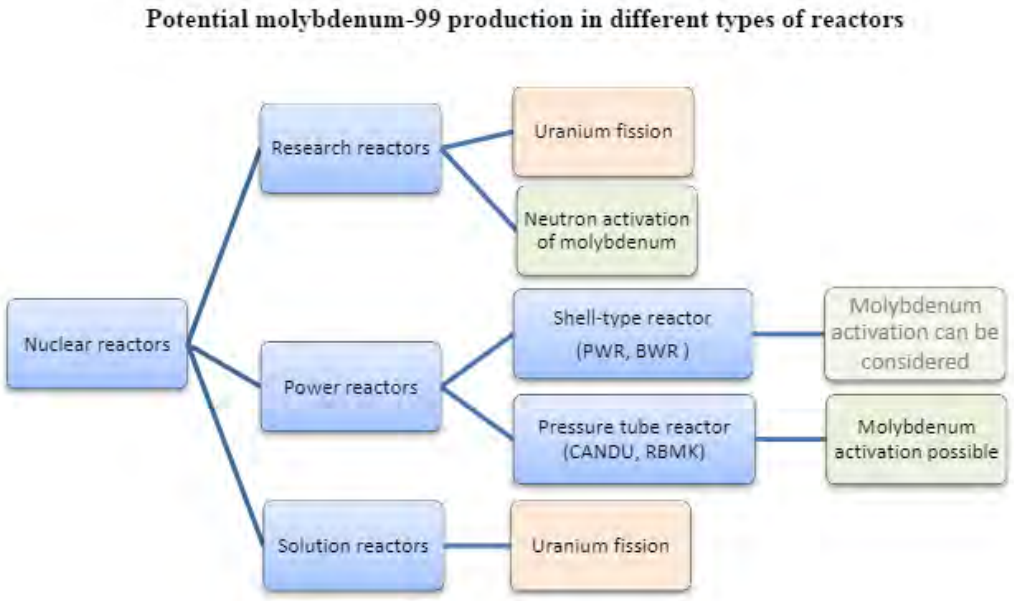

Figure 1.5. Reactor based methods of production [5].

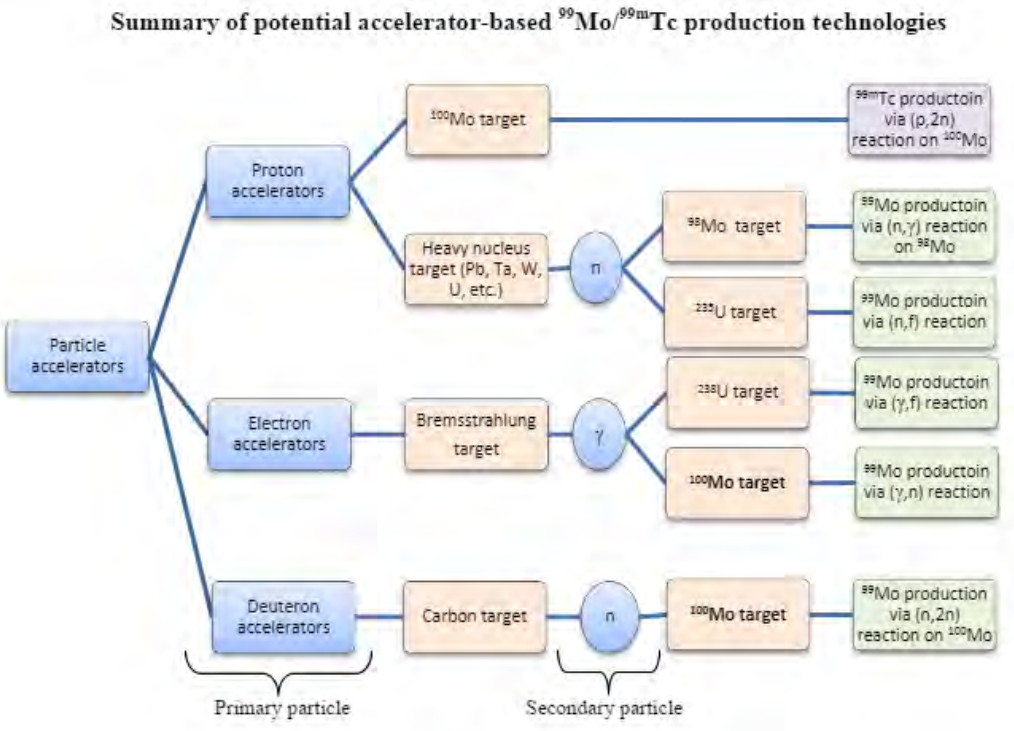

Figure 1.6 Accelerator based methods of production [5].

Comparison Against the Current Method

Advantages

A major advantage in adopting this design is that the processing time for post-irradiated targets can be significantly reduced. The current standard of practice utilizes the concept of the six-day curie which is the amount of molybdenum-99 a hospital would purchase. The current reactor based approach takes approximately six days for a target to begin processing after irradiation to arriving at the consumer. This design, will be able to process the targets in the same afternoon and only have to ship them to the facility since it does not handle any fission fragments. This means that instead of taking six days for our product to arrive, it only would take two because of logistics. This is important because that means this design does not have to produce as much initial activity as the current reactor based approach. For example, if a hospital orders 20 six-day curies, the reactor based approach would have to produce 93.32 Ci in order for it to decay to 20 Ci before arrival. However, the accelerator based design would only have to produce 33.42 Ci in order to also provide the hospital with 20 Ci. Figure 1.7 demonstrates the two decay curves associated with these processes.

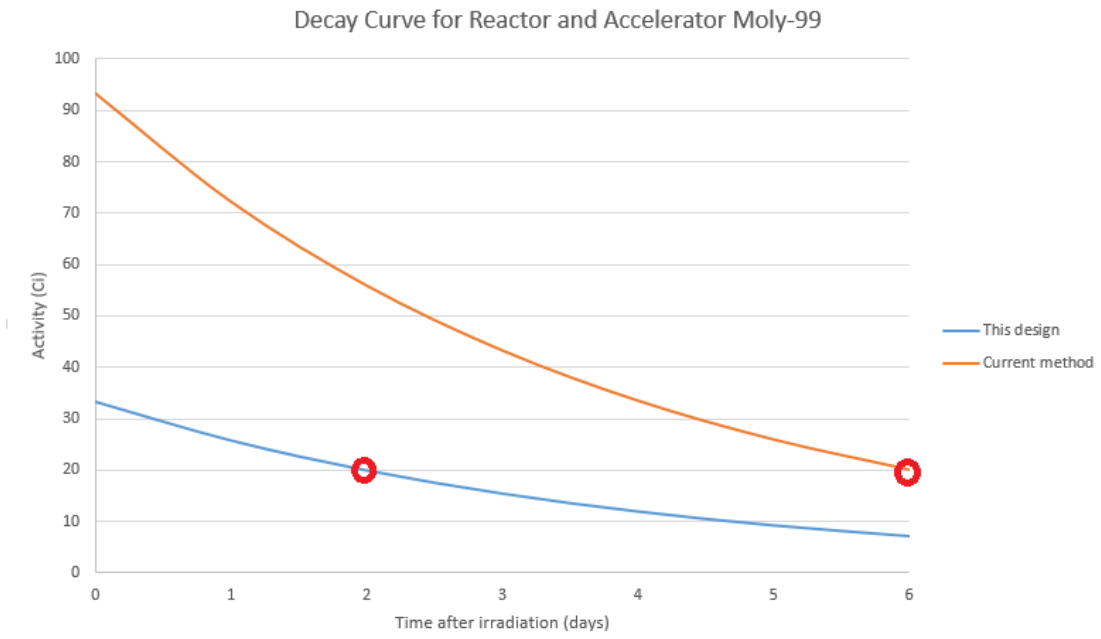

Figure 1.7. Decay curve for the current reactor method and this design. The red circle marks the arrival at the hospital.

Another advantage to using the photon-neutron process is the reduction in NRC regulations as opposed to a uranium based production method. Because of proliferation concerns, there is political pressure to move away from a HEU target system. This design however, just utilizes enriched molybdenum-100 targets which does constitute a proliferation risk.

Stability is also a major advantage in the accelerator based approach. Accelerators are able to be turned off and on as opposed to the current reactors which require significant startup times. By introducing accelerators into the molybdenum-99 supply chain, it will diversify the current system. They will also allow for simpler estimates since an accelerator would be easier to adapt to a specific demand on a given day instead of over-producing molybdenum-99 due to over predicting the demand using the current reactor method.

Waste is also heavily reduced in this design since it does not have to handle uranium fission wastes. There are no fission products for molybdenum-100 reactions and the equipment used to handle the molybdenum-99 would be low level medical waste.

Disadvantages

The major disadvantage to using this design is that the initial capital costs can be quite expensive. However, this initial investment when compared to reactor-based production of molybdenum-99 is insignificant. Enriched molybdenum-100 can cost anywhere between $600-$2750 per gram [6]. This disadvantage can be circumvented by recycling the molybdenum-100 after the chemical separation process has occurred.

Another disadvantage is that the specific activity of a reactor based method is smaller than the current reactor method. This prompted the need to develop a new chemical separation process and generator and was done by TRIUMF national laboratories [7].

The final main disadvantage is that this design has never been attempted at an industry level. This leaves potential investors believing that this could be a high-risk investment and that it might not meet their economic goals. In order to establish credibility, a pilot program needs to be implemented in order to verify the viability of this design. Also, because it hasn't been done, than no FDA approval currently exists for this method of production. The FDA would have to approve this method before commercial distribution of molybdenum-99 would be possible using this design.

Design Objective and Goals

The design objective of this project is to utilize the photon-neutron interaction in order to produce molybdenum-99 from a series of enriched molybdenum-100 targets. The photons will be produced via the bremsstrahlung process with a tungsten plate. The design goal is to optimize the production of molybdenum-99 in order to meet its demand while maintaining both economic feasibility and diversified utility.

Design Summary

Target Design forms the base of the project. This part is responsible for producing molybdenum-99 out of molybdenum-100 targets. Thermodynamics identifies whether or not the power level of Target Design is within safe material limits. Target Design is then free to increase power level, Thermodynamics repeats analysis, and the parts continue to cooperate until optimization is reached.

Once Target Design is optimized, it sends activity of molybdenum-99 produced to Chemical Separation, which separates technetium-99m from molybdenum, determines how much final activity of technetium-99m can be produced for the customer, and returns unused molybdenum-100 to Target Design.

Shielding Design ensures Target Design, Chemical Separation, the final deliverable, and every aspect in between are sufficiently shielded to comply with federal safety regulations.

Quality Management System oversees the entire project and ensures that all aspects comply with current good manufacturing practices and FDA radionuclidic, radiochemical, and microbiological purity regulations. Figure 1.8 represents a graphical overview of the project layout.

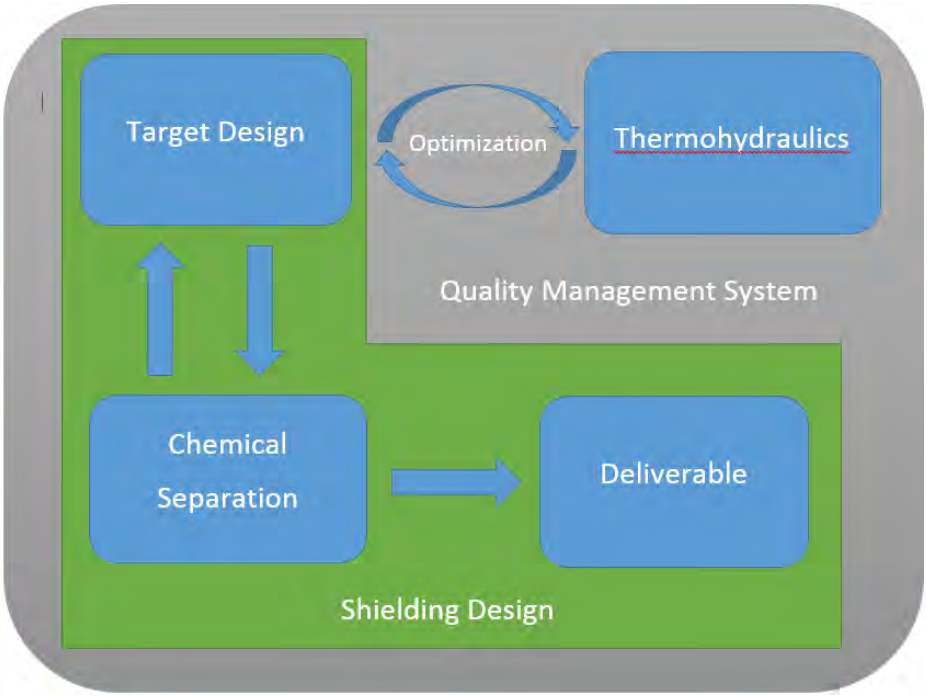

Figure 1.8. Diagram describing the coupling of various design aspects. This approach to design will be able to encompass all aspects of the molybdenum-99 supply chain and ultimately meet the design goals.

SECTION II
TARGET DESIGN – MATT SCHAPER

Introduction to Target Design

Target design is the first step in the process of producing molybdenum-99. During this step, molybdenum-100 targets will be irradiated with bremsstrahlung photons in order to invoke the photon-neutron interaction and produce molybdenum-99. In order to produce the bremsstrahlung photons, a high-energy electron linear accelerator will be utilized and the resulting electrons will undergo the bremsstrahlung process on a tungsten surface. After this target system has been irradiated, it will be transferred to a hot-cell where it can be further processed in order to have a deliverable syringe of technetium-99m for medical use. The purpose of this section, is to analyze the particle physics behavior and determine the amount of molybdenum-99 capable of being produced.

Design Basis

The current state of molybdenum-99 production research involves prospective methods from both accelerator or reactor based production. As stated in SECTION I, this project's purpose was to demonstrate a proof-of-concept for the production of molybdenum-99 by utilizing the photon-neutron reaction in Equation 2.1.

$$^{100}_{42}Mo(\gamma,n)^{99}_{42}Mo \tag{2.1}$$

By choosing this process, the need for uranium is eliminated since it is a direct method of production. Therefore, this method also removes proliferation concerns and is simpler to regulate from the NRC. Also, since an accelerator based method is chosen, it provides for a stable irradiation cycle and efficient extraction methods.

The important design goals from this section is to optimize target geometry, enrichment of target material, energy of incident electrons, current of the accelerator beam, the energy deposition produced as a result of target irradiation, and maximize the activity produced by the target system. Some of these variables involved collaboration with other sections of this report in order to reach the final design.

Physical Concepts

The following sub-section will provide the concepts of physics that are especially important to the analysis of target design. The major processes that are of concern are cross sections, bremsstrahlung, photon effects, activity and decay.

Cross Sections

Cross sections are the most important characteristic of designing the target since it determines the physical viability of producing molybdenum-99 as well as the possibility for any other undesirable isotope species. Cross sections characterize the probability that a certain nuclear reaction will occur and is defined in terms of a probability per effective area. For this design, it was important to determine the cross-sections for the desired production of molybdenum-99 in order to determine the most efficient photon energy range. This data was obtained using JANIS 4.0 [8] and is shown in Figure 2.1.

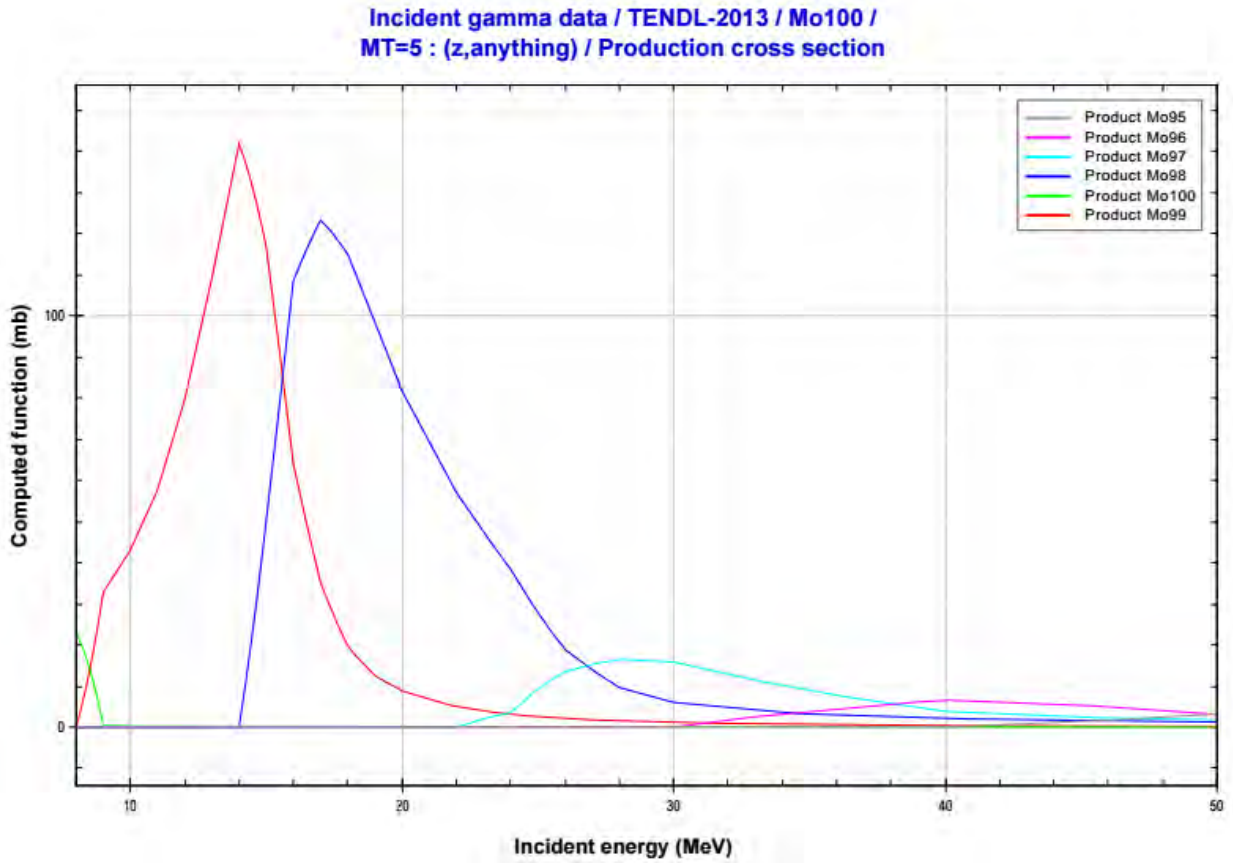

Figure 2.1. Linear-linear cross section data for incident photons on molybdenum-100.

As demonstrated by Figure 2.1, molybdenum-99 can only be produced with photons that have energies greater than 8 MeV and increases until a maximum of ~140 mb which occurs at 14.5 MeV. It is also important to notice that as you increase beyond 14.5 MeV, the production rate of molybdenum-98 increases and becomes more favorable at >15.5 MeV. In order to favorably produce molybdenum-99, the photon energy range must be within 9 MeV-15 MeV.

Bremsstrahlung

Bremsstrahlung is the method used in order to generate the high-energy photons needed in order to produce the molybdenum-99 in the target system. Bremsstrahlung is when an electron passes near a positive ion and the Coulomb force between the electron and the positive ion deflects the electrons from its initial path and also slows it down. In order to conserve energy during this process, a photon is emitted from the electron's change in momentum. This process can be illustrated in Figure 2.2.

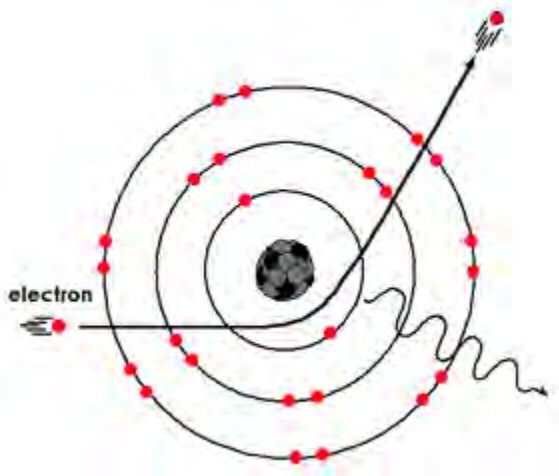

Figure 2.2. Illustration of the bremsstrahlung process.

The probability of this process occurring is larger in higher Z material as a direct of result of Equation 2.2 which is known as the Thomas-Fermi approximation [9].

$$-\frac{dE}{dx} \approx 4\alpha r_c^2 N_0 E Z^2 \, ln\left(\frac{183}{Z^{1/3}}\right) \tag{2.2}$$

Where $-\frac{dE}{dx}$, describes the energy loss per electron and path length, E, is the electron energy, N_0, is the atomic density of the medium, Z, is the atomic number of the medium, r_c, is the classical electron radius, and α is the fine-structure constant. This was an important characteristic of our design since tungsten was chosen as our bremsstrahlung material since it has a $Z = 74$.

A good rule of thumb is that the average photon energy produced is roughly one-third of the incident electron energy in high Z materials [9]. This led us to our preliminary guess that the electrons needed to be between 30-51 MeV in order to produce favorable photons in the range of 10-17 MeV.

Pair Production/Positron Annihilation

Pair production and positron annihilation is also an important characteristic in our design since the photon energies used are quite high and this would therefore be the dominating photon effect. Pair production is the process when high-energy photons are converted into an electron/positron pair. In order to conserve momentum, this process has to occur close to the nucleus of the atom. In order to conserve energy, the photon must also be at least as large as twice rest mass-energy of the electron (i.e. at least $2 * (0.511\ MeV) = 1.022\ MeV$). Even though this is the minimum threshold for pair production to occur, it is more favorable at higher energy photons. Since our photon energy spectrum is much larger than this, pair production commonly occurs in our target system.

Positron annihilation is the reverse process of pair production and occurs because positrons don't exist in nature when they come to rest. Positrons are generated from pair production and have a certain kinetic energy which is attenuated as the positron moves through medium. Once this positron slows down to rest, it is favorable for it to interact with the nearest electron and annihilate, producing two $0.511\ MeV$ photons that travel $180°$ apart. This interaction will not produce any molybdenum-99, but it will deposit energy into our target system. Figure 2.3. illustrates the pair production and annihilation process.

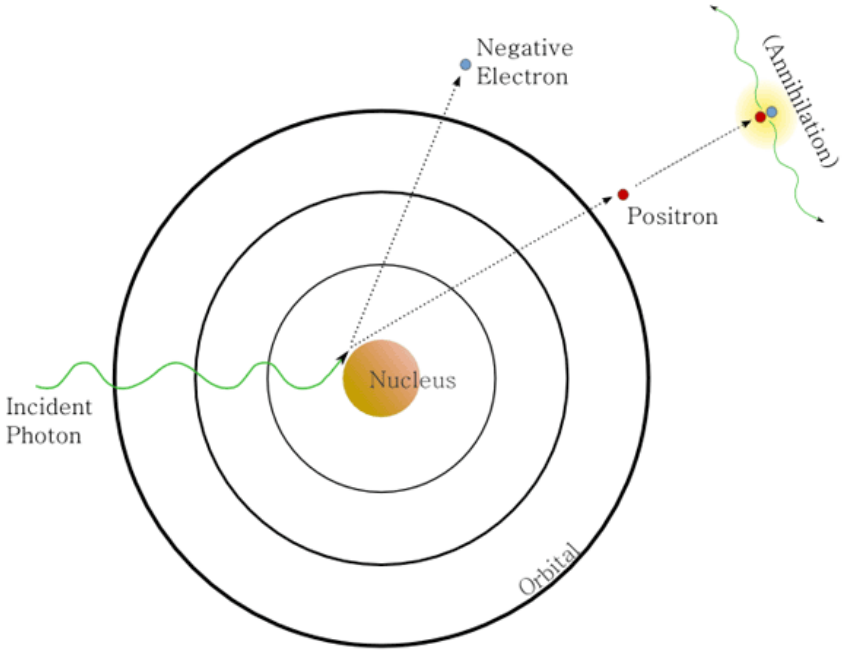

Figure 2.3. Illustration of the pair production and annihilation process.

Compton Scattering

Compton scattering occurs with mid-energy photons in medium. This effect occurs when a photon collides with an electron and then the photon and electron both deflect at some scattering angle determined by conservation of momentum and energy. These resulting photons will generally not be high enough energy to produce molybdenum-99 but will also deposit energy into the target system. An illustration of Compton scattering can be shown in Figure 2.4.

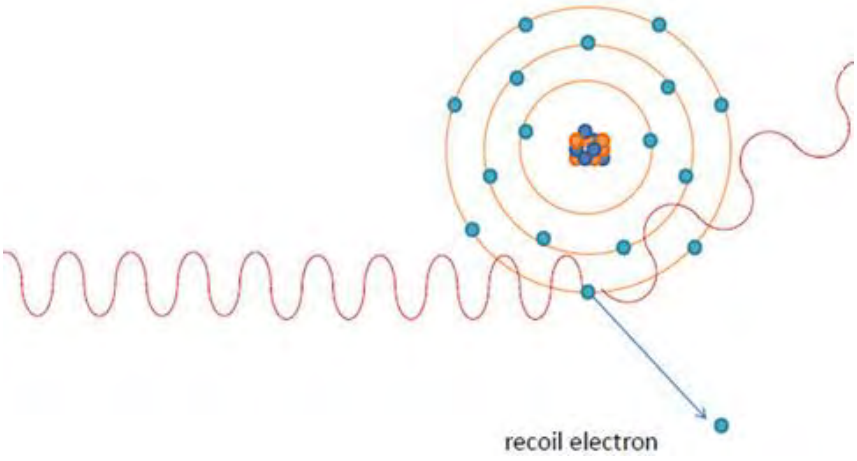

Figure 2.4. Illustration of Compton scattering.

Photoelectric Effect

The photoelectric effect is another method for which low-energy photons interact in medium. The photoelectric is when an incident photon interacts with an orbital electron and is fully absorbed. Due to conservation of energy, this increases the electrons energy and is sufficient to eject the electron from its electron shell and creates a void in the atom which much be filled to become stable. The photoelectric effect is only likely to occur when the incident photon is only slightly larger than the binding energy of the electrons and therefore occurs at low photon energies. A diagram of the photoelectric effect can be shown in Figure 2.5.

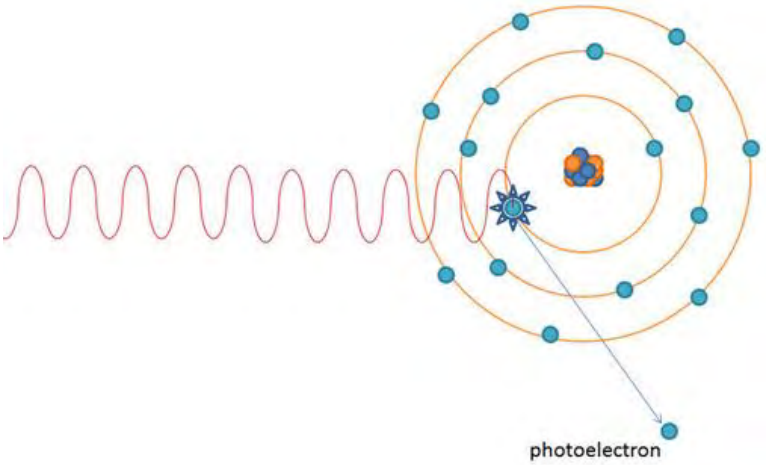

Figure 2.5. Illustration of the photoelectric effect.

Activity and Decay

Activity and decay are important concepts when maximizing the design goal of producing as much molybdenum-99 as possible. Radioactive decay is the process which an atom changes its physical form and emits a conservation particle. In this design, the radioactive decay of interest is the decay scheme of molybdenum-99 which undergoes beta decay as shown in Equation 2.3.

$$^{99}_{42}Mo \rightarrow {}^{99m}_{43}Tc + {}^{0}_{-1}\beta \tag{2.3}$$

Strictly speaking, decay is follows a Poisson distribution as shown in Equation 2.4.

$$P(X = k) = \frac{(\lambda t)^k e^{-\lambda t}}{k!} \tag{2.4}$$

Where $P(X = k)$ is the probability of exactly k decays, λ is the decay constant and t is the time period of interest. However it is more convenient to express decay in terms of the number of atoms that have survived at time t, in which case Equation 2.5 is often used.

$$N(t) = N_0 e^{-\lambda t} \tag{2.5}$$

Where $N(t)$ represents the number of atoms remaining at time t and N_0 is the initial amount of atoms. This concept can be expanded in terms of the strength of the radioactive source which is measured in activity. Activity is the rate which an isotope decays and emits radiation and can is represented in Equation 2.6.

$$A(t) = \lambda N(t) = A_0 e^{-\lambda t} \tag{2.6}$$

Where $A(t)$ represents the activity remaining at time t. Equation 2.5 and 2.6 represents the decay equations assuming no more activity is currently being produced. For this design, the activity during the irradiation process will be calculated in order to determine activity yields as a function of time of irradiation. To derive an expression for this behavior, begin with Equation 2.7.

$$\frac{dN(t)}{dt} = G - \lambda N(t) \tag{2.7}$$

Where G, is a simulated production rate constant in units of $[\frac{atoms\ of\ Mo99}{sec}]$ and will be estimated from GEANT4. The assumption that this production rate is constant is a fair approximation because the amount of atoms in the targets are very much larger than the atoms being produced. The $\lambda N(t)$ term represents the loss rate due to decay during the process. Solving Equation 2.7 for $N(t)$ yields Equation 2.8.

$$N(t) = \frac{G}{\lambda} - \frac{G}{\lambda} e^{-\lambda t} \tag{2.8}$$

Likewise an expression for the activity can be derived using Equation 2.6 and Equation 2.8 which yields Equation 2.9.

$$A(t) = G - Ge^{-\lambda t} \tag{2.9}$$

Equation 2.9 will be used in order to determine the activity produced as a function of irradiation time in the accelerator and is important because medical facility order radioisotopes in terms of activity by standard.

Methods

Tools

In order to optimize these parameters, computational models were developed in order to simulate this process. These models provided important preliminary results in order to estimate how an experiment would actually behave if conducted. Computer programs used to simulate the processes includes GEANT4 [10], Microsoft Excel, and KaleidaGraph.

GEANT4 is an open-source, C++ based code for modeling the passage of particles through matter. This program includes a complete range of functionality that includes tracking, geometry, and physics. GEANT4 also covers a large energy range from a few hundred eV to TeV range particles. This code was used in order to construct a Monte-Carlo simulation of our target system in order to simulate the particle interactions in our target system. GEANT4 was chosen as opposed to other Monte-Carlo physics codes because of its ability to accurately simulate photon effects and bremsstrahlung based reactions. The code developed was able to track the energy and position of electrons, photons, positrons, protons, neutrons, ions, and other physical particles.

The photon behavior was of specific interest and the output data files of the simulation were input into KaleidaGraph in order to produce plots. KaleidaGraph was used because of its ability to conveniently manage large sets of input data and produce histograms of this data.

The amount of molybdenum-99 and molybdenum-98 was also calculated and input into Microsoft Excel where further calculations were performed on the data. Microsoft Excel was used because it is simple to use the data analysis tools in order to generate plots.

Conceptual Design

This project began with by constructing a simple paradigm for irradiating the molybdenum-100 targets. The process begins with a linear accelerator producing 35-50 MeV electrons which than interact with a tungsten surface in order to produce bremsstrahlung photons. This energy range was chosen in order to generate photons that were in the desired cross-section range. Tungsten was chosen because it is a high-Z material and has also been used in other bremsstrahlung applications, such as X-rays. The high-energy photons than have a probability of interacting with molybdenum-100 and producing molybdenum-99 or molybdenum-98. Molybdenum-98 is undesirable, although it is also a stable molybdenum isotope and will not contribute to radiation concerns. A concept diagram can be shown in Figure 2.6 that illustrates a simple starting point of this design.

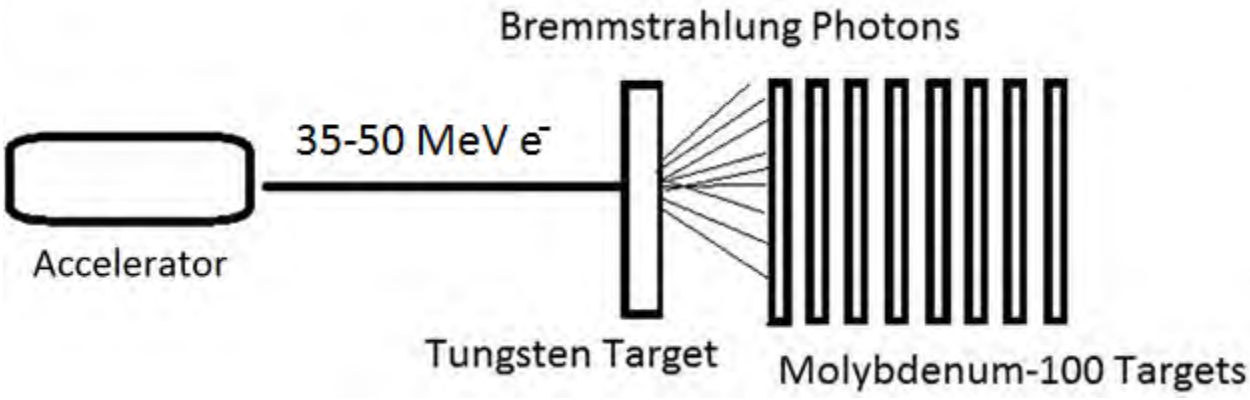

Figure 2.6. Concept design of target system.

After the molybdenum-100 targets are irradiated, they continue to the hot-cell where they are chemically processed into technetium-99m for medical use.

Assumptions

The following section outlines assumptions that went into the GEANT4 simulation and justifications for these assumptions. The geometry was constructed in small, circular discs in order to minimize the amount of enriched molybdenum-100 since the electron beam spreads in a circular shape. These molybdenum-100 discs were 1 cm in radius and 1 mm thin and separated 1 mm of water for cooling purposes. In front of these molybdenum-100 discs is a tungsten surface that is 3 mm thick in order to generate the bremsstrahlung photons. 20 molybdenum-100 discs were chosen in order to reach two irradiation lengths (1.92cm) and corresponds to ~50% of the photons to be utilized within the target system. Extending beyond two irradiation lengths was determined to be too expensive and inefficient

since the discs get exponentially less photons but take the same amount of material to manufacture. The incident electron beam is assumed to be Gaussian in energy with 41 ± 2 MeV. The electron beam is also assumed to be Gaussian spread across the disc surface with a radius of $0 \pm 1/3$ cm, which implies that ~99.7% of electrons will initially interact with the tungsten surface. The beam power was assumed to be 100 kW to increase the total yield of the molybdenum-99 while maintaining target cooling concerns. It was also assumed that the molybdenum-100 targets were 100% enriched, which is a reasonable assumption since >99% enrichment is available from Trace Science International in the form of a metal powder [6]. A sample of 100,000 electrons was simulated in order to provide the large sample size necessary for Monte-Carlo approach.

Results and Discussion

Several iterations were run in order to reach the optimal geometry, enrichment, and beam energy. The inputs under the assumptions is the final result of the design process that optimizes these parameters in order to generate the highest yield in the target irradiation process. The data provided in this section outline the important figures of interest in the target design portion of the design process.

Spatial Photon Distribution

The spatial distribution of the photons upon the first molubdenum-100 discs was plotted using the output files from the GEANT4 simulation and is shown in Figure 2.7.

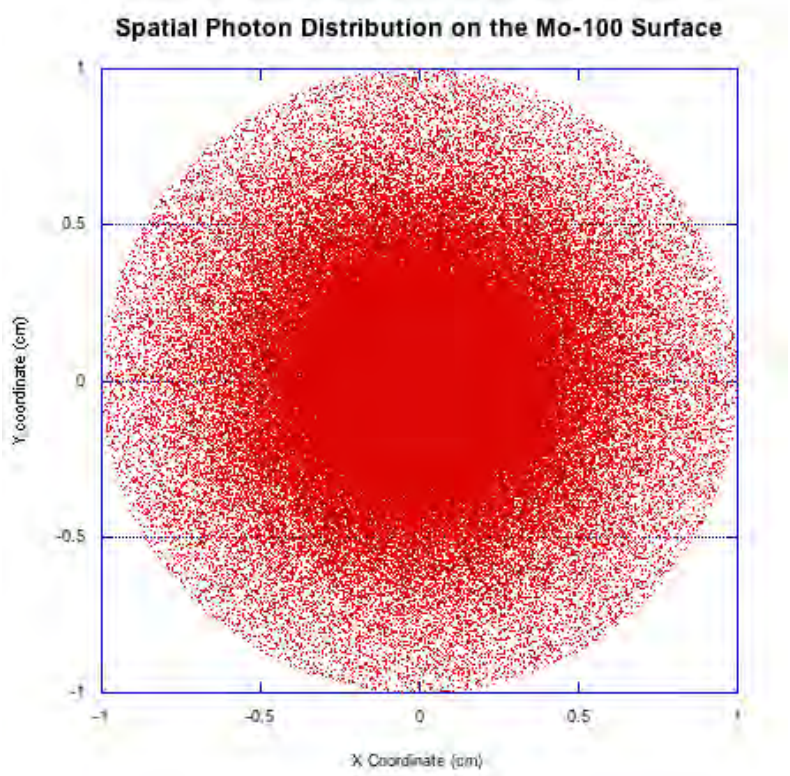

Figure 2.7. Spatial distribution of bremsstrahlung photons on the first molybdenum-100 target.

As demonstrated by Figure 2.7, the center of the target discs will be irradiated with a larger magnitude of the photons and will create a hotspot at this location. These plots also demonstrate that there isn't any specific scattering direction using this target system.

Photon Energy Distribution

The photon energy distribution was calculated using the GEANT4 output file in order to determine the amount of useable photons that are generated as a result of the bremsstrahlung process. The photon distribution shown in Figure 2.8 begins at 8 MeV since the cross sections for molybdenum-99 (as shown in Figure 2.1) is negligible below 8 MeV.

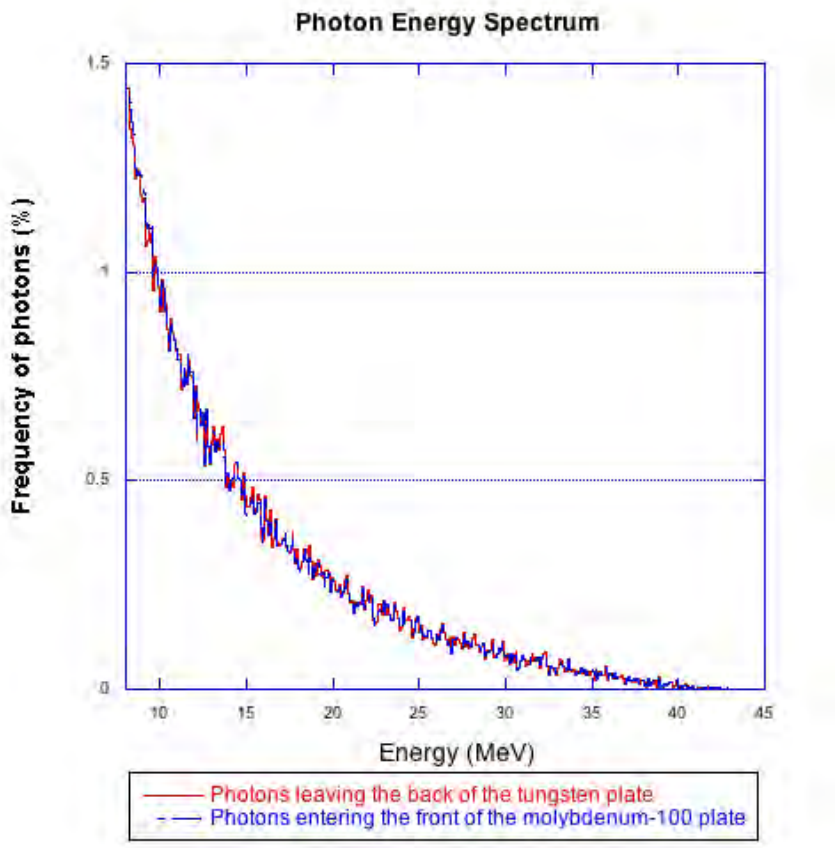

Figure 2.8. Photon energy spectrum for photons leaving the tungsten (red) and entering the molybdenum-100 (blue) for photons above 8 MeV.

Figure 2.8 is the histogram of the photon energy and is binned into 500 data intervals. The Y-axis of this plot is the frequency of photons in terms of a percentage of photons in between 8-45 MeV that falls into one of these 500 intervals. From this plot and the cross section plot (Figure 2.1), one can conclude several important design optimization parameters. The first is that photon energies are present in significant amounts for photon energies above 15 MeV and therefore molybdenum-98 will also be produced. Although molybdenum-98 is not desirable, it is a stable isotope of molybdenum and will not contribute to the activity making it relatively harmless. The second major conclusion is that the majority of the photons are in between 8-15 MeV range and these are capable of producing molybdenum-100. The third is that Figure 2.8 contains a plot of the photon energies for photons leaving the back of the tungsten plate, as well ass, the photons entering the molybdenum-100 plate. Taking the difference between these determines the amount of attenuation present in the 1 mm gap of water between these

two targets and one can determine that this water gap does not attenuate the photons significantly based on Figure 2.8.

Energy Deposition Profile

In order to accurately determine the amount of heat that needs to be removed, the energy deposition profile was calculated using the GEANT4 output file. This information was provided to the target cooling portion of the design and feedback was received in order to optimize the irradiation beam operating power. The energy deposition profile, shown in Figure 2.9, was calculated using a 4 mm thick molybdenum disc.

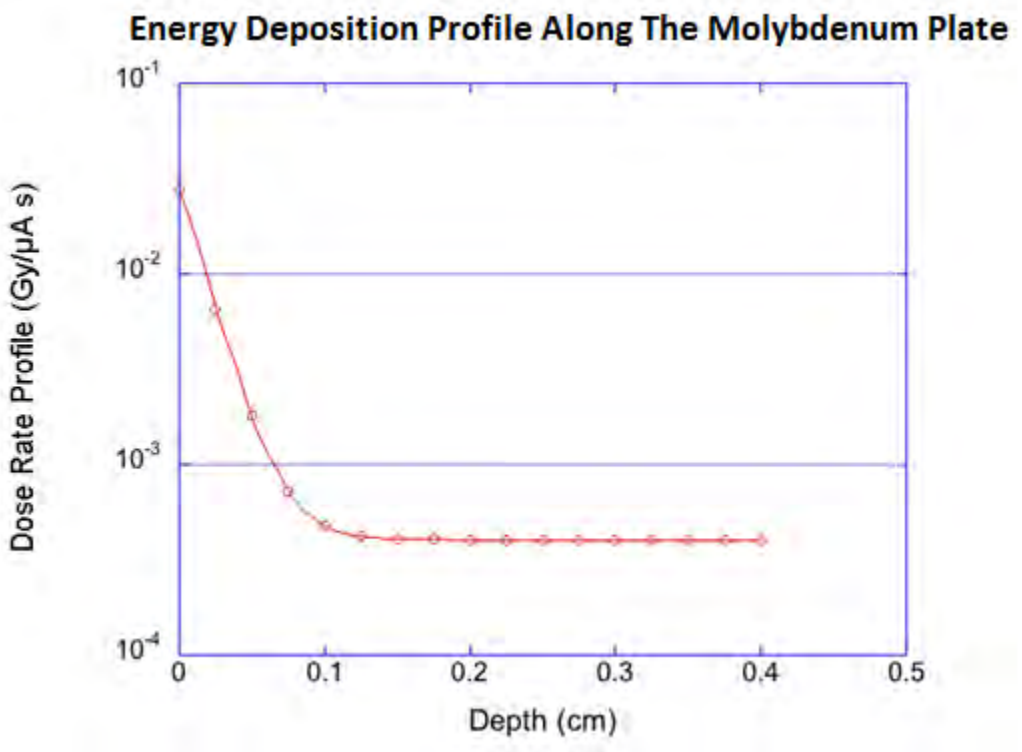

Figure 2.9. The energy deposition profile along a 4 mm molybdenum disc.

Figure 2.9 shows where the photons deposit their energy and is normalized to a 1 μA current. This means that simply multiplying this plot by the beam current will yield the dose rate in the molybdenum-100 discs. The results of Figure 2.9 led the design team to make the targets thinner (1 mm) since over 100 times more energy is deposited on the surface of the first 1 mm of the molybdenum-100 disc. An additional advantage to shrinking the disc size is also that it will dissolve in the NaOH solution more rapidly when the targets are being chemically processed post-irradiation. Figure 2.9 also shows that the

most significant target cooling concern is the first molybdenum-100 discs since that is where the majority of low energy photons deposit their energy. For the target cooling portion of this design, this plot acts as the heat source generation rate over the molybdenum-100 disc system.

Activity

The most important goal of this design is to maximize the activity yield during irradiation in order to produce molybdenum-99 efficiently. In order to calculate this, the GEANT4 code output the amount of atoms of molybdenum-99 produced for the assumed 100,000 electron sample and will be represented by the constant, C. The following ratio was obtained from the GEANT4 code under the assumptions outlined in this section (Section II).

$$C = \frac{144\ atoms\ of\ ^{99}Mo}{100{,}000\ electrons}$$

Next, the amount of electrons per second was calculated using the assumed 100 kW beam power. Equation 2.10 below gives us the beam current necessary to operate at in order to remain at 100 kW.

$$\frac{100\,kW}{41\,MeV} = 2.272\,mA \tag{2.10}$$

Since our beam is operating at $2.272\ mA$, this result can be used in order to determine the amount of molybdenum-99 atoms produced. The below expression, Equation 2.11, assumes that the amount of molybdenum-99 atoms produced is constant because the amount of atoms produced is significantly smaller than the amount of atoms present in the molybdenum-100 target material.

$$2.272\,mA * \left(\frac{6.241\times10^{15}\,e^{-}/\,sec}{1\,mA} \right) * C = 2.042\times10^{13}\,\frac{atoms\,of\,Mo99}{sec} = G \tag{2.11}$$

G is the amount of atoms of molybdenum-99 produced per second in the target system and is assumed to be constant. Now that G has been calculated for the target system, Equation 2.9 was used in addition to the fact that the decay constant, $\lambda = 2.91845 \times 10^{-6}\ sec^{-1}$, for molybdenum-99 to produce Figure 2.10.

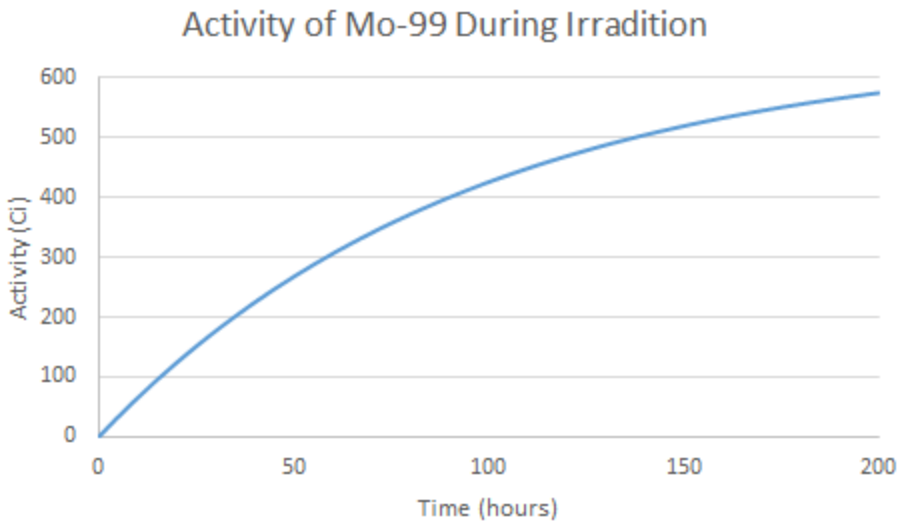

Figure 2.10. Activity of molybdenum-99 as a function of irradiation time.

Figure 2.10 represents the main optimization parameter in target design; the amount of molybdenum-99 that can be produced in the target system. In industry, hospitals order the amount of molybdenum-99 in terms of Ci at the date and time of calibration and typically range from 1-20 Ci. [11]. If it takes two days for the molybdenum-99 to reach the hospital because of post-processing and chemical separation, this means 33.1 Ci would have to be produced in order to supply a hospital with 20 Ci because of decay during shipment and processing. According to Figure 2.10, this 33.1 Ci would take approximately 5 hours of irradiation time. This means that irradiating the target system for a day to two days would produce 146 Ci to 249 Ci and be able to meet many hospitals demand for molybdenum-99 with just one target system and one accelerator.

Conclusion

In conclusion, using this design is a viable method for meeting the demand of molybdenum-99. Accelerators capable of meeting the 100 kW and 2.27 mA requirement are commercially available from the MEVEX accelerator company and can be shown in Figure 2.11 [12].

Figure 2.11. MEVEX accelerator used for the production of molybdenum-99. Also, these MEVEX accelerators can come in a clustered accelerator facility which can have up to four accelerators in one facility and is shown below in Figure 2.12 [12].

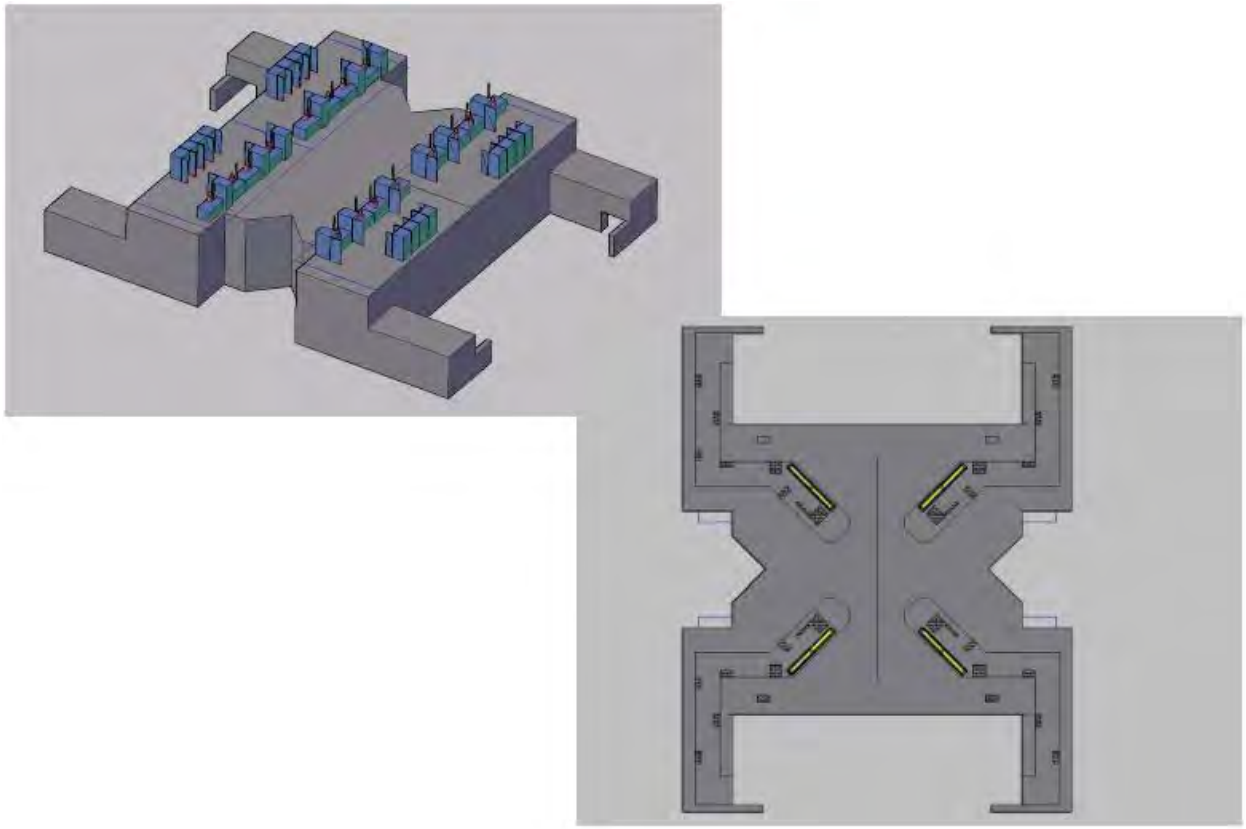

Figure 2.12. MEVEX diagram for four-accelerator facilities. [12]

The MEVEX accelerator company has been contacted by myself and Dr. Gamal Akabani and is willing to work with Texas A&M University to begin a pilot-program for the local distribution of molybdenum-99. Also, the data provided in this section was in coherence with the other sections of this project and feedback was obtained in order to maximize these values. The remainder of the process will be discussed in the following sections.

CHAPTER III

THERMODYNAMICS – EDEN MARROQUIN

Introduction

The thermodynamic analysis was a vital component of the target design process since it imposed many restrictions on the overall design of the procedure, ultimately affecting all other aspects of the system including but not limited to the chemical separation process and shielding requirements. The system contains a pure water loop which is chilled in order to remove the heat being generated by the photo-neutron interactions in the molybdenum targets. The primary concerns were the maximizing the production of the molybdenum, while maintaining the target and water integrity. The optimization of our design involved optimizing the target system geometry, flow velocity of the coolant, entrance temperature of the coolant, internal heat generation rate of the targets, and discharge pressure of the coolant. All of these parameters were manipulated to produce an effective target design which met the total target production of molybdenum, whilst maintaining target integrity and coolant integrity. The end result is a target system which can be commercially deployed to meet the future medical demands of technetium, once reactor production of technetium is phased out, due to ever increasing costs.

Overview of System

The central component to the target system can be seen in Figure 3.1. The tungsten block holds up to nineteen molybdenum disks in place to be irradiated at any given time. The solid tungsten block is machined in order to allow for the precise positioning of each molybdenum disk. The two tungsten parts are then fused together securely encapsulating the targets in preparation for irradiation of the targets. The molybdenum targets need to be securely held in place due to the water flow, which will be flowing across the surface of the targets. Depending on the water flow rate the targets may be exposed to laminar or a turbulent flow regime. The flow velocity can thus cause vibrations which could potentially dislodge one of the targets, hence negatively impacting the cooling capability of our design.

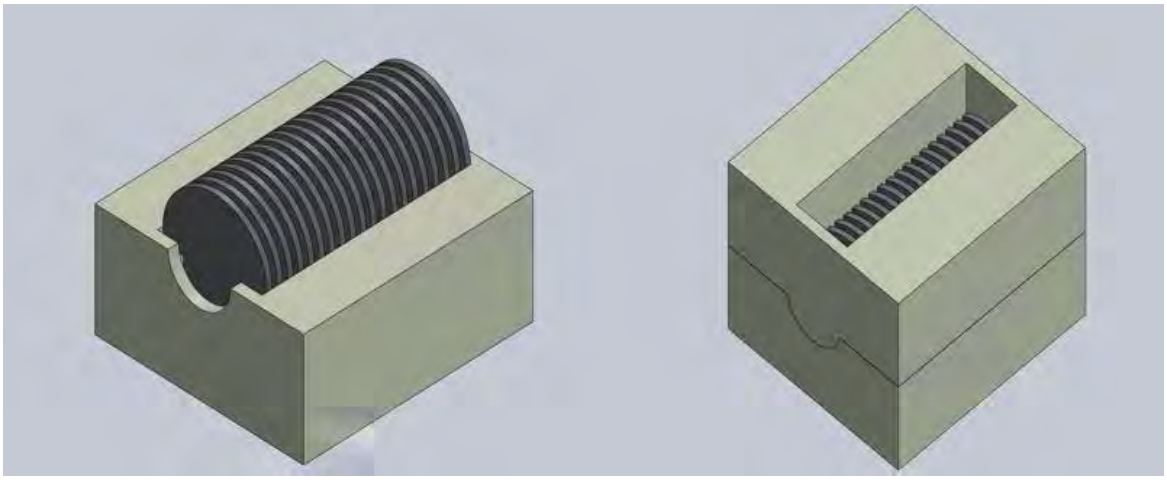

Figure 3.1. Basic target system coolant enters through rectangular opening in tungsten block.

The coolant is carried away to be returned to the nominal boundary condition temperature by the use of a secondary and unaddressed method, since the inventory of coolant needed is not expected to be significant. The tungsten target will be cooled while gamma rays are being imparted via an accelerator. The generated gamma rays will be centered on the molybdenum targets and will be generated in a vacuum. After sufficient irradiation the desired activity will be reached and the target system will be removed from the accelerator for post processing. The post processing will be conducted through the dilution of the molybdenum target in an aqueous solution.

Objective of the System

The primary objective of the target system is to maximize the production of molybdenum-99, while providing a sufficient heat removal rate. The purpose of this is to keep the cooling fluid, namely the water from boiling. As previously mentioned a variety of parameters were optimized in order to achieve the desired outcome.

The target holder is composed of tungsten. The target holder can accommodate up to nineteen molybdenum targets. The spacing in-between the targets was chosen to be one millimeter to allow water to pass through the gaps in the target system and keep the targets from nearing melting point temperatures. All of the targets are exactly parallel to each other to enhance the cooling. In should be noted however that all of the targets do not need to be inserted in order to successfully operate the device.

A possible concern when using the cooling water is the consideration for its disposal since it is possible that the circulation of through the system could cause the water to absorb tungsten or molybdenum. Thus, depending on the concentration of tungsten or molybdenum in the coolant, special precaution might need to be taken before disposing of the water. Depending on the total time of irradiation a signification inventory might be needed in order to ensure that the discharge coolant can be chilled back to operational temperature.

Target System Assembly

As previously discussed the target system is composed of a maximum of twenty-two parts nineteen of those being the molybdenum targets. The other two parts are the top and bottom parts of the tungsten holder. The procedure should take place in the following order first the chosen number of molybdenum targets will be chosen. Next, the top and bottom parts of the tungsten will be mated while the molybdenum targets are contained within. Finally, the assembly will be placed in the path of the gamma rays to being irradiation. In order to cool he molybdenum targets a water flow will enter through the top of the geometry and exit through the bottom, a depiction is shown in Figure 3.2. The coolant used is nothing more than chilled pure water. Moreover, the system will be pressurized in order to ensure that the coolant does not boil within the system. After irradiation is completed the target system will be removed from the accelerator and be furthered processed. To being the chemical separation process the tungsten parts will be dismantled and the molybdenum parts will be ground to a very fine powder.

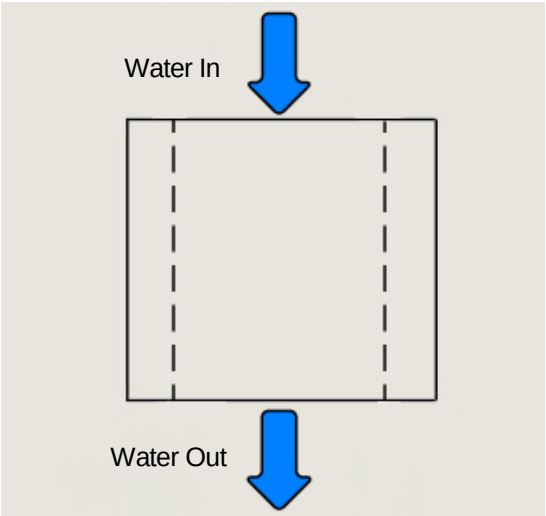

Figure 3.2. The coolant direction and outflow of thermal energy is indicated by the arrows.

Theory

Program Used

The thermodynamic analysis performed in order to optimize the target design was facilitated through the use of COMSOL 4.2a. COMSOL is a general-purpose software platform, based on advanced numerical methods. [13] Specifically, the analysis was used using a concept introduced by COMSOL, namely *conjugate heat transfer*. All notation used in the discussion of *conjugate heat transfer* and the theory can be found in the Appendix under the thermodynamics section. COMSOL is fully capable of modeling both the heat transfer and fluids phenomena required to analyze the proposed target system. Moreover, COMSOL is not only easy to use but is all encompassing. Furthermore, the output from the results is an excellent way to visualize the solution. COMSOL output is not only efficient but an aesthetically pleasing manner of presenting the results.

Governing Equations

Conjugate heat transfer is the combination of heat transfer in solids and heat transfer in fluids. In this analysis the heat transfer between the fluid and the solid are closely linked. It is essential to remember, however that conduction dominates in heat transfer through solids, while heat transfer in fluids is dominated by convection. The theory behind conjugate heat transfer will be discussed in depth before addressing the results of the performed analysis. Heat transfer in solids due to conduction is governed by Fourier's law, the heat flux is proportional to the temperature gradient. The general form of the equation is shown in Equation 3.1 [14].

$$q = -k\nabla T \tag{3.1}$$

If a solid contains a heat source within it, the problem becomes time dependent. The general form is shown in Equation 3.2.

$$\rho C_p \frac{\partial T}{\partial t} = \nabla \cdot (k\nabla T) + Q \tag{3.2}$$

In this analysis however only the steady state solution of the problem will be considered as transients are assumed to be short lived. The transients are also assumed to not exceed any of the parameters presented in the steady state solution of the problem. Furthermore, the equation can be generalized further, since the fluid in our model will by definition transport thermal energy away

from the structures. Therefore, a convective heat transfer term must be added the equation. Moreover, the viscous effects of the fluid and the changes in density of the fluid must be accounted for as well. Finally, we arrive at the most general form of the heat transfer equation which COMSOL uses to couple together the heat transfer in fluids and solids. This equation accounts for pressure changes as well. Equation 3.3 is the most general form used in conjugate heat transfer by COMSOL [15].

$$\rho C_p \frac{\partial T}{\partial t} + \rho C_p \mathbf{u} \cdot \nabla T = \alpha_P T(\frac{\partial P_A}{\partial t} + \mathbf{u} \cdot \nabla P_A) + \tau : S + \nabla \cdot (k \nabla T) + Q \tag{3.3}$$

The temperature field in the solids, namely the tungsten and molybdenum, do not change drastically within the solids however the temperature field does change drastically within the fluid. The temperature field in the fluid changes rapidly over the span of the thermal boundary layer. The size or thickness of the thermal boundary layer is reflected by the Prandtl number. The Prandtl number is dimensionless and represents the ratio of momentum diffusivity over the thermal diffusivity of the fluid. [16] Thus, the Prandtl number is given in Equation 3.4.

$$\mathrm{Pr} = \frac{C_p \mu}{k} \tag{3.4}$$

The changes in the temperature field within the fluid are drastic in comparison to the changes in the temperature field of the flow. Nonetheless, the fluid temperature field still maintains a relatively small gradient, due the Prandtl number in our system. Furthermore, the Grashof number is another indicator of the flow regime and is dimensionless and represents the ratio of buoyant to viscous forces. [17]. The Grashof number as is derived from the Buckingham Pi Theorem is shown in Equation 3.5.

$$Gr = \frac{\beta g \Delta T L^3}{\upsilon^2} \tag{3.5}$$

Furthermore, the Rayleigh number is shown in Equation 3.6.

$$Ra = \frac{\rho^2 g C_p}{\mu k} \Delta T L^3 = PrGr \tag{3.6}$$

The Rayleigh number can be rewritten as the product of the Prandtl number and the Grashof number, thus when the Rayleigh number is small typically less than one-thousand then natural

convection is usually negligible since the flow regime is expected to be purely laminar flow. It is completely possible, however that the flow regime is characterized to be turbulent in nature. It is not uncommon for outside phenomena to dominate the buoyancy effects. In order to characterize the flow regime the Reynolds number can be considered. Reynolds number represents the ratio of inertial forces to viscous forces [18]. At a high Reynolds number the dampening of the system is low and small perturbations can grow into larger oscillation and into the turbulent regime. On the contrary a very small Reynolds number in contrast conveys that small perturbations in the system will be eliminated and the flow will remain in the laminar regime. Reynolds number is expressed in Equation 3.7.

$$Re = \frac{\rho UL}{\mu} \tag{3.7}$$

Moreover, since radiative heat transfer is governed by Equation 3.8. It is clear from the results that our target system did not sustain the high enough temperature differences to consider radiative heat transfer a significant heat transfer mode in this analysis. Radiative heat transfer is usually a heat transfer mode associated with significant temperature gradients since the total amount of radiation increases very rapidly as the temperature rises since it grows to the power of four [19].

$$q_r = \varepsilon n^2 \sigma (T_{amb}^4 - T^4) \tag{3.8}$$

In our target system the heat transfer occurs both in solids and in fluids, this is because our solids are immersed in a fluid flow. COMSOL allows the precise description of our geometry and material properties. Also, COMSOL allowed the analysis of the temperature and flow fields. Furthermore, provides insight in the flow regimes at various locations in and around the target system.

Assumptions & Imposed Conditions

Material Assumptions

Various assumptions were made in order to simply the complexity of the problem at hand. The first assumption made was to set a no slip condition an all of the walls. The materials were also assumed to be homogenous in nature and of a high purity. All materials were assumed to be free of defects and maintain nominal properties during operation. The materials were also assumed to

maintain their integrity during the normal operations of the system, the only variables being considered were the oxidation temperatures and melting points of the solid materials.

Coolant Assumptions

The fluid being used was also assumed to be of high purity and not undergo chemical changes due to the rapid change in temperature. Furthermore, it was assumed that the water was chilled to a constant and uniform temperature. It was assumed that the fluid cooling the system may approach the target system with a uniform velocity field, which is normal to the molybdenum targets. The targets were assumed to be internal heat generation sources when in reality there is a distribution in the thermal energy generation within the molybdenum targets. This assumption was made since the targets are only one millimeter in thickness and the thermal conductivity of the material is relatively high to that of the cooling fluid. The inlet temperature was assumed to be user controlled.

Additionally, it was assumed that thermal energy only exited the geometry through the fluid which exited the geometry, hence it is implied that thermal energy does not leave the geometry through cross flow. The system was also assumed to be pressurized to prevent the boiling of the cooling fluid. The outlet boundary wall was assumed to experience no viscous stress.

Details of the Input

Geometry Creation

The target system was created using a multi-physics file, which is the standard file input for COMSOL. The geometry was created using the various software tools, which are integrated into the software. The geometry was created using a 3D-CAD model. To begin the tungsten rectangular prism was sketched and extruded. Next a top sketch was made on the tungsten solid and an extruded cut was made to create the rectangle which cuts through the solid. Next, creating individual planes of reference for each of the nineteen molybdenum targets. Finally, centered circles with a diameter of twenty millimeters were created on each individual plane and extruded to create the chosen geometry. Furthermore, the material properties used were integrated with COMSOL, however the thermal conductivity and heat capacitance of the tungsten and molybdenum were chosen by the user. The chosen thermal conductivity and heat capacitance were of tungsten and molybdenum which do not contain any impurities. Moreover, the properties of water a function of temperature. COMSOL, therefore does not have a fixed value for the properties of water, but rather values as a function of temperature and pressure.

Table 3.1.

Properties of materials

Material	Density (kg/m)	Specific Heat (J/kg K)	Dynamic Viscosity (Pa s)	Thermal Conductivity (W/m K)
Molybdenum	10200	250	0	138
Tungsten	17800	130	0	173
Water	1000	4208	1.57E-03	0.569

A significant error could have been introduced due to this error. A graph of the temperature dependence of conductivity for tungsten and molybdenum is shown in Figure 3.3. The error introduced is limited, however, since the maximum temperature reached was less than 650 K.

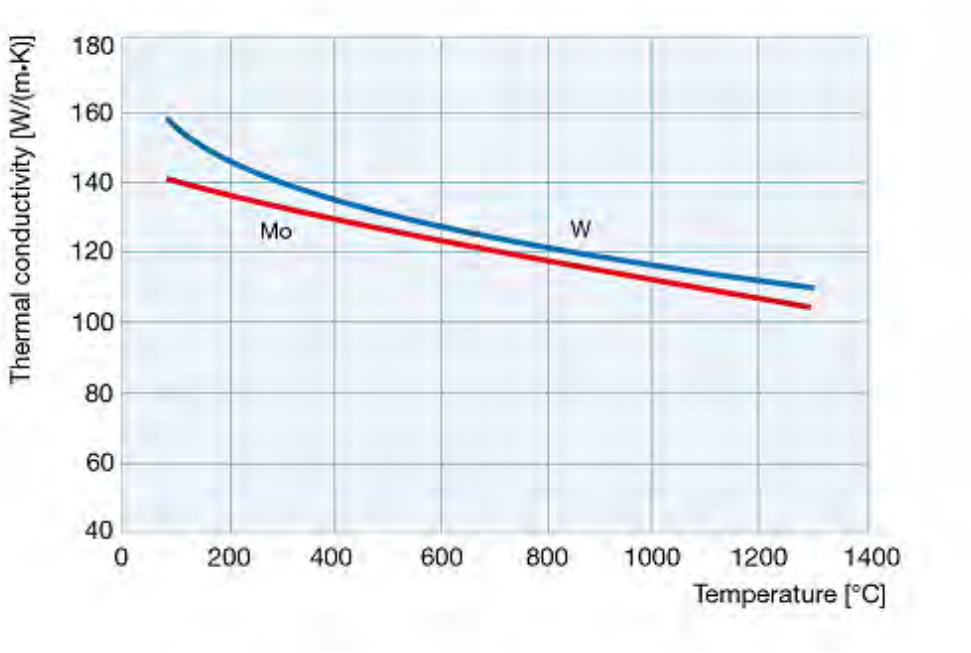

Figure 3.3. Thermal conductivity of molybdenum and tungsten as a function of temperature [20].

Target specifications

The fluid approached the geometry as a normal inflow velocity field, which was uniform across the boundary condition. The outlet boundary condition was set by a discharge pressure. The outlet boundary was also allowed to carry away thermal energy through the fluid discharge. All molybdenum target domains were assigned an effective total power to be uniformly generated throughout the target. The simulation was carried out by partitioning the target system into twenty-

three domains. The first domain was the water, followed by the two domains containing the tungsten holder. Finally, the remaining nineteen domains were for the individual molybdenum targets.

Mesh Specifications and Iterative Methods

The mesh type used was a free tetrahedral mesh. The molybdenum targets were assigned a mesh size, while the cooling fluid and tungsten shared a different mesh. The meshes were distinct in their sizes. The mesh containing the molybdenum targets was much tighter in order to improve the resolution of the simulation. The bigger mesh over the tungsten target was chosen in order to decrease computational time. Finally, the conjugate heat transfer module was simulated until the solution converged. The converged solution was a steady state solution. COMSOL used successive over-relaxation (SOR) which is a variant of Gauss-Seidel method for solving systems of equations, SOR is typically faster converging than its Gauss-Seidel counterpart. SOR is applied to solve the equation through the use of a simple algorithm which takes an initial guess to the answer and slowly converges on each iterative loop to the true solution.

Validation

Normalized Coolant Velocity

As a first means to validate our design the following conditions were used as an input file for COMSOL. The cooling fluid was chosen to enter the geometry at a temperature of four degrees centigrade. The inlet velocity of the cooling fluid was chosen to be one meter per second, with a discharge pressure of one atmosphere. Moreover, the boundary condition of the fluid were defined to be one meter per second as to simulate the target system being submerged in a bigger pool of water. Finally, the outlet boundary condition was chosen as the only location through which thermal energy could escape the configuration. Since the velocity was chosen to be one meter per second, the velocity field is, thus normalized to one. A vertical slice of the one meter per second normalized flow field around the target system is shown in Figure 3.4.

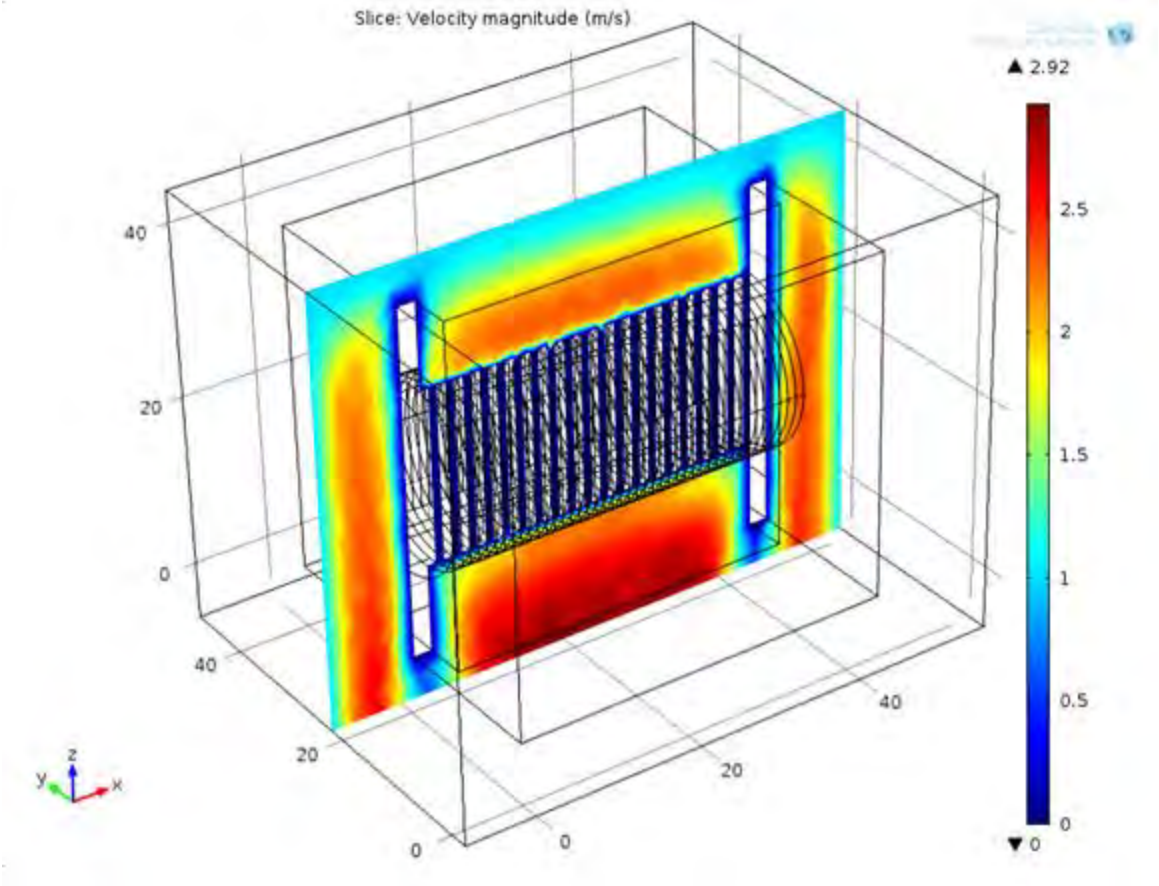

Figure 3.4. The velocity field magnitude can be seen to peak at the outlet of the discharge boundary. Furthermore, the velocity magnitude never exceeds three times the inlet velocity.

Velocity Field yx Plane

The velocity magnitude field in the yx plane can be found in Figure 3.5. As expected it can clearly be seen that the velocity field magnitude is not resolved between the molybdenum targets due to the lack in resolution of the mesh. The velocity field does not appear to be non-symmetric, indicating that the temperature field should as well be symmetric in nature.

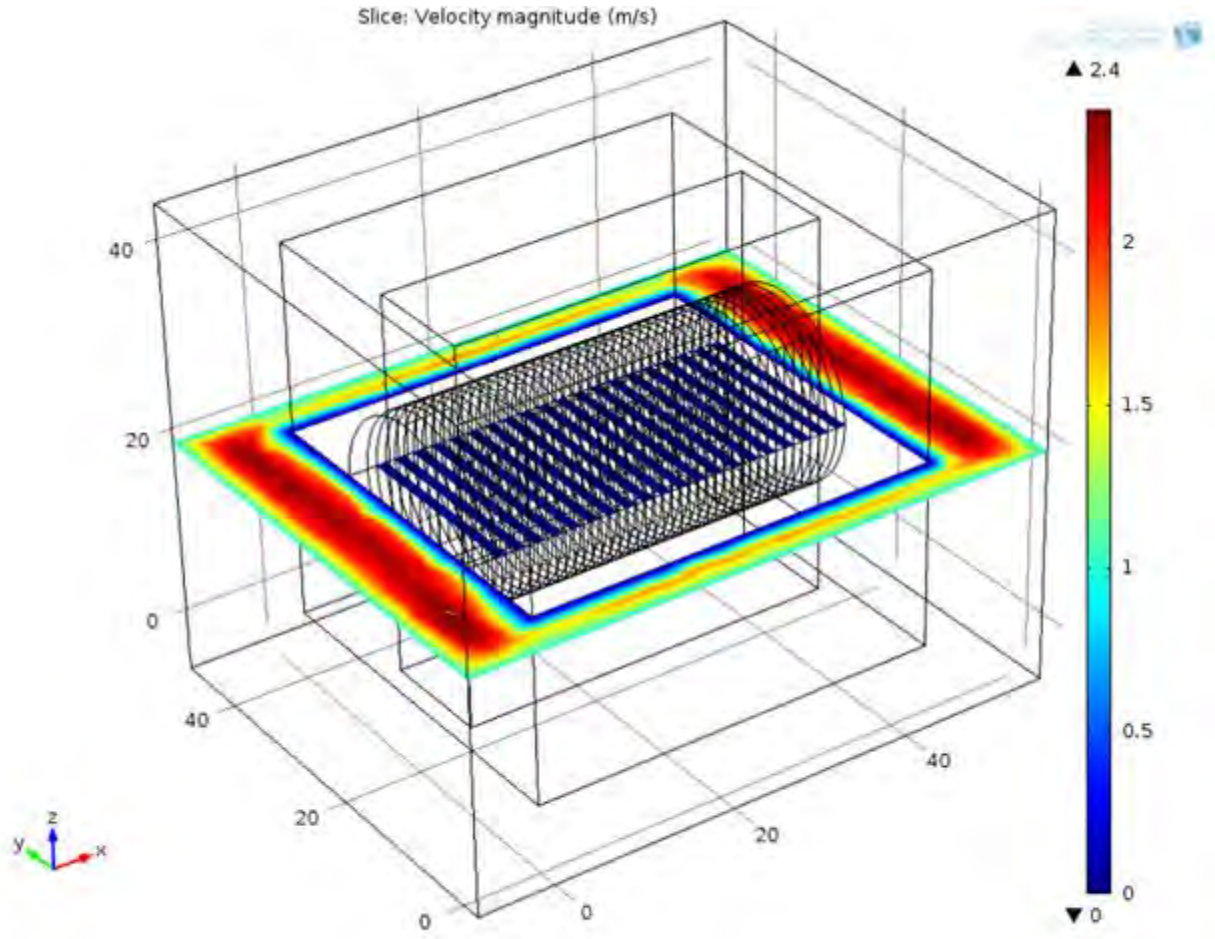

Figure 3.5 The velocity field in the xy plane

Furthermore, a cross section of the velocity field which intersects the target system in between two parallel molybdenum targets is shown in Figure 3.6. It is important to note that all walls have been placed under a no-slip condition.

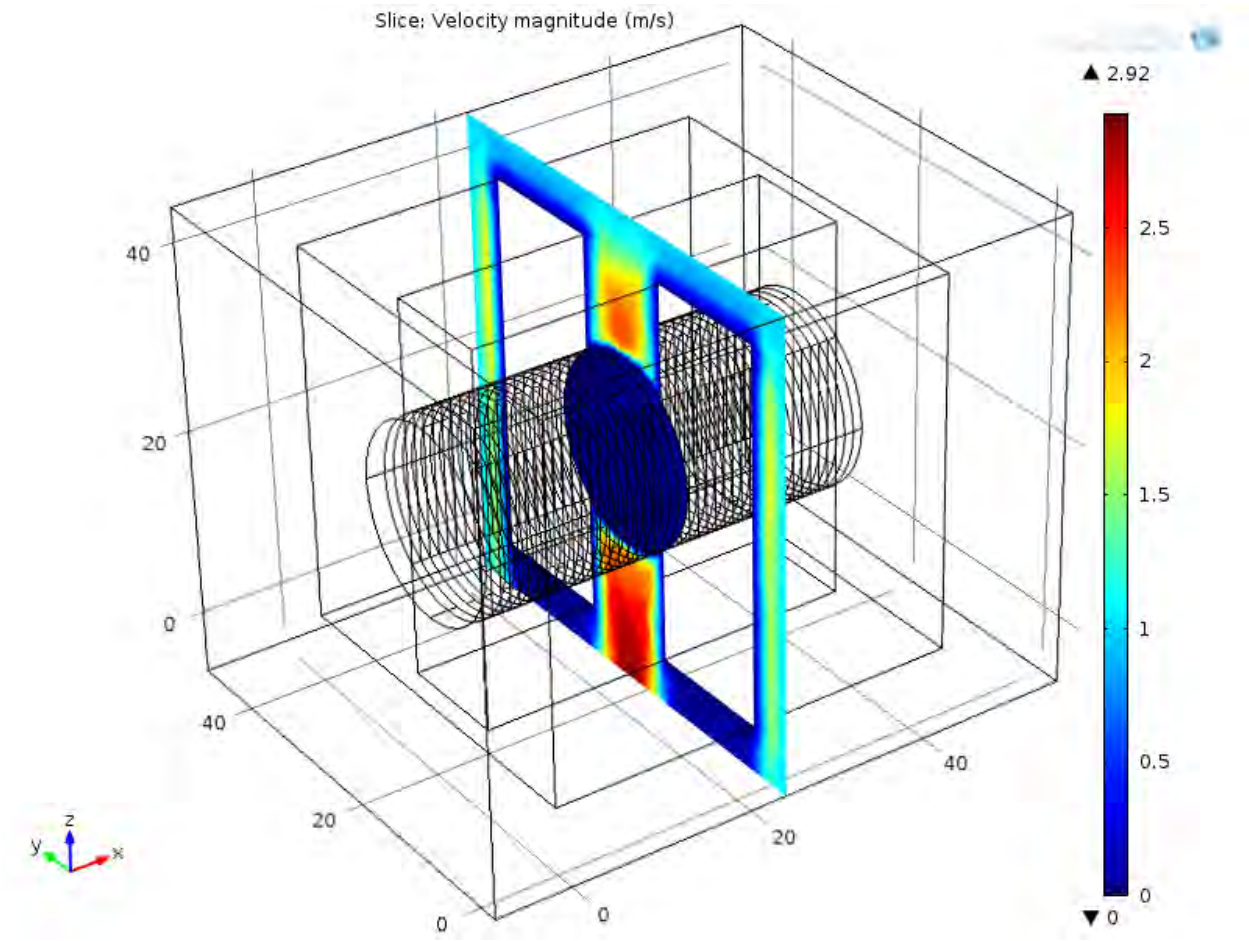

Figure 3.6. The velocity field is obstructed in the planar cross section over the molybdenum target due to the no slip condition imposed on the face of the target. The no slip boundary is displayed due to a lack in resolution of the simulation.

Resultant Temperature Field

A vertical cross section across the target system of the temperature field is shown in Figure 3.7. The temperature field far exceeds the boiling point of our cooling fluid. Nevertheless, the general distribution of the thermal energy is depicted in the figure. The resolution on the temperature field is not very precise since a coarse mesh was used in order to save computational time.

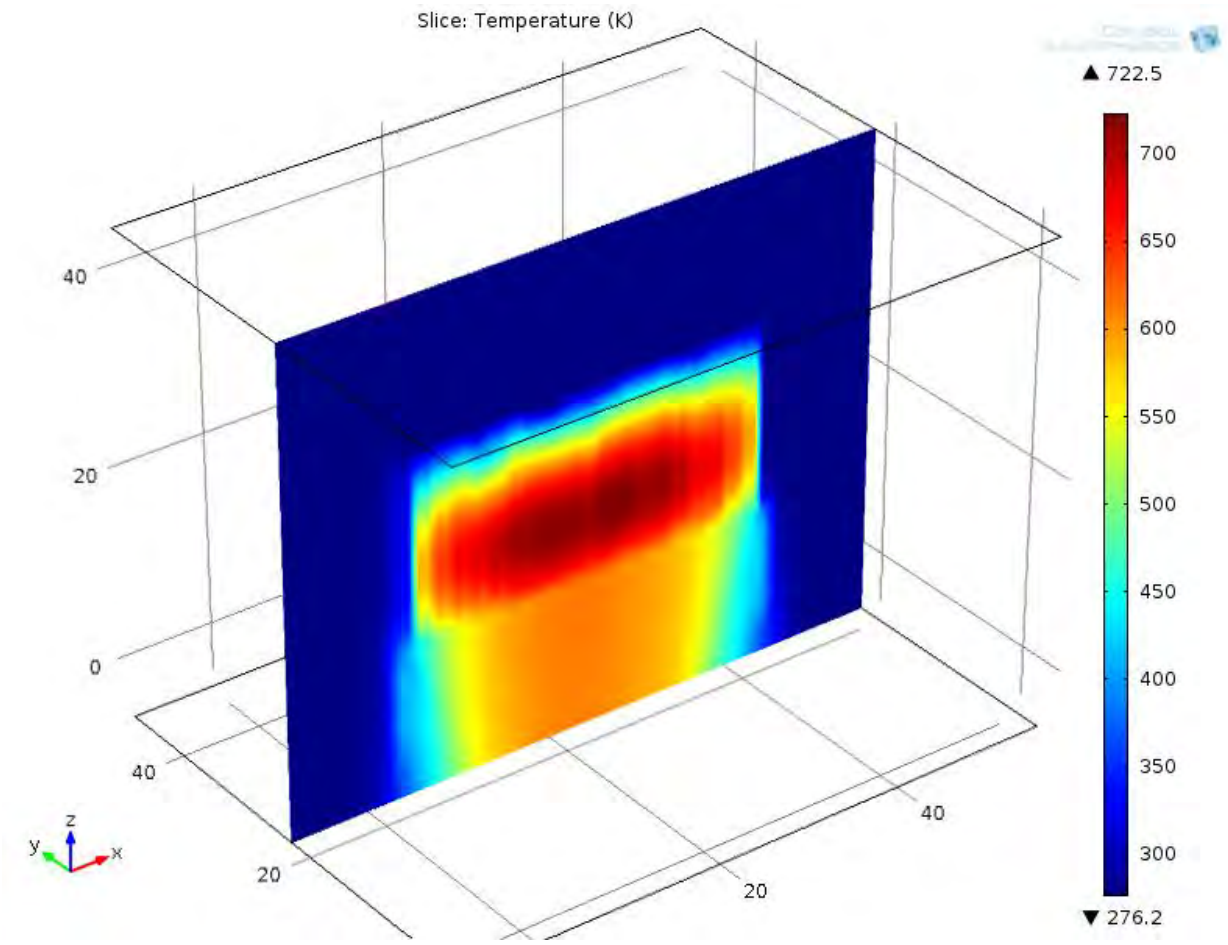

Figure 3.7. The temperature field indicates that the fluid would absorb in significant amount of thermal energy at a flow speed of one meter per second.

As it can be easily seen in Figure 3.7, the coolant attains a temperature which is much higher than its boiling point. Thus, it is easy to see that the flow velocity must be increased to avoid this problem.

Temperature Field zx Plane

The temperature magnitude field in the zx plane can be found in Figure 3.8. As expected it can clearly be seen that the temperature field magnitude is not resolved between the molybdenum targets due to the lack in resolution of the mesh. The temperature field that is shown in the image is not the temperature of the fluid but it is the temperature of the molybdenum, this is because of the lack of resolution in the simulation.

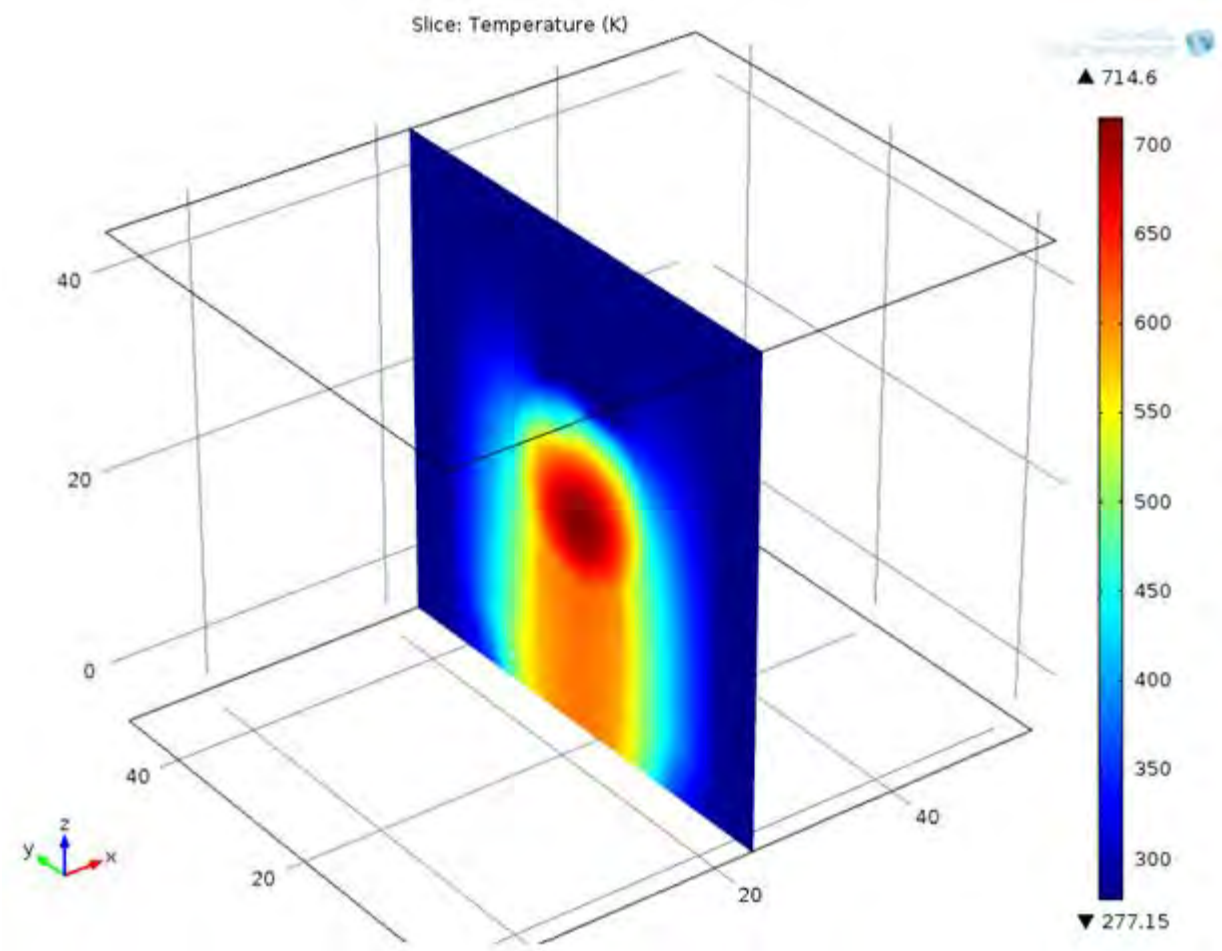

Figure 3.8. The temperature field in the xz field

Ten Meter per Second Coolant Velocity

In order to fully validate the results the coolant inlet speed was increased in order to ensure that the coolant would be maintained in a sub-cooled state through the entire system. All of the other boundary condition and properties were maintained with the exception the discharger pressure, which was increase to three and a half atmospheres. A vertical cross section across the target system of the temperature field is shown in Figure III.9. As a result of the inlet coolant speed being increased to ten meters per second the coolant only exceeds its boiling point at atmospheric pressure by a few degrees kelvin. Thus, in a pressurized system the coolant will not boil.

Direct Implications on Fluid Regime

Since the coolant velocity will be increase it is expected that the flow regime will turn turbulent at some critical point. Turbulent mixing is indicated by the Reynolds number and improves

convective heat transfer substantially. A turbulent flow regime will, however increase vibration and introduce perturbations in both the flow and temperature field. Thus, a much tighter mesh is needed to obtain a smooth velocity and temperature field. Hence, the simulation increase in computational cost. An increase in computational cost means that the simulation time increase geometrically.

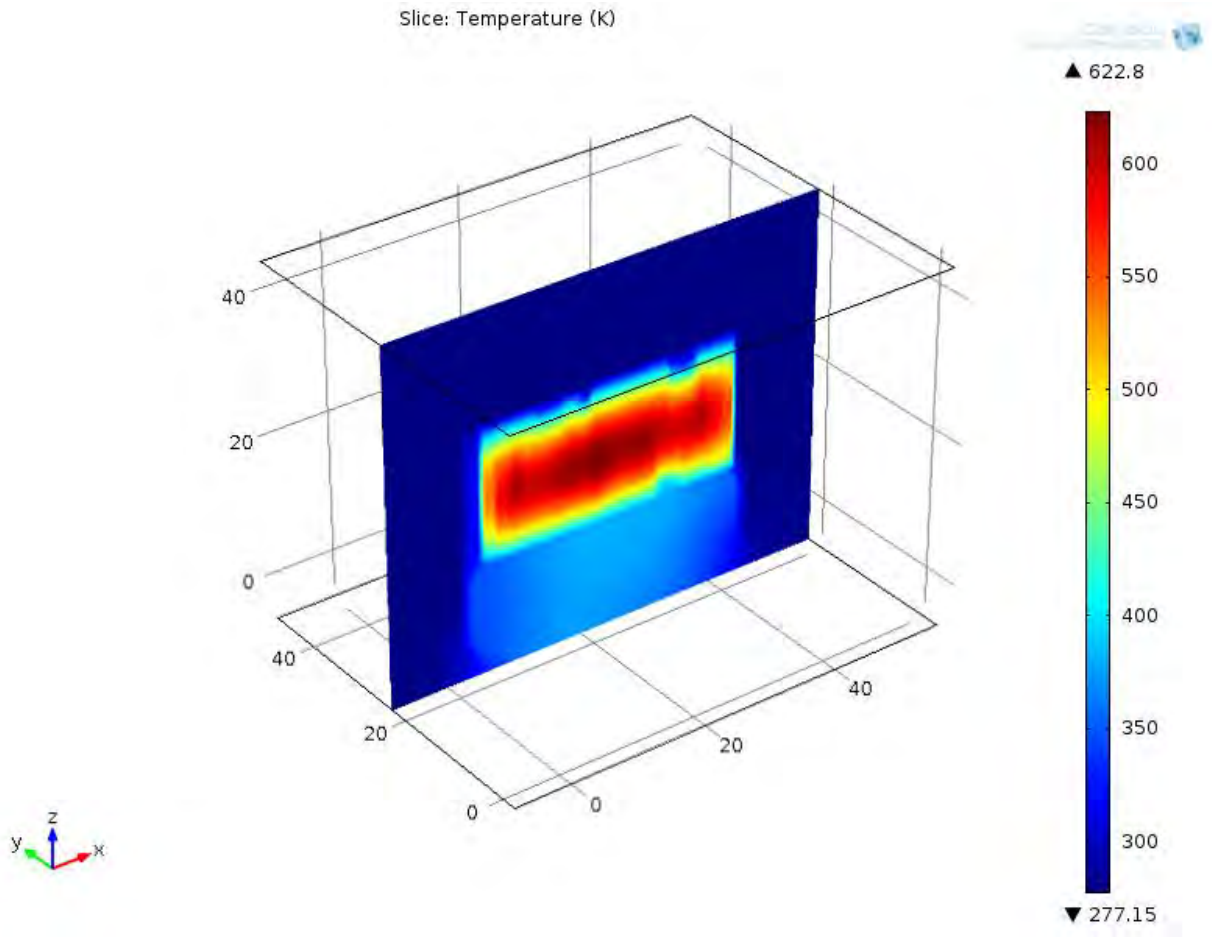

Figure 3.9 The temperature field indicates that the fluid would absorb significantly less thermal energy at a flow speed of ten meters per second.

Flow Regime

A vertical cross section across the target system of the Reynolds number is shown in Figure 3.10. A Reynolds number greater than two-thousand typically indicates that the flow has entered into the turbulent flow regime.

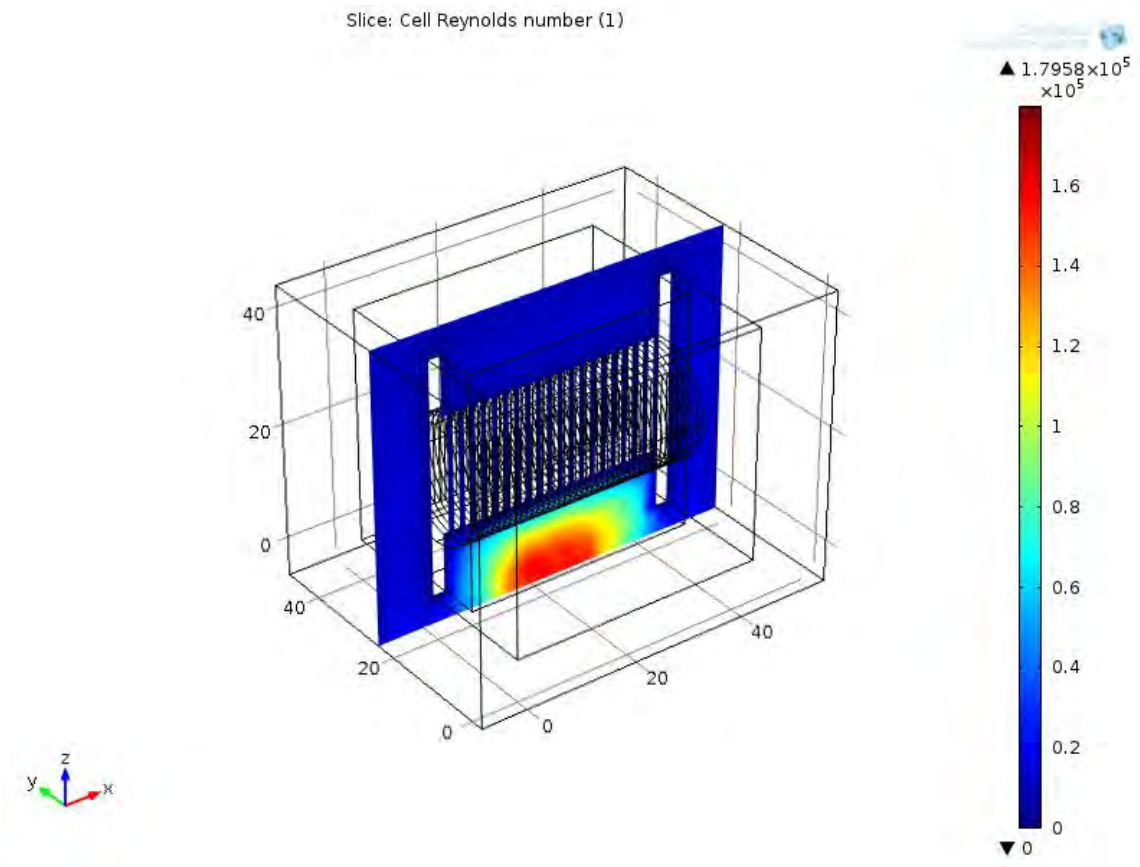

Figure 3.10 The Reynolds number indicates the flow regime in which the fluid resides.

For all practical purposes the flow is entirely in the laminar flow regime, except at the point at which it is discharged from the molybdenum targets. This is not only a function of the pressure drop across the molybdenum targets, but also caused by the thermal energy being absorbed into the coolant. There is an enormous pressure drop associated with forcing a flow rate of ten meters per second through slits that are only one millimeter wide. Moreover, the enormous energy deposition in the coolant is another reason why the Reynolds number increases drastically over a short distance.

Another vertical cross section across the target system of the Reynolds number is shown in Figure 3.11. The range of the figure however has been changed to show the detail of the rest of the image. The range has been limited in color to a Reynolds number less than two-thousand. Clearly, from this alternative image rendering it is east to see that the flow does stay within the laminar regime throughout the rest of the geometry.

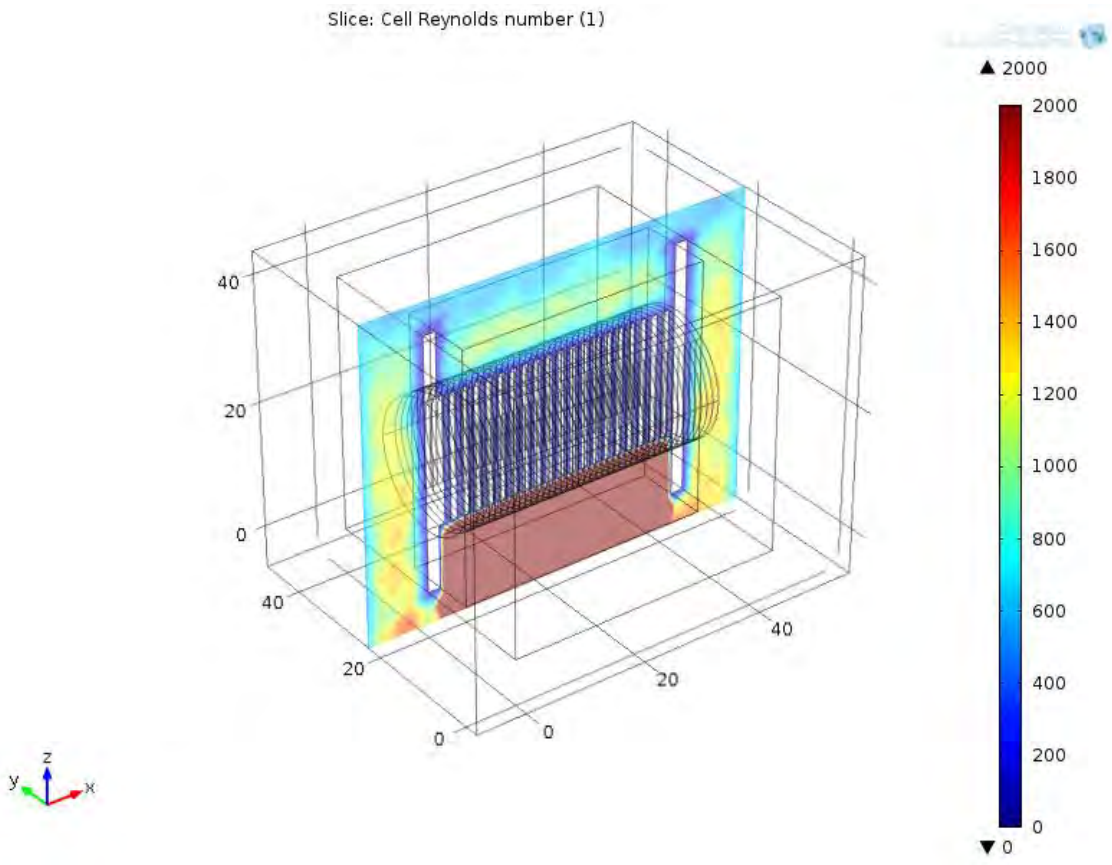

Figure 3.11 Reynolds number for the rest of velocity field cross section.

Fifteen Meter per Second Coolant Velocity

In order to fully validate the results the coolant inlet speed was increased in order to ensure that the coolant would be maintained in a sub-cooled state through the entire system. All of the other boundary condition and properties were maintained with the exception the discharger pressure, which was increased. A vertical cross section across the target system of the temperature field is shown in Figure 3.12. As a result of the inlet coolant speed being increased to fifteen meters per the coolant did not exhibit a significant reduction in the overall temperature. Therefore, as previously discussed the system will have to be pressurized in order to keep the coolant from boiling within the system.

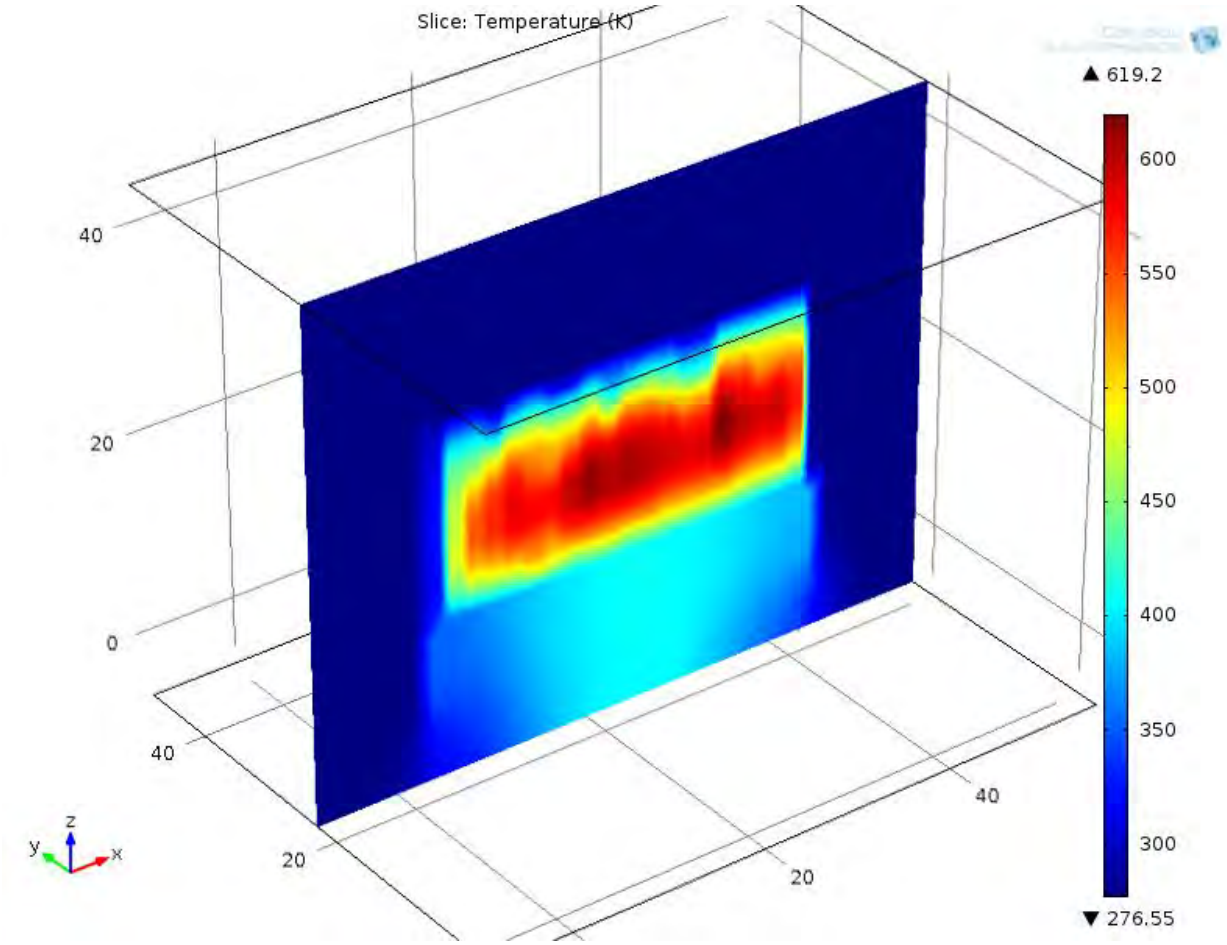

Figure 3.12 Temperature cross section with a coolant inlet velocity of fifteen meters per second.

Discussion

The proposed target system has been design with inherit flexibility in mind. The proposed plan is an effective tool in maximizing the production of molybdenum, however the procedure is not rigid and can be used in case specific situations. Case specific situations, for example, in which the user may want to produce less molybdenum at a faster rate, while still maintaining the target system properly cooled.

The normalized coolant velocity test case, provides an accurate representation of the relative expected fluid velocity field. On the contrary, it cannot be an adequate representation of the flow regime expected field, since these quantities cannot be normalized the same fashion.

The simulation in which the inlet velocity of the fluid was chosen to be then meters per second is the final validation that the design could be properly implemented to produce technetium in a grand scale. The coolant velocities required to maintain the molybdenum targets is not unreasonable and could be easily implemented by a commercial entity. Furthermore, the potential to produce molybdenum in large quantities, increases the practicality of the proposed procedure.

Results

There are two distinct set of results one for the case in which the entrance coolant velocity was normalized to one and in the second set of results the entrance coolant velocity was increased to ten meters per second to ensure that the coolant, namely the water would not boil in the system. Additionally, the system must be slightly pressurized in order to avoid the boiling.

In the normalized case we saw that the velocity magnitude was at most three times higher at some locations within a cross section of the geometry. Moreover, the temperature field indicated the coolant was boiling within the system. It was also assumed that all of the targets contained a uniform internal heat generation source. In this test case the system would need to be highly pressurized in order to avoid the coolant from boiling.

In the second study the average inlet velocity magnitude of the coolant was increased to ten meters per second while the mesh size had to be increased in order to bring down the computational cost, the solution did however show that the coolant could be kept from boiling under a few atmospheres of pressure. The velocity field maintained its distribution however the flow regime is no longer laminar. The turbulent mixing further increases the heat transfer capability of the coolant. Ultimately, the coolant should be able to adequately cool the targets and provide the necessary specific activity required.

Conclusions and Recommendations

Cost Benefit

The proposed procedure can be implemented within a few months and could potentially meet the technetium needs of the world. The applicability of this procedure will become gradually more and more important as the demand for technetium continues to rise, and the costs associated with producing it with a reactor continue to increase.

Further Analysis

One aspect of the design that was neglected is the exact pressure the system will need to maintain in order to avoid boiling the cooling fluid used to cool the target system. Further investigation will need to be made in this area, however it is not expected that the system will need to be pressurized further than a few atmospheres. There is a lack of information at the interfaces of the targets and therefore tighter more computationally expensive simulations are needed to observe the phenomena. On the contrary this information is not vital since we know the system level behavior or the target system.

SECTION IV

SHIELDING DESIGN– TALAL HARAHSHEH

Background

When projects involve radiation, shielding is crucial to protect the workers, the general public, and the environment from unnecessary radiation exposure. Our aim is to reduce this unnecessary radiation exposure to insignificant levels. Accelerators, generally produce radiation of high energy and intensity. Protection is achieved by attenuating the radiation to tolerable levels by altering the thickness and materials of a proposed shield.

The shield's preliminary requirements depend on the applicable dose limits, the amount of radiation allowed by the facility's administrative limits, and the radiation source terms. The radiation source terms are derived from the accelerator's beam parameters related to energy, type, and intensity of the beam particle. Furthermore, the shielding design should take into account the accelerator's maximum capability. Shield design should account for cases when accelerator capability at the time of construction is lower than its potential after a series of output upgrades. This avoids liabilities of costly shield redesign.

Shields will not be able to block all the radiation from escaping into the environment. Thus, dose limits should be measured and distributed to the workers and public. This will serve as quality assurance as well as useful information for the intended audience. Using the dose rates, workers will be able to determine how much time they can spend operating without passing the applicable dose limits.

Another form of radiation to be considered for attenuation by the shield is neutron radiation. Neutrons will be produced as a result of the photon-neutron interaction of the molybdenum-100 targets. In order to get an estimate of the neutron energy, the photon-neutron interaction for molybdenum-100 was used to calculate the net change in energy, see the Appendix for the calculation. Assuming an incident photon of 14.5 MeV, the neutron energy released would be 6.21 MeV. This means that the shielding required must be capable of handling at least 6.21 MeV neutrons. A safety factor will be implemented in order to provide an estimate for the shielding required. The optimal attenuation approach for the neutron radiation in question would be thermalization in hydrogenous material. However, a high atomic number material such as lead or steel would be able to attenuate neutrons with energies above 20 MeV.

The main factors in deciding the shielding material include cost of installation and maintenance, required thickness and weight, shielding potential against photons and neutrons, uniformity, and chance of inducing radioactivity.

Design

SolidWorks was used to design the needed shielding designs for this project. Designs made include the molybdenum target disk holder (Fig. 4.1) transportation shield (Fig. 4.2) as well as the container used to transport technetium-99m to medical facilities (Fig 4.7).

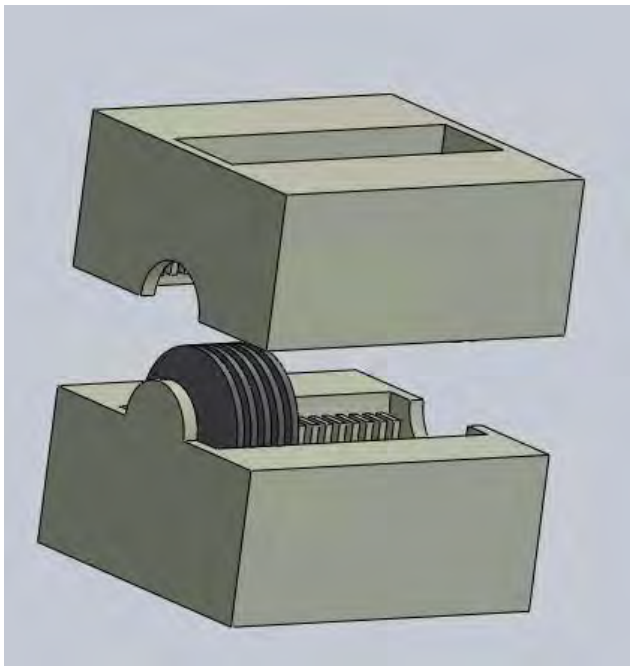

Figure 4.1. Molybdenum Target holder made of Tungsten

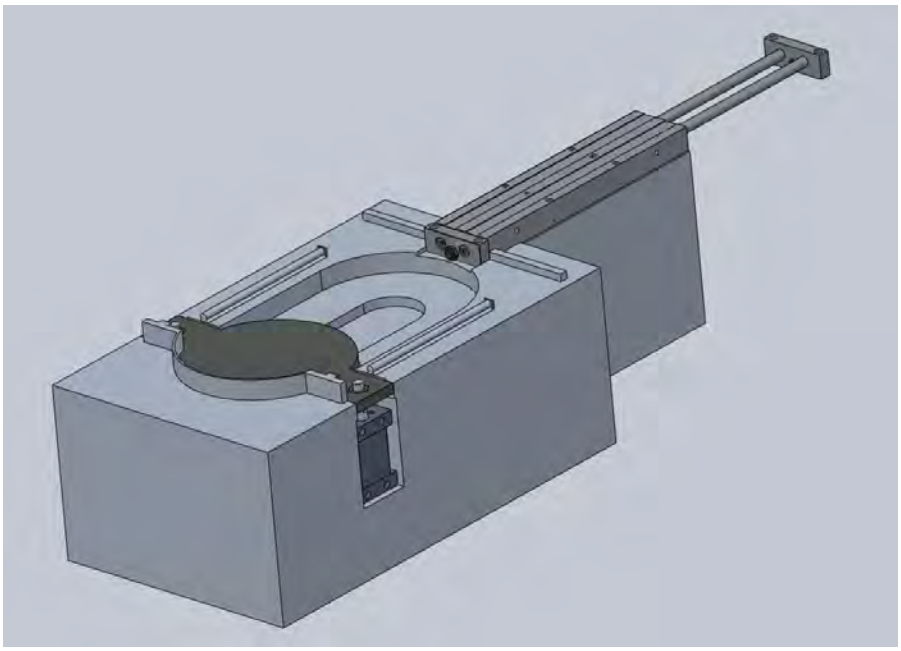

Figure 4.2. Complete autonomous assembly in which target holder would be transported.

The transportation of the molybdenum target disk holder was designed to have autonomous capability in order to reduce human interaction which would reduce unnecessary prompt radiation. The transportation shield consists of 4 main components. The lead container in which the target holder would be dropped from the accelerator, two single action actuators, one double-action air guided dual rod actuator, and the Aluminum base/holder. The aluminum base will accommodate the lead shield container and hold the actuators needed in their respective positions.

The shielding design main component is the lead container (Fig. 4.3) with a volumetric capability of 167.283 cm^3 (inner diameter of 64mm and inner height of 52mm). With a thickness of 50 mm (2 inches), the total height is 140mm. The cover component of the lead container was designed to be able to slide vertically and horizontally along the Aluminum base (Fig. 4.4).

Figure 4.3. The lead container in which the target will be shielded completely.

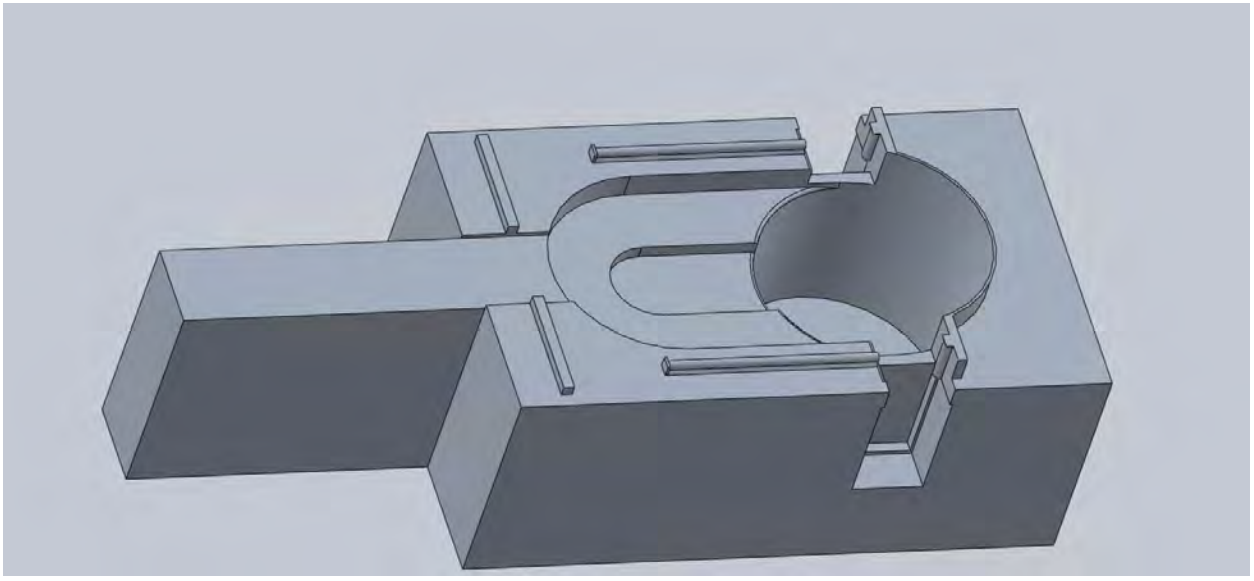

Figure 4.4. Aluminum base used to accommodate lead container and the three actuators.

The transportation shield will be used to transport the irradiated targets within the tungsten target disk holder from the accelerator to the laboratory where the molybdenum disks would be dissolved in Sodium Hydroxide for final stages of product processing.

The mechanics of the transportation shield is autonomous, meaning that little to no human interaction is needed from accommodating the dropped targets from the accelerator and subsequent shielding to uncovering the shield for the targets to be removed at the laboratory. We have adopted the actuator technology from SMC technologies. SMC technologies develop and manufacture pneumatic actuators that can be applied in various fields. The actuators are necessary in order to direct the cover of the lead shield container to respective positions during active loading and unloading of the target disks. Since the actuators are placed on the aluminum base external to the lead container where the disks would reside, no special radiation heat requirements were necessary to ensure efficiency and durability. An example of a side actuator to be used from SMC technologies is shown below in figure 4.5.

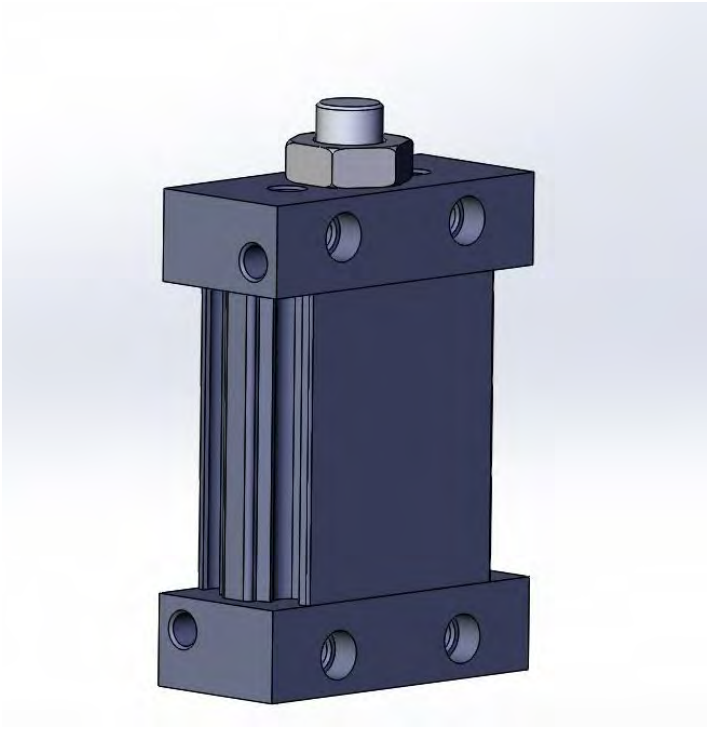

Figure 4.5. Compact actuator MUB series by SMC technologies used to lift the lead shield cover vertically in the transportation shield.

The description provided by SMC Pneumatic Technologies states that the MU plate cylinder, with its elliptical design, provides a low profile while maintaining force output. The MU cylinder can eliminate the need for higher operating pressures that may be required for typical flat cylinders. The oval piston shape also provides an intrinsic non-rotating function without having to use a rod with flats, offering increased bearing and seal life. Special characteristics of the actuator include: Single acting, spring return/extend, plate cylinder, possible to mount without brackets, auto switch mounting grooves prevent projection of auto switches, auto switches can be mounted in 4 directions, strokes up to 20mm [21].

The necessary stroke needed by the side actuators to lift the shield cover to the applicable height is 10mm. Once the actuator has lifted the cover 10 mm, an actuator placed on the upper surface of the aluminum base would take over to provide horizontal pulling motion to the lead shield cover. An example of the actuator that is placed on the upper surface of the aluminum base is a dual rod guided actuator CXW series by SMC Pneumatic Technologies shown in figure 4.6.

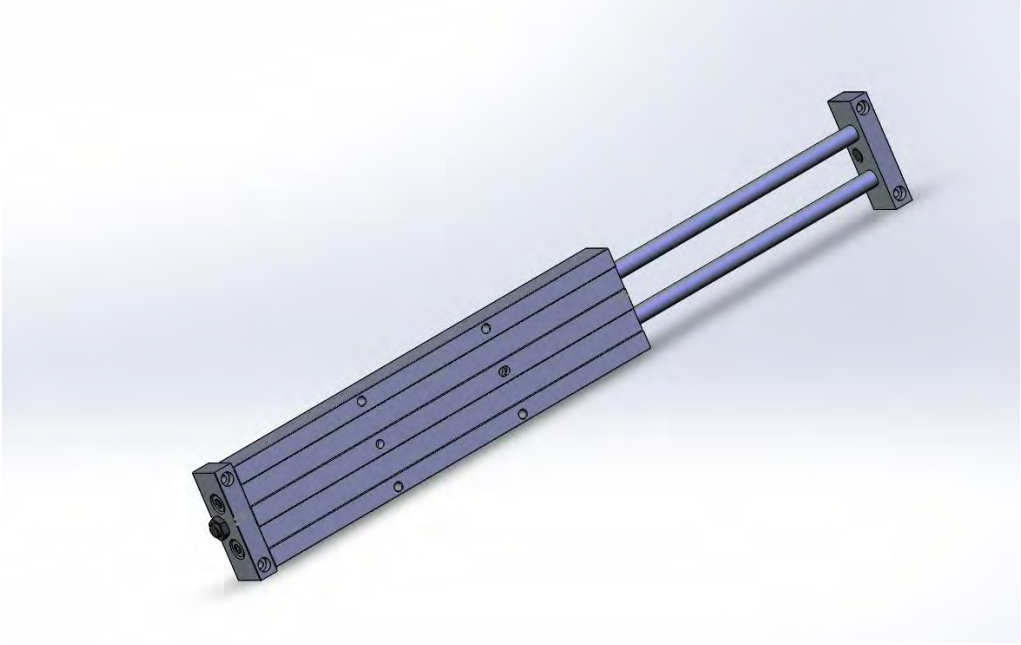

Figure 4.6. CXW, slide unit with built in shock absorber guided dual rod actuator used to slide the lead shield cover horizontally.

The description provided by SMC Pneumatic Technologies states that the Slide unit series CXW can absorb energy in a wide range, in high-speed, low-load applications to low-speed, high-load applications, without requiring adjustments. The slide unit can be mounted on the housing or on the plate, depending on the application. Slide bearing or ball bushing bearing is available. Auto switches can be installed. Actuator has capability of stroke up to 200mm [21].

This dual action actuator was chosen for its high-load ability to push and pull the 22.57 pounds lead shield cover. The stroke required to push and pull the lead shield cover to application positions is 164mm, which lies favorably within the CXW's capability range.

After targets are done being processed at the laboratory where the molybdenum disks would be dissolved in Sodium Hydroxide, the next step would be to transport the dissolved molybdenum solution to the hospital where it would be separated using the proposed chemical separation apparatus. The transportation shield for this step is shown in figure 4.7.

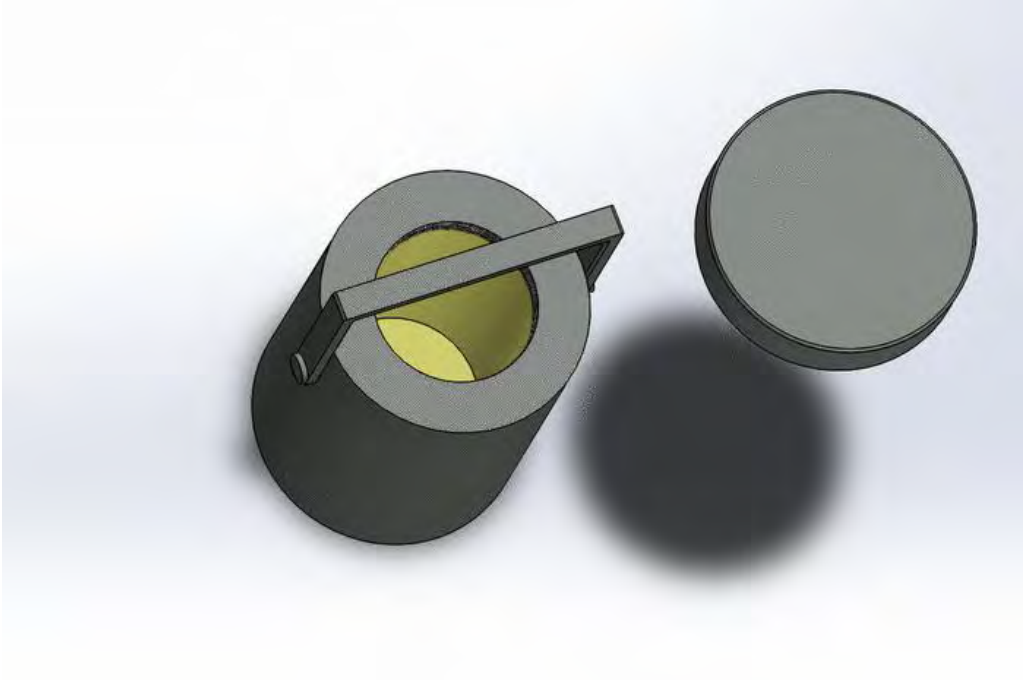

Figure 4.7. Lead canister lined with plastic on the inner surface used for transportation of the solution to customers.

The design for this shield is lead based with the inner area lined with plastic. The purpose of the plastic lining inner surface is to shield beta radiation [22]. Plastic is used before lead to absorb beta particles.

This practice is based on the well-established theory that bremsstrahlung production are more prevailing in higher Z materials than in low Z materials.

The lead canister measures 9 inches in diameter and 14 inches in total height excluding the handle. Thickness was established at 1.8 inches resulting in a volumetric capacity of 4 Liters.

After the product has reached the customers, our job would be to advise customers on what the requirements for shielding are. The main requirement for shielding by customers in their chemical separation apparatus is that it should satisfy Class V shielding. Class V shielding would shield against betas and gammas and have a full exhaust flow.

Dosimetry

In order to ensure safe levels of radiation during transportation, dosimetry calculations were done. Figure 4.8 below shows the package labels which specify radioactive content and quantity in curies as well as transport index obtained from the Radiation Emergency Medical Management website.

Label	Radiation Level Associated With Intact Package	Symbol
Radioactive White-I	Almost no radiation --0.5 mrem/hr (5 μSv/hr) maximum on surface	
Radioactive Yellow-II	Low radiation levels --50 mrem/hr (0.5 mSv/hr) maximum on surface; 1 mrem/hr (10 μSv/hr) maximum at 1 meter	
Radioactive Yellow-III	Higher radiation levels --200 mrem/hr (2 mSv/hr) maximum on surface;* 10 mrem/hr (0.1 mSv/hr) maximum at 1 meter Also required for fissile class III or large-quantity shipments, regardless of radiation level	

Figure 4.8. Radioactive materials shipping labels and placards [23].

Assumptions made were based on extreme case scenarios which is the general practice of shielding design. Since the molybdenum-99 decays in the transport shield after it has been dropped in the transport shield, technetium-99m was accounted for as well. Activity was assumed to be 1E+9 Bq for each the molybdenum-99 and technetium-99m. Using the equation for dose rate shown in the Appendix, the results for molybdenum-99 and technetium-99m dose rates at 1 meter distance with ~5 cm (2 inch) of lead shielding are shown in Table 4.1.

Table 4.1.

Summary of the dose rates received at 1 meter from the lead shield.

Molybdenum-99	Activity(Bq)=1.00E+09			
Yield (1/Bq.s)	Energy (MeV)	μ(cm2/g) [Pb]	μen(cm2/g) [Tissue]	Specific Dose
1.06E-02	0.04058	1.38E+01	0.062422	0.00E+00
6.14E-02	0.18110	1.27E+00	0.028684	9.54E-50
1.20E-02	0.36640	2.72E-01	0.032289	3.51E-25
5.76E-04	0.52880	1.49E-01	0.032656	3.07E-23
1.23E-01	0.73950	9.67E-02	0.031968	1.77E-19
4.30E-02	0.77790	9.14E-02	0.031797	8.78E-20
1.35E-03	0.82300	8.61E-02	0.031592	3.95E-21
9.56E-04	0.96080	7.37E-02	0.030903	6.50E-21
			Dose Rate (Gy/s)	**2.75E-10**
Technetium-99m	Activity(Bq)=1.00E+09			
Yield 1/(Bq.s)	Energy (MeV)	μ(cm2/g) [Pb]	μen(cm2/g) [Tissue]	Specific Dose
8.90E-01	1.41E-01	2.6463	0.027011	0
4.03E-02	1.84E-02	114.66	0.62562	0
2.12E-02	1.83E-02	116.41	0.63554	0
1.24E-02	2.06E-02	78.379	0.43581	0
			Dose Rate (Gy/s)	**3.27465E-74**
Total Dose Rate (Mo-99+Tc-99m)			**(Gy/s)**	**2.75E-10**
			(Gy/h)	**9.91E-07**
			(mGy/hr)	**9.91E-04**

Data used for calculations were gathered from the National Institute of Standards and Technology [24] Photon Cross Sections Database and the National Nuclear Data Center [25]. Nuclear Decay Data and respective gamma energies. Concluding the results of the calculations, transportation of our molybdenum enclosed in the lead shield would be classified as Radioactive Yellow III which is shown in Figure 4.8 above.

Conclusion

Our design of the lead shielding is optimized at 2 inches of thickness with respect to transportability, price, and shielding. Any increased thickness would result in higher transportation and manufacturing costs as well as added weight that might hinder transportation logistics.

Shields have been designed for transportation from the accelerator to the laboratory where the target processing on hot cells occurs (Fig. 4.2) and transportation from the laboratory to the customer (Fig. 4.7). Main concern of shielding was the beta and gamma radiation. The shield in Figure 4.2 was designed to function autonomously at times of loading and unloading. Shield in Figure 4.7 is composed of lead and plastic to block beta particles.

Dose rates have been calculated to be 0.991 mSv/hr at 1 meter distance during the transportation of the irradiated target disks from the accelerator to the laboratory. This dose rate makes the material transportation fall under Radioactive Yellow III category as defined by the Radiation Emergency Medical Management**.**

SECTION V

CHEMICAL SEPARATION – MILTIADIS KENNAS

Introduction

Technetium-99m's half-life of 6.02 hours makes it impossible to ship in usable quantities over long distances. This necessitates the use of its radioactive precursor molybdenum-99 ($t_{1/2}$ = 66 hours) as a means to transport and generate technetium-99m. Following a completed irradiation at an accelerator facility, the entire set of molybdenum-100 targets (now containing molybdenum-99 atoms following photon-neutron interactions from the accelerator) are dissolved in a sodium hydroxide (NaOH) solution, achieving a final concentration of 4 moles per liter. This 4 M NaOH and molybdenum solution is placed in a suitable container as described in Figure 4.7 and shipped to the customer.

In order to separate usable technetium-99m from molybdenum, a chemical separation process is required. Molybdenum is present in the NaOH solution in the form of a molybdate. Molybdate exists in the chemical form of MoO_4^{2-}, and as the molybdenum-99 atoms in the molybdate beta decay, they form technetate in the chemical form of TcO_4^-. Figure 5.1 shows the chemical configuration of technetate. The key aspects of the separation process are removing technetate from molybdate, ensuring that the basicity of the technetate has been neutralized while forming a pertechnetate, and purifying the final pertechnetate prior to final customer applications.

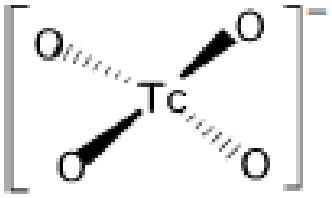

Figure 5.1. Chemical configuration of TcO_4^-. [26].

Design Basis

The chemical separation apparatus and its specific configuration selected for this project requires a list of components available from various chemical, medical, and radiological health engineering companies including Biodex Medical Systems, Inc., Waters Corporation, Dionex Corporation, and PCAS Biomatrix, Inc. Additionally, sufficiently shielded laboratory facilities are required as described in Section IV.

The apparatus is composed of Pharmacopeia grade VI plastics, with 1/16-in (1.6-mm)-diameter silicon tubing (Tygon), polypropylene barbed connectors, and Luer adapters, as well as standard disposable syringes [7]. There are three primary elements that perform the separation of technetium-99m from the initial NaOH/Moly solution and transfer it to the final product syringe: the PCAS BioMatrix ChemMatrix, the Dionex OnGuard II H Cation Exchange Resin, and the Waters Sep-Pak Alumina A Plus Light Cartridge.

The first integral component of the chemical separation apparatus is ChemMatrix, a Cross-Linked Polyethylene Glycol Bead Resin that has the effect of separating technetium-99m from molybdenum in a 4 M NaOH solution. ChemMatrix is available in a variety of material configurations, and is produced and distributed by PCAS Biomatrix, Inc, a division of the PCAS Group.

ChemMatrix was designed initially to provide an alternative to polystyrene resins and polyethylene glycol grafted resins for the synthesis of peptides, but was also found to have applications in combinatorial synthesis [27], for the synthesis of oligonucleotide derivatives [28], peptide nucleic acids [29], asymmetrically substituted phthalocyanines [30], and peptide hybrids incorporating non-natural chemical residues [31]. More recently, it was confirmed to be effective in the separation of technetium-99m from molybdenum-99 and molybdenum-100 [7]. ChemMatrix excels at separating all isotopic forms of technetate from all isotopic forms of molybdate, highlighting its use in the separation apparatus. ChemMatrix is available in at least 15 different chemical configurations [32], each of which provide varying degrees of elution and load percentages, with additional dependencies on the mass of the resin and the value of the elution

load (mL/min) [7]. The varying structures are shown in Figure 5.2 and the specific differences are tabulated in Table 5.1.

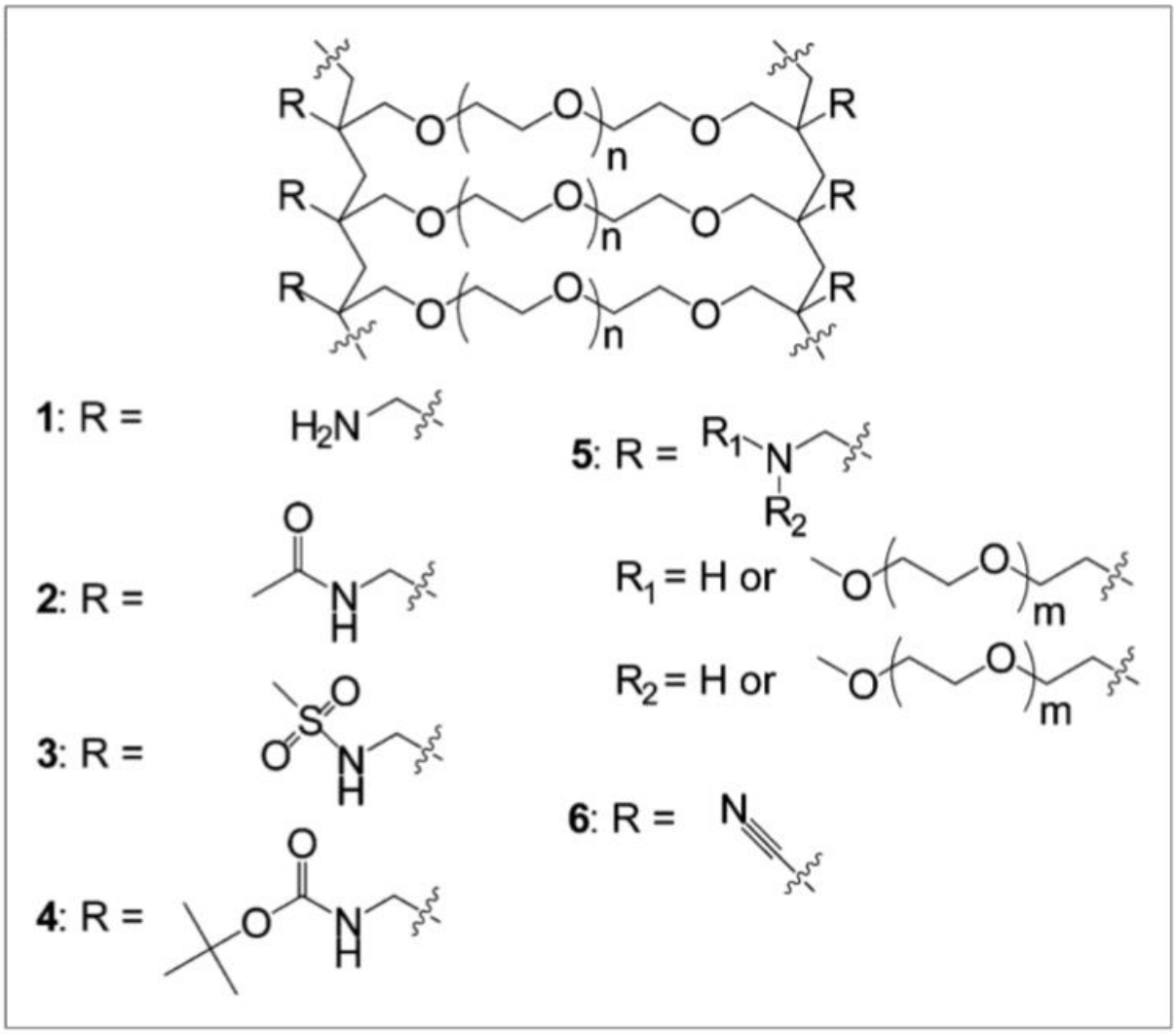

Figure 5.2. Some configurations of the ChemMatrix chains. 1 represents aminomethyl, 2 represents acetyl, 3 represents mesyl, 4 represents BOC, 5 represents PEG, and 6 represents nitrile [7].

Table 5.1.

Results of quality control tests performed on the ChemMatrix structures. [7].

Resin	Mass (mg)	Load (mL/min)	Elution (mL/min)	Load (%)	Elution (%)
Aminomethyl-ChemMatrix	200	1	1	86	85
Aminomethyl-ChemMatrix	300	0.5	0.5	100	97
Aminomethyl-ChemMatrix	300	1	2	88	96
Aminomethyl-ChemMatrix	300	0.75	2	88	97
Aminomethyl-ChemMatrix	300	0.5	5	100	94
Aminomethyl-ChemMatrix	600	1	1	100	85
Aminomethyl-ChemMatrix	600	2	10	97	69
Aminomethyl-ChemMatrix	600	2	1	99	77
Acetyl-ChemMatrix	600	2	1	100	95
Acetyl-ChemMatrix	300	2	2	54	100
Acetyl-ChemMatrix	500	2	2	99	98
PEG-ChemMatrix	500	2	2	97	98
Mesyl-ChemMatrix	500	2	2	100	100
BOC-ChemMatrix	500	2	2	100	98
Wang-ChemMatrix	500	2	2	100	100
Nitrile-ChemMatrix*	500	2	2	100	100

*Multiple repeated experiments confirmed results.

A key aspect of ChemMatrix's use is its ability to operate with essentially any solute, most notably water [32]. Distilled water creates swelling in the polyethylene glycol beads when compared to sodium hydroxide, allowing for variations in the resin's ability to capture and release technetium. Figure 5.3 shows an image of the PEG beads' solute-dependent swelling.

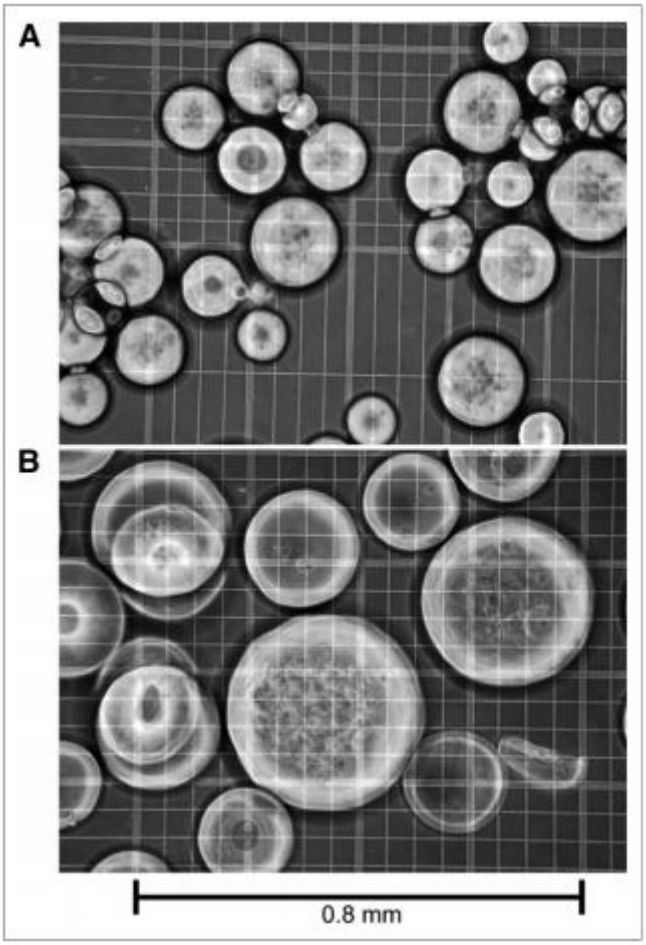

Figure 5.3. Images of PEG beads in ChemMatrix growing with differing solutes. Picture 'A' shows the beads in a 4 M NaOH solution, while picture 'B' shows the beads in distilled water. [7].

The second key component of the chosen separation apparatus configuration is the Dionex OnGuard II H Cation Exchange Resin. The 'H' model was chosen for this apparatus because this is the only model that adjusts basic solutions. The OnGuard comes in the form of cartridges that contain a styrene-based, strong acid resin in the H+ form. The resin has a very high selectivity for multivalent cations such as calcium and the transition metals. The cartridge is designed primarily for the removal of high levels of alkaline-earth metals and transition metals from sample matrices, for the neutralization of caustic samples, and for the removal of carbonate.

The cation exchange capacity is 2.0 - 2.5 meq/1.0 cc cartridge on a water-swollen basis and 5.0 - 5.5 meq/2.5 cc cartridge. With one 1.0 cc cartridge, 10 mL of 0.2 M NaOH may be neutralized

before analysis; with a 2.5 cc cartridge, 25 mL of 0.2 M NaOH may be neutralized before analysis. The resin is stable over a pH range of 0-14 [33]. When working with 4M NaOH, the 1 cc cartridge can neutralize 0.5 mL, while the 2.5 cc cartridge can neutralize 1.25 mL. The 'H' model was chosen for this apparatus because this is the only model that adjusts basic solutions. During the neutralization process in the OnGuard cartridge, the $^{99m}TcO_4^-$ technetate is converted to $Na^{99m}TcO_4$ pertechnetate. Because this separation method can produce approximately 15 mCi per mL [7], the 1 cc cartridge can be effectively used to supply a safe amount of activity to a patient (approximately 7 mCi for a single procedure) [11], but the 2.5 cc cartridge can be selected as well to allow for more control in final product activities.

The final key component in the separation apparatus is the Waters Sep-Pak Alumina A Plus Light Cartridge. The alumina cartridges contain a highly active grade of alumina with an acidic surface chemistry. The aluminum oxide surface provides an extremely polar surface for analyte retention and has properties of a Lewis acid. This normal phase sorbent is similar in use to silica; however, it is slightly more stable than unfunctionalized silica under high pH conditions. This acidic alumina is also low-capacity ion exchanger in aqueous media. Unlike polymer-based ion exchangers, this sorbent is unaffected by high-energy radioactivity and can be used for radioactive compound isolation. These cartridges have a distinctive finned outer body and a reduced internal diameter, which results in an interstitial volume about one-third that of the corresponding Plus-style cartridge. This design allows you to elute fractions in a minimal volume to improve recoveries and reduce solvent consumption, a benefit especially for applications where samples are limited or where excessive dilution is a concern [34]. The alumina cartridges can each contain 280 mg or 1170 mg of sorbent and operate for particle sizes of 50 to 300 microns.

Methods

The selected method for this project is the use of a chemical separation apparatus composed primarily of the three main components described above. The apparatus is largely automated and can operate with a load of 2 mL/min of solution. The key components are each connected in series and are all disposable cartridges. A layout of the separation apparatus is shown in Figure 5.4.

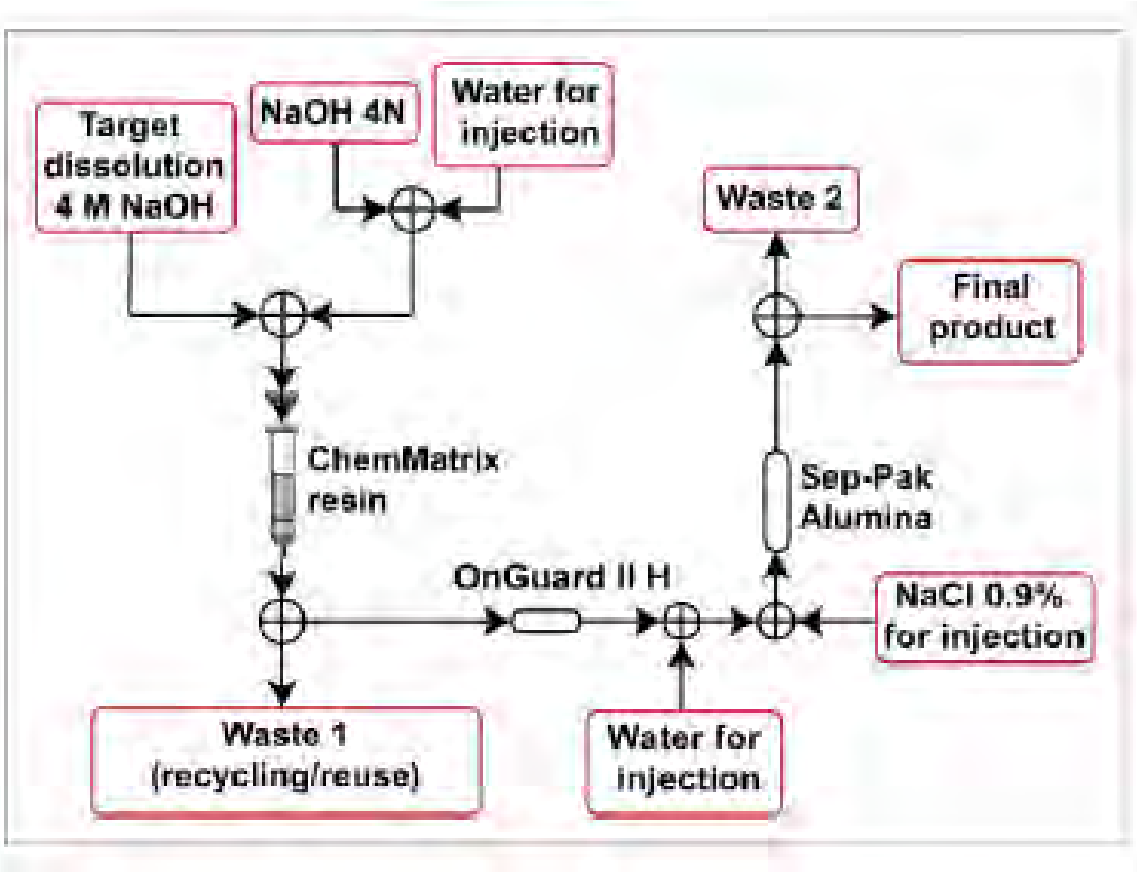

Figure 5.4. Layout of the chemical separation apparatus. Solution is passed through the ChemMatrix and into waste. Captured technetate in the ChemMatrix is transported by water through the neutralizing cation exchange resin and into the alumina for purification. A saline solution then transports the technetate into the final product.

The 35-45 minute long separation procedure begins with the preconditioning of the Chem Matrix polyethylene glycol bead resin with a 4N NaOH solution. Preconditioning allows ions in the resin to dissociate and activates binding sites prior to the separation. The crude 4 M NaOH solution with dissolved molybdate ($^{98}MoO_4^{2-}$, $^{99}MoO_4^{2-}$, $^{100}MoO_4^{2-}$), technetate ($^{99m}TcO_4^-$, $^{99}TcO_4^-$), and other trace products of target irradiation will then be injected through the resin, which separates the

technetate from all other dissolved materials and the NaOH solution. The NaOH/molybdate solution will diffuse through the resin and flow into a reuse beaker.

Immediately following separation, the ChemMatrix resin is washed with 4 N NaOH, purged with nitrogen gas, and eluted with water that will capture technetate from the resin. The eluent is then passed through the OnGuard II H cation exchange resin for neutralization and in the process converting the technetate to a pertechnetate in the chemical form of $Na^{99m}TcO_4$. From here, the eluent passes through the apparatus in series to the Sep-Pak Alumina A Plus Light Cartridge, which captures the pertechnetate and allows the water to flow into a waste bin to be discarded. Extra water can be inserted to wash the alumina and enhance radiochemical purity of the final product. Finally, a 0.9% NaCl saline solution is passed through a 0.22μm sterile filter and through the alumina, capturing the pertechnetate and flowing into the final container bin.

Technetium-99m pertechnetate is an ionically neutral molecule that acts as the foundation for the construction of a radiochemical tracer used in radiographic imaging. This is because the chemical reactivity of the pertechnetate is negligible; it does not bind directly to any ligand. Thus, for the production of technetium-99m pharmaceuticals, reduction to lower oxidation states in the presence of a suitable ligand is a perquisite for the synthesis of technetium-99m labelled molecules. During reduction, the ligand stabilizes the lower oxidation state, otherwise, colloidal TcO_2 is formed in aqueous media [26]. Examples of technetium-labelled pharmaceuticals are tabulated in Table 5.2.

Table 5.2.

Table of some technetium-labelled radiopharmaceuticals formed from pertechnetate. [26]

Compound	Oxidation state core	Geometry	Coordinated number	Charge	Reference
Gluconate	$Tc(V)O_3^+$	Square pyramid	5	–1	Johannsen and Spies 1988
Glucoh-eptonate	$Tc(V)O_3^+$	Square pyramid	5	–1	De Kieviet 1981
DMSA	TcO_3^+ or Tc(III)	Octahedral	5	0 or –1	Bandoli et al. 1984; Ikeda et al. 1977
Penicillamine	$Tc(V)O_3^+$	Octahedral	6	0	Franklin et al. 1982
EDTA	$Tc(V)O_3^+$	Heptahedral	6	0	Davison and Jones 1982
HMPAO (Ceretec)	$Tc(V)O3^+$	Heptahedral	6	0	Fair et al. 1984
MRP20 (Neuroscint)	$Tc(V)O_3^+$	Heptahedral	6	0	Morgan et al. 1990
DADS	$Tc(V)O_3^+$	Square pyramid	5	0	Davison et al. 1980
DADT	$Tc(V)O_3^+$	Square pyramid	5	0	Watson et al. 1987
ECD (Neurolite)	$Tc(V)O_3^+$	Square pyramid	5	0	Edwards et al. 1990
MAG (MAG$_3$)	$Tc(V)O_3^+$	Square pyramid	5	0	Nosco et al. 1989
Tetrofosmin (Myoview)	$Tc(V)O_2^+$	Octahedral	5	+1	Kelly et al. 1993
NOEt	$Tc(V)N_2^+$	Octahedral	5	0	Pasqualini et al. 1994
EDTA	Tc(IV) or Tc(III)	Dimeric	7 or 6	0 or –1	Davison and Jones 1982; Burgi et al. 1981
DTPA	Tc(IV) or Tc(III)	Monomeric	?	–1(?)	Gorski and Koch 1970
MDP	Tc(IV)	Monomeric	?	0	Lisbon et al. 1980
HIDA (Choletec)	Tc(III)	Octahedral	6	–1	Loberg and Fields 1978
DMPE	Tc(III)	Octahedral	6	+1	Deutsch et al. 1981
Q12 (Technecard)	Tc(III)	Octahedral	6	+1	Deutsch et al. 1987
BATO (Cardiotec)	Tc(III)	Octahedral	6	0	Bandoli et al. 1982
MIBI (Cardiolite)	Tc(I)	Octahedral	6	+1	Abrams et al. 1983

After separation from technetate in the ChemMatrix, the NaOH/ molybdate solution can be reused in the same process by the customer several times to maximize the amount of technetium-99m activity received. The process of separating technetate from molybdate and processing it for use is known as 'milking' the technetium-99m 'generator.' In this project, the generator is the NaOH/ molybdate solution, and is referred to as thus because after the initial milking, remaining molybdenum will continually decay into additional technetium. The optimal milking interval of the generator is approximately 24 hours, as shortly after this period any decay gains of technetium-99m from the molybdenum-99 will be overshadowed by decay losses into technetium-99. This is a chain of two decays scheme, which can be best described by Equation 5.1.

$$A_B(t) = \frac{A_{A_0}\lambda_B}{\lambda_B - \lambda_A}(e^{-\lambda_A t} - e^{-\lambda_B t}) \tag{5.1}$$

In Equation 5.1, $A_B(t)$ represents the activity of technetium-99m with respect to time, A_{A_0} represents the initial activity of molybdenum-99, λ_B represents the half-life of technetium-99m, $\lambda_A$represents the half-life of molybdenum, and t represents time. Figure 5.5 shows a plot of this decay scheme and five milkings of the generator. It should be noted that, upon initially receiving the generator, the customer typically milks the generator straight away and discards the first final product from the apparatus. This is because a high ratio of technetium-99 to technetium-99m in the final product has the effect of clouding radiographic imaging. During shipping from the accelerator to separator facilities, a large enough amount of essentially stable technetium-99 will be found in the generator. After the initial product is discarded, the 24-hour cycle described by Figure 5.5 begins.

Results and Discussion

Experiments performed by TRIUMF Labs confirmed the ability of ChemMatrix and the above separation apparatus configuration to produce high radiochemical purity (98.9-99.0%) of technetium-99m in the final product. Impurities in the final product are due to trace amounts of technetium radioisotopes. The Sep-Pak Alumina was able to successfully filter all traces of molybdenum and other impurities from the system. Tests performed with Biodex Tec-Control Aluminum Breakthru kits confirmed the lack of presence of aluminum from the alumina in the final product [7].

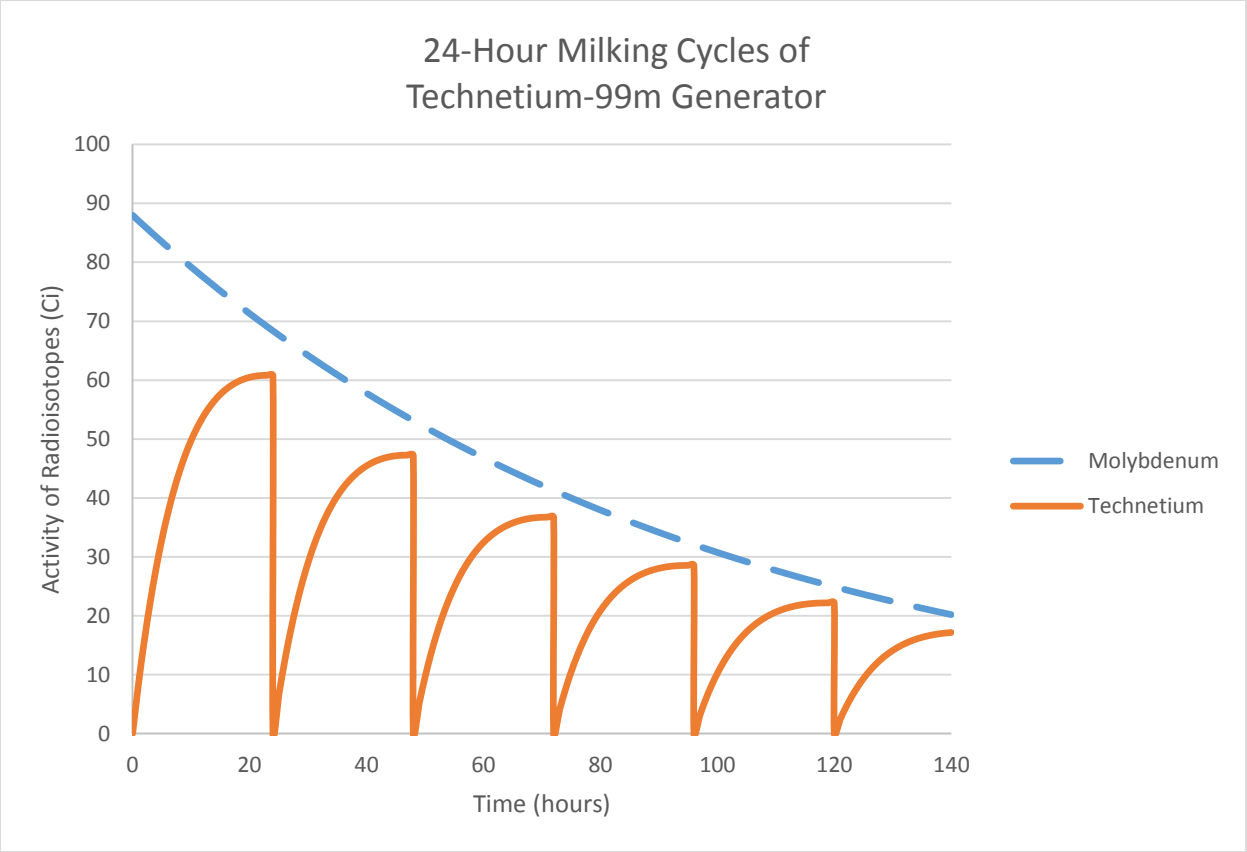

Figure 5.5. Plot of 24 hour generator milking cycles. The dashed curve represents the activity over time of molybdenum-99 present at the separation facility. The solid line represents the activity over time of technetium-99m during repeated milking in 24 hour intervals. The curve represents sum totals of all separation facilities, assuming each has received desired initial activities after two days of shipping and processing. Values are sourced from Section II.

After accounting for the loss of technetium-99m in the chemical separation apparatus, approximately 92.7% of all initially extractable activity remains for customer applications. 6.6% of the activity is found in waste bins, 0.19% remains in the ChemMatrix, 0.014% in the cation exchange, and 0.59% in the alumina. The remaining percent is lost in disposable syringes [7].

From the data in Table 5.1, it appears that as a result of the differing efficiencies of ChemMatrix, not every version can be considered for efficient use in the separation of technetium-99m from molybdenum. 300 mg of Aminomethyl-ChemMatrix provided insufficient load and elution percentages; that is, the matrix did not sufficiently trap technetium and release it into the water solution, respectively. Increasing the mass of resin to 600 mg increased the load percentage to nearly 100%, but still did not provide an adequate elution percentage. Similar results were noted for Acetyl, PEG, and BOC-ChemMatrix. However, 500 mg of the Mesyl, Wang, and Nitrile-ChemMatrix were found to provide 100% efficiencies in trapping and releasing technetium-99m [7]. As a result of these findings and the availability of the ChemMatrix variants, Wang-ChemMatrix is the optimal variant for use in the separation apparatus.

From data in Section II, approximately 88 Ci of molybdenum-99 can be received by customers after a single irradiation and an assumed two day transportation and processing period. Also assuming that the generator is immediately milked upon being received and the first product is discarded to eliminate technetium-99 induced clouding, a total of 181.16 Ci of technetium-99m can be produced after 5 days from every separation facility. The 92.7% efficiency of the separation method has been taken into account for this finding. This value was found by summing the activities of each 24 hour milking cycle from Figure 5.5 for five days. Typical patient procedures require between 10 and 50 mCi per technetium-99m administration [11].

SECTION VI

TARGET QUALITY AND MANAGEMENT SYSTEM – YOUSIF ALMAAZMI

Introduction

A Quality Management System is the policy conceived by an entity to meet its quality objectives. In the medical industry, the Federal Drug Administration (FDA) in partnership with the manufacturers, articulates the general parameters of the Quality Management System to be followed by all manufactures in producing radiopharmaceuticals. This Quality Management system is called the Current Good Manufacturing Practice (cGMP) and it is the minimum standard used to ensure that radiopharmaceuticals meet or exceed the safety, quality, and purity specified by the FDA [35]. This means that a successful cGMP program requires certain facility design parameters, along with competent staff training and management, and finally a good Quality Assurance (QA) and Quality Control (QC) management [36]. Therefore cGMP is a Quality Management System approved by the Federal Drug Administration (FDA) that should be followed when producing Radiopharmaceuticals. The FDA regulations on cGMP has been developed for different radiopharmaceuticals depending on their production methods. However, since this design utilizes a new method of producing molybdenum-99, there are no FDA regulations concerning how cGMP would apply to our method. Therefore, a new cGMP had to be developed to meet the goals set by the FDA. This new model of cGMP is based on the cGMP for Positron Emitting Tomography (PET). But, there are several differences to address the differences in radiochemical characteristics of molybdenum in comparison to other PET isotopes. Furthermore, since this is a new method of production, a risk analysis of the production of molybdenum is conducted.

Facility Requirement

The design of the facility needs to be such that no outside contamination affects the molybdenum, while also reducing radiation emissions to a minimum as required by state and national laws. Public safety is more important than radiopharmaceutical quality, which can be discarded if it does not meet quality standards [36]. One of the ways in which environment contamination is prevented is by designing the airflow direction to flow from the lowest radiation level to the highest radiation level as to minimize the chance of radiation escaping the facility [36]. This is achieved by having the accelerator room and vault pressure at below atmosphere level, and subsequent hot cells at

slightly higher pressure, and finally the dispensing units being at a slightly below atmospheric pressure [37]. Separating the production procedures into separate rooms with their own hot cells and High-Efficiency Particulate Arrestence (HEPA) filter can prevent contamination to the molybdenum [36]. In addition, human contact must be limited to prevent microbiological contamination of the molybdenum. Human contact with the molybdenum should be reduced using master slave manipulators. An example of the master slave manipulators can be shown in Figure 6.1 which contains the HWM AP200 design [38].

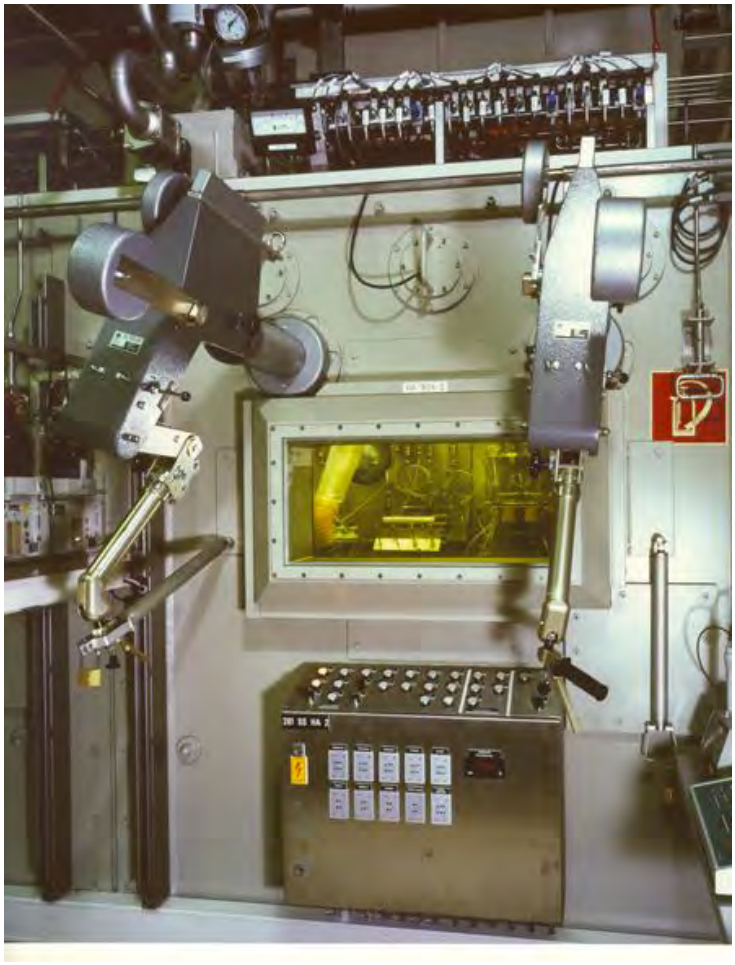

Figure 6.1. HWM AP200 master slave manipulator in a hot cell.

This would reduce the chance that the molybdenum gets contaminated, and it reduces to staff exposure to adhere to the principle of As Low As Reasonably Achievable (ALARA). ALARA principle is based on the Linear Hypothesis, which states that any radiation amount is harmful, and thus should be avoided.

Personnel Management

A cGMP will succeed only if qualified staff is employed, and constant retraining programs are implemented as to ensure that no skill degradation occurs over time. Properly trained employees are essential to prevent radioactive contamination, and unnecessary employee exposure [37]. QC cannot be implemented without employees understanding the significance of cGMP [37]. Therefore, cGMP review sessions must be instituted periodically. This is to make staff aware that in order to have a successful cGMP program every procedure must be performed per Standard Operating Procedures (SOP). Well-trained employees are also necessary to implement QA requirements. Employees in production and QC must wear protective clothes to ensure that they do not contaminate the molybdenum, and that they are not exposed to unnecessary radiation, and contaminations that can affect their health [39].

The essence of a successful QA requires that the quality and production control functions to be independent of each other [40]. Therefore, every employee's responsibility must be clearly identified without ambiguity. This is achieved by having a separate independent Quality Team, headed by a Quality Manager whose main task is to ensure that the molybdenum is not contaminated, and that no radiation escapes their designated areas and the facility. The Quality Team will have to perform regular audits of the different stages of production, to ensure that nothing is contaminated. In addition, the Quality Team must ensure that the Production Control Team performs the Standard Operating Procedures (SOP), and that the any deviations are recorded and that necessary check are made to ensure that quality objectives are not compromised. On the other hand, the Production Control Team has two objectives, the first is to perform the SOPs tasks diligently, and report any industrial accidents the Quality Team [40]. The second objective is to work as efficiently as long as it does not compromise quality. QA therefore follows every step of the molybdenum production. The QA team would independently verify that the steps taken by the operators and would conduct their own calculations as to make sure that the SOP is not violated [40]. On the other hand the QC team would test the molybdenum to verify that the identity, strength, quality, and purity of it content is within specifications [41].

Molybdenum Testing Procedures

The parameters that need to be controlled in molybdenum production are radionuclidic purity, specific activity, radiochemical purity, and microbiological purity. The methods in which those parameters will be controlled is by having the QA team ensure that the SOP are followed, and by having the QC team checking the products of each stage of production.

As the molybdenum disks are irradiated and transported to the hot cells for further processing, several tests will be conducted. Firstly, High Purity Germanium (HPGe) counters will analyze samples from the disks to assess the radionuclides purity (see Figure 6.2). The radionuclidic purity is important and should be maintained as high as possible because other impurities will affect the imaging quality of the technetium and will affect whether the batch conforms to FDA standards [37]. Furthermore, HPGe will tell the operators the specific activity of the molybdenum, which is essential to meet the customer's sales orders, which will be different for different customers. The specific activity is also important in that it would help the operators predict, how much molybdenum will be left after the customer has exhausted the technetium produced. This is important in reprocessing of the molybdenum. Secondly High Pressure Liquid Chromatography (HPLC) should be used to find the radiochemical purity of the samples (see Figure 6.3). This is achieved by channeling the sample through a radiation detector, and a chemical detector consisting of sodium iodide detector to measure the radiation and an ultraviolet detector to measure the chemical content of the sample. Thirdly, microbiological purity test is conducted on the sample to ensure that the molybdenum pharmaceutical quality is not compromised. Once the QC verify that the samples are within specification, then the molybdenum can be shipped to the customer.

Figure 6.2. A High Purity Germanium Spectroscopy system [42].

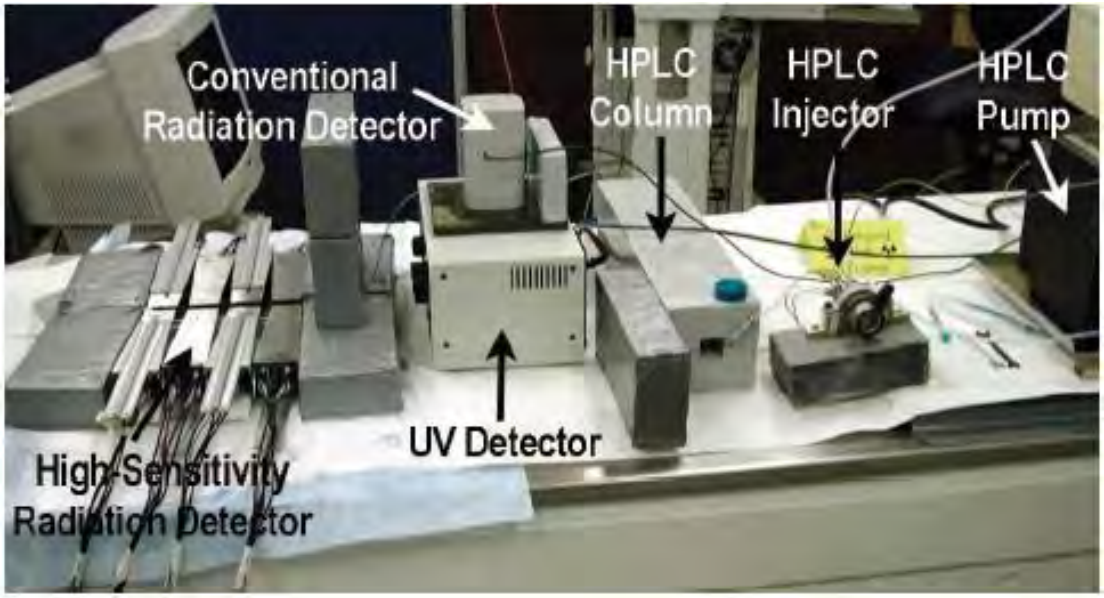

Figure 6.3. A High Pressure Liquid Chromatography with a UV detector and a sodium iodide radiation detector [43].

Using samples of molybdenum does not ensure that the entire batch is of high quality, because the sample taken from the molybdenum constitutes small segment of the batch, and therefore other parts of the molybdenum may fail one or more of the tests that were conducted on the sample [40]. Therefore, to ensure that the entire molybdenum shipped adhere to FDA regulation, the processing equipment needs to be maintained at aseptic conditions by regular cleaning using cleaning solution, hot treatment of equipment. In addition, microbiological testing of the hot cells and air must be conducted periodically. Swabs should be taken from surface of the work area of the molybdenum and air samples should be taken between batch processes, and analyzed to see if there is a microbial growth that can compromise the microbiological quality of the facility. Another item that should be monitored is the employees' gloves and laboratory gown. If at end of work shift, it is found to be contaminated then it means that the molybdenum was at high risk to contamination.

All the test procedures listed earlier must be validated to ensure that results are reliable, accurate, and precise. Calibration of the HPGe is necessary to ensure that the radiation count is accurate, precise and reliable [36].The HPLC can be checked for accuracy and precision by ensure that the entire sample flows through the chromatographer, by looking at the sample, and double flushing of the HPLC [44]. On the other hand, reliability can be checked for in a HPLC, by measuring and

comparing the mass of the different samples tested to ensure that the same size samples are always measured [44].

Batch Records (BR) that contains details of the production, and measurements of the molybdenum radionuclidice, radiochemical, and microbiological purity is necessary requirement of cGMP [40]. BR must contain enough detail that if there was a deviation of results the source of deviation can be located [40]. Furthermore, the BR should have enough information that another operator can produce the same results as stated in the BR [40].

Risk Analysis

Using an accelerator to produce molybdenum-99 is inherently safer than producing it using a reactor. This is because the radiation produced by the accelerator consists of the accelerator beam, the irradiated target, and the equipment used to handle the target. On the other hand, there are more sources of radiations in a reactors, the sources includes the fuel, its fission products, the reactor equipment, and the different materials used to process the fuel to extract the molybdenum. Nevertheless, the risk entailed by accelerator use must be analyzed.

Accidents can be separated into five levels based on consequences. The order of those levels rise with seriousness of the impact. There are several causes of possible accidents. However, the consequences of the accidents receive the most focus, the first level accidents would just result in production stoppage. Second level accidents would be molybdenum contamination. Third level accidents would be contamination of the accelerator and adjacent facilities. Fourth level accidents would involve high radiation exposure by the staff. The fifth level would be radiation leaking from the facility.

The causes of the first level accidents could range from accelerator malfunction to a malfunction in one of the processing equipment. These accidents can be solved quickly by the staff, with just a delay in delivery. Second level accidents, are most likely to occur in the molybdenum processing areas, including the hot cells, and dispensation. Third level accidents can be caused by target failure in the accelerators due to thermal stress. This would be a serious event because it would cause a major stoppage of the facility and staff evacuation. In addition, cleanup efforts will be costly and require long time. However, this is unlikely because the accelerator will not be operating

near the thermal limit of molybdenum. Fourth level accident can occur as a result of staff mishandling of equipment or equipment failure that leads to a radiation leak that only affects that specific processing room. The fifth level accidents are most serious, because it would involve a major leak that are caused by several factors combined together, such as an accelerator explosion, and failure of accelerator vault and emergency systems leading to the destruction of the entire facility. This scenario is extremely unlikely because it involves the failure of several systems simultaneously, and even then the damage to the public would be minimal because the amount of radiation produced will be limited to just the irradiated targets, and those in storage.

SECTION VII

ECONOMICS – MATT SCHAPER

Introduction

The economic section in this report seeks to analyze the demand for molybdenum-99, estimate the capital and variable costs of production, and calculate the cost of an industrial accelerator facility dedicated to the production of molybdenum-99. This design seeks to calculate the cost to the customer for 1 mCi of technetium-99m using certain economic variables and assumptions.

Current Demand

Currently there are over 50 million worldwide radioisotope imaging studies done every year, 80% of which use technetium-99m (50% in cardiology and 25% in oncology). In addition to this, the global demand of molybdenum-99 is about 12,000 6-day curies per week and the United States' demand is about 6,000 6-day curies per week. [3].The current cost to the customer is about $1 per mCi, but can vary depending on location. [12].

Assumptions

In order to estimate the cost of the facility, certain assumptions have to be made for both capital and variable costs. These assumptions allow us to calculate and estimate for the customer cost for 1 mCi of technetium-99m and this can be compared with the current cost as mentioned in the demand section.

Capital costs

Since our method seeks to recycle molybdenum-99, this means that the initial targets can be treated as a capital cost and the recycling/refilling will be a variable cost assumption. The first major assumption is the cost of >99% enriched molybdenum-100 targets. To help gain an estimate, Trace Science International was contacted during the week of April 20, 2015 in order to get the most up to date price for molybdenum-100 and returned a quote of $2,750 per gram and will take 7-8 weeks for delivery [6]. Bulk deals may be possible if an industry level facility is constructed and may be able to get as low as ~$600 per gram for large quantities. [12]. Since our system is composed of roughly 60 grams of material, this implies that the target system will cost in between $36,000 to $165,000 per system. If the system is irradiated for one day, according to Figure 2.10, this means

that it would be possible to obtain 146 Ci per target system (before recycling). The recycle time is also set by the decay of the molybdenum-99 in solution. In order to recycle targets, one must wait for molybdenum-99 to decay to a handled amount of 10 mCi which takes ~40 days. This implies that this design would need ~60 grams per day for the first 40 days which implies 2400 grams of molybdenum-100 target material. 2400 grams at $600 per gram of target material would cost roughly $1440k for the capital costs of the targets. The building is expected to contain two to four MEVEX accelerators at $7000k each. [12]. The infrastructure requirement for a building requires 3500ft^2 and at an assumed $1,000 per ft^2 could cost $3500k. [12]. A hot cell is required for the irradiated targets to be processed and typically cost about $3000k. [12]. The lab equipment is relatively inexpensive compared to other capital costs but total to be roughly $200k. [12]. To summarize the data, Table 7.1 was constructed and contains the capital costs of the accelerator facility.

Variable costs

For the variable cost it was assumed that both of the accelerators would be run 24 hours/day, 5 days a week and the following assumptions are on an annual basis. Also, the six-day curie concept was used in the following calculations even though it should be possible to ship in less than two days. The first assumption is that the cost of capital is 20% in order to obtain investors. The operation of the facility requires 8 operators at $80k each, 4 supervisory or scientific positions at $120k each, and 2 target processing technicians at $80k each. The facility would require roughly 2 MW of power at current price of 13 cents/kW-hr which totals to $1600k. It is assumed that the recycling efficiency of molybdenum-100 is roughly 93% (7% loss per cycle) and there is 9 cycles per year which implies that the replacement molybdenum-100 costs roughly $907.2k. Another assumption is that the accelerator maintenance and repairs is 10% of capital. Shipping is expected to cost roughly $2500 per day for 260 operating days. [12].

Annual Outputs

Since the facility is operating for 260 day/year and producing 292 Ci/day, this yields an annual production rate for the end of beam curies to 75,920 Ci per year. Using the six-day curie concept, this equates to roughly 16,960 six-day curies. Assuming a five milk cycle before recycling, this yields 50072 Ci of technetium-99m per year. To separate molybdenum-99 from technetium-99m is assumed to cost $0.05/mCi. [12].

Results

The capital costs is summarized in Table 7.1, the variable costs is summarized in Table 7.2, and the production outputs in Table 7.3.

Table 7.1.

Capital costs of the accelerator facility.

Capital	**Cost ($k)**
Two 35 MeV, 100 kW accelerators, $7M each	14000
Building, infrastructure, 3500 ft^2, $1000/$ft^2$	3500
Hot cells	3000
Initial Mo-100 Targets	1440
Laboratory equipment	200
Total capital	**22140**

Table 7.2.

Variable costs of the accelerator facility.

Variable	**Cost ($k)**
Cost of capital, 20 %	4428
Operator salaries (8 operators, 80 $k each)	640
Supervisory, scientific salaries (head, two engineers, physicist, 120 $k each)	480
Utilities, 2 MW, at 13 cents/kW-hr	1600
Target processing (two technicians, 80 $k each)	160
Replacement Mo-100 (9 cycles/year, 7 % loss per cycle)	907
Accelerator maintenance and repairs (10 % of capital)	1400
Shipping (50 units per day, 260 days per year, $50 per unit)	650
Total variable	**10265**

Table 7.3.

Outputs of the accelerator facility.

Facility Outputs	
Yearly output of Mo-99, 360 Ci/day, EoB, 260 days per year	75920 Ci
Yearly output of six-day curies of Mo-99	16960 Ci
Yearly output of Tc-99m, for five milkings	50072 Ci
Separator costs	5.0 ¢/mCi
Unit cost of Tc-99m	**~20.5¢/mCi**

As calculated using the results shown in the above tables, the cost of technetium-99m is $0.205/mCi using this design which is less than a quarter of the current cost customers pay for this isotope.

Decommissioning

In comparison to reactor based methods for the production of molybdenum-99, the decommissioning of an accelerator facility is insignificant. The costs of decommissioning a nuclear reactor can cost $300 million to $400 million according to the 10 CFR 50.75c. The cost of decommissioning for an accelerator facility is less than $1 million because there is no fission waste produced. The only cost of decommissioning is simply hauling away your accelerators. This also means that the cost for decommissioning a nuclear reactor is, in itself, over 10 times as expensive as the investment required to open an accelerator facility.

SECTION VIII

CONCLUSION

This project addresses the demand for molybdenum-99 while also being economically viable. Currently, there are five reactors that supply the majority of technetium-99m. Those reactors are reaching their end of operational life, and there are no new modes of molybdenum-99 production. Thus, the nuclear medicine industry is facing imminent shortage of technetium-99m that would reduce the ability of medical providers to carry out diagnostic imaging procedures. The present design eliminates the need for reactors in favor of a more stable system that addresses the supply of molybdenum-99 in the long-term.

The present project proposes an alternative method of technetium-99m production that utilizes a high energy electron linear accelerator to produce molybdenum-99, which is a precursor of technetium-99m. The most promising method of production was based on a photon-neutron interaction with enriched molybdenum-100 targets. This design efficiently addresses the demand of molybdenum-99 by maintaining economic feasibility and using a commercially available accelerator utilizing molybdenum-100 as target disks.

The Monte Carlo transport code Geant4 was used to simulate the bombardment of molybedum-100 with photons produced by bremsstrahlung. The design of the molybdenum targets consists of 1 cm radius disks with a width of 1 mm contained in a tungsten target holder. The results showed that the majority of the photons resulted with energies between 8 and 15 MeV. In addition, it was found that most photons are attenuated in the first disk, and that water has negligible effects on photon attenuation. In comparison to reactor-based production of molybdenum-99, the time required for distribution in the present proposal will be reduced from six days to two days. Based on our calculations, these time savings represent cost savings of a factor of approximately three. The demand of molybdenum-99 could be met for several hospitals by irradiating the target system for a period of two days that will produce approximately 250 Ci with just one target system and one accelerator.

The thermal energy generated by the reaction and the cooling efficiency of water were analyzed using COMSOL. Several assumptions were made regarding the target and the target holder. Firstly, a no slip condition is assumed to exist between the objects and the fluid. Secondly, it is

assumed that the water is chilled at a constant and uniform temperature. It is also assumed that the fluid cooling the system approaches the target system with a uniform velocity field normal to the molybdenum targets. Thirdly, it is assumed that the targets are internal heat generation sources while in reality there is a distribution in the thermal energy generated within the molybdenum targets. Fifthly, it was assumed that thermal energy only exited the geometry through the fluid which exited the geometry, hence it is implied that thermal energy does not leave the geometry through cross flow. Lastly, the system was assumed to be pressurized to prevent the boiling of the cooling fluid, and that the outlet boundary wall is assumed to experience no viscous stress.

There are two sets of results for the thermal hydraulics analysis conducted by COMSOL. The first case, which represents a normalized results. In that set, the temperature field indicated the coolant was boiling within the system. Therefore, the system would need to be highly pressurized in order to avoid the coolant from boiling. The second set of results, which averages the inlet velocity of the coolant, it is found that the velocity field maintained its distribution however the flow regime is no longer laminar. The turbulent mixing further increases the heat transfer capability of the coolant. Ultimately, the coolant should be able to adequately cool the targets and provide the necessary specific activity required. Further analysis of the effects of pressure need to be considered. However it is not expected that the system will need to be pressurized further than a few atmospheres. Furthermore, there is a lack of information at the interfaces of the targets and therefore tighter more computationally expensive simulations are needed to observe the phenomena. On the contrary, this information is not vital since we know the system level behavior or the target system.

SolidWorks was used to design the required shielding of the project. Shielding was designed for the transportation of the target disks from the accelerator to the transfer processing on hot cells in the laboratory. Shielding was also designed for the container that will be used for transportation from the laboratory where the molybdenum disks were dissolved in sodium hydroxide to the customer's facility.

Lead was the choice of material used in the focal shielding design in order to attenuate the beta and gamma radiation to acceptable dose levels. Thin layer of plastic was also used in conjunction with lead to absorb the beta particles. Thickness of the lead used in shielding designs was calculated to be optimal at 2 inches with respect to weight, cost, and shielding efficiency. Dose

calculations show that at a 1 meter distance, dose rates are approximately 0.991 mSv/hr. This dose rate implies that the transportation of the molybdenum disks would be categorized as Radioactive Yellow-III due to higher radiation levels.

Furthermore, a chemical separation process is necessary to separate the technetium-99m from the dissolved molybdenum targets. Once the customer receives the molybdenum targets in a 4 M NaOH solution, they will pass the solution through a chemical separation apparatus composed primarily of a polyethylene glycol bead resin, a cation exchange resin, and an alumina column. The polyethylene glycol bead resin, known as ChemMatrix, acts as the separator of technetium-99m in the form of technetate ($^{99m}TcO_4^-$) from molybdenum-99 and molybdenum-100 in the form of molybdate ($^{99}MoO_4^{2-}$ and $^{100}MoO_4^{2-}$). The resin captures technetate and releases it when distilled water is injected into the system, while allowing the NaOH/ molybdate solution to flow into a recycling/reuse container. The cation exchange resin, known as the OnGuard II H, then neutralizes this water/ technetate solution before passing into the alumina, known as the Sep-Pak Alumina A Plus Cartridge. The OnGuard also converts the technetate into a pertechnetate in the form of $Na^{99m}TcO_4$. The alumina captures pertechnetate from the water, radiochemically purifies it, then allows an injected 0.9% saline solution to recapture the pertechnetate and transport it into a final product container.

After the NaOH/ molybdate solution has filtered through the ChemMatrix, the customer has the option of letting the solution sit for 24 hours before repeating the process. In this 24 hours, an optimal amount of technetium-99m will decay from molybdenum-99 still present in the solution. This technetium-99m can then be separated in the chemical separation apparatus as before. It is recommended that this process be repeated over five days to ensure substantive activity is collected from the initially received solution.

Finally, after separation has been completed over the five day period, the remaining molybdenum-100 from the initial solution will be returned to the accelerator facility and reprocessed and re-purified into new targets for irradiation.

For optimal results, 500mg of the Wang-ChemMatrix variant should be selected with a solution load of 2 mL/min. This configuration of the chemical separation apparatus is capable of producing a 99% radiochemically pure final product while providing 92.7% of the initial activity received. The remaining 7.8% is due to technetium-99m losses throughout the separation apparatus.

A new method of quality management that adheres to the principle of cGMP was developed. This is because our proposal implements a new production techniques for techniteium-99m. Several parts pertaining to the radionuclidic purity, radiochemical purity and microbiological purity. HPGe counters coupled with HPLC to identify the chemical content of the molybdenum should be an integral part of QC. This with several QA procedures during the molybdenum production will create an effective cGMP program. This can then be the driving force for an effective Quality Management System. The procedures proposed in the design, can serve as the basis in which other facilities can design their Quality Management System.

An economics analysis of our proposal shows that our proposal is economically competitive with the current method of production. The total capital cost is $22140.00, the variable cost is $10265.00, while the marginal unit cost is found to be 20.5 ¢/mCi. This shows that our design would reduce the cost of the customer by over 75% from current cost paid by the customer.

REFERENCES

[1] R. S. J., The Encyclopedia of the Chemical Elements, New York: Reinhold Book Corporatoin , 1968.

[2] C. Westmacott, "The Supply of Medical Radioisotopes: The Path to Reliability," *Nuclear Energy Agency,* vol. 1, no. 6985, p. 173, 2011.

[3] C. o. M. I. P. W. H. E. Uranium, Medical Isotope Production Without Highly Enriched Uranium, Washington, D.C.: The National Academies Press, 2009.

[4] N. R. Canada, "Government of Canada Announces Extension National," [Online]. Available: http://www.canada.ca. [Accessed 27 April 2015].

[5] N. E. Agency, "Review of Potential Molybdenum-99/Technetium-99m Production Technologies," *The Supply of Medical Radioisotopes,* vol. 1, no. 1, p. 74, 2010.

[6] T. S. International, "Accelerator Isotope Targets," TRACE SCIENCES INTERNATIONAL, 2015. [Online]. Available: http://www.tracesciences.com/acceleratorisotopes.html. [Accessed 27 April 2015].

[7] F. B. &. P. Schaffer, "Cross-Linked Polyethylene Glycol Beads to Seperate Pertenetate from Low-Specific-Activity Molybdenum," *The Journal of NUCLEAR MEDICINE,* vol. 1, no. 1, p. 6, 2014.

[8] N. E. AGENCY, "Nuclear Data Services," JANIS, [Online]. Available: http://www.oecd-nea.org/janis/. [Accessed 27 April 2015].

[9] Z. H. H., Handbook of X-Ray Data, Berlin: Springer-Verlag Berlin Heidelberg, 2007.

[10] "Geant 4," 22 April 2015. [Online]. Available: http://geant4.cern.ch/. [Accessed 27 April 2015].

[11] *Ultra-TechneKow DTE,* Kirkland: Mallinckrodt, 2014.

[12] "THE ACCELERATOR TECHNOLOGY COMPANY," MEVEX, [Online]. Available: http://www.mevex.com/index.html. [Accessed 27 April 2015].

[13] "COMSOL Multiphysics," COMSOL, [Online]. Available: http://www.comsol.com/comsol-multiphysics. [Accessed 27 April 2015].

[14] F. J., The Analytical Theory of Heat, New York: Dover Publications, 1955.

[15] P. Talukdar, "Heat Conduction Equation," IIT, Delhi.

[16] F. M. White, Viscous Fluid Flow, New York: McGraw-Hill, 2006.

[17] C. Y. A., Heat and Mass Transfer: A Practial Approach, Boston: McGraw-Hill, 2003.

[18] N. A. A. S. ADMMINISTRATION, "Reynolds Number," Glenn Reserch Center, 12 June 2014. [Online]. Available: http://www.grc.nasa.gov/WWW/BGH/reynolds.html. [Accessed 27 April 2015].

[19] K. B. S. Blundell, Consepts in Modern Physics, Oxford: Oxford University Press, 2006.

[20] "Molybdenum. The all-rounder among the specialists.," PLANSEE, 2014. [Online]. Available: http://www.plansee.com/en/Materials-Molybdenum-402.htm. [Accessed 27 April 2015].

[21] "MANUFACTRUING PNEUMATICS WORLDWIDE," SMC, 2013. [Online]. Available: http://smcusa.com/smc.aspx. [Accessed 27 April 2015].

[22] "NCBI," National Center for Biotechnology Information, [Online]. Available: http://www.ncbi.nlm.nih.gov/. [Accessed 27 April 2015].

[23] U. D. O. H. &. H. SERVICES, "RADIATION EMERGENCY MEDICAL MANAGEMENT," REMM, [Online]. Available: http://www.remm.nlm.gov/. [Accessed 27 April 2015].

[24] NIST, "Physical Measurement Laboratory," Physical Reference data, 1998. [Online]. Available: http://nist.gov/pml/data/xcom/. [Accessed 27 April 2015].

[25] "National Nuclear Data Center," Brookhaven National Laboratory, [Online]. Available: http://www.nndc.bnl.gov/. [Accessed 27 April 2015].

[26] l. Zolle, Technetium-99m Pharmaceuticals, Berlin: Springer, 2007.

[27] S. A. C. Mariela M. Marani, "Screening of One-Bean-One-Peptide Combinatorial Library Using Red Fluorescent Dyes. Presence of Positive and False Positive Beads," *University of Barcelona,* vol. 1, no. 1, p. 5, 2009.

[28] R. E. Sefani Mazzini, Synthesis of Oligonucleotide Derivatives Using ChemMatrix Supports, Zurich, 2008.

[29] F. MM, "Efficient inhibition of MiR-155 function in vivo by peptide nucleic acids," *PubMed,* vol. 1, no. 1, 2010.

[30] R. P. H. S. Sibel Erdem, "Solid-Phase Synthesis of Asymmetrically Subtituted Type Phthalocyanines," *Journal of Organic Chemistry,* vol. 1, no. 1, p. 4, 2008.

[31] J. Spengler, "A Novel Protecting/Activating Strategy for B-Hydroxy Acids and Its Use in Convergent Peptide Synthesis," *Journal of Organic Chemistry,* vol. 1, no. 1, p. 4, 2008.

[32] M. Junkers, "CHemMatrix Resin- A major advanced in solid phase peptide synthesis," *ChemFliles,* vol. 11, no. 1, p. 1.

[33] Thermo Fisher Scientific, *Dionex OnGuard II Cartiges,* 2015.

[34] Waters, "Sep-Pak Alumina A Plus Light Cartidge, 208 mg Sorbent per Cartridge," *Sample Preparation Products,* 2015.

[35] A. U. Government, "CFT Ch. 1," 2008.

[36] I. A. E. AGENCY, "Cyclotron Produced Radionuclides: Guidelines for Setting Up a Facility," *TECHNICAL REPORTS SERIES,* vol. 1, no. 1, p. 229, 2009.

[37] Food and Drug Administration, *PET Drugs-- Current Good Manufacturing Practices,* New Hampshire: Federal Drug Administration, 2009.

[38] WALISCHMILLER, "Master-Slave Manipulator System," HWM, [Online]. Available: http://www.hwm.com/36-1-Manipulator+A200.html. [Accessed 27 April 2015].

[39] P. E. T. Drugs, "Positron Emission Tomography Drugs for Compounding Invertigational and Reserch Uses".

[40] D. M. Bliesner, Establishing a CGMP Laboratory Audit System, New Jersery: Wiley-Interscience, 2006.

[41] S. Ahuja, HPLC METHOD DEVELOPMENT FOR PHERMACEUTICALS, AP.

[42] C. D. NORDIQUES, "RADIOCHRONOLOGY LABORATORY," *AMS,* 2015.

[43] G. J.S. Huber, "Development of a High-Sensitivity Radiation Detector for Chromatography," *Nuclear Science Symposium Conference Record,* vol. 1, no. 1, p. 5, 2009.

[44] R. L. Yuri Kazakevich, HPLC for Pharmaceutical Scientists, New Jersey: Wiley, 2007.

APPENDIX

APPENDIX A: THERMODYNAMICS

Notations

C_p	heat capacity at constant pressure, J/kg/K
g	gravity acceleration, m/s^2
Gr	Grashof number
k	thermal conductivity, W/m/K
L	characteristic dimension, m
n	refractive index
p_{A}	absolute pressure, Pa
Pr	Prandtl number
q	heat flux, W/m^2
Q	heat source, W/m^3
Ra	Rayleigh number
S	strain rate tensor, 1/s
T	temperature field, K
T_{amb}	ambient temperature, K
$\mathbf{u}$	velocity field, m/s
U	typical velocity magnitude, m/s
α_p	thermal expansion coefficient, 1/K
δ_{M}	momentum boundary layer thickness, m
δ_{T}	thermal layer thickness, m
ΔT	characteristic temperature difference, K
ε	surface emissivity
ρ	density, kg/m^3
σ	Stefan-Boltzmann constant, W/m^{2}T^4
τ	viscous stress tensor, N/m^2

APPENDIX B: SHIELDING DESIGN

Equations used to calculate the neutron energy that must be shielded.

$$^{100}_{42}Mo + (14.5MeV)\ ^{0}_{0}\gamma = \ ^{99}_{42}Mo + \ ^{1}_{0}n$$

$$Q = 931.5MeV(99.907477149 - (98.907711598 + 1.008664923))$$

$$Q = \ -8.29\ MeV\ which\ corresponds\ to\ requiring\ 8.29\ MeV\ to\ react$$

Since the incident gamma has 14.5 MeV:

$$E_{neutron} = 14.5MeV - 8.294\ MeV = 6.206\ MeV\ neutrons$$

Equation used for Dose Rate

Dose Rate (Gy/s):

$$=1.602 \times 10^{-13}\frac{J}{MeV} \cdot Yield\frac{1}{Bq \cdot s} \cdot E(MeV) \cdot \mu_{en(tissue)}\frac{cm^2}{g} \cdot \frac{\exp(-\rho_{Pb} \cdot \mu_{Pb} \cdot x_{Pb})}{(L^2)} \cdot A(Bq)$$

Molybdenum-99 Decay Data in the Medical Internal Radiation Dose Format

Radiations	y(i) (1/Bq-s)	E(i) (MeV)	y(i)xE(i)
β- 6	1.64×10^{-01}	1.332×10^{-01} *	2.18×10^{-02}
β- 8	1.16×10^{-02}	2.897×10^{-01} *	3.36×10^{-03}
β- 9	8.22×10^{-01}	4.429×10^{-01} *	3.64×10^{-01}
γ 1	**1.06×10^{-02}**	**4.058×10^{-02}**	**4.32×10^{-04}**
ce-K, γ 1	3.45×10^{-02}	1.954×10^{-02}	6.74×10^{-04}
γ 5	**6.14×10^{-02}**	**1.811×10^{-01}**	**1.11×10^{-02}**
ce-K, γ 5	7.69×10^{-03}	1.600×10^{-01}	1.23×10^{-03}
γ 8	**1.20×10^{-02}**	**3.664×10^{-01}**	**4.41×10^{-03}**
γ 15	**5.76×10^{-04}**	**5.288×10^{-01}**	**3.05×10^{-04}**
γ 21	**1.23×10^{-01}**	**7.395×10^{-01}**	**9.07×10^{-02}**
γ 23	**4.30×10^{-02}**	**7.779×10^{-01}**	**3.35×10^{-02}**
γ 24	**1.35×10^{-03}**	**8.230×10^{-01}**	**1.11×10^{-03}**
γ 26	**9.56×10^{-04}**	**9.608×10^{-01}**	**9.19×10^{-04}**
Kα1 X-ray	1.81×10^{-02}	1.837×10^{-02}	3.33×10^{-04}
Kα2 X-ray	9.53×10^{-03}	1.825×10^{-02}	1.74×10^{-04}
Listed X, γ, and γ± Radiations			1.43×10^{-01}
Omitted X, γ, and γ± Radiations**			6.79×10^{-04}
Listed β, ce, and Auger Radiations			3.91×10^{-01}
Omitted β, ce, and Auger Radiations**			1.26×10^{-03}
Listed Radiations			5.34×10^{-01}
Omitted Radiations**			1.93×10^{-03}

Technetium-99m Decay Data in the Medical Internal Radiation Dose Format

Radiations	y(i) (1/Bq-s)	E(i) (MeV)	y(i)xE(i)
ce-M, γ 1	7.79×10^{-01}	1.629×10^{-03} a	1.27×10^{-03}
ce-N+, γ 1	1.03×10^{-01}	2.105×10^{-03} a	2.16×10^{-04}
γ 2	**8.90×10^{-01}**	**1.405×10^{-01}**	**1.25×10^{-01}**
ce-K, γ 2	8.79×10^{-02}	1.195×10^{-01}	1.05×10^{-02}
ce-L, γ 2	1.07×10^{-02}	1.375×10^{-01} a	1.47×10^{-03}
ce-M, γ 2	1.94×10^{-03}	1.400×10^{-01} a	2.72×10^{-04}
ce-N+, γ 2	3.27×10^{-04}	1.404×10^{-01} a	4.59×10^{-05}
ce-K, γ 3	6.50×10^{-03}	1.216×10^{-01}	7.90×10^{-04}
ce-L, γ 3	2.02×10^{-03}	1.396×10^{-01} a	2.82×10^{-04}
ce-M, γ 3	3.96×10^{-04}	1.421×10^{-01} a	5.62×10^{-05}
Kα1 X-ray	4.03×10^{-02}	1.837×10^{-02}	7.40×10^{-04}
Kα2 X-ray	2.12×10^{-02}	1.825×10^{-02}	3.87×10^{-04}
Kβ X-ray	1.24×10^{-02}	2.060×10^{-02} *	2.55×10^{-04}
Auger-K	2.05×10^{-02}	1.550×10^{-02} *	3.18×10^{-04}
Auger-L	1.04×10^{-01}	2.170×10^{-03} *	2.26×10^{-04}
Listed X, γ, and γ± Radiations			1.26×10-01
Omitted X, γ, and γ± Radiations**			4.41×10-05
Listed β, ce, and Auger Radiations			1.54×10-02
Omitted β, ce, and Auger Radiations**			1.32×10-05
Listed Radiations			1.42×10-01
Omitted Radiations**			5.73×10-05

Total Attenuation with Coherent Scattering for respective photon energies in Lead.

Photon Energy	Photoelectric Absorption	Total Atteniation w/ Coherent Scattering
MeV	cm2/g	cm2/g
4.00E-02	1.34E+01	1.44E+01
4.06E-02	1.28E+01	1.38E+01
5.00E-02	7.29E+00	8.04E+00
6.00E-02	4.43E+00	5.02E+00
8.00E-02	2.01E+00	2.42E+00
8.80E-02	1.55E+00	1.91E+00
8.80E-02	7.32E+00	7.68E+00
1.00E-01	5.24E+00	5.55E+00
1.50E-01	1.82E+00	2.02E+00
1.81E-01	1.10E+00	1.27E+00
2.00E-01	8.46E-01	9.99E-01
3.00E-01	2.93E-01	4.03E-01
3.66E-01	1.76E-01	2.72E-01
4.00E-01	1.42E-01	2.32E-01
5.00E-01	8.26E-02	1.61E-01
5.29E-01	7.24E-02	1.49E-01
6.00E-01	5.41E-02	1.25E-01
7.40E-01	3.40E-02	9.67E-02
7.78E-01	3.05E-02	9.14E-02
8.23E-01	2.70E-02	8.61E-02
9.61E-01	1.96E-02	7.37E-02